# GEOMETRICAL AND KITAEV FRUSTRATION IN SPIN-ORBIT COUPLED MAGNETS

by

**Thomas Halloran**

A dissertation submitted to Johns Hopkins University
in conformity with the requirements for the degree of
Doctor of Philosophy

Baltimore, Maryland
March, 2023

# Abstract

In materials with significant interactions between magnetic spins, the reduction of temperature below the scale of the magnetic interaction of the spins $J \approx k_B T$ generally results in the formation of static spin textures. Frustration between interactions can result in either the significant reduction of the ordering temperature or the formation of an exotic and long sought after spin-liquid state. The origin of the frustration originates from the arrangement of spins on lattices with geometric frustration, such as the triangular and kagome lattices, where no ordered state can satisfy all interactions. Exchange anisotropy induced by strong spin-orbit coupling has emerged as another route towards frustration in so-called Kitaev materials.

In this dissertation, the low energy properties of five different strongly spin-orbit coupled frustrated magnets are investigated experimentally. Through a variety of measurements and theoretical studies, we achieve an understanding of the unusual forms of magnetism in $Ba_4Nb(Ru,Ir)_3O_{12}$, $\beta$-$Li_2IrO_3$, $D_3LiIr_2O_6$, and $BaCo_2(AsO_4)_2$, all of which are investigated for potential spin-liquid behaviour. $Ba_4NbRu_3O_{12}$ and $Ba_4NbIr_3O_{12}$ are "traditional" quantum spin-liquid candidates in that the origin of their frustrated interactions lies in the triangular lattice upon which $(Ru,Ir)_3O_{12}$ $J_{eff} = \frac{1}{2}$ trimers sit. Neutron

scattering measurements and bulk characterization are used to characterize the magnetic ground states and excitations in each material.

The lithium iridates $\beta$-$Li_2IrO_3$ and $D_3LiIr_2O_6$ are Kitaev materials in which strong ferromagnetic bond-dependent interactions are the result of the strong spin-orbit coupled $Ir^{4+}$ ions in octahedral crystal fields on a honeycomb lattice. Isotope enriched powder samples are examined by inelastic neutron scattering, and both materials show evidence of Kitaev interactions. $D_3LiIr_2O_6$ in particular does not show any evidence of magnetic order, and polarized inelastic neutron scattering combined with THz spectroscopy reveal low energy excitations suggestive of a Kitaev spin-liquid ground state.

The final part of the thesis describes extensive work on $BaCo_2(AsO_4)_2$, a material recently examined for its potential realization of Kitaev physics. Detailed analysis of single crystal inelastic neutron spectroscopy in an in-plane field is performed by the application of linear spin-wave theory and molecular dynamics simulations, and we rigorously show that BCAO is not a Kitaev material but instead is driven by competing interactions between first and third neighbors with an XXZ type planar anisotropy.

# Thesis Committee

## Dissertation Readers

Collin Broholm (Primary Advisor)
Professor
Department of Physics and Astronomy
Department of Materials Science
Johns Hopkins Kreiger School of Arts and Sciences

Natalia Drichko
Professor
Department of Physics and Astronomy
Johns Hopkins Kreiger School of Arts and Sciences

Petar Maksimovic
Professor
Department of Physics and Astronomy
Johns Hopkins Kreiger School of Arts and Sciences

Jacob Khurgin
Professor
Department of Computer Engineering
Johns Hopkins Whiting School of Engineering

Todd Hufnagel
Professor
Department of Materials Science and Engineering

Johns Hopkins Whiting School of Engineering

# Acknowledgments

In the years that I spent in my studies, 2016-2023, I have leaned on countless people and have gotten nothing but support in return. For that I am incredibly lucky and grateful, and I could not have finished this without that support.

To begin, I will thank my family for supporting me all of the way along this journey, from Manito Elementary to JHU. To my mom and dad, and my siblings Kevin and Meghan, thank you so much for everything you've done to support me. To Straya, my dog, thank you for keeping me on a routine (willing or not) and for greeting me with a goofy hug no matter what happened that day.

I have many collaborators to thank, but I will try to name a few. Fellow students Loi Nguyen, Emily Zhang, and Félix Desroches were not only essential to much of the work in this dissertation, but were wonderful peers to work with. Kemp Plumb, a postdoc when I arrived, was extremely patient with my limited (zero) knowledge of condensed matter physics, alongside Allen Scheie who was my office mate and friend for many years. Their guidance was irreplaceable in those first few years, and I attribute much of my success to them. I am also grateful to postdocs Yishu Wang and Jonathan Gaudet, who in my later years were wonderful colleagues and mentors.

Within JHU, I thank Prashant Chauhan, Austin Ferrenti, and Tong Chen, who contributed directly to the work presented here. Tyrel McQueen, Natalia Drichko, Peter Armitage, and Seyed Koopayeh, are all brilliant scientists who I have had the pleasure to work with in my time here. I made many friends along the way, too many to list. But from Wellington or Keswick festivities to trivia to board game nights, I will cherish the memories of my time in Baltimore.

My advisor, Collin Broholm, has been the force behind my growth as a scientist throughout the last seven years. I am immensely grateful for all of his patience, kindness, and support. Collin's endless curiosity and calm persistence took my studies in directions that I could have never anticipated. I hope that I can continue to pursue physics with the interest and vigor that Collin helped to foster.

Finally, this journey would have been impossible without my wife Devin. Her love has made this process not just possible but a special time in my life, I will never forget the memories we made together here in Baltimore. This dissertation is as much a product of her efforts as my own, and I am so lucky to be have her in my life.

# Table of Contents

# List of Tables

# List of Figures

# Chapter 1

# Introduction

The concept of symmetry breaking is ubiquitous in the realm of condensed matter physics. In the mean-field formulation, the transitions between different phases of matter are characterized by a so-called order parameter, which appears upon cooling below the critical temperature and characterizes the ordered phase. Consider a simple example, the uniaxial ferromagnet belonging to the group $Z_2$, meaning that it contains only two elements of spin-up or spin-down. This means that the Hamiltonian governing the spin exchange interactions is invariant under transformations belonging to the $Z_2$ group. As spins of this ferromagnet are constrained to be in the $\hat{z}$ direction, the order parameter is then the thermodynamic average of the magnetization in the $\hat{z}$ direction $\langle m_z \rangle$. Provided ferromagnetic interactions between neighboring spins, upon cooling the spins will eventually align to be along the same direction once the energy scale of the interactions exceeds that of thermal fluctuations, breaking the $Z_2$ symmetry.

This prescription of phase transitions is known as the Landau theory of phase transitions, and in its simplest form relies upon mean-field theory [1].

Magnetic phase transitions, structural transitions like that from a solid to a liquid, transitions in liquid crystals, and more are all well described by this paradigm, where a symmetry element is lost upon the emergence of the order parameter. While mean theory breaks down when local fluctuations are strong, the traditional view of a phase transition in condensed matter physics is that it must be associated with a broken symmetry and an order parameter[2].

In magnetic systems such as the simple ferromagnet described above, this concept holds true. An order parameter associated with the uniform magnetization emerges upon cooling which constitutes time reversal symmetry breaking, hereafter referred to as magnetic ordering. There exists one species of magnetism without symmetry breaking. No order parameter exists and there is no symmetry breaking phase transition, but quantum entanglement and new quasiparticle excitations emerge from collective effects differentiating this state from a correlated paramagnet. Proposed by Anderson in 1973, this was called the resonating valence-bond state, and has since been called the quantum spin-liquid (QSL) [3].

The work in this dissertation is centered around the QSL phase of matter. First and foremost, can such an exotic state of matter exist in nature? Secondly, if no features are associated with the QSL phase transition beyond its excitations, how can one hope to identify it? Many resources available that discuss these details in much greater depth than will be covered here [4–6]. Instead, I will focus on the question of which microscopic mechanisms in materials constitute the most promising route for the realization of the QSL phase. I hope that this work helps to inspire the direction of future studies.

## 1.1 Magnetic exchange interactions

The first step in discussing magnetism in correlated electron systems is to introduce the concept of the exchange interaction. In insulating solids with unpaired valence electrons, both spin and orbital degrees of freedom may give rise to magnetic interactions between sites. Typically, the dipolar interaction between spins is weak enough to be considered irrelevant (with exceptions including high spin rare-earth systems like $Ho_2Ti_2O_7$ [7]). A rough estimate of the dipolar interaction between spins on the length scale of an atomic lattice is $\approx 0.1$ meV [8]. Instead, the interaction is governed almost purely by the electrostatic repulsion between electrons subject to the Pauli exclusion principle known as direct exchange, which typically is on an energy scale of 1 meV or greater and decreses rapidly with atomic spacing. I will not be discussing exchange interactions in conducting materials, as they are not relevant to the contents of this dissertation.

### 1.1.1 Common exchange interactions

Direct exchange processes originate from orbital overlap, and when the interactions are isotropic in spin space, they are known as Heisenberg interactions. They may be expressed by

$$\mathcal{H} = -\sum_{\langle i,j\rangle} J_{ij} \boldsymbol{S}_i \cdot \boldsymbol{S}_j. \tag{1.1}$$

Here, the indices $i$ and $j$ denote lattice sites consisting of distinct spin pairs, $J_{ij}$ is the exchange coupling between these ions, and $\boldsymbol{S}$ is the magnetic spin. This exchange originates from Coulomb repulsion and Pauli exclusion, and is the most common starting point for the analysis of magnetic system. The expression may be derived in a number of ways, but all arrive at the same form [8].

This Hamiltonian is extremely flexible. Many insulating magnetic materials may be described in detail through careful analysis of different exchange energies defining an interacting system of spins upon a crystalline lattice [9]. When there are orbital contributions to the magnetic moment and spin-oribt interactions then the magnetic interactions can be anisotropic. In other words, the $x$, $y$, and $z$ Cartesian components of the spin vector will have different exchange interactions. Along with crystal field effects that define the anisotropic nature of the individual spin in these anisotropic interactions are of great importance to determining the lowest energy spin configuration[10]. One example of this that will be relevant in Chapter 5 is known as the $XXZ$ model, which is written as

$$\mathcal{H} = -\sum_{\langle i,j \rangle} \left\{ J_{ij}^{x} (\mathbf{S}_i^x \cdot \mathbf{S}_j^x + \mathbf{S}_i^y \cdot \mathbf{S}_j^y) + J_{ij}^{z} \mathbf{S}_i^z \cdot \mathbf{S}_j^z \right\}. \tag{1.2}$$

Although not an exchange interaction, magnetic ions with an orbital component of magnetization experience what is known as single ion anisotropy. Such crystal field effects, rely on linking spin and orbital moments relativistic spin-orbit coupling. A famous example can be found in rare-earth pyrochlore systems like $Ho_2Ti_2O_7$ and $Tb_2Ti_2O_7$. Here, the large orbital moments and spin-orbit coupling leads to a single ion anisotropy that energetically constrain spins to point along the $\langle 111 \rangle$ direction, which when combined with ferromagnetic interactions on the pyrochlore lattice leads to a state with local

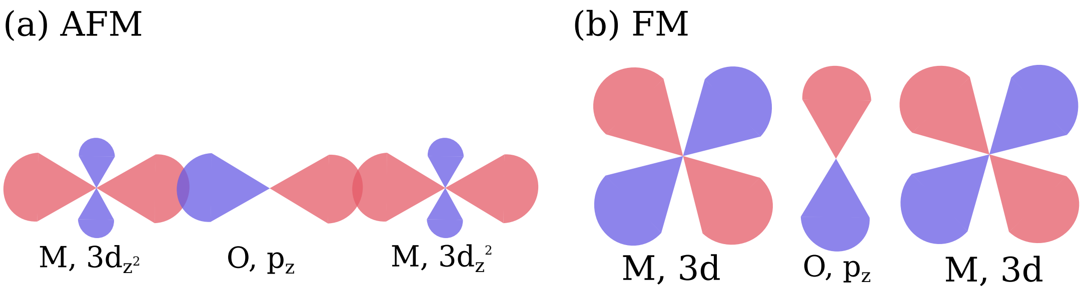

**Figure 1.1:** Sketch of superexchange processes between transition metal ions mediated by oxygen for the antiferromagnetic case (a) and ferromagnetic case (b).

order defined by the so-called "ice rules" [11–13].

Many other types of exchange interactions exist, including the anisotropic Dzyaloshinskii-Moriya (DM) interaction [14] and itinerant interactions between conduction electrons. One additional type of interaction is the anisotropic Kitaev interaction, which will be discussed in detail.

### 1.1.2 Superexchange

The direct Heisenberg exchange described cannot explain antiferromagnetic orders commonly found in transition metal oxides, as the spacing between the *d*-orbitals of the metals is too large to allow for direct overlap. Instead, a process called superexchange takes place, wherein magnetic interactions proceed through an intermediary ion typically with a shared ligand. The idea was first formulated by Anderson [15], and later refined into a semi empirical set of rules by Goodenough and Kanamori [16, 17]. The sign and strength of the interactions are extremely sensitive to the precise M-O-M (Where M is a transition metal ion) bond angle.

Quite often, this process involves two transition metal ions with *d*-orbitals mediated by an oxygen $p$ orbital. The sign and strength of the superexchange process is generally dictated by the Goodenough-Kanamori rules. This process drives the interaction in many of the materials discussed in this thesis, where transition metal ions surrounded by edge-sharing oxygen octahedra allow for strong super-exchange interactions.

### 1.1.3 Magnetic frustration

In the mean-field picture, one expects that the temperature below which a magnetic material forms a static spin structure rather than a paramagnetic phase is controlled by the strength of the exchange interaction. For unfrustrated three dimensional materials with large $S$, the characteristic temperature scale known as the Curie-Weiss temperature, $\theta_{CW}$, provides a quantitatively accurate estimate for the magnetic ordering temperature $T_N$. When there are competing interactions, symmetry breaking may occur at temperature scales far lower than $\theta_{CW}$. Often, this is due to degeneracy between ground states induced by geometrical frustration. Geometrical frustration is a phenomenon where spins are arranged in such a way that the lattice geometry supports a nominally degenerate magnetic ground state. This competition between different ground states is easiest to illustrate for an Ising-type interaction on the triangular lattice, where six different spin configurations are energetically equivalent. Two other famous frustrated lattices are the two-dimensional kagome lattice and the three-dimensional pyrochlore lattice. A relatively unexplored frustrated lattice is the honeycomb lattice, which is not frustrated for only nearest neighbor interactions but requires the introduction of further

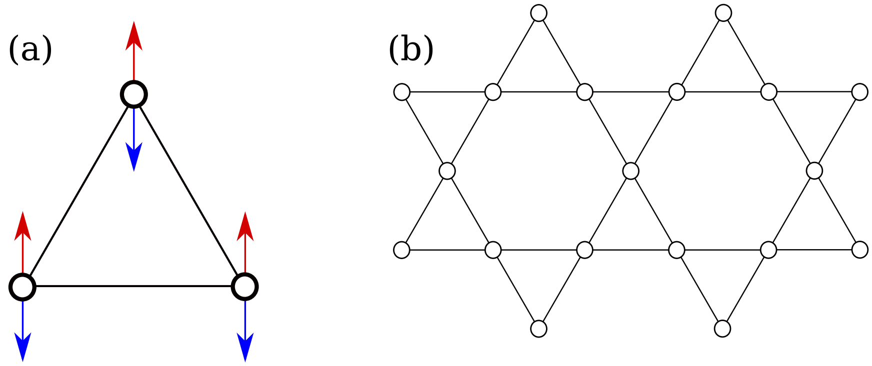

**Figure 1.2:** Examples of geometrically frustrated spins on the antiferromagnetic Ising triangular (a) and Heisenberg antiferromagnetic kagome (b) lattices. For the triangular case, six different spin configurations minimize the total exchange energy in the triangle.

neighbor exchange to induce frustration. Chapters 4 and 5 will investigate materials featuring this lattice in detail, whereas Chapter 3 will focus on the triangular lattice.

## 1.2 Quantum spin-liquids

### 1.2.1 Anderson's model

The origin of the quantum spin-liquid (QSL) may be traced back to Anderson's proposal in 1973 of the so-called resonating valence bond state, which originally was proposed to help explain the bonding structure in benzene rings [3]. The idea was revived again in 1987 in the context of superconducting cuprates, where the RVB picture was suggested to explain the unconventional high temperature superconductivity in these systems [18].

A QSL may be described as a state in which magnetic spins on a periodic lattice do not order magnetically upon approaching $T = 0$ K, but instead form a ground state that does not break any lattice symmetries with a wavefunction that is a linear combination of singlets covering the lattice. The wavefunction has long ranged entanglement of the spin-degree of freedom, giving rise to a large length scale quantum mechanical phase that is entirely unique in magnetism. No order parameter is associated with this type of phase, instead the ground state is characterized by exotic quasiparticle excitations that are topological in nature. This means that the presence of the quasiparticle is apparent in the pattern of singlet coverings even far from the quasiparticle itself. Many varieties of spin-liquids exist depending upon the type of magnetic lattice, the quantum spin number of the magnetic ion, and the exchange interactions, but all are defined by their quantum entanglement and by the quasiparticles that they support.

This is an extremely simplified description, and many resources are available to those interested in further details [4, 19, 20]. Numerical studies have shown that spin-liquids can exist in theory, but in practice the most compelling examples are in 1D spin chain systems like $LiCuSbO_4$ [21] and $CuSO_4{\cdot}5D_2O$ [22]. Although these may be technically called quantum spin-liquids, a much more satisfying realization would be in higher dimensions where quasiparticle interactions are less constrained by momentum and energy conservation. Geometrical frustration is one possible route to a QSL beyond one dimension, but although a number of promising materials exist [5, 23–25] there still is no definitive example of a QSL beyond one dimension in a real material.

### 1.2.2 Kitaev's model

Among QSL's, a special subset of spin liquids exist, which are the Kitaev quantum spin-liquids (KSL) [26]. The KSL has attracted significant attention, both theoretically and experimentally, since the initial proposal in by Alexi Kitaev 2006. Among its appealing features are the fact that unlike all other spin-liquids beyond one dimension, the KSL has an exactly solvable spin-liquid ground state. All other proposed QSL's require the use of approximate numerical methods like density matrix renormalization group (DMRG) [27] studies to support their existence theoretically. As a famous example, the $S$=1/2 kagome lattice with antiferromagnetic interactions between nearest neighbor spins has been shown by DMRG to possibly support a QSL ground state [28], but this is different from the Kitaev case in that it is not an exact result and there remains significant uncertainty about whether ground state is a quantum spin liquid or a valence bond solid.

The Kitaev model may be described as a honeycomb lattice of $S$=1/2 spins with nearest neighbor bond-dependent Ising interactions. The easy axis of these interactions are Cartesian $x, y, z$ axes perpendicular to the bonds. The Hamiltonian may then be compactly written as

$$\mathcal{H} = \sum_{\langle ij \rangle_\gamma} K_\gamma S_i^\gamma S_j^\gamma. \tag{1.3}$$

Here the index $\langle ij \rangle_\gamma$ is over the $x$, $y$, and $z$ type bonds. This is summarized in Fig. 1.3. The balance between the three exchange constants permits different QSL phases. If any one constant is significantly larger than the two others, a gapped phase emerged as shown in Fig. 1.3(b). However, almost all modern

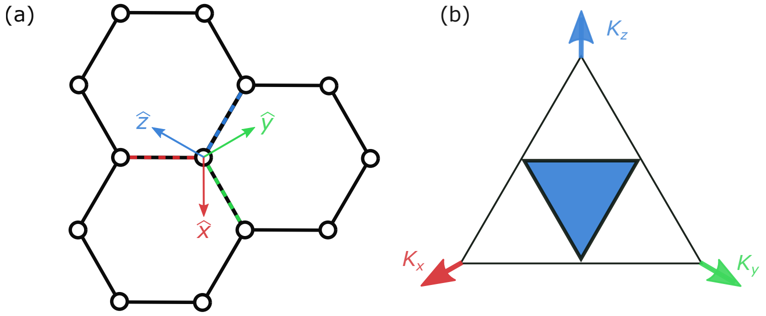

**Figure 1.3:** (a) Sketch of Cartesian $xyz$ axes as defined in the Kitaev model. The axes are orthogonal and tilted out of the plane. (b) Permitted spin-liquid states in the Kitaev spin-liquid versus the $x$, $y$, and $z$ bond exchange. The white shaded areas are gapped spin liquids, and the blue area is the gapless spin liquid containing the isotropic $K_x = K_y = K_z$ point.

studies only consider the isotropic point for $K_x = K_y = K_z$ which results in a gapless state. The full solution of the model is beyond the scope of this dissertation, but it may be summarized in the following way [29]. The original work [26] contains the detailed solution. For each honeycomb plaquette as shown in Fig. 1.3(a), we define a flux operator

$$\hat{W}_p = \prod_{j \in p} K^{\gamma}_{j,j+1}. \tag{1.4}$$

The quantity $K^{\gamma}_{j,j+1}$ is a bond operator where $\gamma \in \{x, y, z\}$ and the subscript denotes the sites forming the bond. This loops over all the bonds in the honeycomb plaquette, and gives eigenvalues +1 for the zero flux configuration and -1 for what is referred to as the $\pi$ flux configuration. The excitation of a plaquette flux is gapped, and we now focus on the ground-state flux sector. The introduction of four Majorana fermion operators allow us to represent the spin degrees of freedom in the form $\sigma^{\alpha}_j = i a^{\alpha}_j c_j$ where $j$ denotes the site and $\alpha$ is the spin component. The bond operators are now given by

$K_{j,k}^{\gamma} = -(ia_j^{\gamma} a_k \gamma) ic_j c_k$. This Hamiltonian is reduced to quartic terms, and may be described as a non-interacting Majorana hopping Hamiltonian in a $Z_2$ gauge field. Interested readers may find the full details elsewhere [26, 29, 30], but the resulting ground state of the KSL may be summarized most succinctly as a quantum spin-liquid with anyonic Majorana fermion and $Z_2$ gauge flux excitations.

Another appealing feature of this model is the nature of the excitations themselves. The Majorana fermions predicted by this result are anyonic, meaning that they obey nontrivial braiding statistics. The braiding of anyonic quasiparticles has been proposed as a method of fault-tolerant quantum computation [31]. The so-called topological quantum computer would have significant advantages over current quantum computing techniques like superconducting qubits or trapped ions, in that the braiding of the anyons would help to prevent decoherence. The first step towards this technology is the discovery of a KSL in a real material.

The exact solubility of the model also permits the calculation of quantities that may be compared to experiment. The dynamical spin structure factor $\mathcal{S}(Q, \omega)$ has been computed in detail [32], along with Raman spectroscopy response [33]. The result is a broad $Q$-independent spectra with an excitation gap (even in the gapless phase), with a second higher energy excitation corresponding to the excitation of the gauge fluxes. Specific heat may also be calculated, and reveals two temperature scales corresponding to the formation of Majorana fermions and then flux ordering at lower temperatures [33, 34] carrying a total magnetic entropy of $\Delta S_{mag} = R \ln(2)/2$ in each peak.

Each of these measurable quantities is not necessarily conclusive evidence for the existence of a KSL state in real materials, as the response is broad and featureless, making the KSL difficult to differentiate from a definitively not quantum correlated paramagnet.

A more direct method for the observation of the fermionic quasiparticle excitations is thermal transport via a finite quantized thermal hall effect for $\kappa_{xy}/T = \pi/12$ [35] upon approaching $T$=0. While this was initially thought to be the correct way to determine if the true ground state of a material is a KSL, experimental studies have resulted in significant controversy regarding the presence of a $\kappa_{xy}$ term in real materials. Thermal transport in general is a difficult measurement technically, as keeping samples and probes thermally isolated is almost impossible, but even for a perfect experiment it has been shown that simple phonons may give rise to a $\kappa_{xy}$ term [36] meaning that background contributions must be removed from these transport measurements before making any conclusions.

So, the prospect of the detection of a KSL state is only slightly better than other spin-liquids. Despite the fact that observable quantities may be exactly calculated, the broad nature of the excitations will always cast doubt on the ground state based on individual measurements. Instead, a combination of different measurements must be used to create a body of work supporting the presence of a KSL state in any given material. A significant part of this is the measurement of the dynamic correlation function using inelastic neutron scattering, which will be featured in this dissertation in Chapter 4.

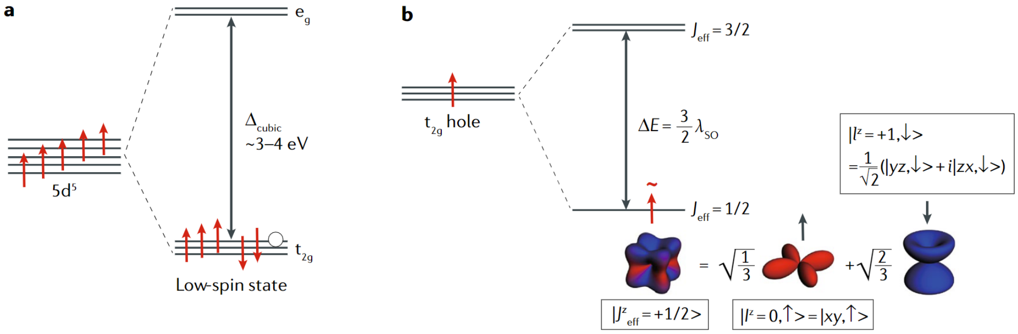

**Figure 1.4:** Realization of Kitaev interactions via spin-orbit coupling in an octahedral field as proposed by Jackeli and Khaliullin, reproduced from Ref. [30].

### 1.2.3 Modern experimental pursuits of Kitaev's model

The peculiar interactions required by the Kitaev model originally meant that it was treated as a toy model, and despite its novel qualities there were no paths to its material realization until a proposal by Jackeli and Khaliullin in 2009 [37]. To realize spatially anisotropic bonding on the honeycomb lattice, spin-orbit coupling was used in heavy transition metal ions with an unquenched orbital moment. For this purpose, $\mathrm{Ru}^{3+}$ and $\mathrm{Ir}^{4+}$ are suitable. We first consider the $d^5$ spin of $\mathrm{Ir}^{4+}$ in an octahedral crystal field, for example in an oxide. For large crystal field splitting, Hund's first rule is broken and the spin configuration may be described as a single hole residing in a $t_{2g}$ orbital manifold of the $xy$, $xz$, and $yz$ orbitals. Considering the single-ion spin Hamiltonian of $\mathcal{H}_0 = \lambda \overrightarrow{l} \cdot \overrightarrow{s} + \Delta l_z^2$, we now consider the effect of spin-orbit coupling on the $\mathrm{t}_{2g}$hole.

Provided that the spin-orbit coupling $\lambda_{SO}$ is great enough, as it is in Ir, the lower energy $\mathrm{t}_{2g}$ manifold is further split into a $\mathrm{J}_{eff}$=1/2 doublet and a $\mathrm{J}_{eff}$=3/2 quartet, with a splitting proportional to $\lambda_{SO}$. The single hole is then accommodated in the $J_{eff}$=1/2 doublet, meaning that each site may be treated as a net $J_{eff}$=1/2 as required by the Kitaev model. The wavefunction of this state is a spin-orbital entangled superposition of the $xy$, $xz$, and $yz$ orbitals of different complex phase, giving rise to spatial anisotropy as visually depicted in Fig. 1.4(b). Considering the hopping between neighboring Ir ions, it may be shown that the effective Heisenberg-type contribution to the exchange has a destructive interference, instead with easy-axis Ising-type interactions emerging where the axes are perpendicular to the bonds. This is precisely the prescription of the Kitaev model, and from this work two main candidate families of materials were proposed. The first is a family known as the honeycomb iridates of the form X-$Li_2IrO_3$ (X=$\alpha, \beta, \gamma$) [38], and the second is $\alpha$-$RuCl_3$ [39].

Both of these materials will be discussed in detail in future chapters, but their status as candidate realization of the Kitaev interaction is worth a brief discussion here. All behave as $J_{eff}$=1/2 Mott insulators. Among this first generation of materials, all show magnetic order upon cooling, thus precluding a pure KSL ground state. For the honeycomb iridate polytypes, the ordering temperatures are $T_N$=15 K, 38 K, and 40 K for $\alpha$, $\beta$, and $\gamma$ respectively [40–42]. The observed orders are of a complex incommensurate spiral as shown through magnetic resonant x-ray spectroscopy [43, 44], while $\alpha$-$RuCl_3$ hosts a zigzag type order [45] for temperatures below $T_N$=7 K. Evidently, there exist non-Kitaev interactions in all of these materials leading to the formation of static spin ordering rather than a QSL phase, and subsequent theory work showed that including a nearest neighbor Heisenberg and off-diagonal exchange originating from direct orbital overlap admits a rich phase diagram of magnetic structures [46, 47] that well describes the observed order in the honeycomb iridates. The case of $\alpha$-$RuCl_3$ is interesting and will be discussed in Chapter 5, but it has been proposed that the observed zigzag order is proximate to a KSL phase. Application of a strong in-plane field of $H_c$=7 T melts the order into an extremely controversial spin-liquid phase that some have called a field-induced Kitaev spin liquid.

With this in mind, what is the future of the study of Kitaev magnetism? The physics of the so-called first generation materials briefly discussed here is already extremely rich, and a better understanding of the precise spin exchange in each is necessary to determine how well the anisotropic Kitaev interaction is realized in each. Despite the materials all being nearly a decade old, only recently has the community begun to converge on these topics. With a better understanding of why these materials fail to realize the KSL, we may then engineer better materials. Both chapters 4 and 5 will discuss examples of these, the first of which is an evolution of the lithium iridates $H_3LiIr_2O_6$ and the second being a honeycomb cobaltate $BaCo_2(AsO_4)_2$. The honeycomb cobaltates have been proposed as a new route for the realization of the Kitaev interaction [48] using a similar method to the Jackeli and Khaliullin mechanism, which will be discussed in detail in Chapter 5.

## 1.3 Overview of thesis

This thesis comprises a brief overview of experimental techniques, and three major research topics. Chapter 2 is a brief overview of the experimental techniques relevant to the results of this dissertation. These techniques include heat capacity, magnetization, susceptibility, and neutron scattering. A brief discussion of experimental strategies for the detection of QSL's is also discussed.

Chapters 3, 4, and 5 each cover different sets of materials. Chapter 3 is a study of a triangular lattice of molecular magnets $Ba_4Nb(Ru,Ir)_3O_{12}$ that may be in a QSL phase, or proximate to one. Chapter 4 discusses inelastic neutron scattering studies of the archetypal Kitaev materials, the honeycomb iridates. These include $\beta$-$Li_2IrO_3$ and $D_3LiIr_2O_6$. Chapter 5 discusses the story of the easy-plane frustrated honeycomb lattice $BaCo_2(AsO_4)_2$, which was originally studied in the context of Kitaev physics but which we shall show is in fact an easy plane magnetic with geometric frustration associated with third nearest neighbor interactions.

Quantum spin-liquids are still an extremely rich area of study, even after decades of research. The contents of this dissertation provide some examples of experimental studies of sufficient quality to make quantitative determinations of the magnetic interactions in highly frustrated quantum spin liquid related materials. My intention in sharing this work is to inform future studies towards the realization of a QSL, and to suggest specific avenues towards that goal that are guided by the results presented in this dissertation.

# Chapter 2

# Experimental techniques

## 2.1 Bulk thermodynamic characterization

As a first step towards understanding exchange interactions in magnetic materials, it is extremely important to first measure their bulk thermodynamic magnetic characteristics. The ones most relevant to this dissertation are specific heat and susceptibility, but there are many other relevant quantities such as thermal and electronic transport measurements that will not be discussed.

The first step towards the study of the phase transitions in magnetic materials is often heat capacity, which detects both the low energy density of excited states and first and second order phase transitions. A first order phase transition will appear as an extremely sharp delta function-like spike in $C(T)$ whereas a second order transition will be a divergent peak or discontinuous jump [2]. Heat capacity measurements also provide a precise measure of the magnetic entropy in a system as a function of temperature

$$\Delta S(T) = \int C(T)/T dT. \tag{2.1}$$

It is often very difficult to separate magnetic specific heat from that associated with phonons, but this information can still be very useful. Phase transitions measured by specific heat can be used to precisely determine critical exponents, from which the dimensionality of the order parameter and of the spin interactions may be deduced [49]. The dimensionality and gap associated with spin-wave excitations in ordered states may be inferred from the low temperature specific heat [50, 51], and a linear Sommerfeld-like contribution to $C(T)/T \propto \gamma$ is often associated with low energy fermionic quasiparticles in spin-liquids and superconductors [52, 53].

Susceptibility, or equivalently magnetization, is also an extremely important tool to measure the effective moment in a system as a function of temperature and field. Susceptibility is formally defined by

$$\chi = \frac{\mathrm{d}M}{\mathrm{d}H}. \tag{2.2}$$

For many electrically insulating spin systems, the fluctuations are in the THz frequency scale or 1 ps time scale. Susceptibility is typically measured in the kHz range, meaning that on the time scale of the probing field the sample magnetization is essentially static. The magnitude of the applied field is also relevant as the fields typically applied in a susceptibility measurement are small compared to the saturation field of the overall magnetization. This means that susceptibility and magnetization in these systems may often be thought of as equivalent.

A high temperature expansion of the Heisenberg model yields what is known as the Curie-Weiss law,

$$\chi = \frac{1}{3}\frac{\mu_{eff}^2}{T - \theta_{CW}}. \tag{2.3}$$

Here $g$ is the Lande $g$-factor, $\mu_{eff}$ is the effective moment of the ion which may also be expressed as $g\mu_B S(S+1)$ where $\mu_B$ is the Bohr magneton, and $\theta_{CW}$ is the Curie temperature. The Curie temperature also gives, to a good approximation at high temperatures, the average magnetic exchange for each ion

$$\theta_{CW} = \frac{\tilde{J}S(S+1)}{3k_B}. \tag{2.4}$$

In this expression, $\tilde{J}$ is the sum of the exchange interactions associated with each ion, or $\tilde{J} = \sum_i J_i$, where the index $i$ is over all unique exchange paths. A positive $\theta_{CW}$ denotes antiferromagnetic interactions, and a negative $\theta_{CW}$ denotes ferromagnetic. Thus, through two relatively simple bulk measurements of specific heat and susceptibility, it is possible to completely map out the phase diagram of the compound of interest, find the effective magnetic moment of the ion, and characterize the exchange interactions.

## 2.2 Neutron Scattering

### 2.2.1 Magnetic neutron scattering

Neutrons are unique as a probe of condensed matter systems in that as a neutral particle, they pass through most matter with ease. The only interactions are the nuclear strong force with atomic nuclei, and magnetic interactions between spin degrees of freedom in the solid and the neutron spin. Neutrons are generated for the purpose of scattering experiments through either a spallation process or in a fission reactor source, and can be moderated with water, liquid hydrogen, or deuterium to produce what are known as thermal or cold neutrons respectively. The energy scale of thermal neutrons makes them ideal for the study of collective modes of excitation in crystalline materials, as their wavelength is on the Å scale which is also the length scale between atoms in solids while their energy matches the 1 meV-100 meV range assosciated with collective modes.

A basic scattering process starts with an incident neutron with wavevector $\boldsymbol{k}_i$. The neutron scatters off the sample and emerges from it with wavevector $\boldsymbol{k}_f$. This process may be elastic or inelastic. The signal to be measured is the scattering probability distribution, which is the Fourier transform of the neutron-sample interaction potential in real space and time, be it nuclear or magnetic in origin. This is also known as the correlation function. In the most general form, the scattering cross-section for magnetic scattering is written as [54–56]

$$\frac{\mathrm{d}^2\sigma}{\mathrm{d}\omega\,\mathrm{d}\Omega} = \frac{k_f}{k_i}\left|\frac{g}{2}F(\boldsymbol{Q})\right|^2 r_0^2 \sum_{\alpha,\beta}(\delta_{\alpha\beta} - \frac{Q_\alpha Q_\beta}{Q^2})S^{\alpha\beta}(\boldsymbol{Q},\omega). \tag{2.5}$$

Here, $r_0 = gr_e = 5.391 \cdot 10^{-13}$ cm is the characteristic neutron magnetic scattering length which originates from the product of the classical electron radius and the neutron gyromagnetic ratio, $g$ is the Lande g-factor, $F(\boldsymbol{Q})$ is known as the magnetic form factor and is the Fourier transformed magnetization density of the ion, the indices $\alpha$ and $\beta$ refer to the Cartesian $x$ $y$ $z$ directions, $k_i$ is the magnitude of the incident scattering vector, $k_f$ is the outgoing scattering vector, and $Q^\alpha$ is the $\alpha$ component of the total momentum transfer $Q$. This process on a triple-axis spectrometer is depicted in Fig. 2.1. An extremely important quantity called the dynamic correlation function $S^{\alpha\beta}(\boldsymbol{Q},\omega)$ appears here. This is defined by [56]

$$S^{\alpha\beta}(\boldsymbol{Q},\omega) = \frac{1}{2\pi\hbar}\int_{-\infty}^{\infty} dt\, e^{-i\omega t} \sum_{\mathbf{r}\mathbf{r}'} e^{-i\mathbf{Q}\cdot(\mathbf{r}-\mathbf{r}')} \langle S_{\mathrm{r}}^{\alpha}(0) S_{\mathbf{r}'}^{\beta}(t)\rangle. \tag{2.6}$$

The double sum is defined as over all pairs of spins in the lattice, and the expectation value $\langle S_{\mathrm{r}}^{\alpha}(0) S_{\mathbf{r}'}^{\beta}(t)\rangle$ is known as the spin-spin correlation function. For elastic processes this is assosciated with $t = \infty$ processes, and inelastic processes have a finite time scale. This quantity may be calculated using numerical or analytical techniques for some systems, making neutron scattering an extremely powerful technique to compare against theoretically predicted excitations.

More detail about various scattering processes, including those from phonons and spin waves, may be found elsewhere [56, 57]. One final note I would like to make is the polarization factor ($\sum_{\alpha\beta}$) in Eq. 2.5. The consequence of this term is that neutrons are only sensitive to the component of the magnetization (static or dynamic) that is perpendicular to momentum transfer. Polarized neutron scattering offers the possibility of further distinguishing the different polarization components as we shall do in 4.

### 2.2.2 Sum rules

The definition of the dynamical spin structure factor $\mathcal{S}(Q,\omega)$ results in useful expressions for its frequency moments, which are defined by [54, 58]

$$\int_{-\infty}^{\infty} (\hbar\omega)^n S^{\alpha\beta}(\mathbf{Q},\omega)d\omega. \tag{2.7}$$

Here the $\alpha$ and $\beta$ superscripts are the Cartesian spin components. The first and zeroth moments are known as "sum rules", which will be used later in this dissertation so a brief discussion of these is valuable. We begin with the $n$=0 moment, which defines the static spin-structure factor $\mathcal{S}(\boldsymbol{Q})$. This is also known as the Fourier-transformed equal-time correlation function and is associated with the energy integrated magnetic scattering, which is related to a measurement with no final energy analysis. It is evaluated as follows,

$$S^{\alpha\beta}(\boldsymbol{Q}) = \sum_{\boldsymbol{r}} e^{i\boldsymbol{Q}\cdot\boldsymbol{r}} \gamma_{\alpha\beta}(l,\infty). \tag{2.8}$$

Here, the sum is over all sites in the lattice and $\gamma_{\alpha\beta}(r,\infty)$ is the infinite-time spin correlation function. The evaluation of this sum gives

$$\sum_{\boldsymbol{r}} e^{i\boldsymbol{Q}\cdot\boldsymbol{r}} \gamma_{\alpha\beta}(l,\infty) = \frac{1}{N}\sum_{ij} e^{i\boldsymbol{Q}\cdot\boldsymbol{r}} \langle S_i^{\alpha} S_j^{\beta}(\infty)\rangle = \frac{1}{N}\langle S_{\boldsymbol{Q}}^{\alpha} S_{-\boldsymbol{Q}}^{\beta}(\infty)\rangle. \tag{2.9}$$

Integrating Eq. 2.9 over the Brillouin zone and taking the trace of the spin indices yields the zeroth moment sum rule

$$\sum_{\alpha}\int S^{\alpha\alpha}(\boldsymbol{Q})\frac{V_0 d^3\boldsymbol{Q}}{(2\pi)^3} = \frac{1}{N}\sum_{i,\alpha}\langle (S_i^{\alpha})^2\rangle. \tag{2.10}$$

The $n$=0 sum rule is also known as the total moment sum rule, which when only considering one species of magnetic ion of identical spin is consequently

$$\sum_{\alpha} \int \int S^{\alpha\alpha}(\boldsymbol{Q}, \omega) \frac{V_0 d^3\boldsymbol{Q}}{(2\pi)^3} d\omega = S(S+1). \tag{2.11}$$

This result is quite powerful in that if the scattering is correctly normalized, the total integrated scattering is a measure of the moment size. This may be compared against the theoretically expected moment or the moment size inferred from magnetization measurements.

We may readily evaluate the first moment sum rule as well, which may be expressed as [54]

$$\int_{-\infty}^{\infty} S^{\alpha\beta}(\boldsymbol{Q}, \omega) d\omega = \frac{-1}{N} \langle S^{\alpha}_{\boldsymbol{Q}} \left[ \mathcal{H}, S^{\beta}_{-\boldsymbol{Q}} \right] \rangle. \tag{2.12}$$

The appearance of the Hamiltonian originates from the evaluation of the first time derivative of the spin-spin correlation function. This result may be applied to various well known spin-systems such as the Heisenberg model [54]. For a Heisenberg magnet, this expression may be used to relate the bond exchange energies $J_n$ to the scattering by

$$\int_{-\infty}^{\infty} \omega S^{\alpha\alpha}(\boldsymbol{Q}, \omega) d\omega = -\sum_{\boldsymbol{d}} J_d \left(1 - \cos(\boldsymbol{Q} \cdot \boldsymbol{d}_n)\right) \langle\langle S^{\beta}_{\boldsymbol{R}} S^{\beta}_{\boldsymbol{R}+\boldsymbol{d}_n} \rangle\rangle. \tag{2.13}$$

Here, the sum is over all unique exchange paths and the quantity $\langle\langle S^{\beta}_{\boldsymbol{R}} S^{\beta}_{\boldsymbol{R}+\boldsymbol{d}_n} \rangle\rangle$ denotes a site-independent lattice averaged spin-spin correlation. When applied to scattering from a powder sample for which scattering is averaged over the isotropic grain orientation distribution, this evaluated cross-section

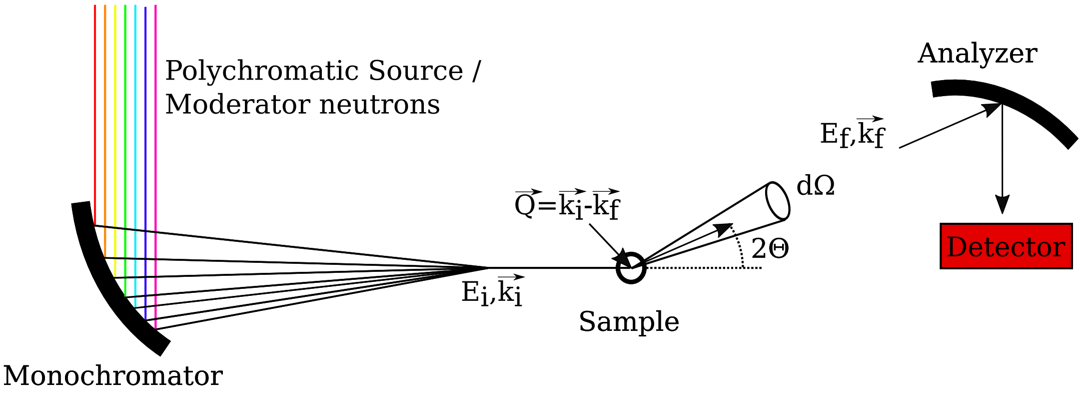

**Figure 2.1:** Sketch of a general scattering process on a triple axis spectrometer.

becomes

$$\begin{aligned}\mathcal{S}(Q) &= -\frac{1}{3}\sum_{d,\alpha} J_d^{\alpha\alpha}\langle \mathbf{S}_o^\alpha \cdot \mathbf{S}_d^\alpha\rangle \int \frac{d\Omega}{4\pi}|F(\mathbf{Q})|^2(1-\cos(\mathbf{Q}\cdot\mathbf{d})). \\ &= \frac{1}{3}\sum_{d,\alpha} J_d^{\alpha\alpha}\langle \mathbf{S}_o^\alpha \cdot \mathbf{S}_d^\alpha\rangle |F(\mathbf{Q})|^2(1-\frac{\sin(\mathbf{Q}\cdot\mathbf{d})}{Qd}).\end{aligned} \tag{2.14}$$

### 2.2.3 Instrumentation

Neutron scattering requires a source of neutrons, which comes in the form of a reactor like the NCNR source at NIST, or in the form of a spallation source like the Spallation Neutron Source at Oak Ridge National laboratory. Both types of facilities exist around the world, but these are the primary sources in the United States and the only facilities that were used for the research in this dissertation. Both types of sources are extremely expensive to operate, meaning that we must travel to national laboratory facilities for these experiments. The principle of both types of sources are the same for direct geometry spectrometers, like the triple-axis spectrometer (TAS) sketched in Fig. 2.1. In the case of the TAS, this is performed by a crystalline array in a monochromator.

An incident neutron energy is selected, and the monochromatic neutron beam then scatters off of the sample. The geometry defined by the incident and scattered beam may be used to determine the momentum transfer to the sample, $\boldsymbol{Q} = \boldsymbol{k}_i - \boldsymbol{k}_f$. Depending on the scattering process, the outgoing neutron may or may not have experienced an energy transfer to or from the sample. To detect this, an analyzing crystal array is used to determine the energy of the neutrons incident on the detector, thereby providing a full description of the scattering process. In a time of flight spectrometer, the incident energy selection is performed by a disk chopper, and the final energy is determined by the time taken for the neutron to travel from the source to the detector via the sample.

### 2.2.4 Normalization of scattering data

As has should be apparent, neutron scattering is an extremely powerful technique to characterize the magnetic properties of samples. One of the many strengths is the ability to calculate exact cross sections given a model of magnetism for comparison to experimental data and perform sum rule analyses that will be used later in the text. This is particularly important in magnetic structure refinements, where magnetic structure factors may be calculated and compared to experimental data after proper convolution with the instrumental resolution function. In order to use these techniques, the experimental data must be normalized to a well-known scattering cross section. There are a number of methods to do this, but we will only discuss those used in the body of this work. A more general review may be found in Ref. [59]. In general the measured intensity from a neutron scattering experiment may be related to a cross section by

$$I(Q,\omega)\mathcal{A} = \left.\frac{\mathrm{d}^2\sigma}{\mathrm{d}\omega\,\mathrm{d}\Omega}\right|_R. \tag{2.15}$$

Here we have defined an overall normalization constant $\mathcal{A}$, the cross section is general and convoluted with the instrumental resolution as denoted by $R$. The cross section to which one normalizes changes depending upon each measurement. A common method is to use a known mass of vanadium which happens to be an almost pure nuclear incoherent scatter with no nuclear Bragg peaks. Assuming that the resolution element is the same (i.e. the same instrumental configurations are used in the measurement of vanadium and the sample), one may find $\mathcal{A}_{van}$ using

$$\frac{\mathrm{d}\sigma}{\mathrm{d}\Omega_{inc}} = \frac{N_{van}}{4\pi}\sigma^{inc}e_i^{-2W}. \tag{2.16}$$

Here $N_{van}$ is the number of vanadium atoms for the known mass of vanadium, the Debye-Waller factor is approximated to be equal to 1, and for elemental vanadium $\sigma^{inc}$ = 5.08 barn. The factor of $\frac{1}{4\pi}$ comes from the fact that $\sigma_{inc}$ is the total scattering cross section whereas the differential scattering cross section is per steradian solid angle, and the energy dimension has been integrated over. It is straightforward to find $\mathcal{A}_{van}$ using the integrated elastic line intensity, which may then be scaled to the sample measurement based on the known mass of vanadium. This is expressed by

$$\mathcal{A}\frac{\int_{Q_{min}}^{Q_{max}}\int_{-\Delta}^{\Delta} I(Q,\omega)d\omega dQ}{\int_{Q_{min}}^{Q_{max}} dQ} = \frac{m_{van}}{50.94}\frac{\sigma^{inc}}{4\pi}. \tag{2.17}$$

Here, the values $Q_{min}$ and $Q_{max}$ are the integration bounds along the $Q$ dimension, $\Delta$ is the integration width in energy around the elastic line, $m_{van}$ is the mass of the vanadium standard in grams, and the factor of 50.94 is the molar mass of vanadium. This is the most straightforward method for normalization. If the sample itself has significant incoherent scattering, one may also normalize to the sample itself in this way but this runs into problems when the sample incoherent scattering is comparable to or less than the instrumental background as is often the case in real measurements.

A second method of normalization is to use structural nuclear Bragg peaks from the sample. The cross section for a Bragg reflection $\boldsymbol{\tau}$ may be written as [57]

$$\frac{\mathrm{d}\sigma}{\mathrm{d}\Omega}_{\boldsymbol{\tau}} = N\frac{(2\pi)^3}{V_0}|\mathcal{F}(\boldsymbol{Q})|^2\delta(\boldsymbol{Q}-\boldsymbol{\tau}) \tag{2.18}$$

$N$ is the number of unit cells, $V_0$ is the unit cell volume, and $\tau$ is the particular Bragg reflection. The nuclear structure factor is expanded as

$$\mathcal{F}(\boldsymbol{Q}) = \sum_d \bar{b}_d e^{i\boldsymbol{\tau}\cdot\boldsymbol{d}} e^{-2W_d} \tag{2.19}$$

The sum in this expression is over one unit cell, with $\bar{b}_d$ being the bound coherent nuclear scattering length of each ion as tabulated in [60] and $e^{-2W_d}$ is the Debye-Waller factor, which generally also depends on $\boldsymbol{\tau}$ and thus is more properly written as $e^{-2W_d(\boldsymbol{\tau})}$. This quantity is readily calculated for any particular experimentally available nuclear Bragg peak. Then, one may compare the integrated intensity of the peak to the calculated cross section in the following manner

$$\int\int d^3\boldsymbol{Q}d\omega I(\boldsymbol{Q},\omega) = \frac{1}{\mathcal{A}}N\frac{(2\pi)^3}{V_0}|\mathcal{F}(\boldsymbol{\tau})|^2. \tag{2.20}$$

For a powder sample, the direction of $\boldsymbol{Q}$ relative to the crystal lattice is randomized by the grain orientation distribution. Thus one measures the spherically averaged scattering cross section

$$\frac{d\sigma}{d\Omega}_{powder} = \int\frac{d\Omega}{4\pi}\left(\frac{d\sigma}{d\omega}\right)_{\tau} = N\frac{(2\pi)^3}{V_0}|\mathcal{F}(\boldsymbol{\tau})|^2\frac{1}{4\pi|\tau|^2}\delta(Q-\tau). \tag{2.21}$$

Finally, this yields the overall normalization condition

$$\mathcal{A}\int\int dQd\omega I(Q,\omega) = \frac{(2\pi)^3}{V_0}\sum_{|\boldsymbol{\tau}|}|\mathcal{F}(\boldsymbol{\tau})|^2\frac{\delta(Q-\tau)}{4\pi|\tau|^2}. \tag{2.22}$$

In this manner, for a powder sample it is straightforward to use all available peaks for normalization in a similar way to how one would perform a Rietveld refinement of the nuclear structure. The sum is performed over the magnitude of momentum transfer $|\boldsymbol{\tau}|$ of the reflections to account for the multiplicity of reflections with the same momentum transfer. For example, in the case of a hexagonal lattice the (001) and the $(00\bar{1})$ reflections both contribute to the scattering over $4\pi$ steradian, meaning that both contribute to the overall intensity at the same $|\boldsymbol{\tau}|$. In the case that a triple-axis spectrometer is used, where one does not have access to the $\omega$ dimension in an elastic scan, the left side of Eq. 2.22 must be multiplied by the FWHM instrumental energy resolution $\Delta_{FWHM}$ to handle the integration along the energy axis. An example of this method applied to $Ba_4NbRu_3O_{12}$ is shown in Fig. 2.2.

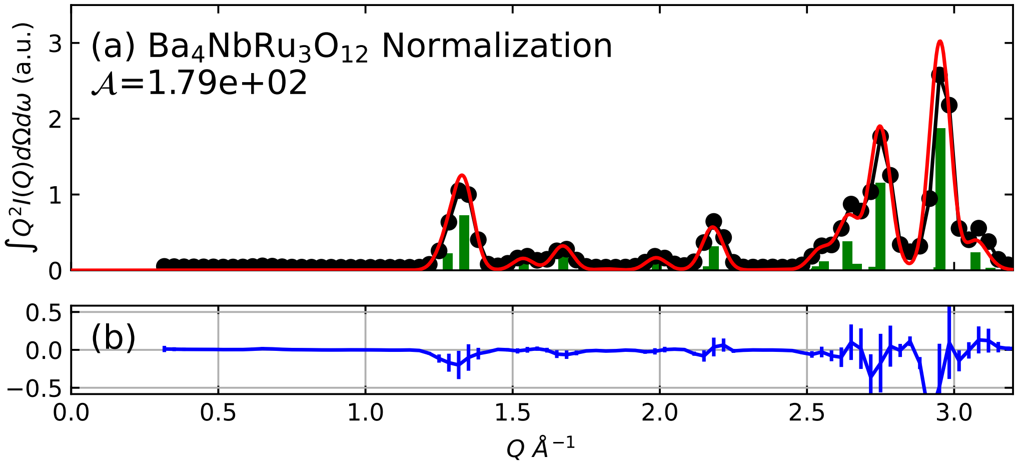

**Figure 2.2:** Example normalization to elastic Bragg scattering for powder Ba$_4$NbRu$_3$O$_{12}$. (a) Black points are the measured intensity integrated over the elastic resolution of the instrument, red line is the fit considering a single Gaussian at every reflection to account for resolution. Green bars represent the structure factor of each reflection in arbitrary units. The fit is used to find the overall normalization scale $\mathcal{A}$. (b) Deviation between fit (red line in (a)) and experimental values (blue line in (a)).

### 2.2.5 Factorization method

For a closer examination of the $Q$ and $\hbar\omega$ dependence of these data, it is expedient to make the assumption that $\mathcal{S}(Q,\omega)$ may be approximated as a product of independent functions of $Q$ and $\omega$. This will be referred to as a factorization analysis, and is written as

$$\begin{aligned} I(Q,\omega) &= 2r_0^2|\frac{g}{2}F(Q)|^2\mathcal{S}(Q,\omega) \\ &= 2r_0^2|\frac{g}{2}F(Q)|^2\mathcal{S}(Q)G(\omega). \end{aligned} \tag{2.23}$$

Within the kinematically accessible range of scattering, this is consistent with these data and has been found to be a good approximation for a number of

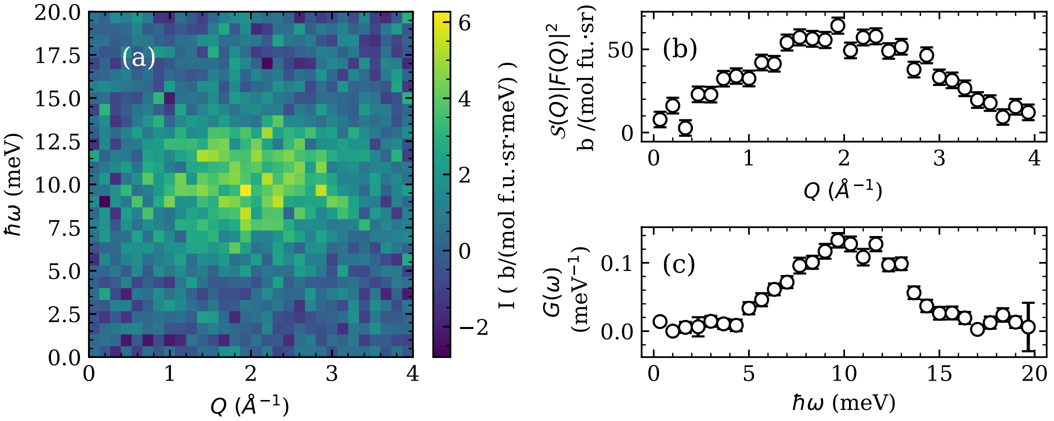

**Figure 2.3:** (a) Simulated scattering consisting of the product of two Gaussian functions with noise, one in the energy dimension and one in the momentum transfer dimension. (b,c) Results of the application of the factorization method to the simulated scattering showing good agreement with the underlying Gaussian forms.

frustrated magnetic materials such as $SrCr_9Ga_{12}O_{19}$ [61, 62] where no long-ranged correlations develop and no dispersion is apparent in the scattering pattern. Here the spectral function is defined to be unity normalized,

$$\int G(\omega)d\omega = 1 \tag{2.24}$$

while the integral over $\mathcal{S}(Q)$ yields the effective moment by a total-moment sum rule:

$$\mu_{obs}^2 = 3g^2\frac{\int \mathcal{S}(Q)Q^2dQ}{\int Q^2dQ}. \tag{2.25}$$

This assumption allows for the full determination of $\mathcal{S}(Q)$ and $G(\omega)$ despite kinematic constraints. A fitting protocol was used to project the $\mathcal{O}(N_Q \times N_\omega)$ experimental pixels onto $N_Q$ values of $|F(Q)|^2\mathcal{S}(Q)$ and $N_\omega$ values of the local excitation spectrum $G(\omega)$ throughout the factorized range of Q and $\omega$.

One of the simplest examples of the results of this procedure is shown in Fig. 2.3(b,c). Here, a simple example of factorizable scattering is generated using the product of two Gaussian functions, with some normally distributed noise. The method does an excellent job of capturing the Gaussians used to generate the scattering, and is more generally applied later in this dissertation.

## 2.3 Observable quantities in quantum spin-liquids

Before moving on to the three major projects of this dissertation, it is important to briefly state how exactly one could hope to detect a QSL state. With no clear order parameter, the excitations are completely different from conventional spin waves and a different approach is needed.

### 2.3.1 Thermal measurements

Although this dissertation focuses on neutron scattering, thermal transport has been proposed as a possible tool for the direct detection of a Quantum spin-liquid state. More precisely, a half-integer quantized Thermal Hall effect would be a direct confirmation of the topological quasiparticles that should be present in a true KSL phase [4]. This may be seen as an analog to the fractional quantum Hall effect seen in graphene [63]. In practice, this quantity is extremely difficult to measure despite some reports of its existence in $\alpha$-$RuCl_3$ that will be discussed later.

### 2.3.2 Dynamical spin structure factor

The dynamical spin structure factor as defined by Eq. 2.6 is a response function related to spin-spin correlations. This quantity may be calculated for a given spin system with a known Hamiltonian by approximate and in rare cases exact theoretical methods. Methods limited in accuracy only by system size include exact diagonalization [64] the density matrix renormalization group method [27]. Approximate methods for the description of excitations from an ordered state include linear spin-wave theory and molecular dynamics, among others. Because the relation between the neutron scattering cross section and the underlying spin dynamics is exactly known, unlike the case for other spectroscopic probes, neutrons are arguably the most powerful tool to probe the nature of the low energy excitations in putative QSL phases. However, no sharp signatures exist in the calculated $\mathcal{S}(\boldsymbol{Q},\omega)$ [23, 32, 65] of the Kitaev QSL due to the lack of long-ranged order. This may be taken as an indication that the scattering occurs through a multi-particle process. The multiparticle continuum is however, difficult to distinguish from the excitations of various disorder dominated states of matter such as the random singlet state that do not have the distinct features of entanglement and fractionalized quasi-particles as for a QSL [66]. Without evidence of quantized thermal Hall transport, the best evidence for a QSL is a collection of scattering data with both theoretical support and other corroborating measurements like heat capacity and susceptibility.

# Chapter 3

# Frustrated triangular lattice $J_{eff}=\frac{1}{2}$ trimer materials $Ba_4NbRu_3O_{12}$ and $Ba_4NbIr_3O_{12}$

## 3.1 Introduction

### 3.1.1 Crystal structure and trimer magnetic units

$Ba_4NbRu_3O_{12}$ and $Ba_4NbIr_3O_{12}$ are two materials in a larger family of perovskites of the form $Ba_4MM'_3O_{12}$ (M=Nb,Ce,Pr) (M′=Mn,Ru,Ir) that all crystallize in the space group $R\bar{3}m$ [67]. A wide family of possible materials exists within this set, and the hexagonal symmetry permits face-sharing $MO_6$ tetrahedra forming dimer, trimer, or longer chain-like units. These geometries are not possible in more widely studied oxide perovskites of the form $AMO_3$ that crystallize with a cubic symmetry where A is a larger ion. The face sharing $MO_6$ octahedra within the magnetic units permit extremely short metal-metal distances and significantly lower M-O-M bond angles than in traditional perovskites.

The magnetic properties of these materials have been explored through bulk characterization studies and their crystal structures are well known, with diffraction data that can be described by a disorder-free structural model. However, little is known regarding the magnetic interactions or excitations in these materials, which will be the focus of the present work. Here we will focus on the relevant family of trimer-based materials of the form $A_4MM'_3O_{12}$, but dimer-based materials of the form $A_3MM'_2O_9$ (A may be an alkali or rare-earth ion) such as $Ba_3InIr_2O_9$[68] and $Ba_3YIr_2O_9$[69] also show interesting magnetic properties and may be of interest in future studies.

Trimer-based materials feature three face-sharing $MO_6$ octahedra, with the $MO_6$ octahedra forming a triangular lattice, introducing the triangular motif and geometrical frustration. A particularly interesting property of these materials (which also exists in dimer-based materials) is that the valence electrons may either be localized around their respective M ions or potentially delocalize within the trimer, which has been proposed for larger 4*d* and 5*d* elements like Ru and Ir. This makes the study of the series of trimer-based materials $Ba_4NbM_3O_{12}$ (M=Mn, Ru, Ir) quite interesting, as the $Nb^{5+}$ site is completely non-magnetic and with increasing atomic number $Z$ the electrons should in principle become further delocalized [70]. Thus, a comparison of these materials with varying spin-orbit coupling on the M-site with $\lambda_{Mn} < \lambda_{Ru} < \lambda_{Ir}$ may be viewed as the transition from a completely localized picture to the more interesting molecular orbital picture of the trimer.

In the completely delocalized picture, the structure consists of well-separated triangular layers of molecular magnets on a triangular lattice. This presents a

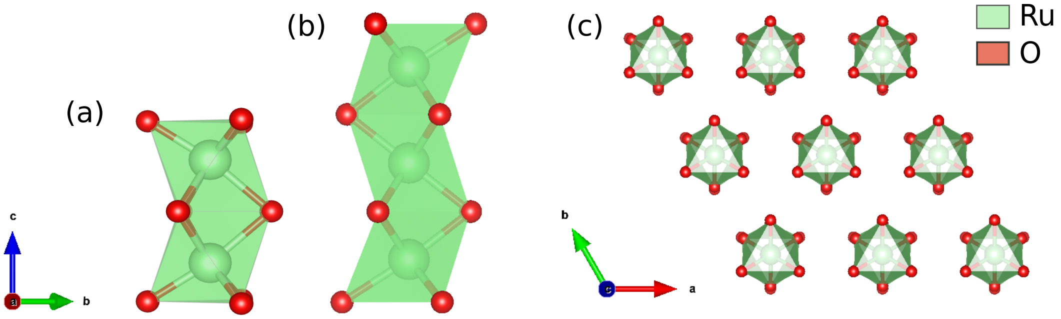

**Figure 3.1:** Depiction of dimer (a) and trimer (b) magnetic units in the hexagonal perovskite materials of the form $A_5Ru_2O_{12}$ and $A_4MM'_3O_{12}$ respectively. The molecular magnetic units themselves arrange within the *a*-*b* plane on a triangular lattice, as depicted in (c). The triangular layers are well separated, which suggests a highly frustrated 2D lattice of molecular spins.

unique scenario. Although frustrated magnetism on the triangular lattice is well-studied, experimental examples of frustrated molecular magnets are few. Notable exceptions to this are organic spin-liquid candidate materials such as $\kappa$-(BEDT-TTF)$_2$Hg(SCN)$_2$Br [71, 72], but our discussion is focused on inorganic materials. Inorganic molecular magnets with triangular frustration in the literature include $LiZn_2Mo_3O_8$, where spin 1/2 degrees of freedom are formed by the $Mo_3O_8$ molecule with a three-fold axis that provides a template for the triangular lattice, and a unique quantum-critical state with short ranged correlations was discovered at low temperature in this material [73–75]. There exists an inevitable site-mixing between the Li/Zn ions to preserve charge neutrality. This has led to suggestions that disorder plays a significant role in this material and may drive it into a random-singlet state like in $YbMgGaO_4$ [76]. These trimer materials differ significantly from $LiZn_2Mo_3O_8$ in that they appear to be chemically clean, with no detectable secondary phases or site disorder apparent in x-ray diffraction refinements[77]. Of course, this does not preclude the presence of site disorder such as oxygen deficiencies in small quantities, but puts an upper limit on their fraction of around 2%.

$Ba_4NbRu_3O_{12}$ and $Ba_4NbIr_3O_{12}$ both have significant spin-orbit coupling from their respective magnetic ions and a net 13 electrons per (Ru, Ir)$_3O_{12}$ trimer, and by an electron counting argument a $J_{eff}$=1/2 ground state doublet emerges from the octahedral crystal field and strong spin-orbit coupling. In an octahedral crystal field, $d$ orbitals split into triply degenerate $t_{2g}$ and doubly degenerate $e_g$ states. Spin-orbit coupling further splits the $t_{2g}$ manifold into two discrete energy levels of a $J = 3/2$ quartet and a $J = 1/2$ doublet[70]. This leads to the picture of $J_{eff}$=1/2 molecular magnets arranged on a triangular lattice, but the validity of the molecular orbital picture in these two compounds is still an open question. Recent DFT studies have supported the idea of a molecular orbital picture in $Ba_4NbIr_3O_{12}$ in particular [78], whereas refinements of magnetic structure and ab initio studies strongly support a localized spin picture for $Ba_4NbMn_3O_{12}$ [79, 80].

With this established, the goal of this portion of the thesis is to determine the nature of the low temperature magnetism in $Ba_4Nb(Ru,Ir)_3O_{12}$, and if that magnetism supports the $J_{eff}$=1/2 molecular orbital picture proposed. There are significant experimental considerations that must be made to achieve this goal. Single crystal samples of these materials are only available in very small $\mu$m length scales, meaning that single crystal neutron studies are impossible. Field dependent measurements are also required to be taken as a powder average. Finally, iridium is a difficult element to work with for neutron scattering as it is prohibitively expensive, has a magnetic form factor that

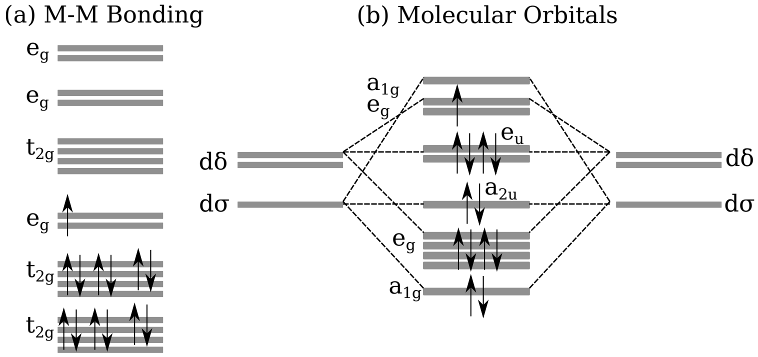

**Figure 3.2:** Two possible energy level diagrams in $MO_{12}$ trimers (M=Mn, Ru, Ir). The electron counting considers the Ru and Ir cases with 13 electrons per trimer giving a net residual spin of 1/2 on each molecule. (a) Direct metal-metal bonding results in a localized picture, as discussed in Ref. [80], whereas the more interesting molecular orbital picture would have the spin degree of freedom spread over the molecule. Diagrams are reproduced from Refs. [67, 77, 80].

disperses strongly with wavevector transfer $Q$, and Ir is furthermore strongly absorbing. For $E_i$=25 meV neutrons, the absorption cross section for natural isotope Ir is $\sigma_{abs} = 425$ b [60].

## 3.2 Magnetic properties

### 3.2.1 Magnetization and susceptibility

$Ba_4Nb(Ru,Ir)_3O_{12}$ are both Mott insulators as indicated by their measured semiconducting band gap despite DFT predictions of a significant density of states at the Fermi energy [77]. Synthesis of both materials was performed by collaborators Loi Nguyen and Robert Cava at Princeton University through a solid-state reaction as reported in Refs [70, 77]. All measurements were performed on pressed pellets of powder samples. High temperature ($T$=1.8-300 K) magnetization and susceptibility measurements were performed in a Quantum Design PPMS (Physical Properties Measurement System) using the VSM (Vibrating Sample Magnetometer) and ACMS (AC Measurement System) options respectively. These measurements used powders enclosed in plastic capsules. For the Ir compound, AC susceptibility measurements were also run in a dilution refrigerator covering a temperature range from $T$=120 mK to $T$=3.8 K, and magnetization measurements were also carried out in a Quantum Design MPMS (Magnetic Properties Measurement System) with the $^3$He option for temperatures from $T$=0.3 K to $T$ =2 K.

The temperature dependent magnetization of $Ba_4NbRu_3O_{12}$ in a magnetic field of $H$=1000 Oe is shown in Fig. 3.3. In the weakly correlated high $T$ regime, the Curie-Weiss law may be used to estimate the exchange interaction $J$. The $\chi = M/H$ vs $T$ curve is fit well to the Curie-Weiss form of $\chi(T) = \frac{C}{T-\theta_{CW}} + \chi_0$, where $\chi_0$ is the temperature independent part of the susceptibility, $C$ is the Curie constant, and $\theta_{CW}$ is the Curie-Weiss temperature. These parameters are found by a least-squares fit to be $\theta_{CW} = -160(20)$ K, $\mu_{eff} = 2.59\ \mu_B$, and $\chi_0$=0.525 memu Oe$^{-1}$ mol-f.u.$^{-1}$. At low temperatures, a signature of spin freezing appears around $T$=4 K, which is the small hump. While $\theta_{CW}$ is not a perfect indication of the true exchange interactions in many materials, its significant magnitude and the absence of any deviations from the Curie-Weiss form down to temperatures $T \ll \Theta_{CW}$ are signatures of geometrical frustration.

We may infer some information about the spin-state of the trimer from the measured moment of $\mu_{eff} = 2.59\ \mu_B$. In a perfect $J_{eff} = \frac{1}{2}$ picture the expected effective moment would be equal to $g\sqrt{S(S+1)} \approx 1.7\mu_B$. In the localized picture, the trimer may either have $S$=3/2 or $S$=5/2. The measured

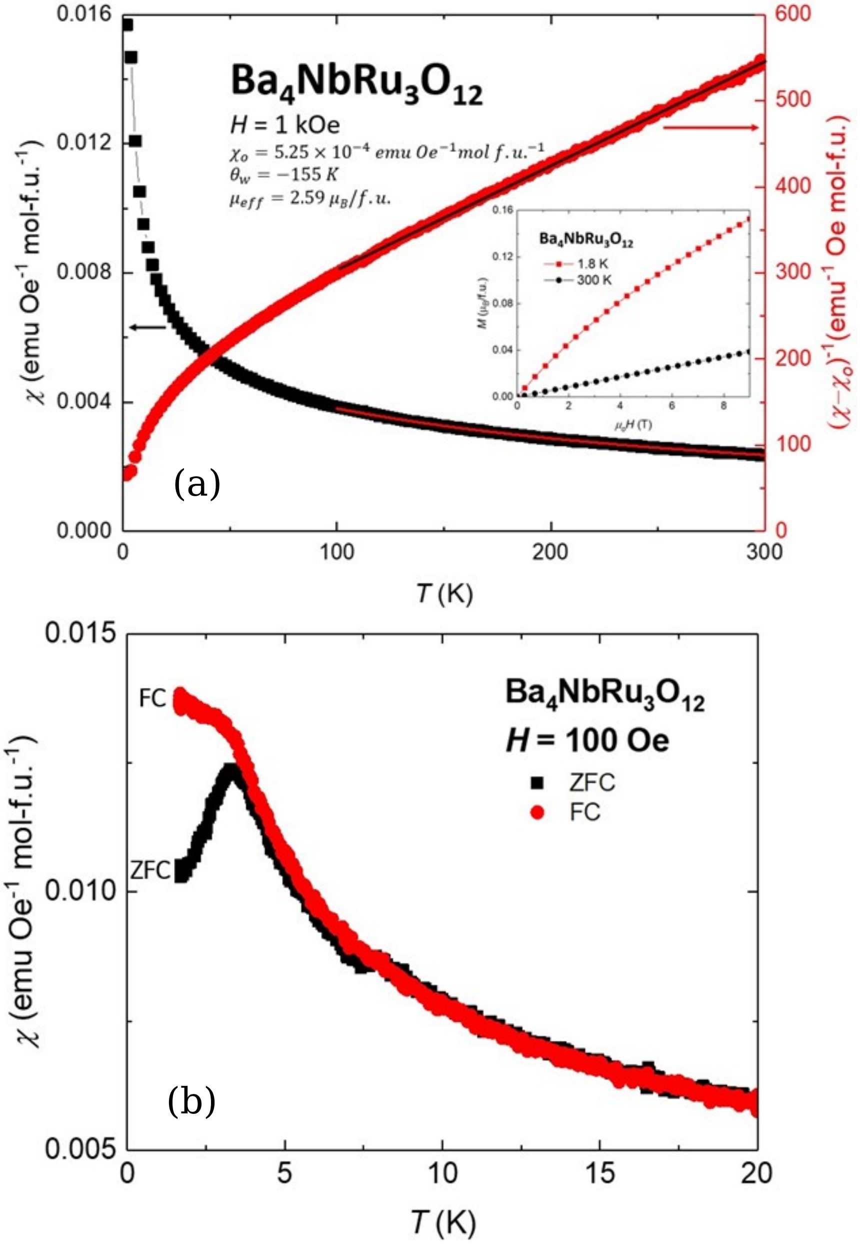

**Figure 3.3:** Susceptibility of $Ba_4NbRu_3O_{12}$ reproduced from Ref.[77].

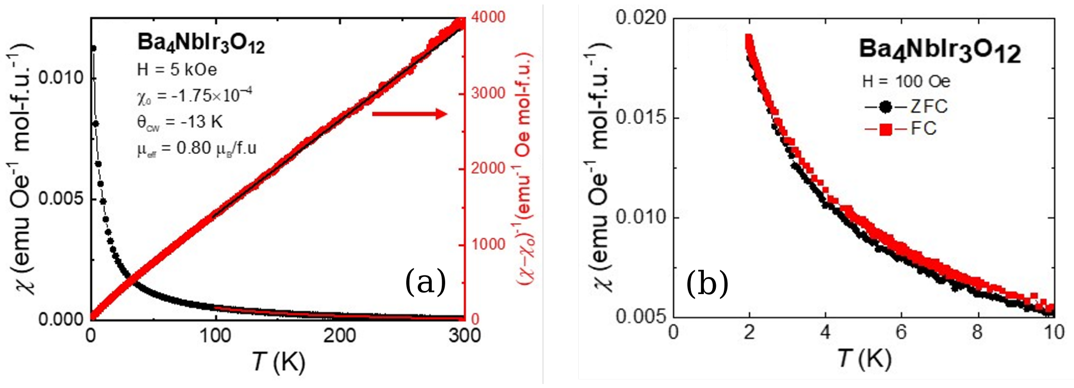

**Figure 3.4:** Magnetization and susceptibility of $Ba_4NbIr_3O_{12}$ reproduced from Ref.[70].

moment is between the pure $g$=2 $J_{eff}$=1/2 picture and the $S$ =3/2 state which would have an expected moment of $\mu = 3.87\ \mu_B$. Magnetization versus field at constant temperatures of $T$=1.8 K and $T$=300 K is shown in Figure. 3.3(b). The magnetization is not saturated at $H$=9 T, with a measured value of $\mu \approx 0.16\mu_B$ f.u.$^{-1}$.

Key evidence of spin-freezing is shown by comparing the field cooled (FC) and zero-field cooled (ZFC) magnetization shown in Fig. 3.3. A clear bifurcation at $T$=4 K is indicative of some form of spin-freezing. This is interesting, as spin-freezing is sometimes indicative of the nucleation of spins to a disordered site, but there is no detectable structural disorder. We conclude that this is the result of strong geometrical frustration.

We now turn to the case of $Ba_4NbIr_3O_{12}$, for which susceptibility versus temperature ($T$=1.8-300 K) is shown in Fig. 3.4(a). The effective moment is quite small at $\mu_{eff} = 0.80\ \mu_B$, and the fitted value of $-\theta_{CW} = 13$ K indicates weak antiferromagnetic interactions between spins[70]. Unlike the Ru case, there exists no bifurcation between FC and ZFC susceptibility, as shown in Fig.

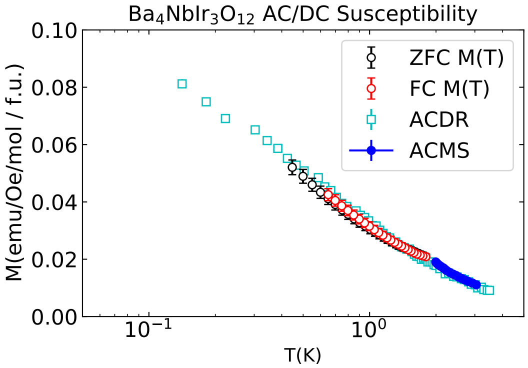

**Figure 3.5:** Low temperature susceptibility of $Ba_4NbRu_3O_{12}$. The lowest accessible temperature of $T$=120 mK shows no signs of spin freezing, and comparisons of the field-cooled versus zero field cooled magnetization performed in an MPMS show no freezing at temperatures above 500 mK. High temperature measurements were performed in the ACMS system as a calibration.

3.4(b). This behavior persists at temperatures as low as $T$=120 mK, as shown in Fig. 3.5. This is extremely interesting and points towards $Ba_4NbIr_3O_{12}$ as a promising quantum spin-liquid candidate, but almost nothing is known at this point about the excitations in the system. For this, we first turn to specific heat capacity measurements.

### 3.2.2 Specific heat

The specific heat capacity of $Ba_4NbIr_3O_{12}$ over a wide temperature range of $T$=100 mK to $T$=300 K is pictured in Fig. 3.6(a). As no nonmagnetic analogue to this material is available, a suitable phonon background was estimated such that the magnetic specific heat, defined as $C_{mag}(T) = C(T) - C_{phonon}(T)$, could be calculated. To do so, a least squares routine was implemented with the following constraints:

1. $C_{phonon}(T) \leq C(T)$, implemented by an exponentially increasing contribution to $\chi^2$. For $C_{phonon}(T) \leq C(T)$, $\chi^2_- = \frac{(C_{phonon}(T)-C(T)^2}{\delta C(T)^2}$, and for $C_{phonon}(T) > C(T)$, the contribution is $\chi^2_+ = \exp\left[\frac{(C_{phonon}(T)-C(T)^2}{\delta C(T)^2}\right] - 1$. Here, $\delta C(T)$ is the measurement error, and the value of -1 in $\chi^2_+$ is required for the overall $\chi^2$ to be a smooth function.

2. In the absence of spin-orbital degeneracy, the full integrated magnetic entropy from an $S$=1/2 system should be equal to $R$ln(2). The magnetic entropy is calculated upon every fit iteration, and deviation from $R$ln(2) contributes to the overall $\chi^2$ by $\chi^2_S = (S_{meas} - R\ln(2))^2$.

3. A minimal functional form must be used that is consistent with harmonic phonons. A superposition of two Debye-type modes and an Einstein (optical) mode were used was found to be the minimal model that satisfies requirements (1) and (2) in the temperature range of $T$=15 K to $T$=200 K.

The functional form used for the Debye modes is

$$C_D(T) = 9RN\left(\frac{T}{\theta_D}\right)^3 \int_0^{\theta_D/T} \frac{x^4 e^x}{(e^x-1)^2}dx. \tag{3.1}$$

Here $R$ is the universal gas constant, $N$ is the number of ions, $\theta_D$ is defined as the Debye temperature, and $x$ is an integration variable. The functional form used for the Einstein mode is

$$C_E(T) = 3Nk_B\left(\frac{\epsilon_E}{k_B T}\right)^2 \frac{e^{\epsilon_E/k_B T}}{(e^{\epsilon_E/k_B T}-1)^2} \tag{3.2}$$

Here $k_B$ is the Boltzmann constant and $\epsilon_E$ is the Einstein frequency. With

| Parameter | Constrained fit |
|---|---|
| $C_{\mathrm{D1,max}}$ (R) | 25.9(5) |
| $\Theta_{\mathrm{D1}}$ (K) | 308(2) |
| $C_{\mathrm{D2,max}}$ (R) | 28(3) |
| $\Theta_{\mathrm{D2}}$ (K) | 813(70) |
| $C_{\mathrm{E,max}}$ (R) | 3.6(1) |
| $T_E$ (K) | 87.2(4) |

**Table 3.1:** Parameters determined by fitting two Debye Models and one Einstein mode to high-$T$ specific heat data of $Ba_4NbRu_3O_{12}$. $\Theta_{\mathrm{D1}}$, $\Theta_{\mathrm{D2}}$, and $T_E$ are the corresponding temperature scales. The high-$T$ limit of each term is denoted as $C_{\mathrm{D1,max}}$, $C_{\mathrm{D2,max}}$, and $C_{\mathrm{E,max}}$. The fit sums to a value of 58(3) $R$, which is consistent with the Dulong-Petit limit of 60 $R$ per formula unit.

these constraints, a model of the phonon specific heat is found that converges to a high temperature specific heat of 58(3)$R$, which is consistent with the value expected by the law of Dulong-Petit of $3nR$ where $n$=20 is the number of atoms in the unit cell. The convergence of the magnetic entropy is shown clearly in Fig. 3.6(b), as well as the resulting $C_{mag}(T)$. The fit parameters of each phonon mode are also reported in Table 3.1. Though this procedure is certainly not as reliable as measurements of a non-magnetic analogue as a background, it qualitatively works very well and its imperfections should not be impactful in the low temperature range where the phonon model is only a small fraction of the signal.

Examining $C_{mag}(T)$ more closely, the entropy is contained in two different peaks. The high temperature peak may be associated with the buildup of short ranged magnetic correlations at the energy scale defined by $\theta_{CW}$, while the low temperature peak is associated with spin-freezing as indicated in the FC/ZFC susceptibility (Fig. 3.3(b)) The low temperature part of the specific heat ($T$<4 K)

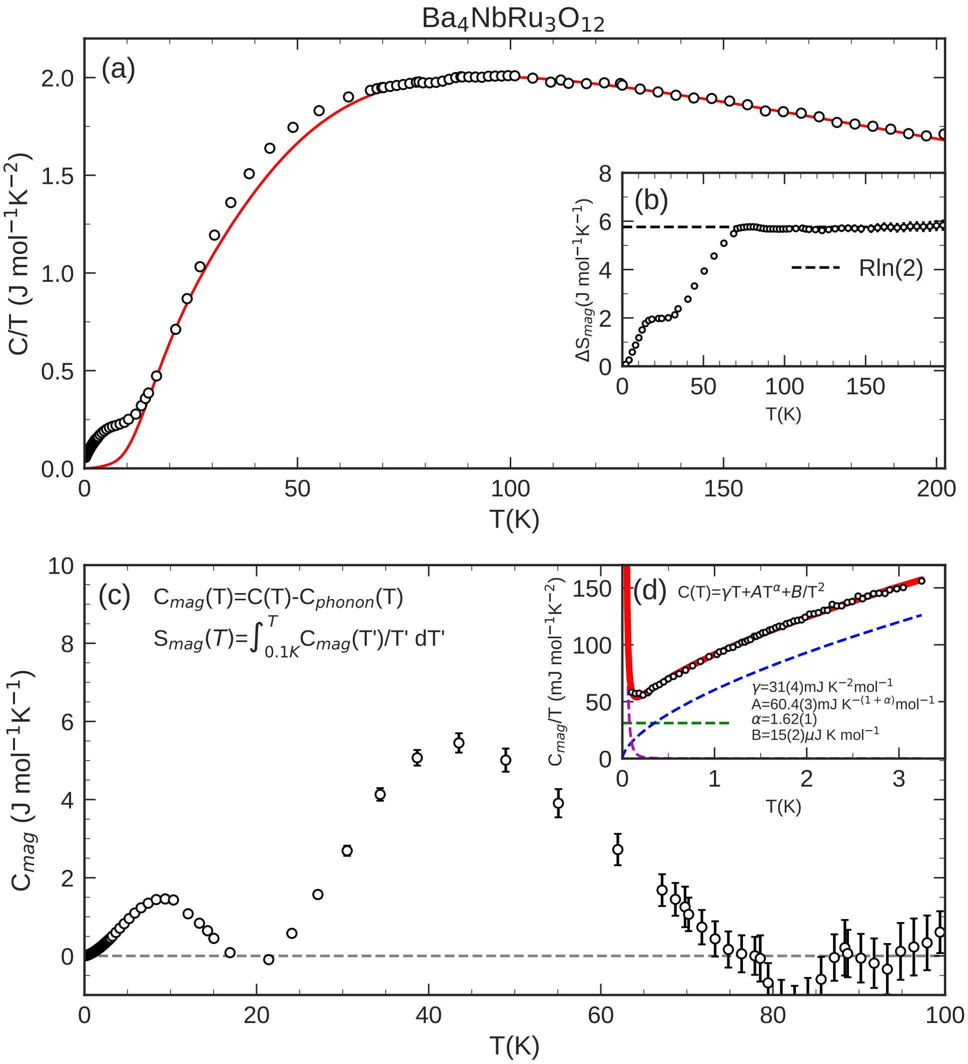

**Figure 3.6:** Heat capacity study of $Ba_4NbRu_3O_{12}$. (a) Full temperature range from $T$=100 mK to 200 K, the red line is the fitted phonon contribution described in the text. (b) Integrated magnetic entropy inferred from the magnetic contribution to $C(T)$ as shown in (c). (d) Low temperature specific heat showing a nuclear contribution and a $\gamma T$ contribution. Individual fit components are represented by dashed lines, with their sum being the red line.

is independent of the rather complicated phonon model previously discussed. At the very lowest accessible temperatures, the small upturn in $C(T)/T$ is associated with the spin-full nuclear isotopes $^{99}$Ru and $^{101}$Ru with a combined natural abundance of 30%. The hyperfine coupling to the frozen ruthenium nuclear magnetism gives rise to a $C_{mag}(T) = B/T^2$ contribution to the total specific heat. The nuclear spin term is an independent confirmation of the presence of the frozen moment, and one can perform a fit to this contribution to the specific heat to extract an estimate of the frozen moment. In this case, the anomaly is centered at too low of a temperature for a consistent fit, but in the case of rare-earth pyrochlore systems with large moments this method works very well [81].

Further examining the low-temperature specific heat using double log plot reveals a clear finite value of $C_{mag}(T)/T \propto \gamma$. An overall model of $C_{mag}(T) = \frac{B}{T^2} + \gamma T + AT^{\alpha}$ accounts well for the data for $T < 3$ K as shown by the solid line and the decomposed dashed lines in Fig. 3.6. The origin of the $\gamma$=31(2) mJ/mole-K$^2$ term is unknown, but often persists in spin-glass materials such as this or may be associated with a spinon-Fermi surface [82] if the remaining unfrozen spins form a spin-liquid like state below the freezing temperature [83]. Another possibility is what is commonly known as a random-singlet state [76]. A final observation that may be made from the specific heat capacity data is that the power law term with $\alpha = 1.62(2)$ contrasts with the power seen in other two-dimensional quantum magnets of $\alpha = 2$ which has been associated with linearly dispersive quasiparticles in two-dimensions [84].

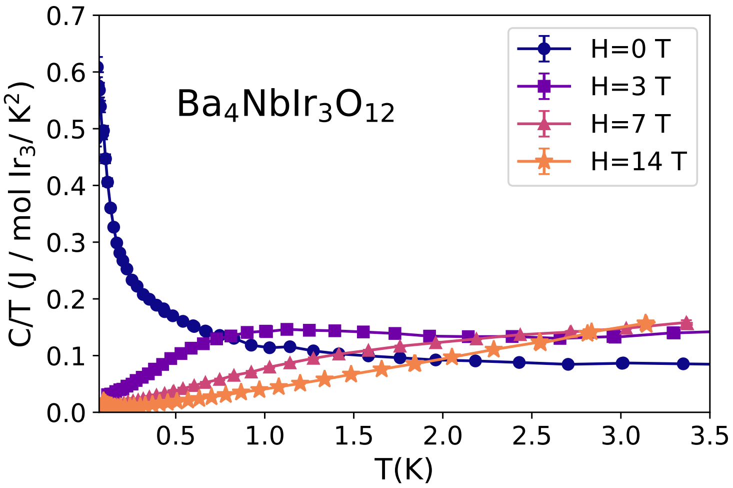

**Figure 3.7:** Low temperature specific heat of Ba$_4$NbIr$_3$O$_{12}$ in the presence of a magnetic field.

The specific heat of Ba$_4$NbIr$_3$O$_{12}$ is even more interesting than the Ru$_3$ case, with the specific heat in the low temperature regime ($T$ <3.5 K) pictured in Fig. 3.7. Even at the lowest accessible temperature of $T$=50 mK no detectable specific heat anomaly associated with magnetic ordering is found. This is consistent with the lack of anomalies indicative of magnetic ordering or spin freezing in the magnetic susceptibility data. Instead, a significant buildup of $C(T)$ is found at very low temperatures, signifying a large density of states of low energy excitations. The zero-field specific heat integrated from over the full range presented in Fig. 3.7 represents only ≈8% of the full expected entropy of $R$ln(2) from a $S$=1/2 system.

This buildup is not consistent with nuclear spin hyperfine splitting, as there is no evidence for magnetic order and in the presence of a field these excitations appear implying the formation of a significant gap. There are few ways to explain this buildup of magnetic entropy at low temperatures without the presence of exotic excitations such as those that would exist in a quantum spin-liquid. One less exotic possibility is a gradient electric which is a consequence of a lack of inversion symmetry on the two $Ir^{4+}$ sites, which could break the nuclear spin degeneracy in the absence of time reversal symmetry breaking magnetism. These data are extremely encouraging, and strongly suggest that $Ba_4NbIr_3O_{12}$ could be a triangular-lattice quantum spin-liquid.

## 3.3 $Ba_4NbRu_3O_{12}$ elastic neutron scattering

The sample used in neutron scattering measurements consisted of 20(1) grams of powder prepared by solid state reaction as described in Ref. [77]. The purity of these samples was confirmed by powder x-ray diffraction refinements which places an upper limit of secondary phases of 3%, but no impurities were detected within this limit. An elastic neutron measurement was performed on the MACS instrument [85] at $T$=2.0(1) K, with $E_i$=$E_f$=3.7 meV neutrons to detect the frozen moment. The intensity of the scattering is normalized to the $(10\bar{1})$ nuclear Bragg peak to obtain an absolute measure of the partial differential scattering cross-section as described in Sec. 2.2.4. The temperature dependent scattering was measured up to $T$=25 K. Temperature dependent magnetic scattering is shown in Fig. 3.8. To isolate the magnetic scattering, we have subtracted the signal at $T$=25.0(1) K. Upon cooling below $T$=15 K, the elastic scattering intensity grows which is indicative of the development of static magnetic correlations or spin freezing. The $T$=8 K maximum in the magnetic specific heat may be the thermodynamic indicator of the freezing transition. The different timescale associated with the measurements typically

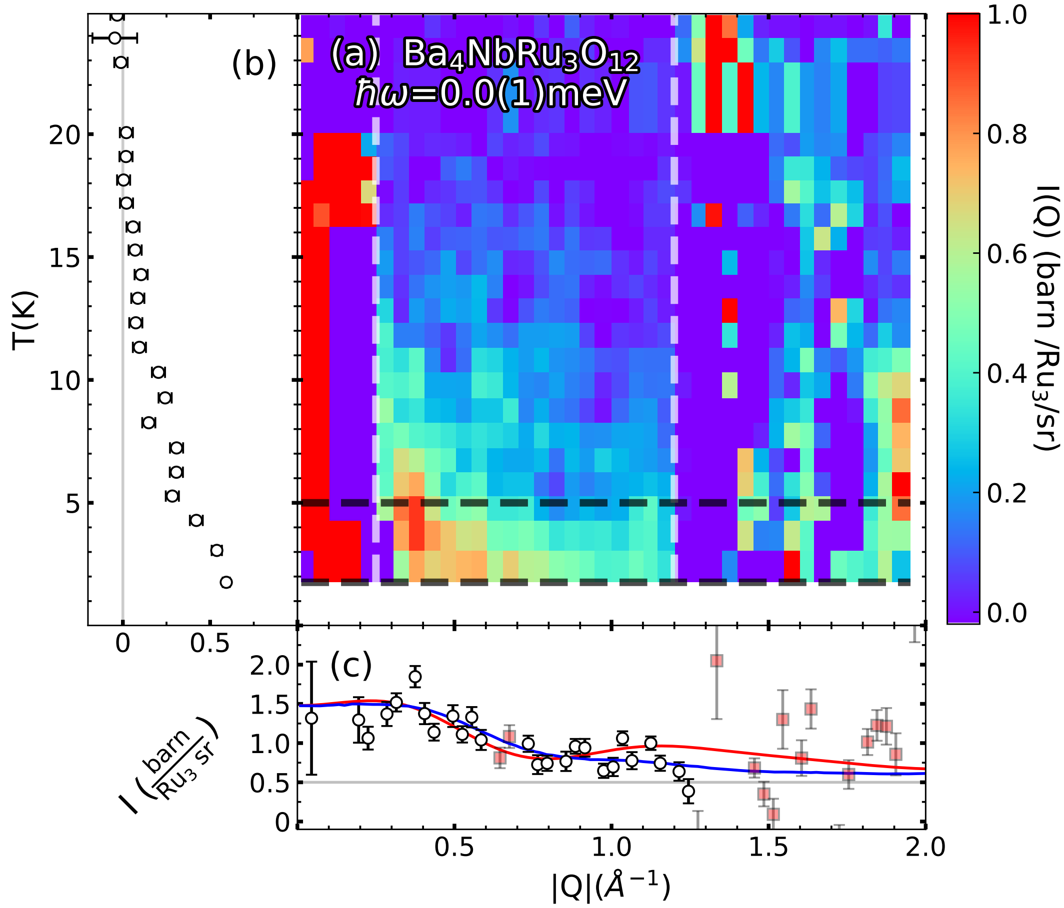

**Figure 3.8:** (a) Temperature dependence of elastic magnetic scattering of $Ba_4NbRu_3O_{12}$ acquired on the MACS instrument with $E_i$=3.7meV. Averaged signals from temperatures ranging from 20 K to 25 K were subtracted as a background to isolate the magnetic signal associated with spin freezing. (b) Temperature dependence of bulk of magnetic signal integrated within the range of the white lines. The signal dramatically increases below temperatures of 10.0(1) K. (c) Cut along $Q$ integrated in the temperature range shown by the black lines. The red line is a fit described later in the text assuming scattering from Ru ions. The blue line is the same fit but using assuming scattering from a trimer molecular magnet. The red boxes denote points that are contaminated by Bragg peaks and were not used in the fit.

leads to different characteristic temperatures of spin freezing transitions. Integrating the observed scattering shown in 3.8(c) over $Q$ yields an observed root-mean-square (RMS) frozen moment of $\mu_{static} = 1.2(3)\mu_B$ which is static on the timescale of 30 ps associated with the 0.15 meV FWHM resolution of the instrument. Though $T << \theta_{CW} = -155$ K, the elastic scattering clearly does not take the form of Bragg peaks, signifying the absence of long-ranged order and a short ranged spin correlations even in the ordered state. The functional form of the solid line fit shown in 3.8(c) is described later, but are theoretical fits involving only nearest-neighbor correlations that will be described in greater detail later.

## 3.4 $Ba_4NbRu_3O_{12}$ Inelastic neutron scattering

Inelastic scattering was measured using the SEQUOIA instrument at Oak Ridge National Laboratory [86] with incident energies of $E_i$=10.5 meV, 25 meV, and 50 meV using the high flux chopper configuration. An equal accumulated proton charge of 14 C was used in all of these measurements, and equal time was spent counting at $T$=4.0(1) K for the magnetic signal and T=300.0(1) K (150.0(1) K) to acquire background data for $E_i$=25 meV and $E_i$=50 meV ($E_i$=10.5 meV). An empty aluminum can was used as a background for all measurement configurations to account for scattering from the sample environment and the sample container. Combining the data obtained with all $E_i$ values, we obtain a full excitation spectrum extending from $\hbar\omega = 1.0(2)$ meV to 45 meV energy transfer that is broad $Q$-space. The high temperature measurements were used to help isolate the magnetic scattering in a process that will now be described in detail. Multiphonon contributions were determined using the OCLIMAX software package [87]. Fig. 3.9 shows a color map of the dynamical correlation function $\mathcal{S}(Q, \hbar\omega)$ at T=4.0 K obtained by a combination of neutron scattering data with different $E_i$ configurations as described previously. Based on the short ranged nature of the frozen magnetic state, the absence of sharp features in the inelastic scattering from a powder sample is expected. Instead, we observe that $\mathcal{S}(Q, \hbar\omega)$ is extremely broad in both momentum and energy transfer space, with a maximum at low $Q$ and an energy transfer dependence resembling $\mathcal{S}(\omega) \propto \hbar\omega^{-1}$. While this is consistent with dynamical correlations of a macroscopic interacting spin-system with short range spin freezing, intramolecular excitations are not observed. These would be sharp features in $\hbar\omega$ resembling discrete crystal field levels.

### 3.4.1 Isolation of inelastic magnetic scattering

The directly measured intensity (after normalization and sample environment background subtraction) for all three incident energy configurations is shown in Fig. 3.10. There are three main contributions to the scattering evident in all measurements that are necessary to separate. The first is the high-$Q$ part of the scattering ($Q > 2$ Å$^{-1}$) that is dominated by optical phonons involving oxygen. The second is the low-$Q$ ($Q < 1$ Å$^{-1}$) contribution to the scattering that is presumed to be of magnetic origin. The final contribution is a pervasive flat background that exists despite the subtraction of an empty aluminum can measurement, which is most clearly seen for $1$ Å$^{-1} < Q < 2$ Å$^{-1}$ in Fig. 3.10(b).

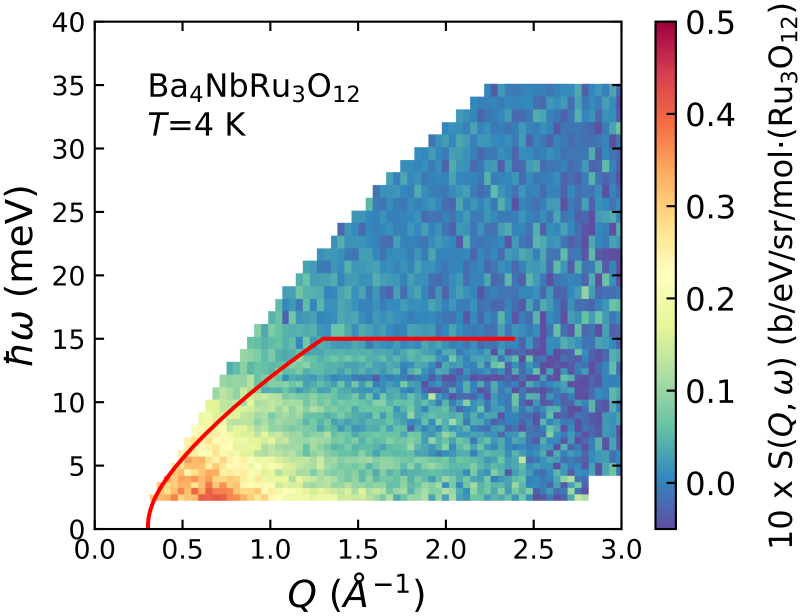

**Figure 3.9:** Extracted magnetic scattering of Ba$_4$NbRu$_3$O$_{12}$. Three incident energies are used in this, E$_i$=50 meV, E$_i$=25 meV. The boundary between these configurations is shown by the dashed red line.

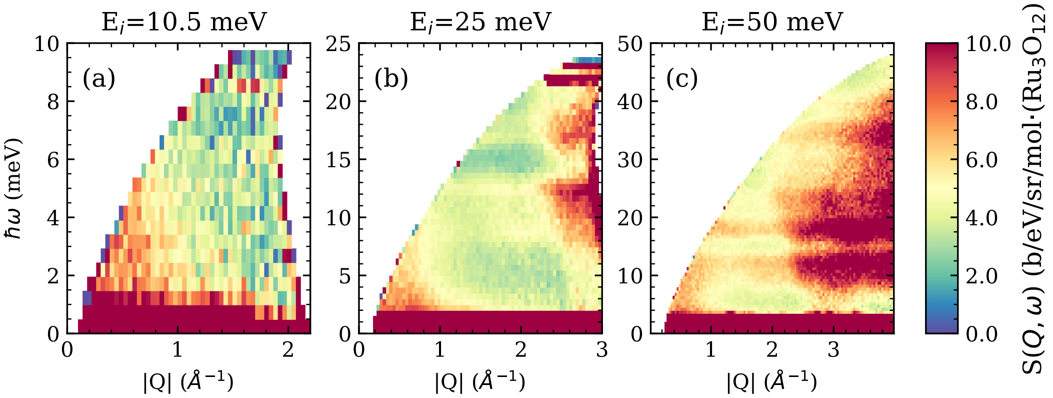

**Figure 3.10:** Normalized scattering from Ba$_4$NbRu$_3$O$_{12}$ at $T$=4 K for the (a) E$_i$=10.5 meV, (b) E$_i$=25 meV, and (c) E$_i$=50 meV configurations.

The isolation of inelastic magnetic scattering in $Ba_4NbRu_3O_{12}$ is a nontrivial task that will be summarized here. If the only contributions to the measured intensity was the magnetic and the one-phonon cross-sections, it is possible to remove phonons from a low temperature measurement by subtracting a high temperature measurement, where phonon scattering dominates after scaling the data by the ratio determined by the Bose-Einstein population factor. This is described by the expression below where the subscripts $H$ and $L$ refer to the low and high temperatures respectively, and $\beta = 1/k_B T$,

$$I_{mag}(Q, \hbar\omega) = I_{low}(Q, \hbar\omega) - \frac{1 - e^{-\beta_H \hbar\omega}}{1 - e^{-\beta_L \hbar\omega}} I_{high}(Q, \hbar\omega). \tag{3.3}$$

This method relies on a number of assumptions that are invalid in the case of $Ba_4NbRu_3O_{12}$. First, the high temperature measurement is assumed to have no magnetic scattering and to constitute a purely non-magnetic background. Second, the only contribution to the background at low temperatures is assumed to be from single-event one phonon scattering. In systems like $Ba_4NbRu_3O_{12}$ with complex unit cells, higher order phonon processes are often present and should be accounted for (though they frequently are ignored). Finally, this subtraction cannot handle the case when multiple scattering contributes significantly to the overall signal.

A simplified model of the different contributions to the measured scattering intensity may be written as

$$I(Q, \hbar\omega) = I_{mag}(Q, \hbar\omega) + I^{1}_{ph}(Q, \hbar\omega) + I^{n}_{ph}(Q, \hbar\omega) + I_{m}(Q, \hbar\omega). \tag{3.4}$$

Here, the total observed intensity is a linear combination of the desired magnetic scattering $I_{mag}$, single-event phonon scattering $I^1_{ph}$, multiphonon scattering $I^n_{ph}$, and multiple scattering $I_m$. To estimate the multiphonon scattering, a DFT simulation was performed using the VASP package [88]. The calculation used the Projector Augmented Wave method to describe the effects of the core electrons, and the Perdew-Berke-Ernzerhof implementations of the generalized gradient approximation for the exchange correlation functional. The electronic structure was calculated on a 6x6x1 Γ-centered mesh. Force constants were calculated using DFPT in VASP, and the vibrational eigenmodes were calculated by solving the dynamical matrix using PhononPy [89]. Finally, the OCLIMAX software was used to convert the calculated phonons into a simulated INS spectra accounting for the instrumental resolution of the SEQ instrument [87]. OCLIMAX provides an exact calculation of phonon cross-sections up to four phonon processes, allowing us to sufficiently account for these at every temperature. The calculated low temperature phonon scattering is shown in Fig. 3.11 normalized to the measurement using integrated intensities at high values of $Q$ where phonons dominate.

$$I^O(Q,\hbar\omega) = I^{O,1}_{ph}(Q,\hbar\omega) + I^{O,n}_{ph}(Q,\hbar\omega),$$

Here, the superscript $O$ refers to the calculated OCLIMAX values. While the phonon cross-section is accounted for, we now consider the effects of multiple scattering. Multiple scattering in powders is difficult to deal with, and can be a significant contribution to the background in cases where (1) the sample has a high elastic incoherent cross-section or (2) there is a large mass of sample, giving neutrons many opportunities to scatter more than once. In this case it

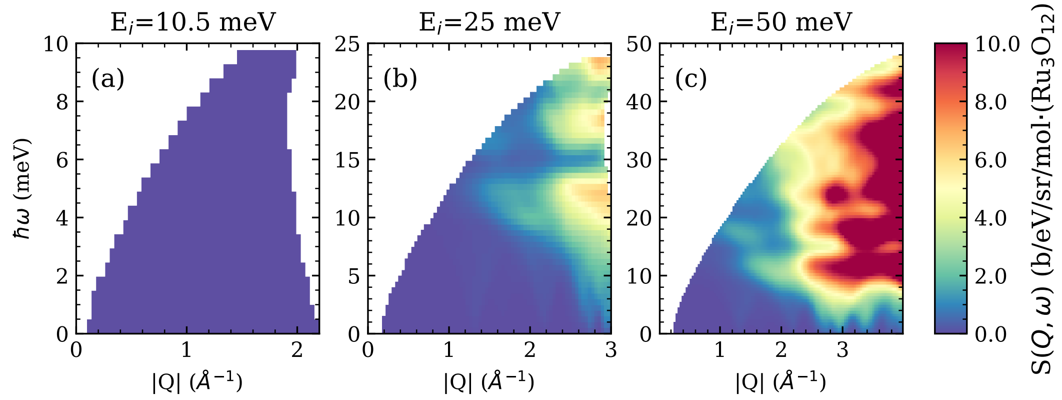

**Figure 3.11:** Calculated phonon scattering for $Ba_4NbRu_3O_{12}$, normalized to the observed phonon scattering intensity.

is the latter, as the sample was of mass 20 g in a cylindrical powder can.

Following Ref. [90], we take the multiple process to be one strong elastic process (such as incoherent scattering) and one inelastic phonon event. Making the assumptions that the incoherent elastic scattering is isotropic and independent of energy and that the sample geometry is not relevant, this process leads to a detected signal of the form

$$I'_{ph}(Q,\hbar\omega) = \mathcal{T} I_{ph}(Q,\hbar\omega) + (1-\mathcal{T}) \int_{|k_i-k_f|}^{k_i+k_f} I_{ph}(Q',\hbar\omega)\frac{Q'dQ'}{2k_ik_f} \tag{3.5}$$

$\mathcal{T}$ is the fraction of single-event phonon scattering processes, the integral represents the solid angle average of the intermediate scattering process, and the prime denotes the full intensity resulting from both single event scattering and multiple scattering. One approach here would be to assume that scattering from phonons takes the form of $I(Q,\hbar\omega) \propto \frac{C}{\hbar\omega} Z(\hbar\omega)$, where $C$ is a constant and $Z(\hbar\omega)$ is a phonon density of states. In our case we have

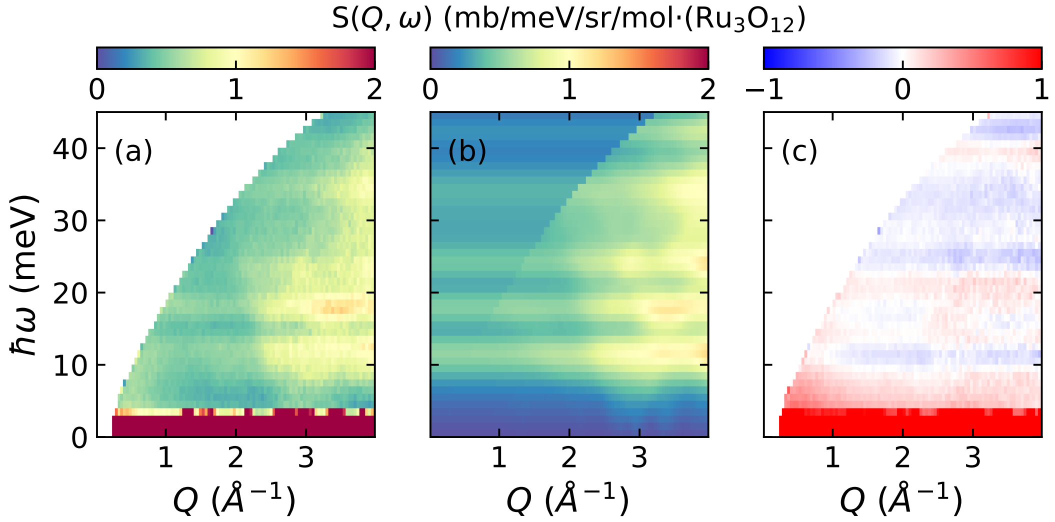

**Figure 3.12:** (a) Normalized direct scattering measured at E$_i$=50 meV, $T$=4 K. (b) Best fit to multiple scattering using OCLIMAX calculations and the form of Eq. 3.6. Scattering below the kinematic limit only includes the calculated $Q$-independent multiple scattering. (c) Difference between the first two plots, showing small deviations that are corrected for by Bose-Einstein subtraction.

detailed calculations of the phonons, so this approximation does not need to be made and the integral can be carried out numerically with the given one-phonon scattering cross section. To calculate the multiple scattering in this way, one needs both an overall normalization for the DFT calculation and the multiple scattering fraction $\mathcal{T}$, which will be defined as

$$I^O_{tot}(Q,\hbar\omega) = \mathcal{A}\left(I^O(Q,\hbar\omega) + (1-\mathcal{T})\int_{|k_i-k_f|}^{k_i+k_f} I^O(Q',\hbar\omega)\frac{Q'dQ'}{2k_ik_f}\right). \tag{3.6}$$

Both $\mathcal{T}$ and the normalization constant $\mathcal{A}$ are treated as free parameters in a $\chi^2$ minimization which is defined by

$$\chi^2 = \sum_i \frac{(I_i - I^O_{tot,i})^2}{\sigma I_i^2}. \tag{3.7}$$

This procedure is repeated for every experimental configuration, with an example for E$_i$=25 meV $T$=4 K shown in Fig. 3.12. Only regions in the highest available $Q$ were used for this fit where no magnetic scattering is expected. The effective fraction of single-event scattering were $\mathcal{T}_{10.5} = 0.77$, $\mathcal{T}_{25} = 0.84$, and $\mathcal{T}_{50} = 0.91$ where the subscripts denote the incident neutron energy.

The procedure qualitatively reproduces the backgrounds observed in the experiment though with some asystematic deviations, as shown in Fig.3.12(c). We denote these differences as

$$I_{sub}(Q,\hbar\omega) \equiv I(Q,\hbar\omega) - I'_{ph}(Q,\hbar\omega) \tag{3.8}$$

$$I_{sub}(Q,\hbar\omega) = I_{mag}(Q,\hbar\omega) + \delta I_{ph}(Q,\hbar\omega) + \delta I_m(Q,\hbar\omega) \tag{3.9}$$

We now assume that the phonon-based errors are dominated by single-phonon processes and subtract them using a standard Bose-Einstein subtraction using Eq. 3.3. The result is the following data, which by design should be dominated by magnetic scattering

$$\bar{I}(Q,\hbar\omega) = I_{mag}(Q,\hbar\omega) + \left\{\delta I_m^{T_L}(Q,\hbar\omega) - \mathcal{B}(\hbar\omega)\delta I_m^{T_H}(Q,\hbar\omega)\right\}. \tag{3.10}$$

Here, $\mathcal{B}(\omega)$ is the $\omega$-dependent ratio of Bose-Einstein factors and the superscripts denote temperature. Even after all of this effort, some intensity remains at high $Q$ and finite energy transfer that cannot be magnetic of origin given the form factor. One possibility is that this is multiple elastic scattering involving the sample environment. The delay becomes associated with a "false" inelasticity in the time of flight geometry. In order to treat the data quantitatively, these events must be removed. The assumption is made that the full spectrum of scattering for $Q$>2 Å$^{-1}$ is non-magnetic and that the

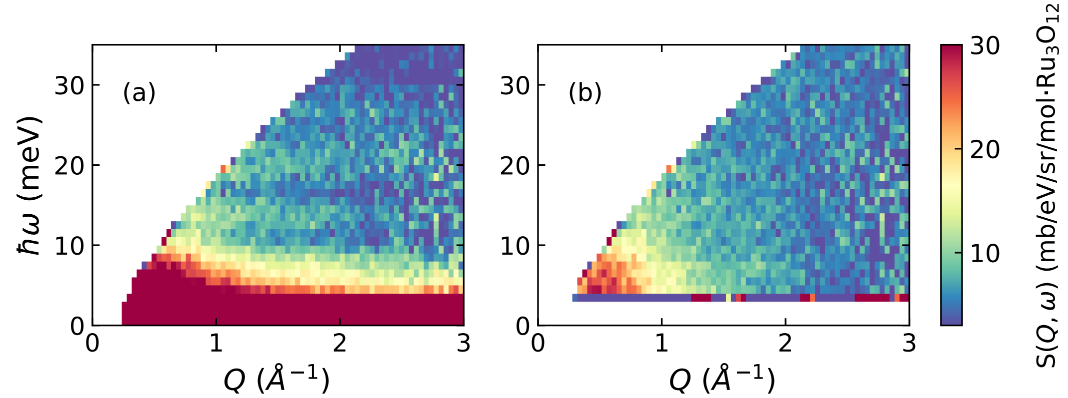

**Figure 3.13:** (a) Inelastic neutron scattering from powder $Ba_4NbRu_3O_{12}$ after subtraction of single-event phonon scattering and multiple event scattering. The presence of scattering with no $Q$ dependence at high $Q$ signifies that some non-magnetic contributions still exist in the data. (b) After making an assumption that the scattering for $Q > 2\text{Å}^{-1}$ is non-magnetic, the high-$Q$ scattering is averaged and subtracted across all values of $Q$ as a background. The result shown is what we take to be the purely magnetic scattering.

remaining multiple scattering contribution is $Q$-independent.

$$\delta I_m^T(\hbar\omega) = \int_{2\ \text{Å}^{-1}}^{Q_{max}} I^T(Q,\hbar\omega)dQ / \int_{2\ \text{Å}^{-1}}^{Q_{max}} dQ \tag{3.11}$$

This process is depicted in Fig. 3.13. The final result is the smooth magnetic continuum presented in Fig. 3.9(b). The $E_i$=10.5 meV data did not have enough access to high-$Q$ to perform the described background subtractions, and was omitted for this reason from the remainder of the analysis.

### 3.4.2 Scattering analysis

### 3.4.3 Anisotropic character of trimer form factor

The magnetic form factor $|F(Q)|^2$ in general is defined by the Fourier transform of the real-space magnetization density, which is given by the wavefunction for the magnetic orbital(s). In neutron scattering studies this is often referenced as $F(Q)$ and is formally defined by

$$F(\mathbf{Q}) = \int e^{iq\mathbf{r}} \rho(\mathbf{r}) d^3\boldsymbol{r}. \tag{3.12}$$

This can be evaluated numerically with the assistance of ab-initio studies [91], but in this case we take a simple analytical approach. In Eq. 3.12, $\rho(\boldsymbol{r}) = |\phi(\boldsymbol{r})|^2$ where $\phi(\boldsymbol{r})$is the valence electron wavefunction. In $Ba_4NbRu_3O_{12}$, there exist two $Ru^{4+}$ ions and one $Ru^{3+}$ ion that combine to form the proposed $J_{eff}$=1/2 trimer magnetic unit. A rough assumption is made to ignore the phase of the wavefunction and assume that these ions then contain identical magnetic form factors. If this is true, then the wavefunction of the trimer's valence electrons is readily calculated. We begin with the approximate valence electron wavefunction of the trimer

$$\phi(\mathbf{r}) \approx \frac{1}{\sqrt{3}}[\phi(\mathbf{r}) + \phi(\mathbf{r} - \mathbf{d}_o) + \phi(\mathbf{r} + \mathbf{d}_o)]. \tag{3.13}$$

Here $\mathbf{d}_o$ is the displacement vector between Ru ions within the $Ru_3O_{12}$ trimer. Given that this is simply a constant along the c-axis, the form factor is evaluated as

$$|F_T(\mathbf{Q})| = \int e^{i\mathbf{q}\cdot\mathbf{r}} \frac{1}{3} |\phi(\mathbf{r})^2 + \phi(\mathbf{r})\phi(\mathbf{r}-\mathbf{d}_o) + \tag{3.14}$$

$$\phi(\mathbf{r})\phi(\mathbf{r}+\mathbf{d}_o) + \phi(\mathbf{r}-\mathbf{d}_o)\phi(\mathbf{r}+\mathbf{d}_o) + \quad \phi(\mathbf{r}-\mathbf{d}_o)^2 + \phi(\mathbf{r}+\mathbf{d}_o)^2| d^3\mathbf{r}$$

where $F_T(\mathbf{Q})$ denotes the trimer magnetic form factor. We now make the assumption of no direct orbital overlap between the ruthenium ions, meaning that the cross terms evaluate to zero. This is of course a major simplification, and more detailed studies of this system would require a more careful analysis. This would perhaps be done by evaluating the form factor numerically through DFT studies. With the approximation the form factor is now the following:

$$|F_T(\mathbf{Q})| = \int e^{i\mathbf{q}\cdot\mathbf{r}} \frac{1}{3} (|\phi(\mathbf{r})|^2 + |\phi(\mathbf{r}-\mathbf{d}_o)|^2 + |\phi(\mathbf{r}+\mathbf{d}_o)|^2) d^3\mathbf{r}. \tag{3.15}$$

This form factor is notably dependent on the z-axis component of the scattering. Finally, the free-ion form factor appears and the expression can be simplified to the following:

$$|F_T(\mathbf{Q})| = \frac{1}{3}\Big[ \int e^{i\mathbf{Q}\cdot\mathbf{r}} |\phi(\mathbf{r})|^2 dr + \tag{3.16}$$

$$\int e^{i\mathbf{Q}\cdot(\mathbf{r}-\mathbf{d}_o)} |\phi(\mathbf{r})|^2 dr + \int e^{i\mathbf{Q}\cdot(\mathbf{r}+\mathbf{d}_o)} |\phi(\mathbf{r})|^2 d\mathbf{r} \Big]$$

$$|F(\mathbf{Q})|^2 = \frac{|F_{Ru}(Q)|^2}{9} (1 + 2\cos(\mathbf{Q}\cdot\mathbf{d}_o))^2. \tag{3.17}$$

This simple form does not yet consider the powder average in the current experiments, but Fig. 3.14 shows the difference in the form factor for in-plane

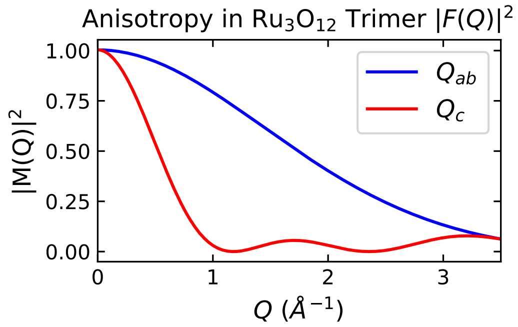

**Figure 3.14:** Analytically derived trimer form factor for in-plane and out of plane directions. The out of plane direction is not precisely $Q_z$, as the trimers are not stacked on top of each other.

versus out of plane scattering. The revised form factor depends on the angle between the momentum transfer $\boldsymbol{Q}$ and the Ru-Ru displacement vector within the trimer $\boldsymbol{d}$ of magnitude $d_o$=2.54 Å. Now consider the equal time structure factor associated with a pair of spin-1/2 molecules displaced by a real space vector $\boldsymbol{d}$ from each other forming a singlet state.

$$\mathcal{S}(Q) = \mathcal{A}|F(Q)|^2(1 - \cos(\boldsymbol{Q} \cdot \boldsymbol{d})) \tag{3.18}$$

Inserting the evaluated form for the magnetic form factor gives the following analytical expression

$$\mathcal{S}(Q) = \frac{|F_{Ru}(Q)|^2}{9}(1 + 2\cos(\mathbf{Q} \cdot \mathbf{d}_o))^2(1 - \cos(\mathbf{Q} \cdot \mathbf{d})). \tag{3.19}$$

The anisotropy in the form factor depends explicitly on the angle between the scattering vector and $\boldsymbol{d}_0$. Let us now consider the structure factor that would be associated with a powder sample:

$$\mathcal{S}_{pow}(Q) = \int \frac{d\Omega_Q}{4\pi}\mathcal{S}(Q) \tag{3.20}$$

In the calculation of the powder average, we take the $\hat{z}$ axis to be perpendicular to the plane formed by dimer displacement vector $\boldsymbol{d}$ and the Ru-Ru displacement vector $\boldsymbol{d}_o$. The $\hat{x}$ axis is taken to bisect these two vectors with the angle between the axis and the vectors being $\psi$. Then, the $\mathbf{d}$, $\mathbf{d}_o$, and $\mathbf{Q}$ vectors can be explicitly written in spherical coordinates as

$$\mathbf{d} = (\hat{x}\cos\psi + \hat{y}\sin\psi)d \tag{3.21}$$

$$\mathbf{d}_o = (\hat{x}\cos\psi - \hat{y}\sin\psi)d \tag{3.22}$$

$$\mathbf{Q} = Q(\hat{x}\cos\phi\sin\theta + \hat{y}\sin\phi\sin\theta + \hat{z}\cos\theta). \tag{3.23}$$

The dot products in the spherical integration in Eq. 3.19 may now be simplified to

$$\mathbf{Q}\cdot\mathbf{d} = Qd\sin\theta\cos(\phi-\psi) \tag{3.24}$$

$$\mathbf{Q}\cdot\mathbf{d}_o = Qd_o\sin\theta\cos(\phi+\psi) \tag{3.25}$$

The deviation from the free-ion Ru behavior is encompassed purely by the angle $\psi$. In this way, we can solve the integral in Eq. 3.19 to get the following analytical form for $\mathcal{S}_{pow}(Q)$

$$\mathcal{S}(Q) = \mathcal{A}\sum_{\boldsymbol{d}}\left[\frac{|F_{Ru}(Q)|^2}{9}\{3+2\frac{\sin\left(2Qd_o\right)}{2Qd_o}+4\frac{\sin\left(Qd_o\right)}{Qd_o}-\right.$$

$$(3\frac{\sin\left(Qd\right)}{Qd}+\frac{\sin\left(Q|2\mathbf{d}_o-\mathbf{d}|\right)}{Q|2\mathbf{d}_o-\mathbf{d}|}+\frac{\sin\left(Q|2\mathbf{d}_o+\mathbf{d}|\right)}{Q|2\mathbf{d}_o-\mathbf{d}|}$$

$$\left.+2\frac{\sin\left(Q|\mathbf{d}_o-\mathbf{d}|\right)}{Q|\mathbf{d}_o-\mathbf{d}|}+2\frac{\sin\left(Q|\mathbf{d}_o+\mathbf{d}|\right)}{Q|\mathbf{d}_o-\mathbf{d}|})\}\right]. \quad (3.26)$$

This form may be further simplified by selecting the bond vector ***d***, but may be evaluated analytically and is used in the fits to the factorized form of $\mathcal{S}(Q)$.

#### 3.4.3.1 Elastic scattering

In the case of elastic scattering the factorization analysis is still applicable, but we must assume that the energy dimension has already been integrated over. The description of the $Q$-dependent scattering then becomes:

$$I(Q) = 2r_0^2|\frac{g}{2}F(Q)|^2S_{el}(Q) \quad (3.27)$$

$$S_{el}(Q) = \frac{1}{3}\sum_{d}^{0,d_1,\ldots}\left\{\langle\mathbf{S}_o(\infty)\cdot\mathbf{S}_d\rangle\frac{\sin(Qd)}{Qd}\right\} \quad (3.28)$$

where the allowed interaction vectors **d** includes the self-correlation term. The corresponding expression for the intensity is

$$I(Q) = \frac{2|\frac{g}{2}F(Q)|^2r_o^2}{3}\sum_{d}\langle\mathbf{S}_o(\infty)\cdot\mathbf{S}_d\rangle\frac{\sin(Qd)}{Qd}. \quad (3.29)$$

The total moment sum rule is also modified slightly, being

$$\mu_{static}^2 = 3g^2 \frac{\int S_{el}(Q) Q^2 dQ}{\int Q^2 dQ}. \tag{3.30}$$

Considering the anisotropic magnetic form factor, the elastic scattering intensity for a powder sample takes on the following form

$$\mathcal{S}(Q) = \frac{r_0^2 g^2}{3} \frac{|F_{Ru}(Q)|^2}{9} \sum_{d}^{0,d_1,\ldots} \langle \mathbf{S}_o^{\alpha}(\infty) \cdot \mathbf{S}_d^{\alpha} \rangle \ldots$$

$$\int \frac{d\Omega)_{\mathbf{Q}}}{4\pi} (1 + 2\cos(\mathbf{Q} \cdot \mathbf{d}_o))^2 \cos(\mathbf{Q} \cdot \mathbf{d}). \tag{3.31}$$

This integral can be carried out numerically or analytically in analogy with the earlier calculation.

## 3.5 Discussion and conclusions

### 3.5.1 Inelastic scattering and dynamic correlations

When applied to the combined background subtracted inelastic neutron scattering data acquired with the three different incident neutron energies, the factorization method results in extracted functions $\mathcal{S}(Q)$ and $G(\omega)$ as depicted in Fig. 3.15. The study of the elastic scattering has already clearly shown the absence of magnetic Bragg peaks, therefore we cannot expect sharp features in the momentum dependence of the inelastic scattering either. Instead, $\mathcal{S}(Q, \omega)$ is peaked at low $Q$ and $\hbar\omega$ decreasing with energy transfer on a scale that resembles the Curie-Weiss temperature. This is consistent with dynamic correlations of a macroscopic interacting spin system that shows no

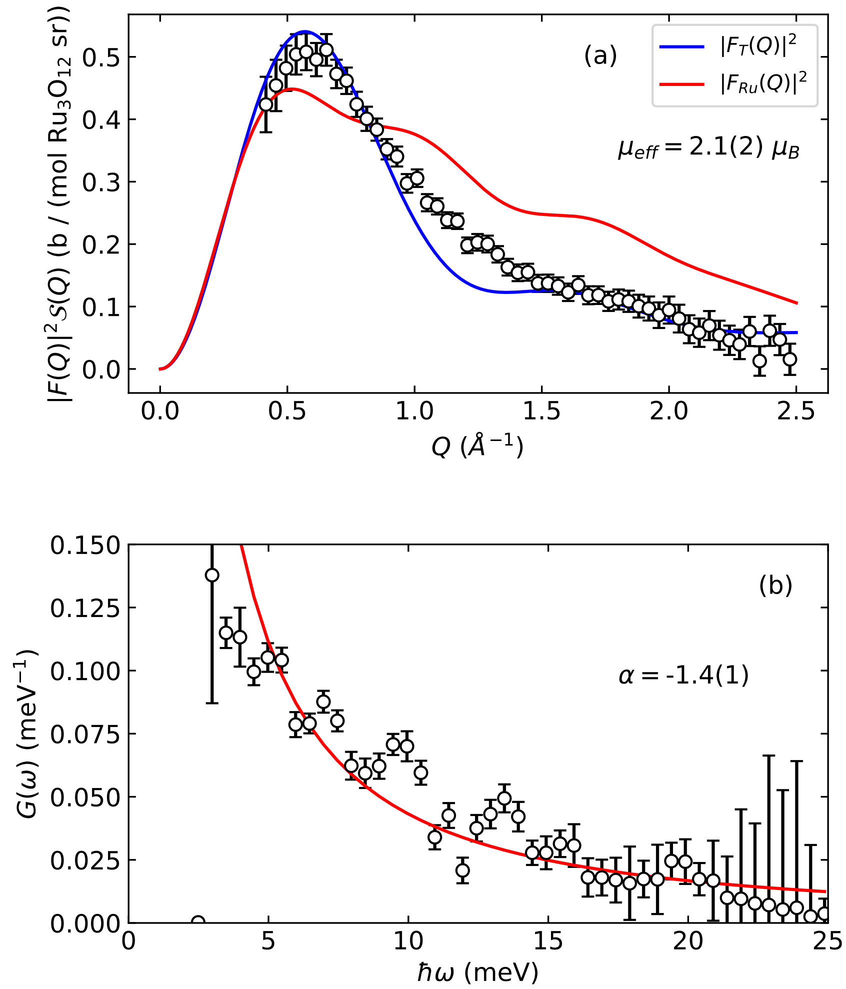

**Figure 3.15:** Result of factorization method on inelastic scattering from $Ba_4NbRu_3O_{12}$. The $Q$-dependent part of the spectrum is used to extract the total dynamic magnetic moment from the from the sample. Fits to $\mathcal{S}(Q)$ assuming the trimer form factor are depicted in red, and assuming the free-ion $Ru^{3+}$ are depicted in blue. The observed fluctuating moment from this fit is found to be 1.3(2) $\mu_B$ (b) G($\omega$) spectral weight extracted by least squares fitting to the diffuse inelastic scattering. This fits well to a phenomenological power law of exponent $\alpha = -1.4(1)$, as shown by the red line.

signs of intramolecular excitations, which would have a discrete spectrum.

The $Q$-averaged spectrum inferred from $\mathcal{S}(Q,\omega)$ is continuous and devoid of any resonances with measurable scattering up to energy scales on the order of 15 meV, which matches the energy scale inferred by the Curie-Weiss temperature. The diffuse spectrum can be approximately described by a power law of the form $(\hbar\omega)^{\alpha}$ with $\alpha$=-1.5(1) as shown by the red line in Fig. 3.15(b). A finite sized spin-cluster as one would expect from the localized trimer picture would produce discrete peaks in the excitation spectrum of the low temperature neutron scattering. As we observe a continuum instead, these data are an important indication that the quantum magnetism of $Ba_4NbRu_3O_{12}$ is collective on the energy scale set by $\Theta_{CW}$.

The dynamic spatial correlations are reflected by $|F(Q)|^2 S(Q)$ as displayed in Fig. 3.15(a). The function very clearly decreases with $Q$, which is consistent with a magnetic signal limited by the magnetic form factor $|F(Q)|^2$. In addition, the scattering displays oscillations that cannot be explained by the $Ru^{4+}$ form factor and must be ascribed to inter-atomic spin correlations. Using the total moment sum rule in Eq. 2.25, we obtain an effective RMS fluctuating moment of $\mu_{dynamic} = 2.1(6)\mu_B$. This may be compared with the RMS static moment of $\mu_{static} = 1.2(2)\mu_B$ from elastic scattering. The total moment from the scattering data is then found to be $\mu_{eff} = \sqrt{\mu_{static}^2 + \mu_{dynamic}^2}$ =2.4(7) $\mu_B$. This is consistent with the inferred value of 2.6 $\mu_B$ from the high temperature susceptibility. However, greater than the expected moment from a $S = 1/2$ ion of $\mu_s = g\mu_B = \sqrt{S(S+1)} = 1.73\ \mu_B$.

For a fully ordered spin-$S$ magnet the ratio of the RMS dynamic to RMS static moment is $(S(S+1)) - S^2)/S^2 = 1/S$. For spin-1/2, this corresponds to a value of $1/S$=2. The value that was obtained in $Ba_4NbRu_3O_{12}$ is $\mu^2_{dynamic}/\mu^2_{static} = 3(1)$, is a suggestion that we are not dealing with a conventional Néel like product state of fully frozen spins. The ratio still falls far short of expectations for a quantum spin liquid where $\mu^2_{static} = 0$.

### 3.5.2 Correlation functions

. The factorized form for $\mathcal{S}(Q,\omega)$ implies the following form for the dynamic component of the equal time correlation function:

$$\mathcal{S}(Q) = \frac{1}{\langle\hbar\omega\rangle}\int \mathcal{S}(Q,\omega)\omega d\omega \tag{3.32}$$

$$= -\sum_{\mathbf{d}} \frac{J_{\mathbf{d}}\langle \mathbf{S_r}\cdot\mathbf{S_{r+d}}\rangle}{3\langle\hbar\omega\rangle}\left[1-\frac{\sin(Qd)}{Qd}\right] \tag{3.33}$$

Here $\{\mathbf{d}\}$ denotes the set of all displacement vectors between spins that interact with each other. The factorization was employed to represent $\mathcal{S}(Q,\omega)$ with the definition $\langle\hbar\omega\rangle = \int g(\omega)\omega d\omega$. We have employed the first moment sum-rule and assume Heisenberg interactions are dominant to obtain Eq. 3.33. The equation implies that the correlation length associated with a factorized dynamic correlation function is capped at the largest spacing between interacting spins $\xi = \max(\mathbf{d})$. We write the Heisenberg spin Hamiltonian as follows:

$$\mathcal{H} = \frac{1}{2}\sum_{\mathbf{r},\mathbf{d}} J_{\mathbf{d}}\mathbf{S_r}\cdot\mathbf{S_{r+d}}. \tag{3.34}$$

Here $\{\mathbf{r}\}$ are position vectors for all spins and since each interacting spin pair appears twice in this summation, and the factor 1/2 ensures that $J_{\mathbf{d}}$ is the exchange energy for spin pair **d**.

Equation 3.33 allows the extraction of bond energies, $J_{\mathbf{d}}\langle \mathbf{S}_{\mathbf{r}} \cdot \mathbf{S}_{\mathbf{r}+\mathbf{d}}\rangle$ from a fit to normalized data for $\mathcal{S}(Q)$ and the value of $\langle \hbar\omega \rangle = 10.1$ meV obtained from $G(\omega)$ (Fig. 3.15). The red line in Fig. 3.15(a) represents a fit to Eq. 3.33 assuming nearest and next-nearest neighbor interactions between spins on the triangular lattice. The blue line in the same figure is the same fit but considering the spatial anisotropy of the $\mathrm{Ru_3O_{12}}$ trimer. The corresponding low $T$ excitation spectrum $G(\omega)$ is gapless to within the 1.5 meV energy resolution and extends to $\langle \hbar\omega \rangle = 20$ meV. $G(\omega)$ decreases monotonically with $\omega$.

For the elastic scattering we directly measure the infinite time spin correlation function, which in the case of diffuse scattering from a powder sample looks like

$$\mathcal{S}_{el}(Q) = \frac{1}{3}\sum_{d}^{0,d_1,\dots}\left\{\langle \mathbf{S}_o(\infty)\cdot \mathbf{S}_d\rangle \frac{\sin(Qd)}{Qd}\right\}. \tag{3.35}$$

where the allowed interaction vectors **d** includes the self-correlation term.

One of the immediate results is the ratio of the frozen and static moment $\mu^2_{dynamic}/\mu^2_{static} \approx 3$, which reveals that at low temperatures the majority of the magnetic moment is fluctuating and that a smaller quantity is frozen. To extract actual bond energies rather than the quantity $J_d\langle S_o(0)\cdot S_{\boldsymbol{d}}\rangle$, we make the following approximation

$$\langle \mathbf{S}_0(\infty)\cdot \mathbf{S}_d\rangle \approx \frac{\mu^2_{static}}{\mu^2_{dynamic}}\langle \mathbf{S}_o(0)\cdot \mathbf{S}_d\rangle, \tag{3.36}$$

The resulting estimates of exchange interactions are shown in Table 3.2.

| Inelastic | d(Å) | $\lvert F_{Ru}(Q)\rvert^2$ | $\lvert F_T(Q)\rvert^2$ |
|---|---|---|---|
| $J_1\langle \mathbf{S}_o(0)\cdot\mathbf{S_d}\rangle$ (meV) | 5.75 | -0.9(4) | -3.3(2) |
| $J_2\langle \mathbf{S}_o(0)\cdot\mathbf{S_d}\rangle$ (meV) | 9.95 | -1.1(4) | -0.2(3) |
| $J_1$ (meV) | 5.75 | -0.3(1) | -0.7(1) |
| $J_2$ (meV) | 9.95 | 0.6(7) | 0.0(1) |

| Elastic | d(Å) | $\lvert F_{Ru}(Q)\rvert^2$ | $\lvert F_T(Q)\rvert^2$ |
|---|---|---|---|
| $\langle \mathbf{S}_0(\infty)\cdot\mathbf{S}_0\rangle$ | 0 | 0.77(7) | 1.5(1) |
| $\langle \mathbf{S}_0(\infty)\cdot\mathbf{S}_{NN}\rangle$ | 5.75 | 1.1(3) | 0.3(2) |
| $\langle \mathbf{S}_0(\infty)\cdot\mathbf{S}_{NNN}\rangle$ | 9.95 | -0.6(6) | -0.8(3) |

**Table 3.2:** Fitting parameters for fits to the inelastic and elastic spectra using Eq. 3.33 and Eq. 3.27. The interactions are the nearest-neighbor and next-nearest neighbor in the plane of the triangular lattice. The columns $|F_{Ru}(Q)|^2$ and $|F_T(Q)|^2$ denote the results of assuming the $\mathrm{Ru}^{4+}$ magnetic form factor $|F_{Ru}(Q)|^2$ and the trimer form factor $|F_T(Q)|^2$ respectively.

The results clearly show that the system has a weak antiferromagnetic nearest-neighbor interaction. The trimer model is far superior when fitting $\mathcal{S}(Q)$ as shown in Fig. 3.15(a), which we take as a good indication of the molecular nature of the system. For the overall exchange interactions summed over all of the bonds, we find $\sum_d J_d = -0.7(1)$ meV. This may be compared to what one would expect from the Weiss temperature, $\theta_{CW} = \mu_{eff}^2/(3k_B g^2)\sum_d J_d$. For $\theta_{CW}$ = -155K, $g = 2$, and $\mu_{eff} = 2.59$ we expect $\sum_d J_d = -1.8$ meV per bond after considering the sixfold nearest and next-nearest neighbor symmetry of the triangular lattice. The extracted values for $J_d$ can only be interpreted as an estimate, but their consistency with what is expected from $\theta_{CW}$ suggests that they are physically reasonable.

Even if the absolute magnitudes of the exchange parameters are not precise, we may still consider the signs and relative magnitudes of the interactions. This would mean that the magnetism in $\mathrm{Ba_4NbRu_3O_{12}}$ can be described by a strong antiferromagnetic nearest neighbor exchange. Our data are not sufficient to constrain further neighbor interactions, but the strongly anisotropic magnetic form factor of the trimer could be directly measured in single crystal experiments.

### 3.5.3 Conclusions

We have already shown that the interactions in $Ba_4NbRu_3O_{12}$ can be approximated as Heisenberg like, and that a large portion of the moment remains fluctuating below the freezing temperature. The NN Heisenberg antiferromagnet has an ordered ground state [92, 93], which is not observed in this case. The nature of the remaining spin fluctuations at low temperatures are not clear from this measurement, but they are consistent with at least two possibilities. The first is a spin-liquid like ground state with some portion of the spins being frozen at low temperatures. The second is a partially frozen random-singlet state, in which the fluctuating spins form into distinct singlets across the lattice rather than in a superposition of singlets as in a spin-liquid. Without single crystalline samples (and often even with them), it is extremely difficult to differentiate these situations.

Before concluding this chapter, I would like to mention the sister compound $Ba_4NbIr_3O_{12}$. As discussed earlier, this material shows no signs of order or spin-freezing unlike the Ru version. Several proposals were written for the study of this material, which will happen some time in the future. The studies on the Ru-variant will inform the understanding of the ground state in $Ba_4NbIr_3O_{12}$.

# Chapter 4

# Determination of Anisotropic Kitaev interactions in honeycomb iridates $\beta$-$Li_2IrO_3$ and $D_3LiIr_2O_6$

## 4.1 Overview

The lithium iridates are the originally proposed realizations of the Kitaev model in the previously discussed proposal by Jackeli and Khaliullin [37, 94]. Although some potential Kitaev materials have emerged since this proposal, including $\alpha$-$RuCl_3$ and $Co^{2+}$ based materials, the iridates were some of the most promising realizations of Kitaev's model. In the iridates, the physical realization of the element of bond-selective spin anisotropy is realized in the form of $Ir^{4+}$ ions with orbital degeneracy that is lifted by strong spin-orbit coupling. In this way, the spatial anisotropy of the 5*d* orbitals is projected onto the spin-state, producing the required bond-dependent exchange.

In real materials, this does not translate into purely Kitaev exchange. Rather than the superexchange Ir-O-Ir exchange paths considered in the original proposal, direct orbital overlap contributes a Heisenberg-type interaction[94]. The magnitude $J$ term compared to $K$ is strongly dependent upon the chemical properties of the charge-transfer gap $\Delta_{pd}$ and direct $dd$ overlap $t'$ between the nearest neighbor Ir $t_{2g}$ orbitals. The interplay between these quantities has been studied theoretically in detail, suggesting exotic ordered magnetic phases alongside the proposed KSL state.

Two additional interactions are allowed by symmetry in the generic nearest-neighbor exchange Hamiltonian, which are known as the $\Gamma$ and $\Gamma'$ terms. The $\Gamma'$ term originates from trigonal distortions of the $IrO_6$ octahedra, which will be neglected for simplicity. The $\Gamma$ term represents a bond-dependent symmetric off-diagonal exchange anisotropy, which turns out be to be significant in many materials and originates from a combination of direct $dd$ hopping and anion mediated $d$-$p$ electron transfer [46]. This was first noticed in response to a study of the magnetic order in $Na_2IrO_3$, in which the simple model of Kitaev and Heisenberg interactions was found to be insufficient to produce the correct magnetic ground state [95]. The full spin exchange Hamiltonian then has the

$$\mathcal{H} = \sum_{\langle ii \rangle \in \alpha,\beta,\gamma} [J\boldsymbol{S}_i \cdot \boldsymbol{S}_j + K S_i^{\gamma} S_j^{\gamma} + \Gamma(S_i^{\alpha} S_j^{\beta} + S_i^{\beta} S_j^{\alpha})]. \tag{4.1}$$

This Hamiltonian has been studied in considerable detail, and all theory work including ab-initio studies points towards the presence of a dominant ferromagnetic $K < 0$ interaction [96, 97]. It permits a rich phase space of magnetic ground states, with $\Gamma$ in particular inducing exotic incommensurate spiral magnetism.

Though there has been significant progress on the theory side of the problem, experimentally, things remained extremely murky. Detailed knowledge of the interplay between the different contributions to the exchange Hamiltonian is severely lacking. In the iridates in particular there are a few reasons for this. First, single crystalline samples are difficult to grow and those that do exist are too small for inelastic neutron scattering studies [40]. Secondly, $Ir^{4+}$ is unforgiving in neutron scattering studies with a neutron absorption cross section of $\sigma_{abs} = 425$ b (assuming the natural isotope distribution), and a magnetic form factor that sharply attenuates the scattering with increasing $Q$. For $Q =3$ $\mathring{A}^{-1}$, only 10% of the magnetic scattering survives. Finally, iridium is simply expensive, making large explorations of single crystal synthesis techniques impossible. Because neutron scattering studies of these materials is extremely limited, little is known beyond bulk characterization and refinements of magnetic order from neutron diffraction and resonant x-ray studies. Little is known about the nature of the excitations in these materials on the energy scale of the magnetism.

This chapter will address this major gap in the literature, and two lithium iridates will be explored experimentally- $\beta$-$Li_2IrO_3$ and $D_3LiIr_2O_6$. In both cases, inelastic neutron scattering studies are performed on isotope-enriched polycrystalline samples. For $\beta-Li_2IrO_3$, where magnetic order is observed at $T_N$=38 K [98], the exchange Hamiltonian is refined with precision using the $JK\Gamma$ model. This is achieved by the simultaneous use of inelastic neutron scattering, time-domain THz spectroscopy, and heat capacity studies. The result is in good agreement with previous works, and quantifies the precise exchange interactions in the sample characterizing $\beta$-$Li_2IrO_3$ as having a dominant ferromagnetic Kitaev exchange with competing $J$ and $\Gamma$ contributions.

$D_3LiIr_2O_6$ shows no observable order and may be a true ground state KSL candidate [99]. The scattering data is difficult to interpret due to absorption and multiple scattering effects originating from the presence of deuterium. Three different inelastic neutrons scattering studies along with time-domain THz spectroscopy are used to characterize the low energy excitations. The result is evidence of broad continua of magnetic excitations at low momentum transfer and energies centered around $\hbar\omega$=2 meV. The extracted magnetic scattering accounts for all of the expected dipole moment and is consistent with nearest-neighbor spin correlations as expected in a KSL. These studies alone are not enough to conclude the presence of a KSL phase, but the results are encouraging and merit further study of the material.

## 4.2 Introduction to hyperhoneycomb iridate $\beta$-$Li_2IrO_3$

### 4.2.1 Structural and Magnetic Properties

It is expedient to define the hyperhoneycomb lattice and its properties before further discussing $\beta$-$Li_2IrO_3$. $\beta$-$Li_2IrO_3$ has $Ir^{4+}$ ions living on the so-called three-dimensional "hyperhoneycomb" lattice, which is a bit of a misleading name. The unit cell is orthorhombic of space group *Fddd*. While the lattice itself may be understood as two alternating twisted zigzag chains running along the crystallographic c-axis (Fig. 4.1), the local environment around each $IrO_6$ octahedra is precisely the same as the two-dimensional case. Indeed,

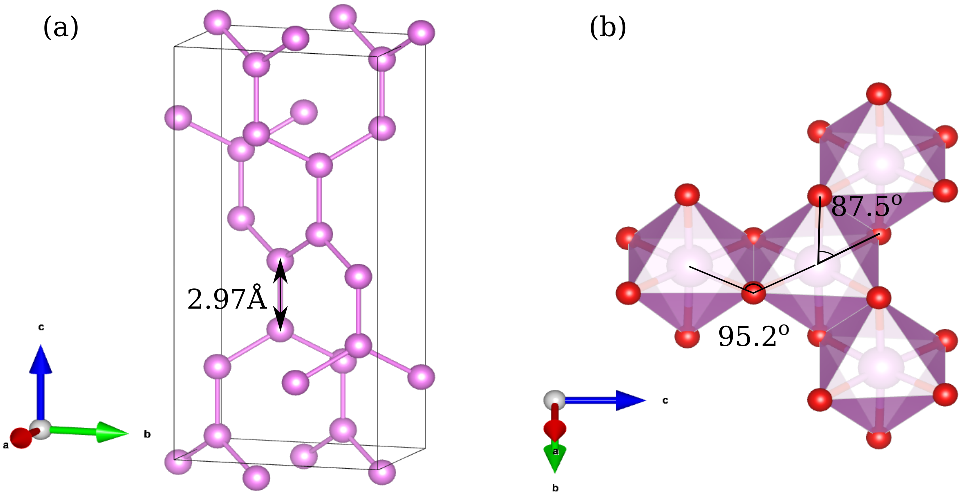

**Figure 4.1:** (a) Hyperhoneycomb lattice of Ir atoms in $\beta$-$Li_2IrO_3$. (b) Local environment of edge-sharing $IrO_6$ octrahedra. Plots were generated using the VESTA software [101].

ignoring any further-neighbor interactions the magnetic properties of the hyperhoneycomb lattice and the potential for Kitaev physics should be precisely the same as in the two-dimensional case. This has been shown rigorously in theory, as Kitaev's exact two-dimensional solution for the honeycomb lattice spin-liquid was repeated in three dimensions on the hyperhoneycomb lattice [100]. The same potential KSL state exists, and the structure has the advantage of the absence of structural disorder typical in two-dimensional van der waals materials. Like $\alpha$-$Li_2IrO_3$, $\beta$-$Li_2IrO_3$ is observed to form a long-range magnetically ordered state at $T_N$=38 K [41, 98]. The observed magnetic order was refined in a 17 $\mu$m diameter single crystal using magnetic resonant x-ray diffraction [43], which is described by counterrorating spirals along alternating zigzag chains with incommensurate ordering wavevector $\boldsymbol{k} = (0.57(1), 0, 0))$ with an ordered moment of $\mu = 0.47(1)\ \mu_B$. The magnetic order vanishes completely in an applied field of magnitude 3 T, and the nature of the magnetic order in an applied field is complex. X-ray diffraction studies suggest that the application of a field along the crystallographic $b$-axis leads to an admixture of a field-polarized phase and a zigzag spin mode, suggesting that the system is a near degeneracy of different magnetic ground states [102]. This study also showed evidence of long-lived fractionalized excitations separating the low-$T$ ordered phase from the high-$T$ paramagnetic regime, suggesting proximity to a Kitaev phase.

The bulk properties of $\beta$-$Li_2IrO_3$ have also been explored using the available small single crystals. Like other iridates, the material is a room temperature insulator with resistivity on the order of 100$\Omega$ cm at room temperature [41]. This classifies the material as a spin-orbital Mott insulator. Magnetic susceptibility studies on polycrystalline samples finds an effective moment of 1.61 $\mu_B$/Ir, which is close to the value of 1.73 expected for $S$=1/2 and validates the $J_{eff}$=1/2 picture. The observed Curie-Weiss temperature is $\theta_{CW} = 40$ K, suggesting dominant ferromagnetic interactions. Further more detailed studies on single crystal samples finds three different values of the Curie-Weiss temperature along the three axes of the unit cell, $\theta_a = -33(3)$ K, $\theta_b = 44(4)$ K, $\theta_c = 53(4)$ K [98]. A high temperature expansion of the $JK\Gamma$ model may be used to find that

$$\theta_a = -(3J + K - \Gamma)/4, \tag{4.2}$$

$$\theta_b = -(3J + K)/4, \tag{4.3}$$

$$\theta_c = -(3J + K + \Gamma)/4. \tag{4.4}$$

Based on these results, a dominant ferromagnetic Kitaev term is inferred, followed by a large Γ and a small $J$. Of course, this method has limitations in large part due to the fact that the local moments themselves have a strong temperature dependence in these types of $J_{eff}$=1/2 materials [103].

Following these encouraging results, theoretical efforts were made to determine the nature of the interactions in $\beta$-$Li_2IrO_3$. *Ab-initio* studies successfully captured the experimentally observed band structure and magnetic order [104], suggesting a dominant ferromagnetic Kitaev interaction. Further study of the ordered state showed that it could be considered a deformation of the nearby commensurate $(\frac{2}{3}, 0, 0)$ type order, and that the observed wavevector and critical field are compatible with again a dominant negative $K$ term, followed by a large negative Γ term, and a small value of $J$ ($\approx |K|/10$) [105].

So, with a wealth of experimental results regarding the magnetic ground state and theory predictions of strong Kitaev interactions, neutron scattering is a natural follow-up in order to determine the nature of the low energy excitations in the system and quantitatively determine the spin Hamiltonian. With this information, it should be possible to determine if the system is indeed proximate to a KSL state.

### 4.2.2 Experimental considerations for honeycomb iridates

In the case of $\beta$-$Li_2IrO_3$, the main experimental consideration for neutron scattering experiments is the prohibitive absorption cross section associated with iridium. For example, the mean free path for natural isotope $\beta$-$Li_2IrO_3$ with $E_i$=25 meV neutrons is merely 1 mm. For $^{191}$Ir, $\sigma_{abs} = 954$ b, and for $^{193}Ir$

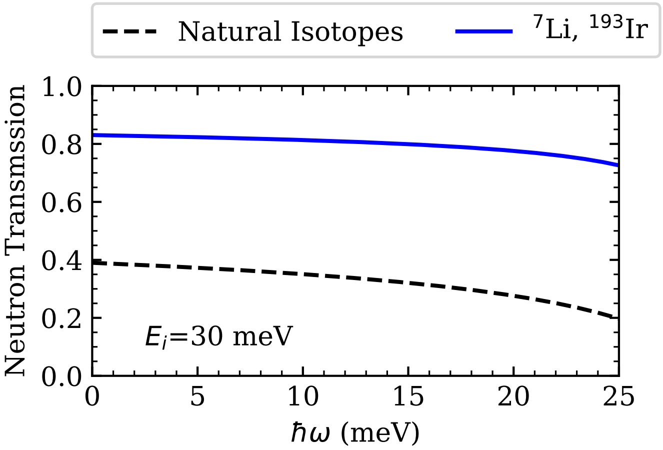

**Figure 4.2:** Plot showing neutron transmission as a function of energy transfer for both natural $Li_2IrO_3$ (black) and enriched $^7Li^{193}IrO_3$ (blue). The assumed $E_i$=30 meV, and the mean path length is 1 mm.

$\sigma_{abs} = 111$ b. For thermal neutrons, neutron transmission may be approximated as

$$T(d,\hbar\omega) = \sqrt{\exp\left[-d\sigma_{abs}^{ref}\lambda_i/(V_0\lambda_0)\right]\exp\left[-d\sigma_{abs}^{ref}\lambda_f/(V_0\lambda_0)\right]}. \tag{4.5}$$

Here, $\lambda_0$ is the reference wavelength for incident neutron energy $E_i$=25 meV, for which the absorption cross section $\sigma_{abs}^{ref}$ was measured with. $\lambda_f$ is the final neutron energy as determined by the energy transfer, and $V_0$ is the volume per iridium atom. The geometric mean of absorption for the initial and final neutron energies is taken to represent the inelastic scattering process through the sample. $d$ is the mean path length of the neutron through the sample, which is dependent upon the sample geometry. While Eq. 4.5 may be used to approximate the energy-dependent absorption, a more accurate method is a Monte-Carlo method implemented in the Mantid software. Still, the absorption increases exponentially with $d$, and to mitigate this a custom

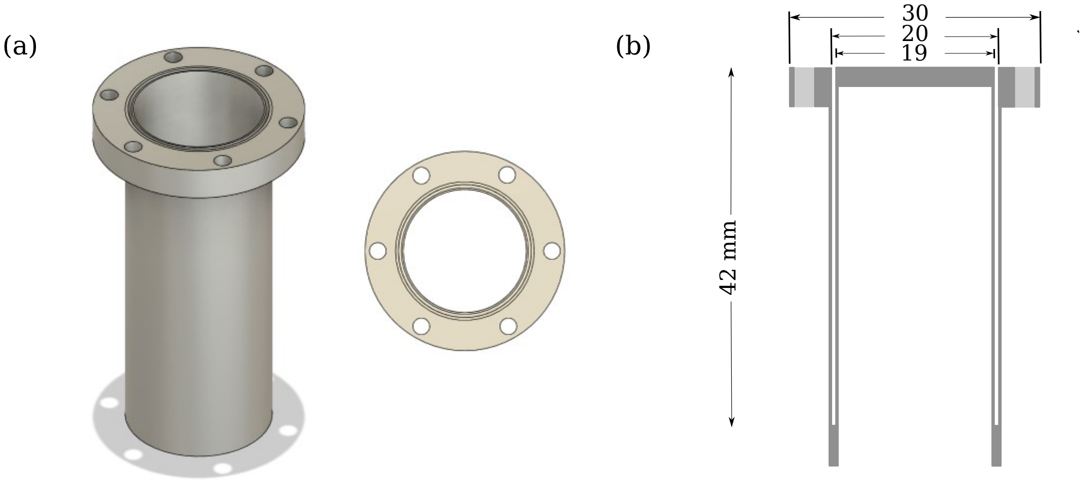

**Figure 4.3:** (a) CAD model of the aluminum can design for iridate experiments. The sample space is of thickness 0.5 mm, minimizing absorption. (b) Cross section showing annulus design. all dimensions in millimeters.

annular aluminum can was developed. The annulus is of inner diameter 19 mm and outer diameter 20 mm, and assembled in such a way that the space in the center of the can is vacuum. This greatly improves upon similar designs that contain much more aluminum and have significant background. This design was made by Yishu Wang, who also worked closely on this project.

Though this design reduces the effective neutron path length in the sample to be on the order of 1 mm, this does not completely fix the issue of absorption. Assuming $d_{eff}$=1 mm and incident neutron energy of 30 meV, the estimated energy transfer dependent transmission is calculated using Eq. 4.5 and shown in Fig. 4.2. Using natural isotopes, only about 40% of neutrons traverse the sample and this becomes even worse at finite energy transfers. To work around this, we decided to use enriched $^7$Li and $^{193}$Ir, which significantly reduces the overall absorption cross section and increases transmission. As a comparison, for natural isotopes $\sigma_{abs}$=556 b/fu, and for the enriched sample

$\sigma_{abs}$ =112 b/fu. Without both the can and the enrichment, these inelastic experiments would have required significantly more beam time to complete successfully.

## 4.3 Experimental results for $\beta$-$Li_2IrO_3$

### 4.3.1 Synthesis

The $\beta$-$Li_2IrO_3$ powder investigated in this study was synthesized by solid state reaction using powders of $Li_2CO_3$ and metallic Ir. The reagents were 99% enriched $^7$Li and $^{193}$Ir to alleviate neutron absorption as well as the strong incoherent scattering from a natural isotope distribution of Ir. Further details of the synthesis may be found in Ref. [41]. A total of 3.6 g of sample was used in the neutron experiments, for which powder x-ray diffraction and susceptibility studies showed no evidence of secondary phases or impurities to at least the 1% level. One batch that was discarded contained trace $IrO_2$ impurities, which may then be present in trace amounts throughout the samples used in these studies.

### 4.3.2 Treatment of neutron scattering data and experimental details

#### 4.3.2.1 Experimental details

The neutron scattering experiment was conducted on the SEQUOIA spectrometer [106] at the ORNL spallation neutron source. The powder was loaded under 1 atm $^4$He at room temperature in an annular aluminum can with an outer diameter of 20 mm and annulus thickness 0.5 mm. The height of the

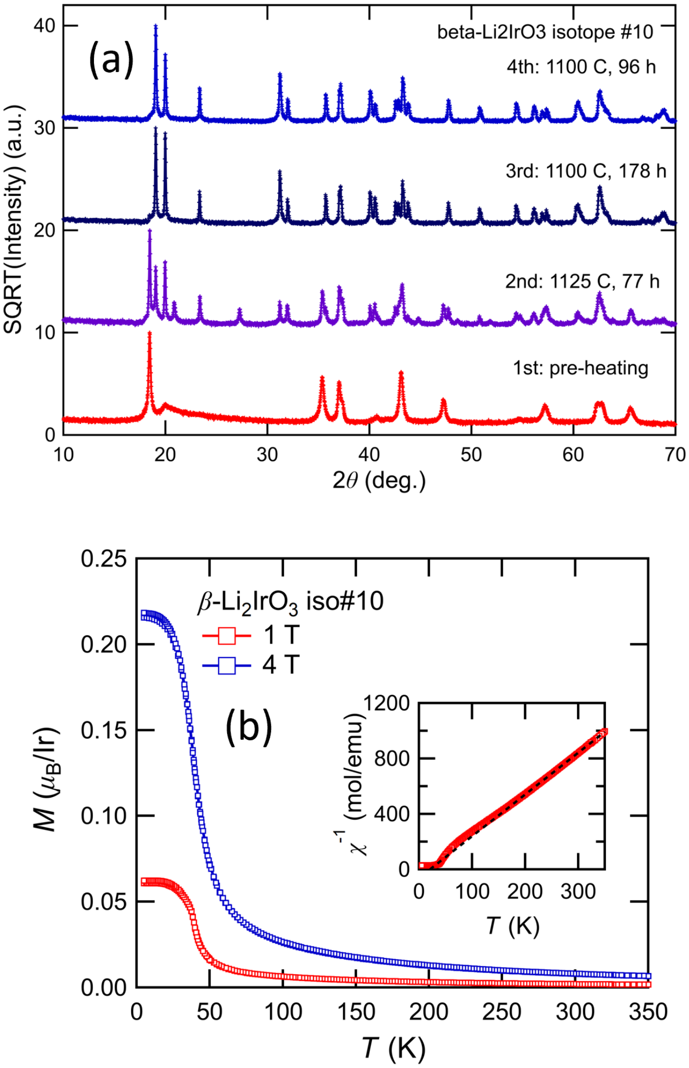

**Figure 4.4:** (a) Powder x-ray diffraction patterns from one batch of $\beta{-}^{7}\mathrm{Li}_2^{193}\mathrm{IrO}_3$ showing the evolution of the diffraction pattern through various annealing steps. No impurity phases were observed in the final product for any of the batches used in this study. (b) Magnetization and susceptibility data for the same powder sample. The main feature in the data indicates the magnetic phase transition expected to occur at $T_N = 38$ K.

corresponding annular powder sample was 34 mm. The total mass was 3.8 g and the packing density was 3.6 g/cm$^3$ which is 50% of the nominal density. The can was attached to the cold finger of a low-background closed cycle refrigeration cryostat.

Data were acquired with fixed incident energy $E_\mathrm{i}$ = 18 meV, 30 meV, and 60 meV for each of the temperatures $T = 4.0(1)$ K, 45.0(1) K, and 200.0(1) K. In addition, $E_\mathrm{i}$=120 meV data were taken at $T = 4.0(1)$ K and 300.0(1) K. For $E_\mathrm{i}$=18 meV and 30 meV we used the fine chopper configuration, while for $E_\mathrm{i}$=60 meV and 120 meV the high flux chopper was used. Energy and momentum transfer dependent absorption corrections determined by a Monte-Carlo method were applied to the data. A temperature independent background was removed from each measurement using the principle of detailed balance, the details of which may be found in 4.3.2.3. The one-phonon scattering was estimated from high temperature measurements where it dominates and then subtracted from the lower temperature data. Elastic incoherent scattering from a vanadium standard sample was used to normalize count rates to absolute units. To cover a broad range of momentum-energy space with the right compromise between resolution and count rate, we combined data acquired for the four different incident energies.

Additional measurements were acquired with fixed incident energy $E_\mathrm{i}$ = 22 meV in the high flux configuration to examine the temperature dependence of the magnetic Bragg Peaks along with the inelastic spectrum. These data were corrected for absorption, normalized to vanadium, and binned in 2.5 K temperature steps.

#### 4.3.2.2 Annular absorption and normalization

Although we have taken care to minimize absorption by means of a custom annular aluminum sample can and isotopic enrichment of both $^{193}$Ir and $^{7}$Li, significant energy transfer dependent neutron absorption still affects the measurement. To account for this, we use a Monte-Carlo method implemented in the Mantid software which takes into account the full neutron path for each pixel as a function of scattering angle and energy transfer [107]. Further details may be found in the Mantid documentation for the AnnularRingAbsorption method. Finally, the measurements were normalized to units of barn/eV/sr/mol·Ir by comparing to the scattering intensity measured for a known quantity of vanadium.

#### 4.3.2.3 Detailed balance correction

To isolate the true inelastic neutron scattering from the sample from various types of background we used the fact that inelastic scattering from the sample at a given temperature $T$ must obey the detailed balance principle $S(-\omega) = \exp(-\hbar\omega/k_{\mathrm{B}}T)S(\omega)$. The component of the scattering that does not obey detailed balance between positive and negative energy transfer processes can be considered an approximately temperature-independent background component. Assuming that there exists a true inelastic signal $S(Q,\omega)$ and a temperature-independent background $I_{\mathrm{bkg}}(Q,|\hbar\omega|)$, the scattering intensity for a particular point in $Q-\omega$ space at temperature $T$, should obey the following relationship:

$$I(T,\delta) = I_{bkg}(\delta) + e^{-\beta\hbar\omega(1-\delta)/2}S(T) \tag{4.6}$$

Here, $\delta = [1, -1]$ and denotes positive or negative energy transfer. Due to kinematic constraints, some values of $Q$ and $|\hbar\omega|$ do not permit $(Q, |\hbar\omega|)$ and $(Q, -|\hbar\omega|)$ to be simultaneously accessed. These points are therefore excluded from the analysis. For every pixel in $Q - \hbar\omega$ space the value of $I_{\mathrm{bkg}}(\delta)$, $I_{\mathrm{bkg}}(-\delta)$, and $S(T)$ are independent free parameters. $S(T)$ can furthermore take on different values for each temperature. This leads to $2N_T$ equations with $2 + N_T$ unknowns, where $N_T$ is the number of temperatures where full $Q - \hbar\omega$ dependent data sets have been acquired. So long as $N_T \geq 2$, a solution can be found for the $Q - \hbar\omega$ dependent inelastic scattering cross section at each temperature.

The system of equations was solved using a weighted ordinary least-squares method [108], resulting in full solutions of $S(T)$, $I_{bkg}(\delta)$, and $I_{bkg}(-\delta)$ for every value of $Q$, $\hbar\omega$, and $T$ where scattering data are available for positive and negative values of $\hbar\omega$ Estimates for the standard error are also obtained. This detailed balance correction was performed separately for each incident neutron energy. We note that the method requires accurate correction for energy-dependent neutron absorption and detector efficiency. Also note that temperature-dependent elastic scattering is not treated correctly with this method.

Fig. 4.5 shows how inelastic scattering with contributions from magnetism and phonons is separated from temperature independent backgrounds and

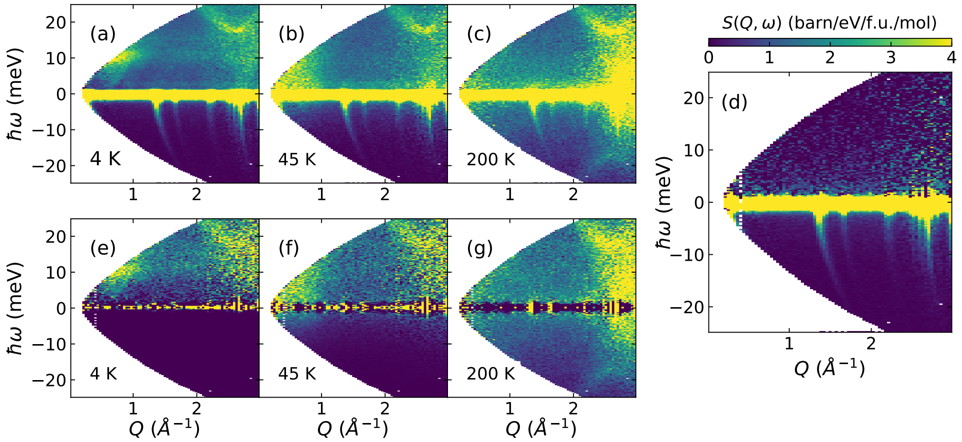

**Figure 4.5:** Inelastic neutron scattering spectra for $\beta$-$^{7}\mathrm{Li}_2^{193}\mathrm{IrO}_3$ before and after background subtraction as described in Sec. 4.3.2.3. (a-c) Spectra measured at $T = 4$ K, 45 K, and 200 K with incident neutron energy $E_\mathrm{i} = 30.0$ meV. The detailed balance correction was performed for measurements with all $E_i$ configurations. (d) The temperature-independent background $I_{\mathrm{bkg}}(Q,\omega)$ (Eqn. 4.6).

elastic scattering. Note the successful removal of the tails of Bragg scattering for $\hbar\omega < 0$. These are clearly seen in the raw data (Fig. 4.5 (a-c)). They are identified as a temperature-independent background (Fig. 4.5(d)), and are no longer present in the inelastic scattering spectra after the procedure (Fig. 4.5 (e-g)). In Fig. 4.6 (a-c), we presented the energy cuts integrating over $1.5\text{Å}^{-1} < Q < 2.0\text{Å}^{-1}$ for both raw data and the inelastic spectra after detailed balance correction. We note that at high energy transfers in panels (a-c), the scattering intensity in the extracted inelastic spectra (blue) exceeds that in the raw data (black) at some $\omega$ values. This is because the detailed balance method is not employing a direct point-by-point subtraction but carries out a least-square fit to the full temperature dependent data set under the assumption that the non-inelastic scattering (backgrounds and elastic scattering) is temperature-independent. Both statistical uncertainty and any temperature-dependence of non-inelastic contributions to the measured count rates can cause the intensity after this background correction process to exceed the raw count rate within error bars (Fig. 4.6).

After this point, the magnetic scattering is isolated by the subtraction of the high temperature $T$=200.0(1) K measurement with the appropriate Bose-Einstein scaling using Eq. 3.3. These procedures were repeated for all incident energy configurations.

### 4.3.3 Inelastic neutron scattering

The scattering discussed from this section will feature only the extracted magnetic contributions. Details about the isolation of magnetic scattering will follow, but the procedures are similar to those used for $Ba_4NbRu_3O_{12}$. Fig. 4.7(a) and 4.7(b) show color images of the inelastic magnetic neutron scattering from the 3.6 g powder sample at $T$=45 K and 4 K, which are above and below the ordering temperature respectively. Representative energy and momentum cuts through the same data are shown in Fig. 4.8. In the paramagnetic phase at $T$ = 45.0(1) K [Fit. 4.8(a) and Figs. 4.8(b) and 4.8(b)], the spectrum extends from the lowest accessible energy transfer of 2 meV to beyond the kinematic limit of the experiment (near 30 meV). The scattering cross section is further attenuated with increasing $Q$ than the iridium form factor [dashed line in Fig. 4.8(b)] can account for. This indicates short-ranged inter-site spin correlations . The spectrum of fluctuations [Fig. 4.8(a)] extends to energies well beyond $k_BT$, which is characteristic of frustrated magnetic materials where competing interactions do not favor a state with long-range spin order. In particular the

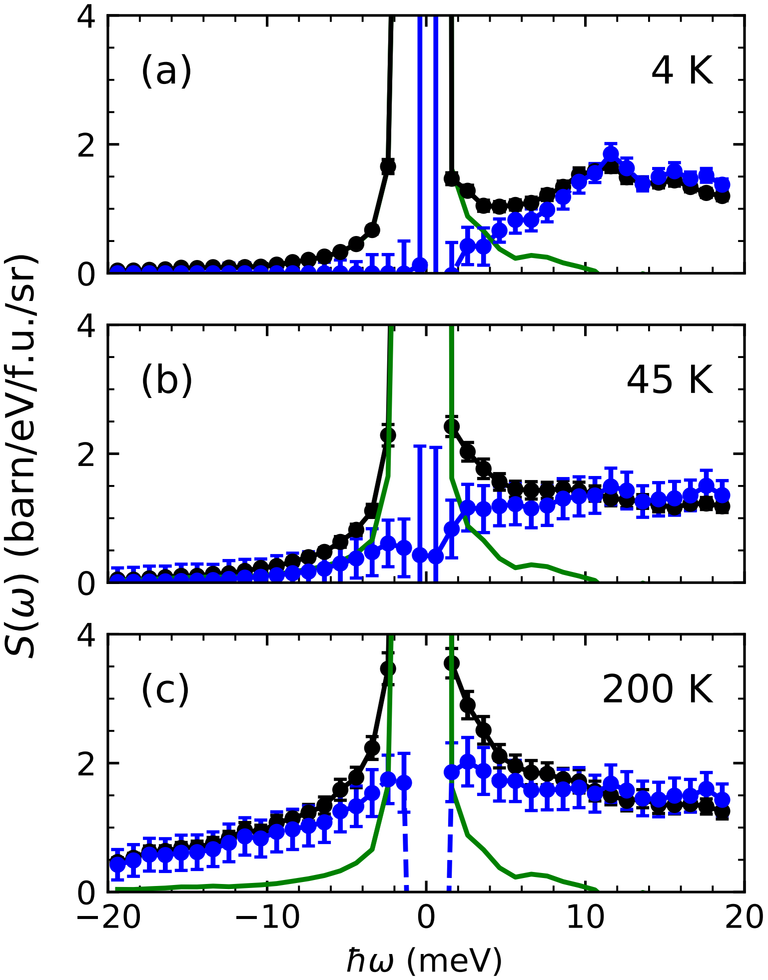

**Figure 4.6:** Energy cuts with integration over $Q \in [1.5, 2]$ Å$^{-1}$ for inelastic scattering from powder $\beta$-$^{7}\mathrm{Li}_2^{193}\mathrm{IrO}_3$ extracted from the data sets shown in Fig 4.5. The black symbols represent raw data before the detailed balance correction was applied. The blue symbols represent the extracted inelastic scattering $I_T(Q, \hbar\omega)$ and the green line represents the inferred temperature-independent background $I_{\mathrm{bkg}}(Q, \hbar\omega)$ as determined by the detailed balance-based routine described in the text.

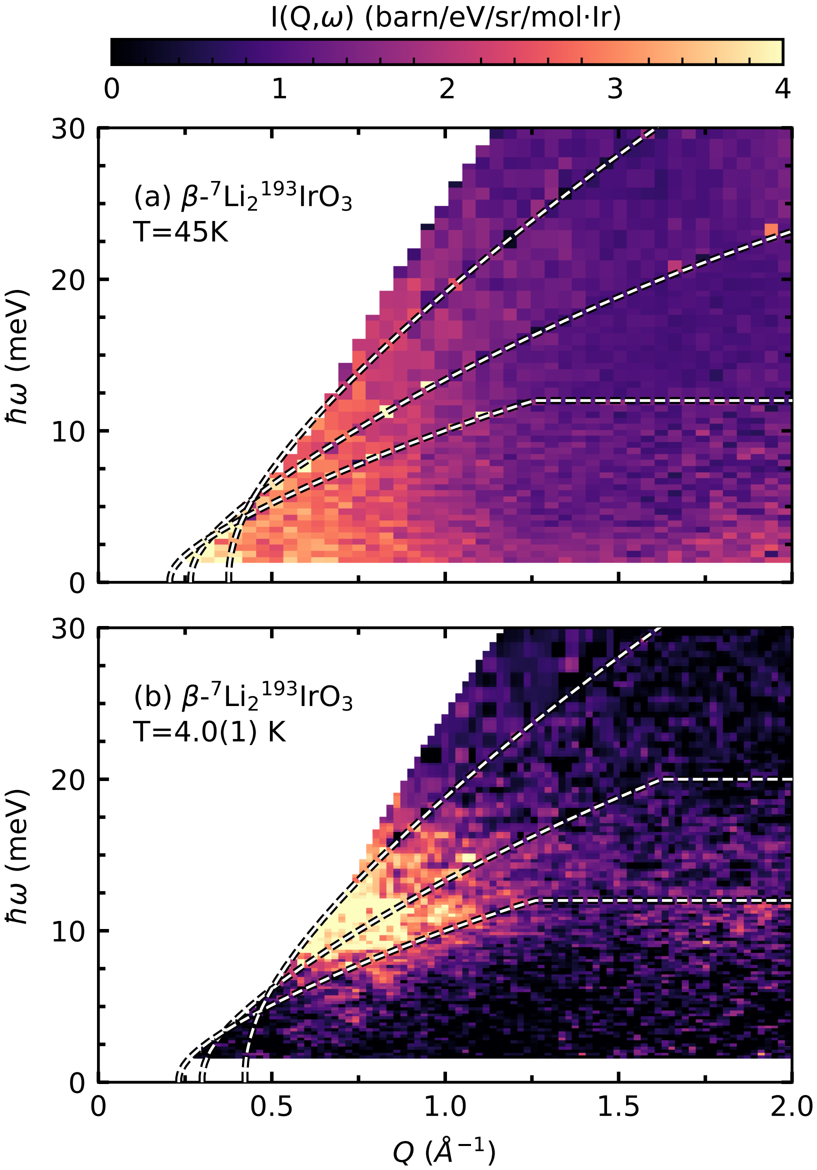

**Figure 4.7:** Magnetic excitation spectrum of $\beta$-$^7$Li$_2^{193}$IrO$_3$ probed by inelastic neutron scattering at (a) $T = 45$ K and (b) $T = 4$ K. The data combines scattering from neutrons of incident energies 10.5 meV, 30 meV, 60 meV, and 120 meV. Data acquired at $T = 200$ K and 300 K were used to determine the temperature dependent one-phonon scattering, which was subtracted to isolate the magnetic scattering. The dashed lines show the kinematic limit for each incident neutron energy employed.

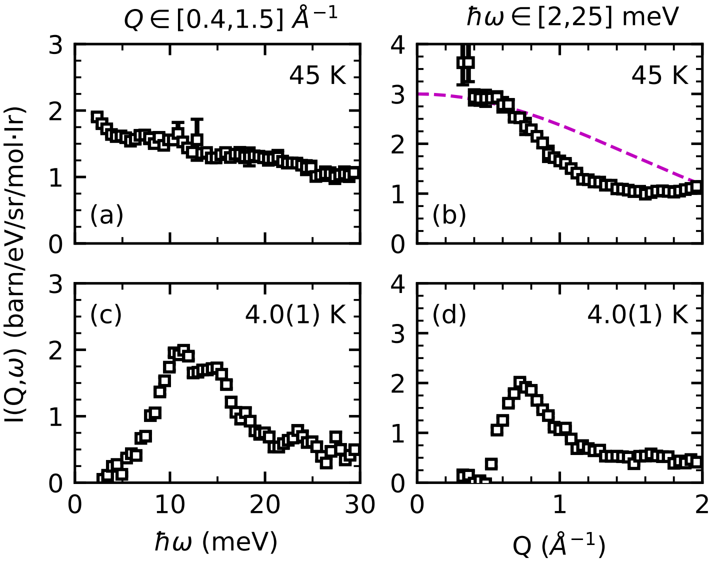

**Figure 4.8:** Cuts across experimental data shown in Fig. 4.7. The spectra in (a) and (c) represent averages over $Q \in [0.4, 1.5]$ $\text{Å}^{-1}$ while the $Q-$dependent scattering intensity in (b) and (d) average over $\hbar\omega \in [2, 25]$ meV. $Q-$averaging is weighted by $Q^2$ to represent the average of $I(Q, \hbar\omega)$ throughout a spherical shell of momentum space. The kinematic limits indicated in Fig. 4.7 impact these cuts as the averages can only be extended over kinematically accessible regimes of $Q$ and $\hbar\omega$. The dashed purple line in (b) shows the scaled magnetic form factor $|F(\mathbf{Q})|^2$ for $\text{Ir}^{4+}$.

$T$=0 dynamic spin correlation function of the Kitaev quantum spin-liquid is virtually $Q$ independent while the spin-flip excitation spectrum is broad and featureless above a gap [32, 109].

A massive rearrangement of spectral weight occurs upon cooling to $T$=4.0(1) K $\ll T_N$ [Fig. 4.7(b)]. Lower energy magnetic neutron scattering shifts to an energy transfer $\hbar\omega \approx 12$ meV intensity maximum. Strong momentum dependence develops in the low-energy regime with a distinct intensity near the incommensurate magnetic wave vector $Q_m = 0.57(1)a^*$ [44]. There is an apparent gap of $\Delta = 2.1(1)$ meV in the magnetic excitation spectrum [4.8(c)].

The detailed temperature dependence of the magnetic neutron scattering from $\beta$-$Li_2IrO_3$ is depicted in Fig. 4.9.

Panel (a) shows the development of elastic magnetic Bragg peaks as an order parameter (squared). The Néel temperature is consistent with a peak in the magnetic specific heat plotted as $\Delta C(T)/T$ versus $T$ in the inset to Fig. 4.11(a). Fixing the critical temperature to $T_N = 38.5(5)$ K inferred from $\Delta C(T)/T$ to be discussed later, a fit to the temperature dependent Bragg intensity yields a rough estimate of the critical exponent $\beta = 0.42(6)$. This value is consistent with the value for the 3D Ising model ($\beta_{\text{Ising}} = 0.326$) but also indistinguishable from the Heisenberg ($\beta_{\text{Heisenberg}} = 0.365$) and XY models ($\beta_{\text{XY}} = 0.345$). Fig. 4.9(b) displays the temperature dependence of the magnetic excitation spectrum as a color image. The data illustrate depletion of low energy inelastic scattering as in an Ising-like phase transition and the transfer of spectral weight into a broad peak centered at 10 meV (Fig. 2(c)).

### 4.3.4 Time-domain THz spectroscopy

Time-domain THz spectroscopy was performed using a custom-built system with frequency range 0.2-2 THz [110] at zero magnetic field. The measurement was performed on a dry pressed powder pellet of $\beta-Li_2IrO_3$ with diameter 5 mm, thickness 0.6 mm and mass 5.0(1) mg. Transmission spectra were collected at temperatures from $T = 3$ K to 40 K. The $T = 50$ K spectrum was used as an approximately nonmagnetic reference.

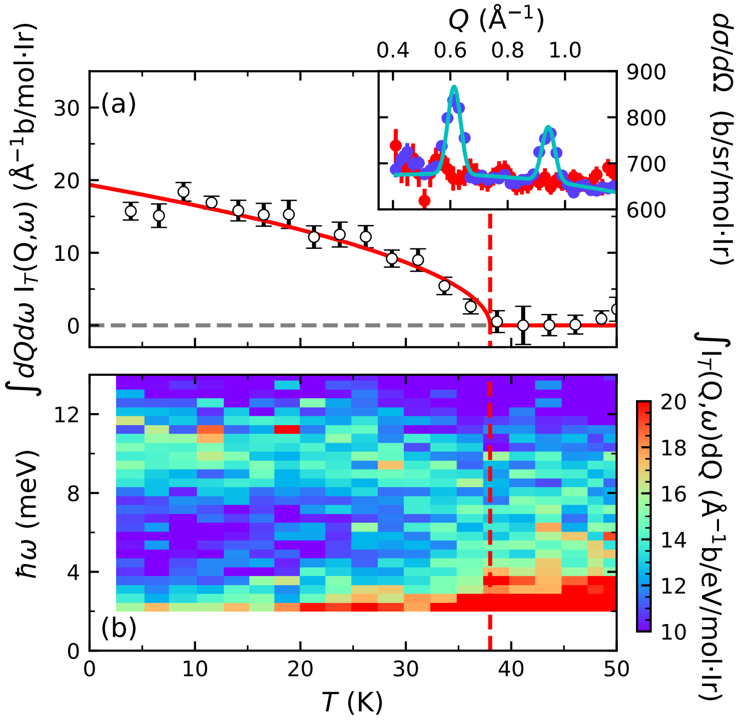

**Figure 4.9:** Temperature dependence of magnetic neutron scattering from $\beta$-$^7\mathrm{Li}_2^{193}\mathrm{IrO}_3$. (a) Temperature dependence of the $Q$-Integrated intensity of the magnetic Bragg peaks (1,1,1)-**k** and (0,0,0)±**k** shown in the inset. The line through the data is that of an order parameter squared with critical exponent $\beta = 0.42(6)$ and the critical temperature $T_N = 38$ K (dashed red line) determined from the specific heat capacity data in Fig. 4.11(a). The inset depicts the integrated elastic scattering around the magnetic Bragg peaks at $T = 3.95$ K (blue points) and $T = 50.0$ K (red points). the cyan line depicts an example of the gaussian fits used to extract magnetic diffraction intensity which is a measure of the staggered magnetization squared. (b) Temperature dependent inelastic magnetic neutron scattering integrated over $Q \in [0.5, 1.0]$ Å$^{-1}$.

The energy dependent complex THz transmission through a slab of material with thickness $d$ may be written as

$$\tilde{\mathcal{T}}(\omega) = \frac{4n_s}{(1+n_s)^2} \exp{(i\frac{\omega d}{c}(n_s - 1))}. \tag{4.7}$$

Here, $n_s = n - ik$ is the complex refractive index of the material. Note, that the real part of the refractive index $n$ indicates the phase velocity, while the imaginary part $k$ is called the absorption coefficient and measures the attenuation of the electromagnetic wave while propagating through the material. We solve for $n_s$ numerically for all temperatures. The index of refraction at temperature $T$ is given by $n_T = \sqrt{\epsilon(1+\chi_M)}$, where $\epsilon$ is the generalized permittivity and $\chi_M$ is the magnetic susceptibility. For a sample that has a magnetic response below a reference temperature $T_{ref}$ and no magnetic response above $T_{ref}$, we derive an expression for magnetic susceptibility by taking the ratio of the refractive indices above and below the transition temperature.

$$\frac{n_T}{n_{T_{ref}}} = \sqrt{1+\chi_M}, \tag{4.8}$$

from which we obtain

$$\chi_M(\omega) = (\frac{n_T}{n_{T_{ref}}})^2 - 1 \tag{4.9}$$

The $Q = 0$ spectrum is of particular interest as it reflects spin-space anisotropy, which is central to the Kitaev model. To measure this, we use THz spectroscopy. The THz transmission spectrum for $\beta - \mathrm{Li_2IrO_3}$ is presented in Fig. 4.10(a), and the absorption coefficient $k$ is shown in Fig. 4.10(b). Low THz transmission at higher energy transfers precluded reliable measurements of spin-wave excitations above 5 meV. The higher energy feature seen in THz

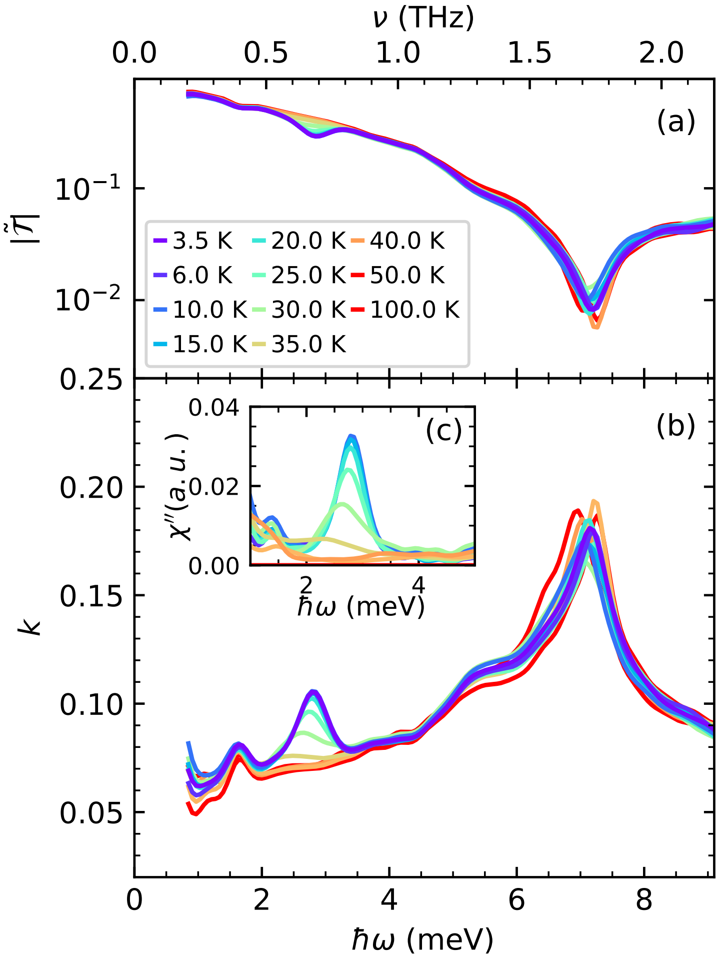

**Figure 4.10:** Time-domain THz spectroscopy of $\beta$-$^7\mathrm{Li}_2^{193}\mathrm{IrO}_3$. (a) Raw THz transmission data at temperatures from 3 K to 40 K. (b) Absorption coefficient $k$ inferred from the transmission data in (a). The sharply defined temperature dependent peak at 2.8(1) meV is associated with a magnetic excitation from the long range ordered state. Based on Eq.4.9, this peak is shown as $\chi''(\omega)$ in the inset. A second excitation is seen around 7.0(2) meV but its temperature dependence is quite different from the 2.8 meV peak and its origin is unclear. The quality of the higher energy data is impacted by the reduced transmission (see frame (a)). The temperature independent peak at 1.6 meV arises from an instrumental interference effect.

transmission near 7 meV is not temperature dependent, and thus we do not attribute it to magnons. Another feature at ≈1.6 meV is an instrumental interference effect that is not associated with the electromagnetic response of the sample. However, the peak at $2.8(1)$ meV has a Lorentzian shape and gradually forms at temperatures below $T_{\mathrm{N}} = 38$ K. The corresponding $T-$ dependent imaginary part of the dynamic magnetic susceptibility $\chi''(\omega)$ at $Q = 0$ is shown in Fig. 4.10(c). We associate this peak with a zone center gap in magnetic excitations from the ordered state. The finite gap in the excitation spectrum is direct evidence of anisotropic magnetic interactions.

### 4.3.5 Specific heat

Heat capacity measurements were performed in a Quantum Design physical properties measurement system (PPMS). To enhance thermal conduction, we used a pellet pressed of equal parts by mass of silver and $\beta$-$\mathrm{Li_2IrO_3}$. Measurements were taken at zero field for the range of $T = 2 - 300$ K and at $\mu_0 H = 14$ T for the range of $T = 2 - 100$ K. The silver contribution to the specific heat was subtracted based on tabulated values in Refs. [111–113]. Low temperature heat capacity measurements for $T = 0.1 - 3.5$ K were performed using the PPMS dilution refrigerator option. This measurement was done on a 1.50(1) mg piece of a pressed pellet of pure $\beta$-$\mathrm{Li_2IrO_3}$ with no silver.

To access the $Q-$averaged magnetic excitation spectrum at the lowest energies, and to probe the critical regime near the magnetic phase transition, we measured the specific heat capacity $C(T)$. The result is shown as a plot of $C/T$ in Fig. 4.11(a). The zero field data set (black symbols) features a sharp

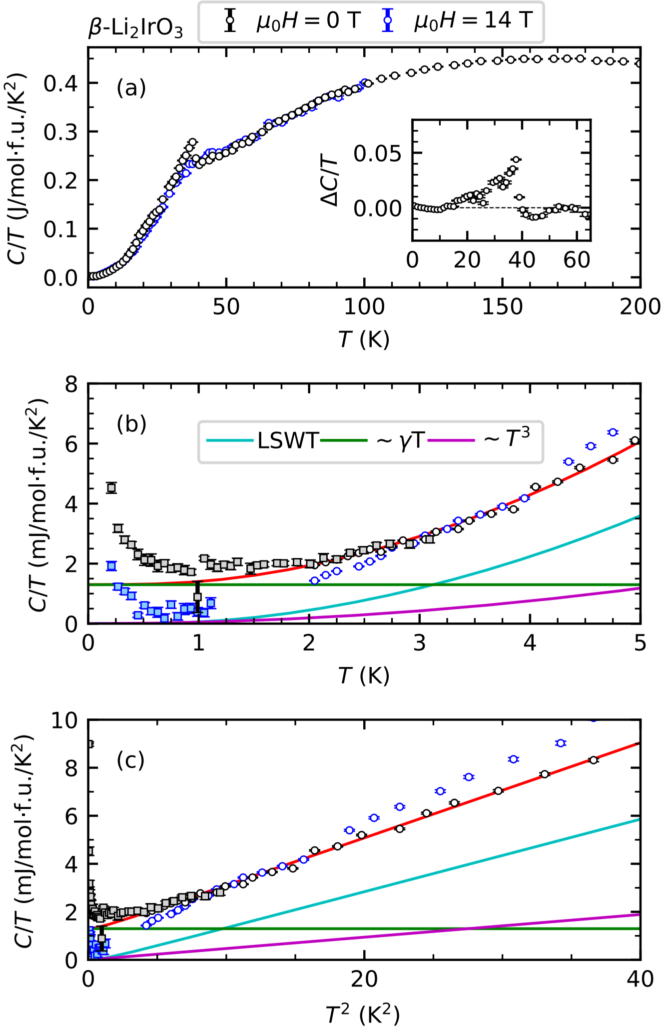

**Figure 4.11:** Specific heat capacity of $\beta$-$^7$Li$_2^{193}$IrO$_3$ plotted as $C(T)/T$. Black points represent zero field measurements, blue points represent 14 T measurements. Square symbols denote data acquired using the dilution refrigerator in a PPMS. Circle symbols denote data from the high temperature configuration of the PPMS. (a) Specific heat at zero-field and $\mu_0 H = 14$ T. (Inset) View highlighting the peak associated with the magnetic phase transition. The quantity $\Delta C(T)/T$ is the difference between the zero field and 14 T measurements. (b) Low $T$ regime with model fitting. The red line is the sum of three terms described in the text originating from the low-energy magnetism and phonons. (c) $C/T$ vs $T^2$. The $T-$linear term in $C(T)$ is visible here as the intercept with the y-axis. The 14 T data (blue points) show a zero intercept so that the $T-$linear term appears to be associated with magnetic excitations.

peak at $T_\mathrm{N} = 38$ K that is suppressed and broadened by the application of a 14 T magnetic field (inset to Fig. 4.11(a)). This indicates a magnetic phase transition in an anisotropic material as detailed in previous studies on single crystalline samples [41, 98, 102]. The change in entropy associated with the temperature regime in the immediate vicinity of the phase transition (10 K to 40 K) is estimated to $\Delta S_m = 0.41(1)\mathrm{Jmol}^{-1}\mathrm{K}^{-1}$. Representing just 7% of the $R\ln 2$ total spin entropy per iridium, this small peak indicates the magnetic order is incomplete and/or develops from a strongly correlated state. This observation is consistent with the small ordered moment (0.47(1) $\mu_B$ [43]) and the fact that the magnetic excitation spectrum extends well beyond $k_B T$ for $T = 45\ \mathrm{K} > T_N$ (Fig. 4.7(a) and Fig. 4.8(a)). Correspondingly, the peak in $C(T)$ marking the phase transition rides on a broad maximum, which in addition to contributions from phonons, is associated with the development of short range spin correlations.

Fig. 4.11(b,c) display $C(T)/T$ in the low temperature regime. While the upturn for $T < 1$ K is associated with hyperfine splitting of the nuclear spin-3/2 of iridium, there is also a Sommerfeld-like term $C(T) = \gamma T$ that is unusual for a long range ordered insulating magnetic material. $\gamma$ is driven to zero in a field of 14 T, which indicates it is associated with gapless electronic excitations.

## 4.4 Analysis - $\beta$-$Li_2IrO_3$

### 4.4.1 Spin Hamiltonian and linear spin-wave theory

The three presented measurements together contain a significant amount of information regarding the low energy excitations in $\beta$-$Li_2IrO_3$. However, even with all of this information the extraction of quantitative information in the exchange Hamiltonian is highly nontrivial. If the Kitaev picture is indeed applicable, the exchange is highly anisotropic, and it is extremely difficult to stabilize the observed magnetic structure in software like SpinW [114]. In order to supplement our experimental efforts, we collaborated with the Perkins group at the University of Minnesota who were already quite familiar with this material and its magnetism [105].

To account for the counter-rotating spin structure, the minimal spin Hamiltonian for $\beta$-$Li_2IrO_3$ is the previously discussed $J$-$K$-$\Gamma$ model [103, 105, 115]

$$\mathcal{H} = \sum_t \sum_{\langle ij \rangle \in t} \mathcal{H}_{ij}^t, \tag{4.10}$$

where

$$\mathcal{H}_{ij}^t = J\vec{S}_i \cdot \vec{S}_j + K S_i^{\alpha_t} S_j^{\alpha_t} + \sigma_t \Gamma (S_i^{\beta_t} S_j^{\gamma_t} + S_i^{\gamma_t} S_j^{\beta_t}). \tag{4.11}$$

Following the nomenclature of Ref. [116], $\mathbf{S}_i$ denotes the pseudo-spin $j_{\text{eff}} = 1/2$ operator at site $i$. The five different types of NN Ir-Ir bond are labeled $t \in \{x, y, z, x', y'\}$ with associated Cartesian components $(\alpha_t, \beta_t, \gamma_t) = (x, y, z)$, $(y, z, x)$, and $(z, x, y)$ for $t \in \{x, x'\}$, $\{y, y'\}$, and $\{z\}$, respectively. For simplicity, we take $K$ to be bond independent though the $z$ type bond by symmetry is distinguishable from the $(x, x')$ and $y, y'$ type bonds. The prefactor $\sigma_t = \pm 1$ determines the sign of the $\Gamma$ interactions which is bond-dependent and prescribed by lattice symmetry [117]. Fixing the overall energy scale to be $J^2 + K^2 + \Gamma^2 \equiv 1$, the Hamiltonian in Eq.(4.11) can be parameterized in terms of polar angles $\theta$ and $\phi$ as

$$J = \sin\theta\cos\phi,\ K = \sin\theta\sin\phi,\ \Gamma = \mathrm{sgn}(\Gamma)\cos\theta. \tag{4.12}$$

Within this parameterization, Luttinger-Tisza (LT) analysis indicates the counter-rotating order is stabilized in the approximate range of $(\theta, \phi) \in [(0, \frac{\pi}{2}), (\frac{3\pi}{2}, \frac{13\pi}{8})]$ [105, 115]. Varying mostly with $\phi$, the incommensurate wave vector $\mathbf{Q} = h\mathbf{a}^*$ takes on values in the range $0.53 \lesssim h \lesssim 0.80$ [117], which may be compared to the experimental value of $h = 0.57(1)$[43]. The LT method does not include the higher harmonic components that are required to ensure a fixed spin length for a general incommensurate order. Instead of using an incommensurate wavevector, we take the magnetic structure to be a long-wavelength deformation of the closest $\mathbf{Q} = (2/3, 0, 0)$ commensurate approximation of the true order [105]. Within the region of phase space with dominant Kitaev interactions, this description accounts for most experimental findings reported so far, including the observed static spin structure factor, the irreducible representation, magnetic structure of two counter-rotating spin sublattices, the response under a magnetic field, as well as Raman scattering [44, 102, 116, 118–120].

Given the Hamiltonian (4.11) and the parameterization (4.12), we employ the standard $1/S$ semiclassical expansion and compute the dynamical spin structure factor. To accommodate the zero-field spiral magnetic order with propagation wavevector $\mathbf{Q} \parallel \mathbf{a}^*$, we use an enlarged magnetic unit cell composed of three orthorhombic unit cells along the $\mathbf{a}$-axis with 48 magnetic sites [105].

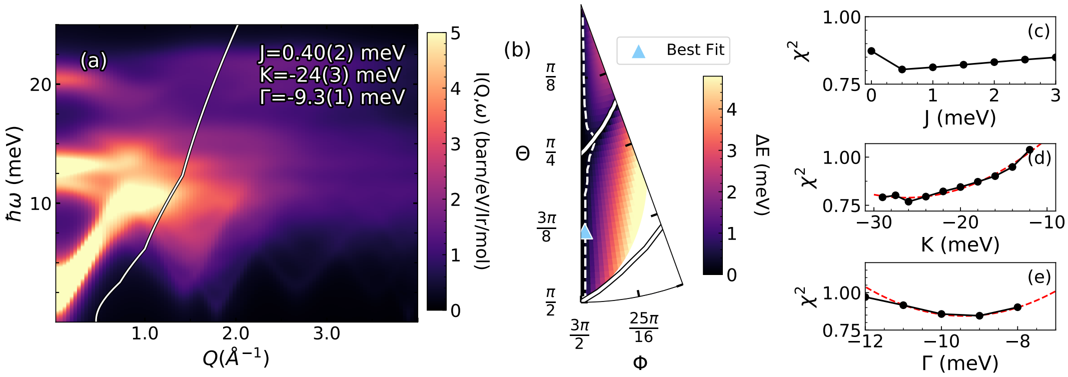

**Figure 4.12:** LSWT fitting results to magnetic neutron scattering data for $\beta$-$^7$Li$_2^{193}$IrO$_3$. (a) Calculated spectrum of inelastic neutron scattering for the best fit parameters. The white line represents the kinematic limit of the experiment which combined four different incident neutron energies. (b) The calculated gap at the $\Gamma$ point in the phase space of $J$-$K$-$\Gamma$ model, as described by parameters $\theta$ and $\phi$ in Eqn. (4.12).The solid white lines depict phase boundaries between dominant $K$ and $\Gamma$ interactions as described in Ref. [105] and the triangle represents the best fit result from our experiment which is used to calculate the spectrum in panel (a). The white space represents the region of phase space in which the observed magnetic structure is not stabilized as the lowest energy ground state. The dashed white line shows the path through phase space where $\Delta E = 0.4$ meV. (c-e) The $\chi^2$ goodness of fit versus the free parameters $J$, $K$, and $\Gamma$. The red dashed lines in (d) and (e) are parabolic fits from which the minima and their uncertainties were extracted.

### 4.4.2 Refinement of exchange parameters

Now, using a linear spin-wave theory description of the antiferromagnetic state of $\beta$-Li$_2$IrO$_3$, we may independently refine the exchange parameters $J$, $K$, and $\Gamma$ by comparison to inelastic neutron scattering, THz spectroscopy, and heat capacity measurements as presented in Sec. 4.3.

Fig. 4.12(a) presents the calculated $\mathcal{S}(Q,\omega)$ with the best fit INS spectra (Fig. 4.7, with $K = -24(3)$ meV, $\Gamma = -9.3(1)$ meV, and $J \approx 0.40(2)$ meV. For $Q$ within the kinematic limits set by the experimental conditions and indicated by the white line in Fig. 4.12(a), the model calculation is consistent with the experimental data in Fig. 1(b). In the $J$-$K$-$\Gamma$ model, the effects of each parameter on the calculated spectra are shown in Appendix 7.1, from which it is immediately clear that the part of $\mathcal{S}(Q,\omega)$ accessed in our neutron scattering experiment is sensitive to $\Gamma$ and $K$. In contrast, the Heisenberg interaction $J$ barely affects the spectrum that is visible in INS, and therefore is not well constrained by the neutron data. The fidelity in refining $J, K, \Gamma$ from INS is quantitatively reflected in the variation of $\chi^2$ with each parameter as shown in Fig. 4.12 (c-e). While $\chi^2$ v.s. $K$ and $\Gamma$ have a parabolic shape, Fig. 4.12 (c) shows the value of $J$ is not well constrained by the INS data. The magnitude of the $Q = 0$ gap $\Delta E$ is however, closely linked to $J$. To determine $J$, we therefore turn to THz spectroscopy, which probes the $\Gamma$ point spectrum and is sensitive to $\Delta E$. The result of calculating $\Delta E$ using LSWT over the phase space consistent with the incommensurate order is shown in Fig. 4.12 (b). Near our best fit point from INS, $\Delta E$ increases strongly with increasing values of $\phi$ or $J$. This is shown explicitly in Fig. 4.10 (a).

Using the values of $K$ and $\Gamma$ and the range of $J$ determined from INS, the LSWT predicts the lowest two modes at $Q = 0$ to be at $0 - 1$ meV and $1 - 5$ meV. We designate these modes as $M_1$ and $M_2$ respectively and their dependence on $J$ within linear spin wave theory is presented in Fig. 4.10. Assigning the 2.8 meV peak observed in THz spectroscopy (Fig. 4.10) to the higher energy mode leads to the refinement of $J = 0.40(2)$ meV and the prediction of the lower energy mode at 0.4 meV. Here we do not consider the effects of magnon anharmonicity, which may renormalize $M_1$ and $M_2$ to be much closer together in energy. The $Q = 0$ mode energy estimates obtained by treating the magnon interactions at the level of a mean-field decoupling of the quartic terms (and disregarding the magnon decay processes driven by the cubic terms) appear to be able to bring $M_1$ and $M_2$ much closer to each other with renormalized energies slightly below and slightly above 3 meV [120].

The temperature-dependent specific heat capacity $C_{\text{mag}}(T) \approx \partial U/\partial T$ can be modeled by bosonic magnons starting from

$$U(T) = \int_{\Delta}^{\infty} \frac{\epsilon\, g(\epsilon)}{e^{\beta\epsilon} - 1} d\epsilon. \tag{4.13}$$

Here, $\epsilon$ is the spin wave excitation energy, $\Delta$ is the excitation gap, $\beta = 1/k_B T$, and $g(\epsilon)$ is the magnon density of states[81]. For a three-dimensional antiferromagnet with a dispersion relation $\epsilon(q) = \sqrt{\Delta^2 + (cq)^2}$ (where $\Delta$ is the spin gap and $c$ is the spin-wave velocity), the density of states is

$$g(\epsilon) = \frac{V\eta}{2c^3\pi^2}\epsilon\sqrt{\epsilon^2 - \Delta^2}\,, \tag{4.14}$$

where $V$ is the unit cell volume and $\eta$ is a constant. The 3D nature of the low energy magnons is reflected in the linearity of $C_{\text{mag}}/T$ versus $T^2$ for temperatures above $\Delta/k_B$ (Fig. 4.11(c)). The values for $c$, $\Delta$, and $\eta = 4$ were fixed by the calculated linear spin-wave dispersion for the lowest energy band at the $\Gamma$ point. Because $c$ and $\Delta$ are closely coupled, the specific heat data do not provide an independent estimate for $\Delta$. To fit the measured specific heat, we must add a $T-$linear term with $\gamma = 1.28(2)$ mJ/mol/K$^2$, an additional $T^3$ term that may be associated with acoustic phonons, as well as a contribution at very low temperatures from the nuclear specific heat ($C(T) \propto 1/T^2$). A $T-$linear term in the specific heat capacity was previously associated with fermionic quasi-particles in spin-1/2 chains [121] and quantum spin liquid candidates [122] though it can also be associated with localized possibly disorder related excitations [123].

## 4.5 Discussion - $\beta$-$Li_2IrO_3$

Using a double isotope powder sample and the high intensity time of flight spectrometer SEQUOIA at the SNS, we have acquired inelastic magnetic neutron scattering data within the paramagnetic and within the incommensurate magnetically ordered state of the spin-1/2 hyper-honeycomb lattice of $\beta-{}^7\mathrm{Li}_2^{193}\mathrm{IrO}_3$. Complementary information about electronic excitations was obtained through time domain THz spectroscopy and specific heat capacity measurements.

To quantitatively establish a spin Hamiltonian for this material we compared the multiple inelastic neutron scattering measurements to detailed spin-wave theory of the anisotropic nearest neighbor $J$-$K$-$\Gamma$ model. This comparison constrained the parameters to $J = 0.40(2)$ meV, $K = -24(3)$ meV, and $\Gamma = -9.3(1)$ meV. The same set of parameters also predicts the excitations at the $\Gamma$ point observed by TDTS and is consistent with the heat capacity measurements.

Furthermore, the extracted Heisenberg exchange $J$ is consistent with the critical field for the ordered state, which is predicted to vary as $\mu_B \mu_0 H_c = 0.46J$ [118]. Using our result for $J$ we find $\mu_0 H_c \approx 3.2(2)$ T, which is consistent with the observed value of 2.8 T. Secondly, the strong absorption feature near $\hbar\omega = 7$ meV in our THz data is close to the prediction of the third-lowest

| Source | $JK\Gamma$ Estimate | Method |
|---|---|---|
| Ref. [105] | $\|K\| > \|\Gamma\| \gg \|J\|$ | LLG using magnetic structure |
| Ref. [98] | $\Gamma = -15(11)$ meV, $3J + K = -11(4)$ meV | Single crystal Magnetization |
| Ref. [118] | $J \approx 0.3$ meV, $\|K\| \gg \|J\|, \|G\| \gg \|J\|$ | $H_c$ and Magnetic Structure |
| Ref. [124] | $K \approx \Gamma < 0$, $J \ll \|K\|, J > 0$ | Diagonalization |
| Ref. [125] | $K = [-15, -12]$ meV, $\Gamma = [-3.9, -2.1]$ meV, $J = [0, 1.5]$ meV | Diagonalization and MRCI+SOC |
| Refs. [119, 126] | $K = -18$ meV, $\Gamma = -10$ meV, $J = 0.4$ meV | Raman Scattering, RIXS |
| This work | $K = -24(3)$ meV, $\Gamma = -9.3(1)$ meV, $J = 0.40(2)$ meV | INS, TDTS, Heat capacity |

**Table 4.1:** Summary of literature estimates of exchange parameters in $\beta$-$Li_2IrO_3$.

excitation at $\hbar\omega = 7.5$ meV at the $\Gamma$ point though low THz transmission precludes definite identification of the 7.5 meV anomaly (Fig. 4.10(b)) with a magnetic excitation. The feature also exists for $T > T_N$ and appears temperature independent even at high temperatures, making its nature rather unclear. However, the main feature in the THz spectroscopy at $\hbar\omega$ meV is consistent with the two peaks seen in recent Raman scattering work. These peaks lie at 2.5 and 3.0 meV and are signatures of non-Loudon-Fleury scattering processes, generated by magnetic-dipole-like terms in the Raman vertex, which are of a similar nature as the excitations probed by THz and INS [120]. Our results are generally consistent with previous theoretical and experimental works that have attempted to estimate these parameters as shown in Table 4.1.

Finally, we discuss the linear term $\gamma T$ in the zero-field heat capacity

(Fig. 4.11). The presence of a linear term in the specific heat of a magnetic origin in $\beta-\mathrm{Li_2IrO_3}$ is interesting because it cannot be accounted for by the spin wave theory that was used here to successfully account for the ordered state as well and the inelastic magnetic neutron scattering spectrum. A $T-$linear term can arise from fermionic quasi-particles with the Sommerfeld constant $\gamma$ proportional to the density of states at the Fermi level. $\gamma$ ranges from mJ/mole/K$^2$ in uncorrelated metals such as copper to J/mol/K$^2$ in heavy-fermion systems [127–129]. With no fermionic charge carriers, a linear term is generally unexpected for insulators. The complete suppression of $\gamma$ for $\beta-\mathrm{Li_2IrO_3}$ under a 14 T magnetic field (Fig. 4.11) indicates its magnetic origin and is consistent with prior NMR and THz data [130]. While a field dependent Sommerfeld term could arise from a metallic impurity phase, powder XRD studies as well as low temperature susceptibility measurements place an upper limit on the concentration of impurities at the percent level. If such impurities are the origin of the $\gamma T$ term they would need to be heavy fermion like.

It seems unlikely that exotic fermionic quasi-particles associated with a proximate spin liquid phase would contribute to the very lowest energy part of the excitation spectrum within a symmetry-breaking long range ordered state of $\beta$-$\mathrm{Li_2IrO_3}$. The incommensurate nature of the order could be relevant as it admits a gapless phason mode as well as complex domain wall structures both of which have the potential to contribute to the low temperature heat capacity. A detailed study of the field dependence of $\gamma$ to determine for example whether its disappearance coincides with the 2.8 T critical field [102] would be informative.

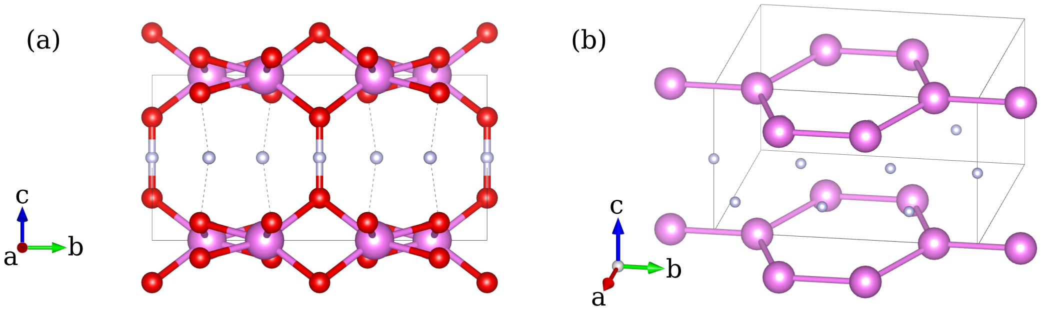

**Figure 4.13:** (a) Nuclear structure of $H_3LiIr_2O_6$ with Li ions removed for clarity. The interstitial hydrogen (white) serves to weaken the magnetic couplings between interlayer Ir ions (purple). Red ions are oxygen. (b) Stacked honeycomb lattice with oxygen ions removed for clarity.

## 4.6 Introduction to Kitaev spin-liquid candidate $(H,D)_3LiIr_2O_6$

### 4.6.1 Magnetic properties

In the context of the search for a Kitaev spin-liquid (KSL), the presence of non-Kitaev perturbations typically results in the formation of symmetry-breaking static spin-spin correlations rather than the condensation of a spin-liquid state. Indeed, even in materials that have been quantitatively shown to have strong Kitaev interactions like $\alpha-RuCl_3$ and the previously discussed $\beta-Li_2IrO_3$, zero field antiferromagnetic order is observed upon cooling. With this in mind, the suppression of non-Kitaev interactions was the motivation behind the synthesis of $H_3LiIr_2O_6$, which is isostructural to $\alpha$-$Li_2IrO_3$, with the interlayer $Li^+$ ions replaced by $H^+$. This was proposed to reduce magnetic coupling between honeycomb layers, and creating a truly two-dimensional iridate as depicted in Fig. 4.13. With this motivation, $H_3Li_2Ir_2O_6$ was first synthesized in 2018 [99]. The synthesis of this material is identical to that of

$\alpha$-$Li_2IrO_3$, and the substitution of the interlayer $Li^+$ ions by $H^+$ is done by a hydrothermal reaction. Initial powder x-ray diffraction studies indicated that though the honeycomb layer itself remains intact, the structure contains significant stacking faults evident from the lineshape associated with out of plane peaks. More detailed studies using synchotron x-ray diffraction and pair-distribution function analyses revealed that the stacking itself is random, and governed by the weak *O-H-O* interlayer coupling [131]. The sample itself is insensitive to air like other oxides, and is available in small single crystals suitable for x-ray or Raman studies, but of unsuitable size for inelastic neutron scattering [40].

Like $\beta$-$Li_2IrO_3$, $H_3LiIr_2O_6$ is a shown to be a spin-orbital Mott insulator of band gap 0.12 eV and an effective moment of 1.60 $\mu_B$ per Ir atom by resistivity and high temperature susceptibility studies [99]. The observed (powder average) value of $\theta_{CW}$=-105 K, indicating ferromagnetic interactions in the high temperature paramagnetic phase. Despite the $\approx$100 K value of $\theta_{CW}$, no magnetic order is observed at the lowest measured temperatures of 50 mK by specific heat and NMR studies. The low temperature NMR spin relaxation rate captures the presence of low-lying spin excitations below $T$=40 K, which are rapidly suppressed by the application of magnetic field. Likewise, specific heat studies show a fascinating scaling collapse of $C(T)B^{1/2}/T$ at low temperatures suggestive of exotic quasiparticles that are rapidly suppressed in field. Combined, these results indicate that $H_3LiIr_2O_6$ is a an exciting candidate for the realization of a ground state Kitaev spin-liquid phase.

### 4.6.2 Possible magnetic ground states

Explanations for these data are varied but the absence of the formation of static spin-spin correlations is highly constraining. One suggestion put forth by the original study was that $H_3LiIr_2O_6$ is a ground state spin-liquid, but without detailed spectroscopy or thermal transport studies to better understand the nature of the excitations this is only speculative. Another explanation for the scaling of the specific heat in field was found in the form of what is known as the random-singlet state. In this state, spins form singlet pairs are allowed to be between any two spins on the lattice and not only nearest-neighbor. Strongly coupled spins will pair first, which are predominantly nearest-neighbor. The spins that are left behind then form pairs, resulting in a power-law distribution singlet-triplet splitting which follows from a renormalization group analysis [132]. This approach was used to explain the scaling collapse of the $C(T)$ data for $H_3LiIr_2O_6$, along with other quantum spin-liquid candidates like $LiZn_2Mo_3O_8$ and Herbertsmithite [76].

Despite these interesting results, only a handful of experimental studies followed this 2018 result. Dielectric spectroscopy showed direct evidence of glass-like freezing of the $H^+$ ion positions between two potential hopping sites, with a crossover from thermally activated hopping to a quantum tunneling mechanism at temperatures below $T \approx 100$ K [133]. Still, the observed hopping frequency is in the mHz range, meaning that on the scale of the magnetism this effect at low temperatures may be viewed as a quasi-static disorder. Only very recently in 2023 did two spectroscopic studies appear, the first used a combination of anisotropic susceptibility and $\mu$SR studies and suggested the presence of both the random-singlet state and a disordered quantum paramagnetic state consistent with a spin-liquid [134]. Resonant inelastic x-ray spectroscopy studies came to a similar conclusion, with a clear $Q$-independent magnetic signal at energy transfer $\hbar\omega \approx 25$ meV in single crystalline samples [135].

The following presented work uses inelastic neutron scattering to map the previously unexplored low energy part of the excitation spectrum. The goal is to provide an accurate scattering description of the low-energy excitations free of non-magnetic backgrounds and to determine if the extracted scattering is consistent with a spin-liquid ground state.

## 4.7 $D_3LiIr_2O_6$ Inelastic Neutron Scattering

### 4.7.1 Experimental considerations

Like $\beta$-$Li_2IrO_3$, $H_3LiIr_2O_6$ suffers from a high absorption cross section from Li and Ir. Again, we mitigate this by a 99% enrichment of $^7$Li and $^{193}$Ir. This brings the total absorption cross section per formula unit to $\sigma_{abs} = 325$ b/(mol f.u.), with an effective transmission length of 3.5 mm for elastic scattering of 25 meV neutrons. We used the identical annular aluminum can design as the $\beta-Li_2IrO_3$ experiment. An additional difficulty in neutron scattering on this sample is the presence of $H$ ions, which have a nuclear spin incoherent scattering cross section of $\sigma_i = 25.3$ b. Normally, this makes the analysis of magnetic neutron scattering data for compounds including $H$ quite difficult as strong incoherent scattering will introduce multiple scattering effects of similar intensity to the magnetism. Without isotope enrichment, the overall incoherent scattering cross section per formula unit would be $\sigma_i$=242 b, and with deuterium enrichment this becomes a more manageable $\sigma_i = 6.9$ b. The end result was a 3.6 g of triply isotope enriched sample made by collaborators at the Max Planck institute.

Three separate neutron scattering measurements were performed. The first was measured on the SEQUOIA instrument at Oak Ridge National Laboratory [136]. Measurements of $D_3LiIr_2O_6$ were performed with incident energies $E_i$=30 meV and 60meV, using the fine chopper configuration at temperatures T=4.0(1) K and T=200.0(1) K. Counting times for the low temperature configurations were 22 hours and 28 hours and counting times at the high temperature configurations were 16 hours and 18 hours for $E_i$=30 meV and $E_i$=60 meV respectively. The sample with mass 3.6 g was loaded into a custom annular aluminum can of 20 mm outer diameter and 19 mm inner diameter with height 4 cm. The sample was prepared by solid state synthesis methods as described in Ref. [99] with triply isotope enriched $^2$D, $^{193}$Ir, and $^7$Li to mitigate absorption and incoherent scattering. A vanadium standard was measured using each experimental configurations to normalize both experiments to barn/sr/eV/mol Ir. Annular angle-dependent absorption was corrected by a Monte-Carlo method in the Mantid software [107]. Magnetic scattering from this measurement is shown in Fig. 4.14(a).

Polarized inelastic neutron scattering was done using the HYSPEC instrument at Oak Ridge National Laboratory [136]. The measurement was performed with incident energy $E_i$=20 meV in the high flux configuration. The same sample as the SEQ experiment was used but reloaded into a 7 mm outer

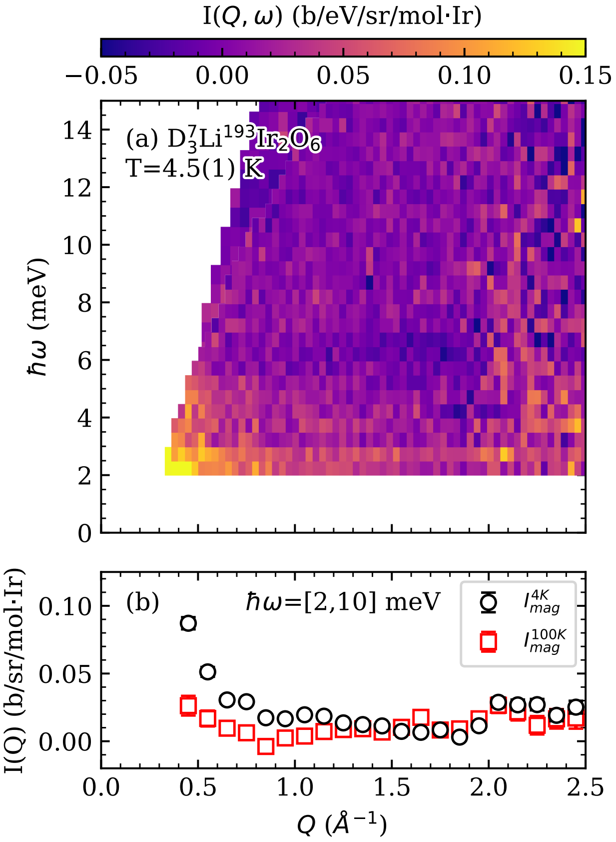

**Figure 4.14:** (a) Magnetic inelastic scattering of $D_3LiIr_2O_6$ at T=4.0(1) K. Scattering at energy transfers below energy transfer 1.8 meV is contaminated by noise from nonmagnetic elastic scattering. (b) Q-dependence of extracted magnetic scattering using average scattering from energy transfer over a wide window of $\hbar\omega = 2$ meV to $\hbar\omega$=10 meV. The low temperature $T$=4 K scattering shows a small but significant rise in intensity for $Q$<1.5 $\mathring{A}^{-1}$ when compared to the $T$=100 K scattering. Both show a finite increase in intensity approaching $Q$=0, as would be expected in a correlated paramagnet.

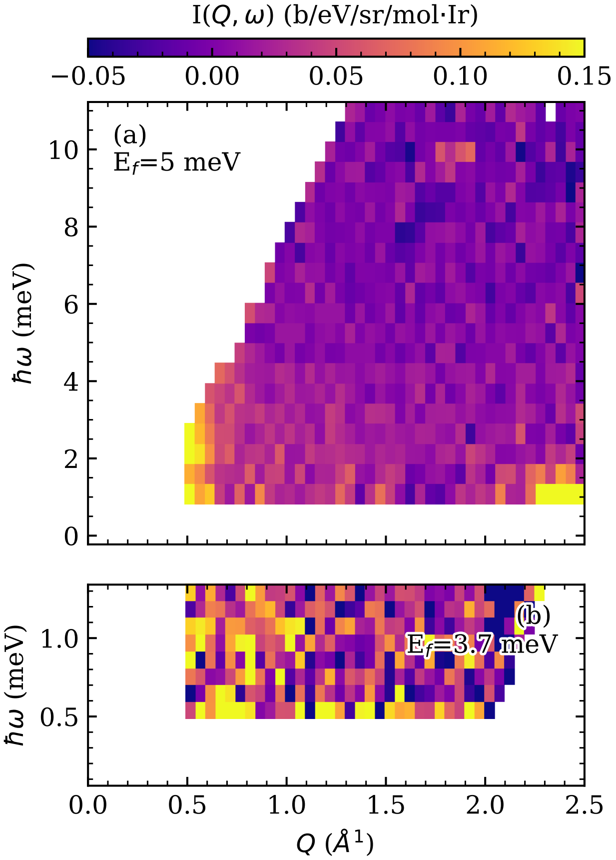

**Figure 4.15:** (a) Magnetic inelastic scattering from the MACS instrument of $D_3LiIr_2O_6$ at T=1.8(1) K using the $E_f$=5.0 meV configuration. Nonmagnetic contributions have been subtracted off as described in the text. (b) Magnetic scattering using the $E_f$ = 3.7 meV configuration.

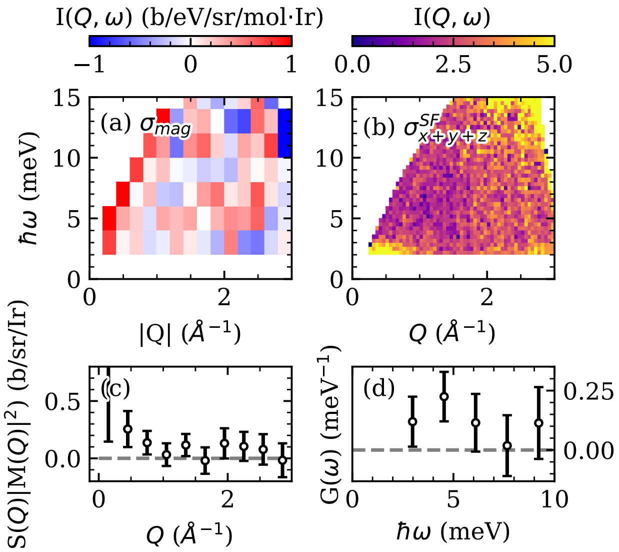

**Figure 4.16:** (a) Magnetic scattering obtained using the Sharpf equations [137]. The scattering does not have any strong enough statistics to draw any conclusions from. (b) Total spin-flip scattering for comparison to magnetic scattering. (c,d) Factorizations of magnetic scattering in (a).

diameter, 6 mm inner diameter annular can used for polarized experiments on HYSPEC. Total counting times for each polarization channel were [30, 30, 66, 12, 12, 8] hours for the [$\sigma_x^{SF}$, $\sigma_y^{SF}$, $\sigma_z^{SF}$, $\sigma_x^{NSF}$, $\sigma_y^{NSF}$, $\sigma_z^{NSF}$] configurations respectively. The $x$ and $y$ polarization directions lie in the scattering plane as defined by the Mezei flipper, while the $z$ is perpendicular to the scattering plane. Superscripts denote the spin-flip (SF) and non spin-flip (NSF) cross sections. The NSF cross sections were measured to apply corrections due to imperfect flipping ratio as well as to provide an overall normalization from the sample Bragg peaks. The same absorption corrections were applied as for the SEQ data.

The third measurement presented is from the MACS spectrometer at the NIST Center for Neutron Research [85]. This sample consisted of 2.0 g of enriched $D_3^7Li^{193}Ir_2O_6$ in an aluminum sachet of 0.5 mm thickness, using configurations of $E_f$=3.7 and $E_f$=5.0 meV with appropriate combinations of cooled BeO and Be filters before and after the sample to suppress higher order contamination. The scattering is shown in Fig 4.15 with the $E_f$=5.0 configuration in subplot (a) and the $E_f$=3.7 meV configuration in subplot (b). Both configurations were measured at $T$=1.7(1) K and $T$=45 K. All four measurements were counted for ten hours along with matching sample out backgrounds. Further details of each of these measurements are provided in the subsequent sections.

### 4.7.2 Isolation of magnetic scattering from SEQUOIA measurement

Little information may be extracted from the directly measured low temperature scattering in the unpolarized MACS and SEQ measurements. Even at low temperatures, the scattering from both phonons and inelastic multiple scattering dominates the overall signal as shown in the directly measured intensity in Figs. 4.17 and 4.18. Still, a qualitative comparison may be made between measurements at different temperatures by examining cuts along the $Q$ dimension averaged in a window of $\hbar\omega$=2 meV to $\hbar\omega$=5 meV shown in Fig. 4.18. Here, the contribution from phonons is roughly normalized between measurements by comparing scattering to only the high-$Q$ part of the scattering ($Q > 2.5$ Å$^{-1}$), resulting in the scales denoted in the legend.

While the two elevated temperature measurements are identical, the $T$ =4 K scattering shows a small buildup of intensity for $Q < 1.5$Å$^{-1}$. This is the

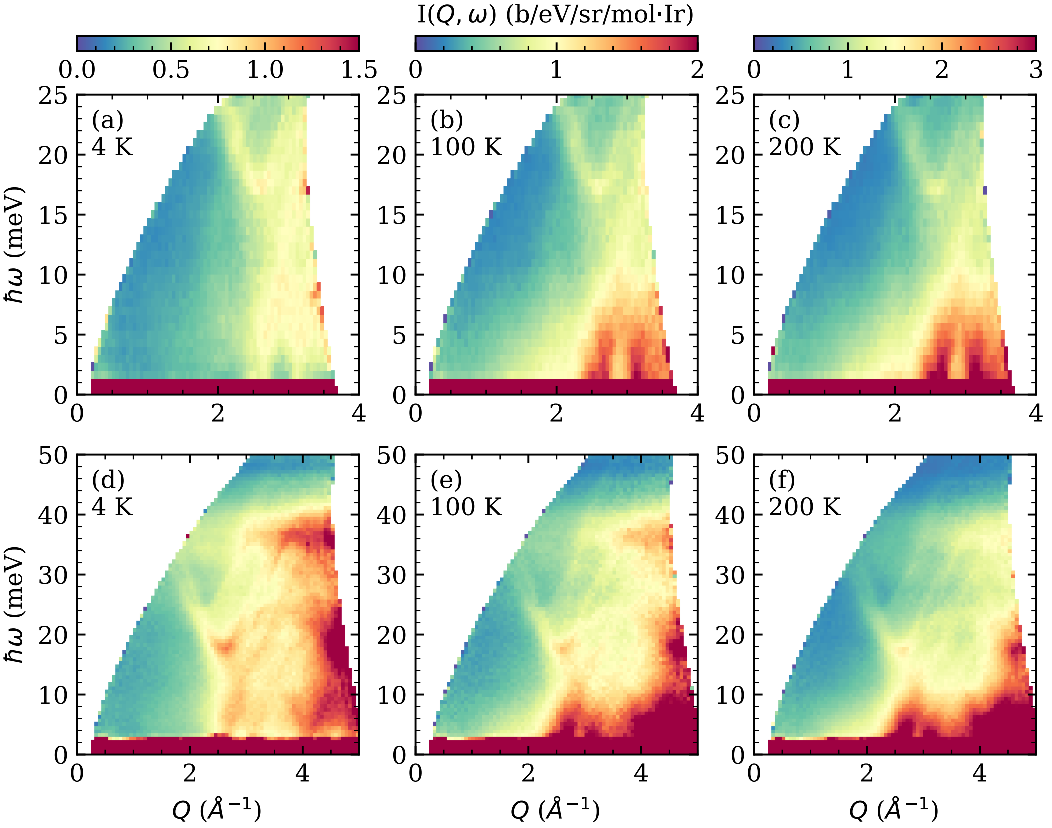

**Figure 4.17:** Directly observed intensity for all configurations in the SEQ experiment on $D_3LiIr_2O_6$. The top column is for $E_i$=30 meV, and the bottom is for $E_i$=60 meV.

direct indication of the buildup of temperature dependent dynamic spin correlations, which we will now extract more rigorously. Scattering normalization to a vanadium standard and absorption corrections are all that have been performed up to this point. Due to the fairly mobile and strongly scattering $H^+$ ions, the Debye-Waller factor should be accounted for as we attempt to subtract the associated background scattering. In general, neutron scattering cross sections include the Debye-Waller factor which is an overall prefactor to intensity that goes as $e^{-\langle u^2\rangle Q^2}$ where $\langle u^2\rangle$ is the mean-squared ion displacement. Of course, this is not a constant for every ion in the unit cell but as a first

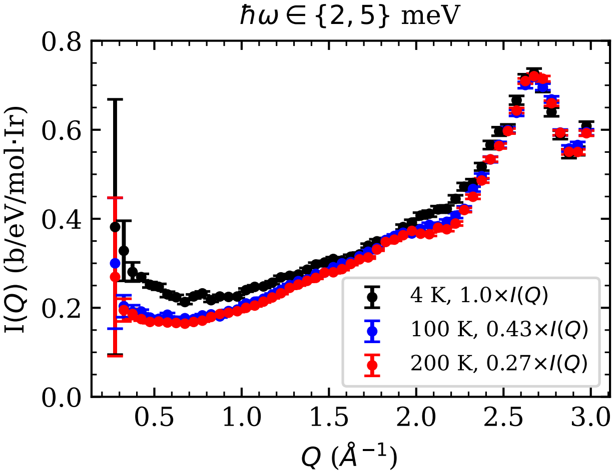

**Figure 4.18:** Scaled cuts of directly measured intensity from SEQUOIA experiment on $D_3LiIr_2O_6$. Cuts are taken from $E_i$=30 meV data.

approximation we take it to be one value for all ions and scattering processes. The elastic scattering should then go as

$$I(Q, \omega = 0) = e^{-\langle u^2 \rangle Q^2}(\sigma_{bragg}(Q) + \sigma_i). \tag{4.15}$$

The mean-square displacement $\langle u^2 \rangle$ is temperature-dependent. Approximating $\langle u^2 \rangle$=0 for $T$=4 K, the difference between elastic cuts as a function of $Q$ may be used to extract the Debye-Waller factor for each elevated temperature (100 K and 200 K). The higher incident energy configuration has access to a wider range of $Q$, so cuts of these measurements averaged from $\hbar\omega = \pm 1$ meV are used for this purpose. The extracted values of $\langle u^2 \rangle$ are $\langle u^2 \rangle_{100K} = 1.1(1) \times 10^{-3}$ Å$^2$ and $\langle u^2 \rangle_{200K} = 3.3(1) \times 10^{-3}$ Å$^2$. An example of the elastic cuts before and after applying this correction is shown in Fig. 4.19.

Because of the relatively large incoherent scattering cross section of D ($\sigma_i$=4.04 b) and the very large incoherent scattering from H which remains

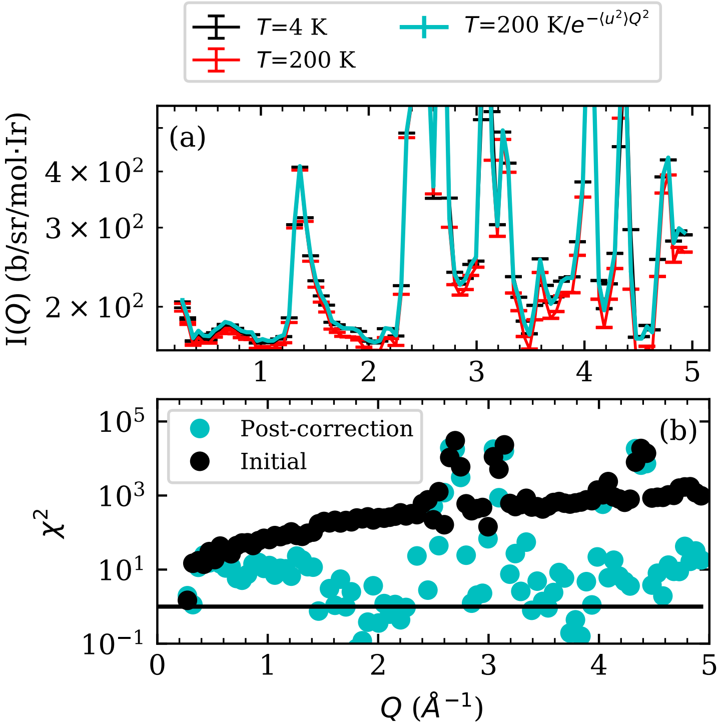

**Figure 4.19:** (a) Elastic cuts of E$_i$=60 meV Elastic scattering for the $T$=4 K and $T$=200 K SEQUOIA measurements averaged from $\hbar\omega = \pm 1$ meV. (b) Deviation between the two measurements as defined by $[\sum(I_{4K}(Q) - I_{200K}(Q))^2/(\delta I_{4K}(Q)^2 + \delta I_{200K}(Q)^2)]$. The black points represent before correcting for the Debye-Waller factor and the cyan points after. The solid black line is fixed at $\chi^2 = 1$.

present at the 1% level due to imperfect enrichment ($\sigma_i^H = 25.274$ b), we attribute the presence of a large flat background across the entire measurement (Fig. 4.17) multiple scattering events that involves a strong elastic incoherent process and weaker inelastic scattering processes namely phonons. The treatment of the process is very similar to that applied to the $Ba_4NbRu_3O_{12}$ scattering data. To model such events, we begin with the individual cross sections for incoherent elastic and incoherent inelastic phonon scattering [56]

$$\frac{d\sigma}{d\Omega}_{el\ inc} = \frac{\sigma_{inc}}{4\pi} N e^{-2W}, \tag{4.16}$$

$$\frac{d^2\sigma}{d\Omega d\omega}_{inel\ inc} = \frac{k_f}{k_i} \frac{N\sigma_{inc}}{4\pi} \frac{Z(\omega)}{\omega} \frac{e^{\beta\hbar\omega}}{e^{\beta\hbar\omega} - 1} \frac{\hbar Q^2}{2M} e^{-2W}. \tag{4.17}$$

We now recall that such a process leads to Eq. 3.5, which for reference may be written as

$$I'_{ph}(Q, \hbar\omega) = \mathcal{T} I_{ph}(Q, \hbar\omega) + (1 - \mathcal{T}) \int_{|k_i - k_f|}^{k_i + k_f} I_{ph}(Q', \hbar\omega) \frac{Q' dQ'}{2k_i k_f}. \tag{4.18}$$

In the previous case, there existed a calculated phonon spectra available for the numerical evaluation of this integral. Here, we do not take this approach, instead solving the integral analytically following Ref. [90]. The result is the easily linearized form of

$$I'(Q, \hbar\omega) = f(\hbar\omega)(k_i^2 + k_f^2) \left( \frac{TQ^2}{(k_i^2 + k_f^2)} + (1 - T) \right). \tag{4.19}$$

An observation to be made about this form is its strong dependence on $k_i$ and $k_f$. For the $E_i$=30 meV measurement with energy transfer $\hbar\omega = 3$ meV, ($k_i^2$+ $k_f^2$)=27.5 Å$^{-2}$, whereas for the MACS measurement with $E_f$ =5.0 meV

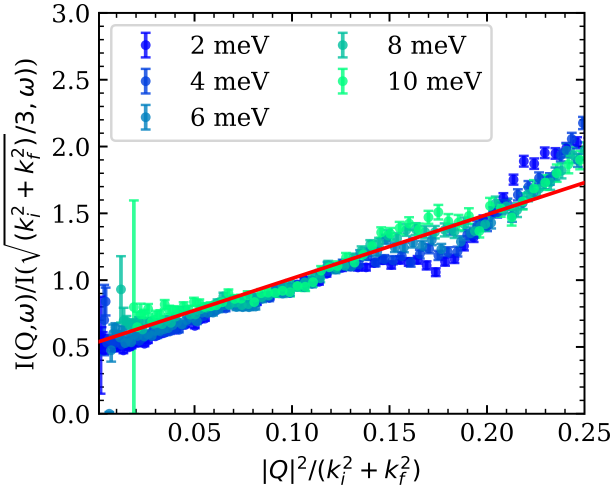

**Figure 4.20:** Collapse of $E_i$=30 meV T=200 K measurement to form of Eq. 4.19. The slope of the collapse provides the quantity of multiple scattering in the system. Cuts average over ± 0.5 meV of the value indicated in the legend.

and energy transfer $\hbar\omega = 3$ meV, $(k_i^2 + k_f^2)$=6.3 $\text{Å}^{-2}$, meaning that this effect would be suppressed by nearly an order of magnitude due to simple kinematics. We assume the single-event scattering fraction $\mathcal{T}$ to be constant across measurements. The value of this parameter is found using the linearized form of Eq. 4.19, which is visually represented in Fig. 4.20. The assumption that the functional form for phonons is simply $I_p(Q, \hbar\omega) = f(\hbar\omega)Q^2$ breaks down significantly at high Q and energy due to the presence of acoustic phonons which is most clearly visible in Fig. 4.17(d), but within the $Q$ and energy range of our interest for magnetic scattering it works quite well and from which we extract an overall single-event scattering fraction of $T = 0.90(1)$.

We now require a form of $f(\hbar\omega)$ from which to compute $I'(Q, \hbar\omega)$. Based on the magnetic form factor of $\text{Ir}^{4+}$ we assume that the extreme values of $Q$

available in each measurement represent the purely non-magnetic contributions to the scattering. These regions in $Q$ are from $Q$=2.5 $\mathrm{\mathring{A}}^{-1}$ to $Q$=3.0 $\mathrm{\mathring{A}}^{-1}$ for the $\mathrm{E}_i$=30 meV measurements and $Q$=3.5 $\mathrm{\mathring{A}}^{-1}$ to 4.0 $\mathrm{\mathring{A}}^{-1}$ for the $\mathrm{E}_i$=60 meV measurements. Within these widows, both a simple cut along the energy transfer dimension or a factorization approach described later works equally well. For completeness, we use the factorization. This particular model of phonon and multiple scattering assumes a form of $\mathrm{I}_p(Q,\hbar\omega)$=$f(\omega)Q^2$ for single-event scattering. It is then sensible that an attempt to subtract $I'(Q,\hbar\omega)$ will fail in $Q-\hbar\omega$ regimes where this assumption does not hold, many of which can be seen in Fig. 4.17. However, we may safely assume that these deviations from the assumed form of $I'(Q,\hbar\omega)$ are dominated by single-event phonon scattering. So, the total scattering intensity may now be written as

$$I_T(Q,\hbar\omega) = I_T^{mag}(Q,\hbar\omega) + I'_T(Q,\hbar\omega) + \delta I_T^{ph}(Q,\hbar\omega). \tag{4.20}$$

The subscript $T$ denotes the temperature, $I^{mag}$ is the magnetic contribution, and $\delta I^{ph}$ is the anharmonic phonon contribution dominated by single-phonon scattering. Equipped with $f^T(\hbar\omega)$, $I'_T(Q,\hbar\omega)$ is readily calculated for each configuration. The dominant single-event phonon contributions are now subtracted using a standard Bose-Einstein form, and assuming no magnetic scattering for high temperatures this leaves

$$\bar{I}(Q,\hbar\omega) = I^{T_L}(Q,\hbar\omega) - \frac{1-e^{-\beta_H\hbar\omega}}{1-e^{-\beta_L\hbar\omega}} I^{T_H}(Q,\hbar\omega) \tag{4.21}$$

$$\bar{I}(Q,\hbar\omega) = I_{T_L}^{mag} + I'_{T_L}(Q,\hbar\omega) - \frac{1-e^{-\beta_H\hbar\omega}}{1-e^{-\beta_L\hbar\omega}} I'_{T_H}(Q,\hbar\omega). \tag{4.22}$$

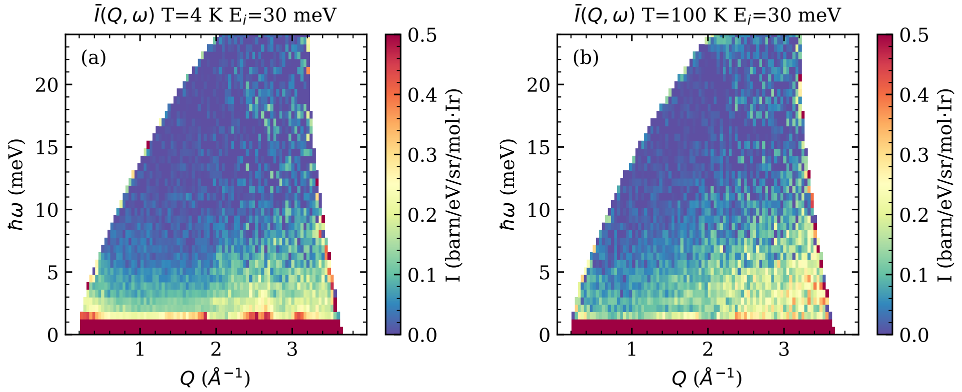

**Figure 4.21:** Remaining scattering after subtracting high temperature measurements. *T*=100 K was used as a background for the *T*=4 K measurement in (a), and the *T*=200 K measurement was used as a background for the *T*=100 K measurement in (b).

The intensity in the quantity $\bar{I}$ for each temperature still retains a non-magnetic background from multiple scattering, which may now be defined as

$$I_{bkg}(Q,\hbar\omega) = I'_{T_L}(Q,\hbar\omega) - \frac{1-e^{-\beta_H\hbar\omega}}{1-e^{-\beta_L\hbar\omega}} I'_{T_H}(Q,\hbar\omega), \tag{4.23}$$

which can be explicitly calculated as depicted in Fig 4.22. An overall normalization factor is applied such that the resulting magnetic scattering at high $Q$ and $\hbar\omega$ fluctuates around zero. Finally, the scattering presented as magnetic is given by

$$I_{mag}(Q,\hbar\omega) = \bar{I}^{T_L}(Q,\hbar\omega) - A I_{bkg}(Q,\hbar\omega). \tag{4.24}$$

The final result in Fig. 4.14 appears to be a very broad continuum of scattering that approaches a maximum intensity upon approaching $Q$=0 and $\hbar\omega$=0. The experiment is clearly energy-resolution limited. To resolve this

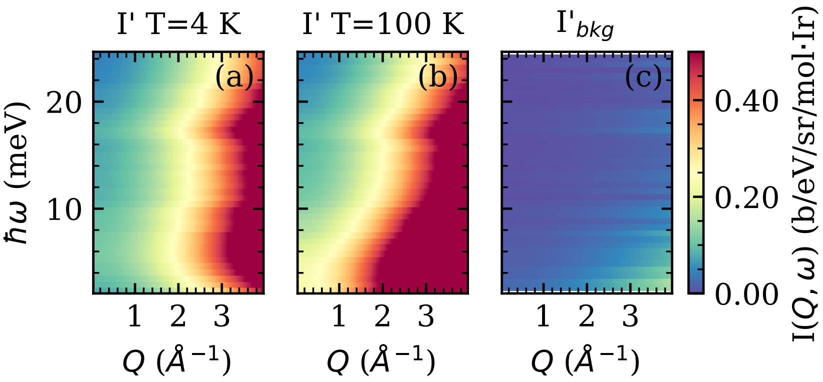

**Figure 4.22:** (a,b) Calculated multiple scattering backgrounds $I'(Q,\hbar\omega)$ for $T = 4$ K and $T = 100$ K E$_i$=30 meV measurements using form of Eq. 4.19. (c) Resulting background after Bose-Einstein subtraction of phonons as defined by Eq. 4.23.

we turn to the measurement on the MACS instrument which has access to a significantly lower energy transfer. A similarly detailed subtraction of scattering was performed in this case, which is left to Appendix 7.2. The resulting magnetic scattering obtained from MACS is shown in Fig. 4.15.

### 4.7.3 3D spin-polarized inelastic neutron measurement

A significant effort went into extracting the magnetic signal from the measurements resulting in the inferred magnetic scattering shown in in Figs. 4.14 and 4.15. The inferred non-magnetic background contributions originating from incoherent scattering are in all cases on the scale of or greater than the intensity of the extracted magnetic scattering. Though the modelling of the non-magnetic terms was rigorous, this many subtractions to the measurement could cast doubt upon the extracted magnetic spectra and hence the conclusions we make regarding the ground state of $D_3LiIr_2O_6$.

Our answer to this was to perform a polarized beam experiment on the

HYSPEC instrument using the 3D polarized configuration. The HYSPEC data is useful in that very few corrections are required to find the purely magnetic scattering. First, a correction is applied to the data to correct for imperfect polarization of neutrons. This effect results in some SF scattering in the NSF channel and vice versa. The corrected intensities are given by $I_{SF} = F(F-1)I_{SF}^{raw} - I_{NSF}^{raw}/(F-1)$ and $I_{NSF} = F(F-1)I_{NSF}^{raw} - I_{SF}^{raw}/(F-1)$, where $F$ is the flipping ratio which is determined by the fraction of Bragg peak scattering in the raw SF measurements as compared to the NSF measurements. For polarized magnetic powder scattering, the magnetic cross section is given by $\sigma_{mag} = 2(\sigma_x^{SF} + \sigma_y^{SF} - 2\sigma_z^{SF})$. While this is a direct way of finding the magnetic intensity, the statistics of our measurement are too poor to present on their own as the polarized beam configuration reduces flux by about a factor of 10, and six different polarization configurations must be measured. Instead, the scattering is used as a verification that the truly magnetic signal does not contain the background that roughly goes as $I(Q) \propto A + BQ^2$.

Outside the standard normalization and absorption corrections, there are two notable treatments of the measured intensity. The first is the necessary correction for the flipping ratio, which is tuned such that the elastic Bragg peaks vanish in the spin-flip cross section. This value is then taken to be 15 for all polarization configurations. The second is more interesting, which is the detector normalization. The HYSPEC instrument's polarization analysis is performed using a state-of-the-art two of a kind supermirror polarization analyzer (As a side note, the sister mirror is at the POLANO beam at JPARC). The design of the mirror uses many slits that absorb or reflect the incoming

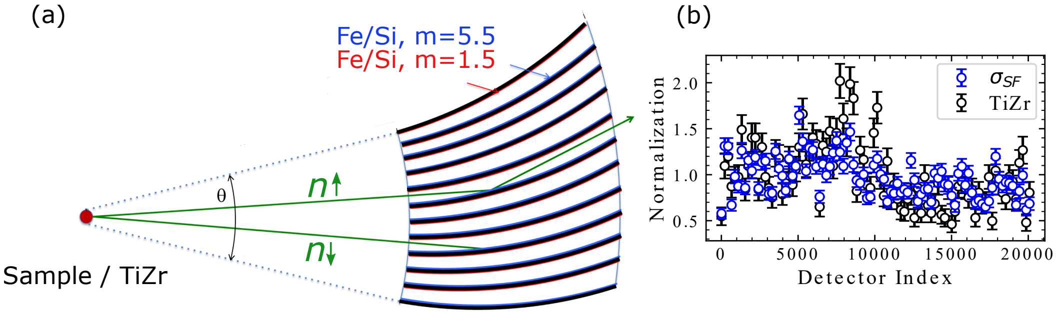

**Figure 4.23:** (a) Design of HYSPEC supermirror polarizer array reproduced from Ref. [138]. Only spin-up neutrons are reflected. (b) Extracted detector normalization from spin-flip scattering compared to standard Ti Zr alloy.

beam based on the neutron polarization, as depicted in Fig. 4.23.

This setup comes with a systematic error which is that the detector visibility to the sample strongly depends on the sample shape. Thus, unless the sample geometry is exactly the same as the sample used to normalize the detector efficiencies, systematic errors will be introduced. To remedy this in the case of $D_3LiIr_2O_6$, we assume that all detector counts in the flipping ratio corrected spin-flip elastic channel originate from sample incoherent scattering. This follows from the absence of Bragg diffraction in the spin-flip channel and the dominant spin-incoherent scattering originating from the $H/D$ ions. Because incoherent scattering is $Q$-independent, we may normalize the detectors to the sample itself, thus avoiding any issues related to differences between our sample geometry and the shape of the TiZr sample normally used to normalize the detectors. The difference between the TiZr normalization and the extracted one from our sample is shown in Fig. 4.23(b).

Resulting scattering data for all six configurations are shown in Fig. 4.24.

Each configuration is nearly identical, but significantly the buildup of excitations observed at low $Q$ and $\hbar\omega$ in the previous experiments is also observed in the spin-flip channels as shown by the cut along $Q$ in Fig. 4.24(i). It is extremely difficult to explain spin-flip inelastic scattering that decreases with $Q$, as is observed here, without invoking magnetism.

Finally, the magnetic contribution to the scattering and its respective factorization is shown in Fig. 4.16. While the statistical accuracy is limited the data are consisted with those obtained in the unpolarized experiments.

### 4.7.4 Time domain terahertz spectroscopy

In addition to the detailed neutron studies, THz spectroscopy is used to capture the response of $D_3LiIr_2O_6$ at the $\Gamma$-point, which naturally complements the observed scattering. The scattering at the $\Gamma$ point is extremely important, as it points to the anisotropic nature of the magnetism. For isotropic Heisenberg spin interactions in disordered spin systems, the powder averaged first-moment sum rule defined by 2.12 reveals that the magnetic scattering should go as $I(Q) \propto 1 - \sin(Qd)/(Qd)$, which would be zero at the $\Gamma$-point. The inelastic quasiparticle continuum predicted for the ferromagnetic Kitaev spin-liquid instead would have a maximum of scattering at the $\Gamma$ point [32], so any signal in THz spectroscopy would be relevant to our results.

Details of TDTS may be found in Sec. 4.3.4. The experiment was done using a dry pressed powder pellet of $D_3LiIr_2O_6$ of diameter 3 mm and thickness 1.0(1) mm. Fig. 4.25(q) shows transmission for temperatures ranging from 3 to 300 K. There are two temperature scales associated with the transmission.

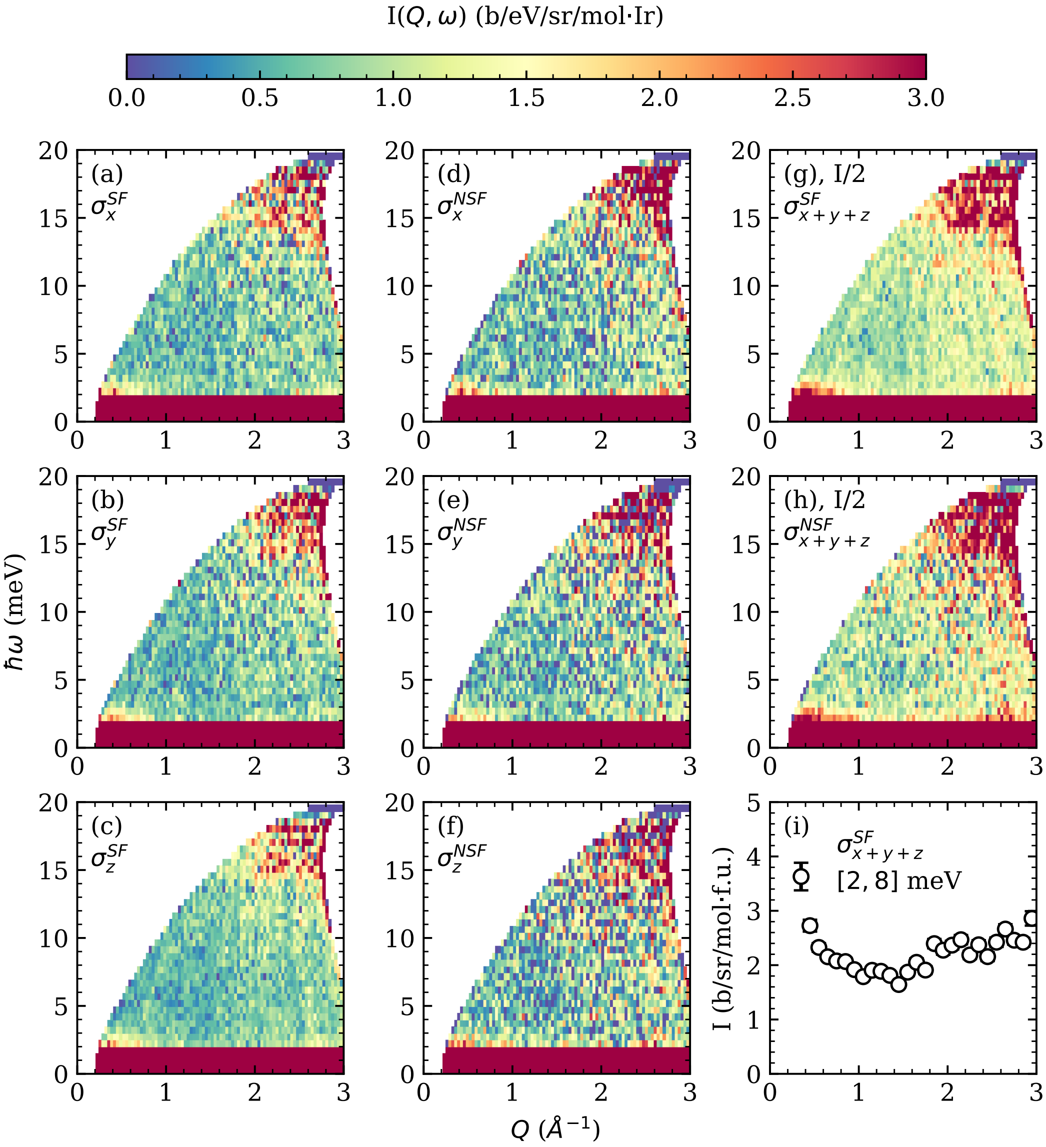

**Figure 4.24:** Full scattering data from 3D polarized experiment on HYSPEC for $D_3LiIr_2O_6$. Polarization configurations are as labeled, with the total spin-flip cross section being shown in (g) and the total non-spin flip in (h). (i) Shows a cut across $Q$ averaged from $\hbar\omega \in \{2, 8\}$ meV, showing a clear buildup of scattering at low $Q$.

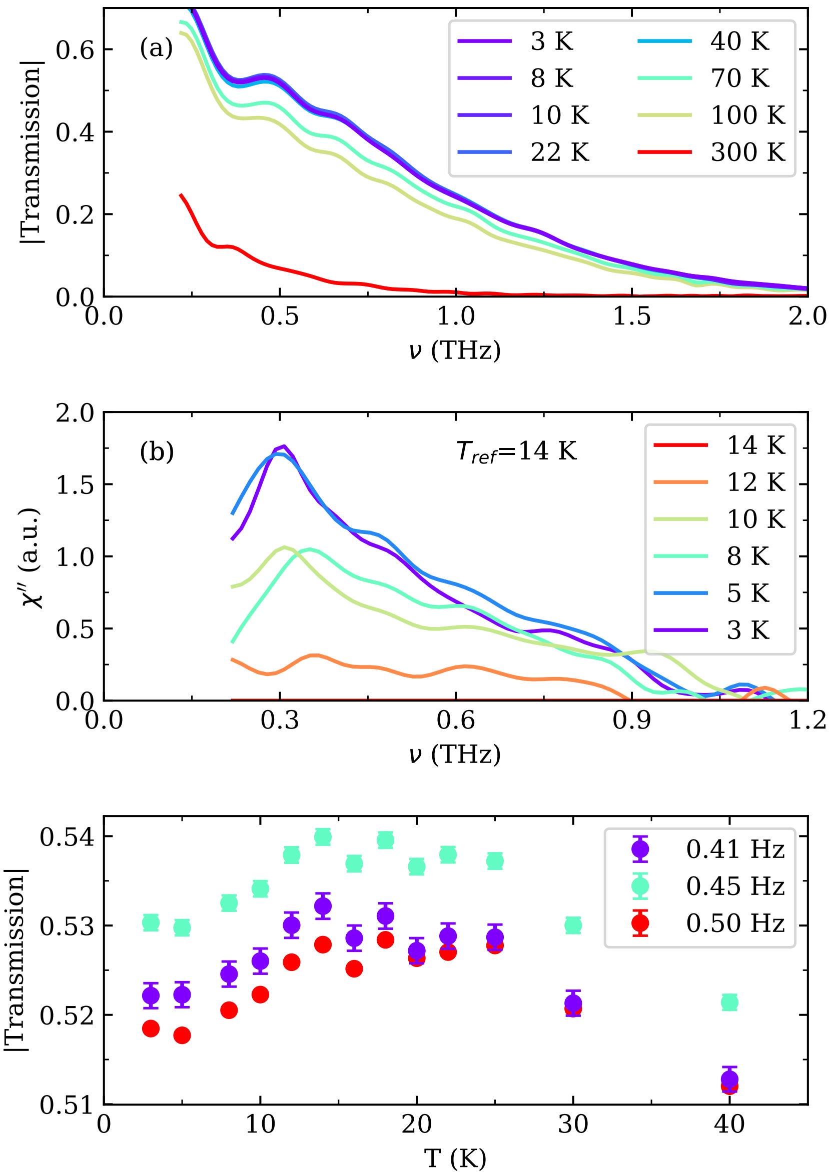

**Figure 4.25:** Time domain THz spectroscopy data from a pressed pellet of $D_3LiIr_2O_6$. (a) Directly measured quantity of the modulus of transmission. (b) Calculated $\chi''$ susceptibility using $T$=14 K as a reference temperature. (c) Temperature dependence of the signal at low energies showing the onset of magnetic signal for $T < 15$ K, and dielectric scattering for $T > 25$ K.

From room temperature to 25 K, the increase in transmission is associated with the reduction of scattering from an electronic degree of freedom, namely the thermally activated hopping of the $H^+$ ion. This effect plateaus below 25 K, and the transmission then decreases below 14 K, which is interpreted as the onset of absorption by magnetic degrees of freedom and is made more clear by Fig. 4.25(c).

This crossover behavior indicates competition between electronic and magnetic excitations, which in general makes optical studies of this material difficult. If one assumes that the dielectric behavior is constant below 15 K, the 14 K temperature may be used as a reference spectrum for which the relative susceptibility $\chi''$ may be calculated as shown in Fig. 4.10(b). Here, a continuum of excitations consistent with the INS studies appears upon decreasing temperature. The oscillations in the data are a consequence of the experimental configuration and should not be taken to be true peaks in $\chi''$.

### 4.7.5 Analysis - $D_3LiIr_2O_6$

Corrections to the scattering aside, the analysis of these data is relatively straightforward. As the sample is a powder and no sharp features in the spectra were discovered, we may return to the factorization method where.

For a powder, the total observed magnetic moment may be found by integrating over $\mathcal{S}(Q)$, i.e. $\mu_{obs}^2 = 3g^2 \int S(Q)Q^2dQ/(\int Q^2dQ)$. For the SEQ and MACS measurements this provides an overall observed moment of $\mu_{eff} = 2.0(6)\ \mu_B$ and $\mu_{eff} = 1.7(4)\ \mu_B$ respectively, where the error is dominated the vanadium normalization. These values are mostly consistent with the moment from high temperature magnetization of $\mu_M = 1.36\mu_B$, as well as the expected moment for $J = 1/2$ of $\mu = g\sqrt{3} = 1.7\ \mu_B$ assuming $g = 2$. The energy dependent $G(\omega)$ suggests a gapless excitation spectra within the $\Delta E$=1.8 meV instrumental resolution that rapidly falls to zero with increasing energy transfer. The MACS data adds more detail to the low energy part of the excitation spectra, but statistics mean that it is difficult to determine if a peak exists in the spectra or not. Finally, the HYSPEC data confirms that the origin of the scattering is in fact magnetic, and that our subtractions to the unpolarized measurements are consistent with the polarized magnetic scattering. A total moment sum rule may also be used on the magnetic scattering inferred from the polarized experiment resulting in $\mu_{eff} = 1.7(7)\ \mu_B$. The compatibility of these measurements are shown directly in Fig 4.26, where the factorizations of each measurement are consistent. The consistency between the distinct experiments gives confidence in the overall results.

### 4.7.6 Modeling of scattering

The exactly solvable ground state of the KSL has allowed a wealth of theoretical studies of its excitations. The dynamical structure factor $S(Q, \hbar\omega)$ has been calculated in a number of studies [32]. This quantity is of particular interest as INS provides a direct measure of $S(Q, \hbar\omega)$, giving a direct route to compare theory and experiment. The response is expected to be nearly featureless as a lack of long range magnetic ordering in real space corresponds smeared features in $Q$-space. In the KSL we expect only on-site and nearest neighbor correlations. With this expectation, the dynamic structure factor

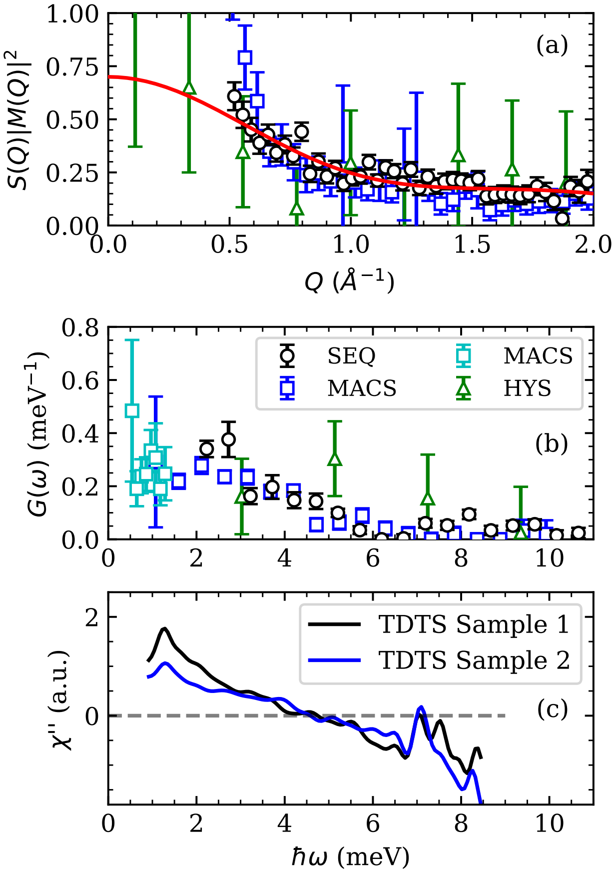

**Figure 4.26:** Factorizations of each INS measurement of $D_3LiIr_2O_6$. (a) $\mathcal{S}(Q)$ extracted from scattering data for each experiment. The red line indicates how these cuts compare to the best fit to a simple model of the KSL as described in the text. Each individual factorization has been scaled to the model. (b) Comparison of the energy dependent factorizations G($\omega$) of the neutron experiments. (c) Time domain THz Spectroscopy showing consistency with neutron result at the Γ point. Black and blue lines represent T=3 K measurements from different samples, showing qualitatively consistent magnetic spectra.

for a crystal is written as $S^{\alpha\alpha}(\mathbf{Q}, \hbar\omega) = 2G(\hbar\omega)(1 - \mathrm{sgn}(K)\cos(\mathbf{Q}\cdot\mathbf{d}_a))$. The Kitaev interaction $K$ is assigned as ferromagnetic based on $\theta_{CW}$ and $\mathbf{d}_a$ refers to the distance vector of a bond in real space. The powder average of this function while considering only on-site and nearest-neighbor correlations is fit to the SEQ data and is shown in Fig. 4.26(a) by the red line.

The combination of spectra presented in Fig. 4.26(b) implies a broad continuum of scattering at excitation energies below 6 meV. We can also state that finite magnetic intensity persists down to the lowest accessible energy transfer of $\hbar\omega = 0.5$ meV.

## 4.8 Discussion - $D_3LiIr_2O_6$

The low energy excitations in $D_3Li_2IrO_6$ have been successfully mapped by inelastic neutron scattering for the first time. Three different measurements were required to do so, but there is compelling evidence that the presented scattering is truly magnetic and originates from the exotic magnetic ground state of the material. After all of the background subtractions which have been discussed at length, the powder averaged spectra may finally be discussed independently in terms of its $Q$ and $\hbar\omega$ dependence. The $Q$-dependent part of the spectra $\mathcal{S}(Q)$ is successfully described using a simple nearest-neighbor interacting model, which is consistent with a nearest-neighbor ferromagnetic interaction. The full expected moment is captured by these measurements, affirming the validity of the background subtraction procedures. The fully magnetic cross section from the polarized measurement also affirms these procedures, and captures the full expected moment for the $J_{eff}$=1/2 $Ir^{4+}$.

A peak is expected in the low energy spectra of the Kitaev spin-liquid, as the ground state is a nonmagnetic singlet that neutrons are not sensitive to. This gives the illusion of a finite energy gap in the dynamical correlation function despite the state being gapless [32]. If a true peak exists at $\hbar\omega \approx$2 meV, this would imply an energy scale for the Kitaev interaction of $K = -10$ meV. However, this is significantly lower than the values expected from both our previous study of $\beta$-$Li_2IrO_3$ and other studies on $\alpha$-$Li_2IrO_3$ and $Na_2IrO_3$ which suggest a higher energy scale around $|K| \approx$25 meV [139]. However, it closely matches what is expected from the high temperature susceptibility of $\theta_{CW}$=-105 K which suggests $K$=-12 meV. This may be due to the fact that $H_3Li_2IrO_6$ is not in an ideal KSL ground state. The coexistence of the random singlet phase and the KSL slightly modifies the quasiparticle spectra as have already been discussed, and the quality of these powder measurements make it difficult to conclude more regarding the excitations.

## 4.9 Conclusions

Two detailed inelastic neutrons scattering studies have been performed in honeycomb magnets which have been proposed to realize Kitaev-type interactions. The first is $\beta$-$Li_2IrO_3$, which has long been known to have an interesting counterrotating magnetic order that was taken as evidence of anisotropic Kitaev interactions. Using a combination of inelastic neutron scattering, heat capacity, and THz spectroscopy, precise exchange parameters were experimentally refined for a lithium iridate for the first time. These types of studies are extremely scarce due in large part to the difficulties associated with neutrons and iridium, and this result is a valuable contribution to the field. A publication of this work may be found in Ref. [51].

The second study was a detailed analysis of $D_3LiIr_2O_6$ scattering data. Three separate powder inelastic neutron studies are discussed, as well as the detailed procedures for background subtractions in each. The isolation of magnetic scattering is highly nontrivial in this case, yet the 3D polarized scattering from the HYSPEC instrument supports that this analysis was correct. The scattering captures the total expected moment and features a low energy spectra with $Q$-dependence that may be described by only nearest-neighbor correlations with a maxima at $Q$=0. This is entirely consistent with a Kitaev spin-liquid ground state, but limited conclusions should be drawn from this due to the quality of the data.

Work remains to be done on both materials. The studies discussed in this dissertation have established that strong Kitaev-type interactions exist in both and that the ground state of $D_3LiIr_2O_6$ may be proximate to a KSL. The simplest path forward for this material would be to run another measurement on a cold neutron spectrometer like CNCS at Oak Ridge National Laboratory or the LET spectrometer at ISIS. These instruments would not suffer from the phonon monochromator scattering that MACS does, have sufficient energy resolution to map the low-energy excitation spectrum, and their low incident energies mean that while absorption effects would be significant, multiple scattering would be significantly reduced as it scales with $(k_i^2 + k_f^2)$.

Outside of this, single crystalline samples are required for further study.

These do exist but are of exceedingly small size, on the order of length 1 mm. A single-neutron study of crystals of this scale is feasible, and something I am considering pursuing in my future studies. For $\beta-Li_2IrO_3$, the application of field along different unit cell directions has already been shown to have extremely anisotropic response in magnetization [98]. This could also be studied in the excitation spectra of coaligned single crystals and is a natural extension of the powder work. The case of $D_3LiIr_2O_6$ is a bit different, in that it is still unclear what the ground state is. Single crystal inelastic neutron diffraction would be an invaluable addition to this effort, and would provide much clearer information than the powder data. Provided enough crystals, I believe that these studies are entirely possible and worth the effort to pursue.

# Chapter 5

# Proximate spin-liquid behavior in highly frustrated $XXZ$-$J_1J_3$ honeycomb magnet $BaCo_2(AsO_4)_2$

## 5.1 Introduction

### 5.1.1 Proposal for Kitaev interactions in $Co^{2+}$ honeycomb oxide materials

Since the proposal of the realization of Kitaev interactions in real materials by Jackeli and Khaliullin in 2007 [37], a significant amount of effort has been put forth towards the realization of a Kitaev spin-liquid. The original mechanism for this requires 4*d* or 5*d* transition metal ions ($Ru^{3+}$ $Ir^{4+}$) with strong spin-orbit coupling in an octahedral crystal field, meaning that the only materials that may realize Kitaev interactions by this mechanism are the honeycomb iridates and $\alpha$-$RuCl_3$. While the lithium iridates have been described in detail in the previous chapter, $\alpha$-$RuCl_3$ is also worth a brief discussion for context.

For the purpose of engineering a Kitaev material the honeycomb iridates have the fundamental issues of limited single-crystal availability and the neutron absorption associated with iridium. $\alpha$-RuCl$_3$, on the other hand, suffers from neither of these issues with large high quality single crystalline samples readily available and an absorption cross section of $\sigma_{abs} = 2.56\ \mu_B$. It should be noted here that although single crystals are straightforward to grow, different sample show different magnetic ordering temperatures suggesting that stacking faults play an important role in the ground state order [140]. Although $\alpha$-RuCl$_3$ orders into a characteristic zigzag antiferromagnetic structure at T$_N$=7 K [45], initial inelastic neutron studies suggested that the material may be proximate to a Kitaev spin-liquid and arguments were made for the presence of a dominant AFM Kitaev interaction with Heisenberg and off-diagonal interactions pushing the system into ordering rather than a quantum spin-liquid phase [45, 141].

More interesting still was the discovery of a mysterious field-induced phase for in-plane fields higher than H$_c$=7 T. No magnetic order is observed by neutron scattering in this phase, and the well-defined spin-waves in the zero field phase melt away into a continuum that is consistent with what one would expect from a Kitaev spin-liquid [142, 143]. Furthermore, thermal transport studies reported a half-integer quantized thermal Hall effect as one would expect of emergent Majorana fermion excitations [144, 145]. This result is controversial and has proven difficult to reproduce, with compelling evidence being that the measured quantity was simply residual phonon scattering [36]. Because of this, there is a small highly fluctuating regime just above the critical field in which the magnetism of $\alpha$-RuCl$_3$ is poorly understood despite great theoretical and experimental efforts [146]. The exchange interactions are very difficult to refine from neutron scattering data, as it is impossible to fully magnetize the system at any reasonable field scale at which one could use linear spin-wave theory rigorously.

This presents an interesting scenario, where even the most "successful" Kitaev material has a poorly understood spin-Hamiltonian and conflicting results even after nearly 15 years of study. The need for a new method of realizing Kitaev interactions is sorely needed provided that it meets the qualifying criteria of minimizing non-Kitaev exchange, having accessible field-scales such that one may polarize the system for study, and availability in single-crystal form.

In 2018, a proposal was put forward for the realization of Kitaev interactions in honeycomb $\mathrm{Co}^{2+}$ materials which fits all of the above criteria. Though the mechanism is quite complex, it will be briefly summarized. This proposal is based upon $d^7$ ions in a $t_{2g}^5 e_g^2$ configuration ($S$=3/2 $L$=1) in octahedral crystal fields. The crystal field environment combined with some quantity of spin-orbit coupling results in a pseudospin $J$=1/2 on each honeycomb site, which has been known for many years in the honeycomb cobaltates. If one goes further and examines the effect of hopping paths between the resulting electrons that remain in $e_g$ orbitals, a full exchange Hamiltonian may be derived [48, 147]. This is significantly different from the case of first generation Kitaev materials where only one hole exists in the ground state manifold, as the hopping terms allowed by the additional electrons are shown to have a destructive interference for non-Kitaev interactions.

While this mechanism for the realization of a Kitaev contribution to the spin exchange is beyond the scope of what I would like to discuss here, the end result is that for a particular value of Hubbard $U$ there should be competing ferromagnetic and antiferromagnetic contributions to the Heisenberg part of the exchange interaction, leading to a dominant Kitaev interaction. This is an appealing prospect experimentally that was immediately embraced, with claims of the discovery of Kitaev interactions in materials like $Na_2Co_2TeO_6$ [148, 149]. Honeycomb cobaltates are available in single crystalline form by traditional methods like flux or Bridgman growth, and with the typically large moment of $Co^{2+}$ these materials are very amenable to neutron scattering experiments. The excitement in the field was understandable, as the introduction seemingly overnight a whole new family of Kitaev materials would be a huge step forward from only having the honeycomb iridates and $\alpha$-$RuCl_3$ to study. However, we should pause and ask a question. In real honeycomb cobaltates is the Kitaev model actually the appropriate description of the spin exchange? Or could these materials be described by more conventional means? This line of inquiry bring us to the most significant work in this dissertation, which is the investigation of $BaCo_2(AsO_4)_2$.

### 5.1.2 Magnetic properties and previous studies of $BaCo_2(AsO_4)_2$

$BaCo_2(AsO_4)_2$ crystallizes in the trigonal $R-3$ space group, with lattice parameters $a$=$b$=5.0$\mathring{A}^{-1}$. Honeycomb layers of edge-sharing $CoO_6$ octahedra are stacked in an ABC pattern along the c-axis such that no direct exchange path exists between layers and the system may be thought of as highly two-dimensional. Additionally, the interlayer bonding is ionic between Ba and

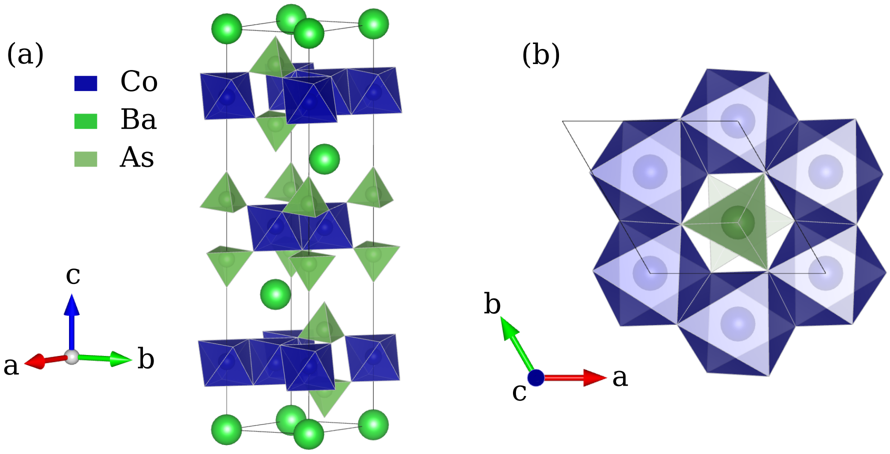

**Figure 5.1:** (a) Nuclear structure of $BaCo_2(AsO_4)_2$ showing idealized ABC stacking pattern. O ions have been removed for clarity. (b) Honeycomb lattice of a single layer of $CoO_6$ octahedra.

$AsO_4$ octahedra, meaning that the material is not van der Waals like $H_3LiIr_2O_6$ or $\alpha-RuCl_3$ and does not have any measurable stacking faults [150]. Magnetic order in $BaCo_2(AsO_4)_2$ has been long known, with the first reports appearing in the literature in 1977 [151]. Here, magnetic susceptibility studies revealed a highly anisotropic response which is indicative of the two-dimensional nature of the system. A phase transition is detected at $T$=5.4 K, and following neutron diffraction studies reveal a dominant in-plane contribution to the moment of $\mu_{ab} = 2.95\ \mu_B$ and $\mu_c = 0.48\ \mu_B$. Upon cooling, incommensurate order is observed with propagation vector $\mathbf{k} = (0.261, 0, -\frac{4}{3})$. This corresponds to an incommensurate spiral structure with no correlations between layers. Upon application of a field at low temperatures in the $ab$-plane, an intermediate commensurate phase of wavevector $\mathbf{k} = (1/3, 0, 0)$ is observed at critical field $\mu_0 H_{c2} = 0.33$ T, and a second critical field of $\mu_0 H_{c2} = 0.55$ T pushes the system into a nearly field-polarized phase [151–154]. Heat capacity and magnetization studies also affirm this, and have been used to map the full $H - T$ phase diagram of $BaCo_2(AsO_4)_2$.

Until recently, $BaCo_2(AsO_4)_2$ (BCAO) remained a peculiar frustrated antiferromagnet outside a sophisticated 3D neutron polarimetry study suggesting that the order was actually that of an ↑↑↓↓ type structure rather than an incommensurate spiral [153]. The proposal of Kitaev interactions in the honeycomb cobaltates inspired a review of long forgotten systems in this context, including $BaCo_2(AsO_4)_2$. The critical field and temperature are all small for a transition metal oxide, indicating the tenuous nature of the magnetic order. Yet, the field driven state is nearly fully magnetized suggesting dominant ferromagnetic interactions. This argument was used to suggested that $BaCo_2(AsO_4)_2$, like $\alpha$-$RuCl_3$ before it, may enter into a field induced Kitaev quantum spin-liquid phase [154], but with large defect-free single crystalline samples available. For a time, BCAO was hailed as a more ideal next generation Kitaev spin-liquid candidate.

## 5.2 Determination of magnetic exchange hamiltonian

Though there was a suggestion of the realization of Kitaev interactions in BCAO, an ab-initio study suggested a different description [155]. Here it was reported that trigonal distortions in the $CoO_6$ octahedra played an important role in the physics of BCAO and that it forms an easy-plane XXZ magnet with nearest neighbor ferromagnetic interactions and frustrated third-nearest neighbor AFM interactions (we refer to this as the XXZ-$J_1$-$J_3$ model). Additionally, previous studies on the isostructural material $BaCo_2(PO_4)_2$ were able to completely describe the ground state using a similar model [156].

The goal of this work was to scrutinize in detail the magnetic interactions in BCAO via a combination of inelastic neutron scattering studies and a classical theoretical analysis. To this point, little experimental work had been done to distinguish the $JK\Gamma\Gamma'$model with large Kitaev interactions from the XXZ-$J_1$-$J_3$ model in BCAO or, in fact, any cobaltates. We take advantage of the fact that BCAO polarizes at relatively low values of field, meaning that unlike $\alpha$-$RuCl_3$ we can access the ferromagnetic regime where linear spin-wave theory describes the excitations very well. In the highly fluctuating zero field state linear spin-wave theory breaks down entirely, as we will demonstrate by detailed comparisons of the scattering to both models.

Here, we will make this determination using one neutron experiment at zero field with wavevector transfer $\boldsymbol{Q}$ in the $(hk0)$ scattering plane and a second experiment with $\boldsymbol{Q}$ in the $(h0l)$ plane with a magnetic field applied along the perpendicular [010] direction. The magnetic excitation spectrum is fully mapped and enables a critical examination of the two competing models. The results tightly constrain where BCAO may lie in parameter space in each model using a linear spin-wave theory model in the field-polarized regime, and an analysis of the allowed classical order from these constraints are used to make conclusions about which model is more appropriate.

Before going into details of the work, in summary it highlights the need for a more thorough examination of exchange interactions in the honeycomb

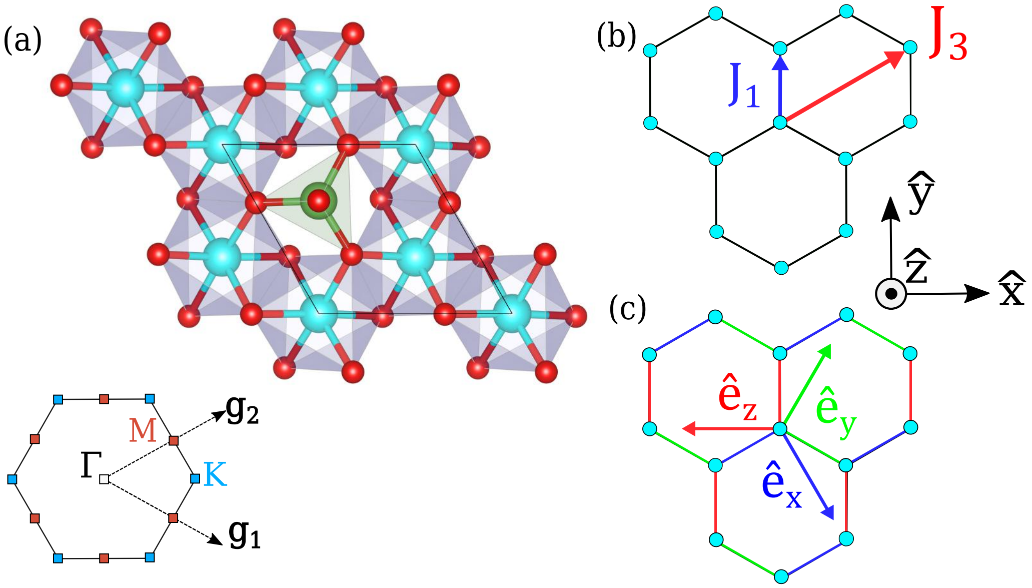

**Figure 5.2:** (a) Honeycomb lattice of BCAO viewed along the *c*-axis. Cobalt ions are in blue, oxygen in red, and arsenic in green. The first Brillouin zone of the hexagonal lattice is presented with the reciprocal lattice vectors $\mathbf{g}_1$ and $\mathbf{g}_2$. The high symmetry points *M* and *K* are depicted by the red and blue squares, respectively. (b) Representation of the couplings in the XXZ-$J_1$-$J_3$ model. The crystallographic frame is shown to the right in the black axes. (c) Local spin-frame for Kitaev interaction on the honeycomb lattice as seen from above. The *x*, *y*, and *z* bonds are shown in blue, green, and red coloring respectively.

cobaltates, a number of which have been proposed as KSL candidates. Even if a set of exchange parameters with a large Kitaev interaction may reproduce observed INS spectra in the field-polarized state using LSWT, it is important to examine if the extracted parameter set is consistent with the zero-field ordered state and other thermodynamic measurements.

### 5.2.1 Experimental methods

Two sets of crystals were grown for these experiments. The MACS experiment used 0.88(1) g of sample while the SEQUOIA and HYSPEC samples totaled 0.96(1) g. All these crystals grown by a flux method and have a dark purple coloring [154]. No stacking faults or secondary phases were detected through single-crystal x-ray diffraction. The $T = 293(2)$ K lattice constants observed are $a = b = 5.007(1)$ Å, and $c = 23.491(5)$ Å [150], and the system crystallizes in space group $R\bar{3}$ (No. 148).

Three neutron scattering experiments were performed. The first was performed on the MACS instrument at NIST in an "orange" $^4$He flow cryostat with a 1.5 K base temperature. For this experiment, many plate-like crystals of BCAO were coaligned in the $(hk0)$ scattering plane. The final neutron energy was fixed at $E_f$=5 meV, and the monochromator was in the double-focusing high flux mode. Measurements were performed at $T = 1.7(1)$ K and $T = 15.0(1)$ K, with 16 hours and 18 hours of counting time respectively. Measurements were taken at energy transfers of 0 meV, 2 meV, 4 meV, and 8 meV for both temperatures. No magnetic field was applied in this experiment.

The second experiment was conducted at the SEQUOIA instrument at

ORNL on a second set of crystals with a total mass of 0.96(1) g. These crystals were coaligned in the $(h0l)$ scattering plane and the experiment was performed in a vertical field magnet such that the field was applied along the **b**-axis, which is parallel to the $(\bar{1}20)$ direction. Measurements were taken using the $E_i = 21$ meV high flux configuration with Fermi chopper frequency of 120 Hz. Measurements were conducted with the samples at $T = 2$ K, 15 K, and 50 K and total proton charge of 74 C, 80 C, and 40 C, respectively.

The third experiment was run on the HYSPEC instrument at ORNL using the same set of crystals as on SEQUOIA aligned in the $(h0l)$ plane. We used an Oxford instruments 14 T vertical field magnet with HYSPEC in the unpolarized high flux 300 Hz configuration with incident energies $E_i = 6$ meV and $E_i = 27$ meV. The main configuration was the low energy $E_i = 6$ meV mode at fields of 0 T, 0.4 T, 0.55 T, 0.75 T, 1 T, 2 T, 3 T, 4 T, and 5 T. The net proton charge on target for each field was 140 C, 72 C, 30 C, 101 C, 30 C, 30 C, 75 C, 30 C, and 30 C respectively, with a Fermi chopper frequency of 360 Hz. The higher energy $E_i = 27$ meV configuration was used for $\mu_0 H = 3$ T with a total proton charge of 44 C and a 420 Hz Fermi chopper frequency. Analysis of the scattering from ORNL experiments was performed using the MANTID software package [107].

Low $T$ Magnetization measurements were performed on a high-quality single crystal of BCAO as a function of the applied magnetic field strength and orientation within the honeycomb planes. The sample was a 0.88(2) mg plate that was aligned using a Laue diffractometer to an accuracy better than 1 degree. The sample was mounted on a quartz rod and oriented such that the applied field was along the $\hat{\mathbf{y}}$ direction as indicated in Fig. 5.2(b). The sample was then cooled from 300 K to 2 K in zero field. A full hysteresis loop was measured at $T = 2$ K in the applied field range $\mu_0 H \in [-1, 1]$ T. The sample was then warmed to 20 K, cooled back to $T = 2$ K in zero field, and the hysteresis loop was remeasured to establish reproducibility. The sample was then carefully rotated in 15° steps until the field was along the $\hat{x}$ direction, repeating the zero field cooled magnetization scans for each orientation. These measurements were run in a Quantum Design MPMS3 SQUID magnetometer.

### 5.2.2 Static and dynamic spin correlations

Two inelastic neutron scattering experiments were performed on plates of single crystalline BCAO. Constant energy slices in the $(h0\ell)$ scattering plane captured in the MACS experiment are shown in Fig. 5.3. Slices at T=1.7(1) K are shown in Fig. 5.3(a-d), and slices at T=15.0(1) K are in Fig 5.3(e-h). Fig. 5.3(a) shows elastic scattering at 1.7 K where the 15 K data in Fig. 5.3(e) were subtracted as a background. Magnetic satellite peaks surrounding the $(0\bar{1}0)$ and $(1\bar{1}0)$ nuclear Bragg peak evidence the incommensurate magnetic order that forms below $T_N$. Magnetic satellite peaks are even apparent near the origin. The different intensities of the six satellite peaks surrounding a given nuclear Bragg peak reflect the structure factor of the magnetic order. The full width at half maximum (FWHM) vertical $Q-$resolution of MACS at $\mathbf{Q} = (100)$ is $\Delta Q = 0.09$ Å$^{-1}$ $= 0.2$c$^*$. Thus this $(hk0)$ plane measurement does not access the nominal $\mathbf{k} = (0.27, 0, -1.3)$ magnetic wave vector. The appearance of the magnetic Bragg peaks in Fig. 5.3(a) despite of this is a first

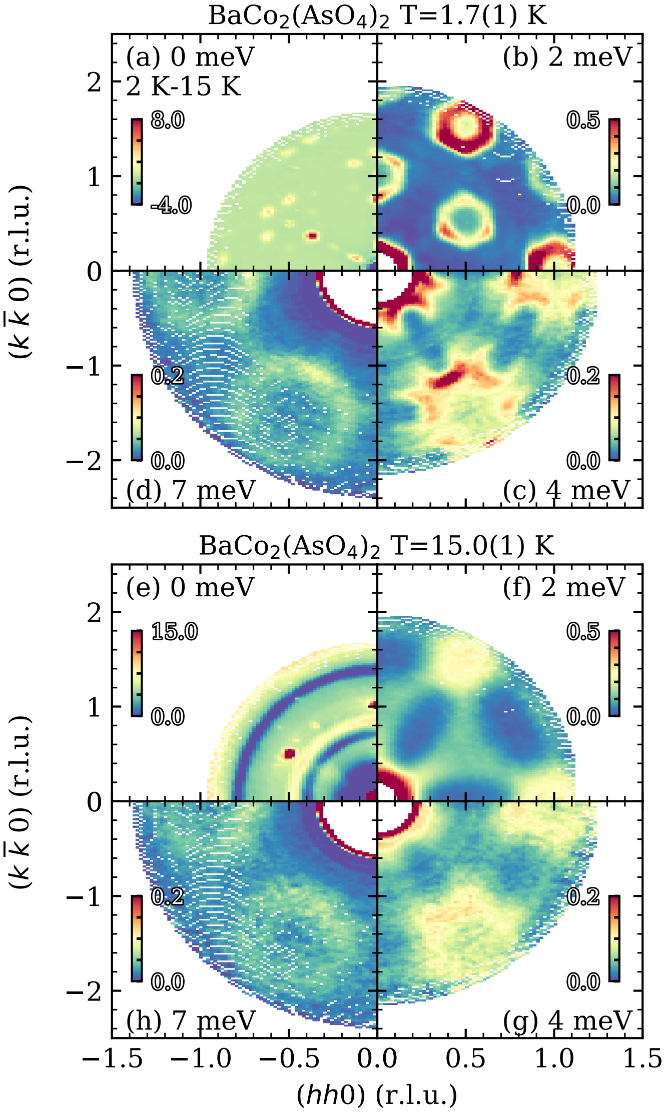

**Figure 5.3:** Zero field neutron scattering intensity for $BaCo_2(AsO_4)_2$ as a function of energy transfer and temperature in the $(hk0)$ scattering plane. Panels (a-d) show scattering at $T = 1.7(1)$ K, and (e-h) at $T = 15.0(1)$ K. Energy transfers for each quadrant varies as labeled. Sample out measurements were used as backgrounds for all measurements except (a), which shows the difference between elastic data acquired at $T = 1.7(1)$ K and $T = 15.0(1)$ K.

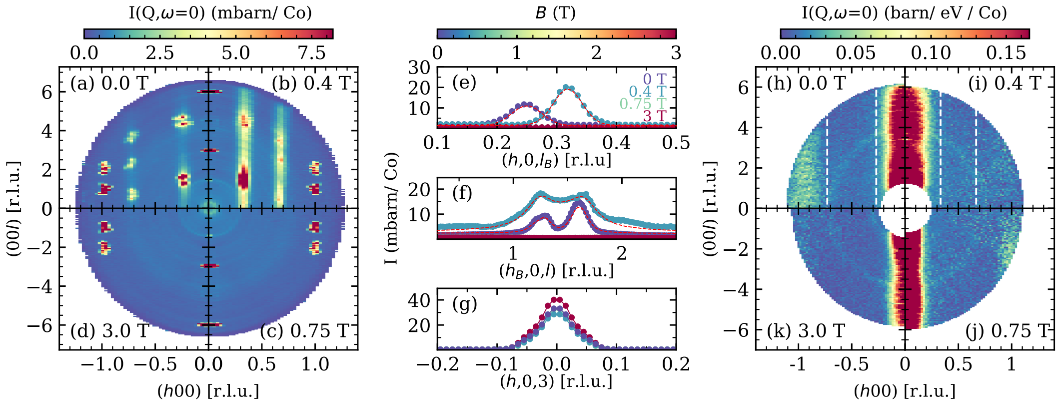

**Figure 5.4:** Elastic magnetic scattering from $\mathrm{BaCo_2(AsO_4)_2}$ at $T = 1.7$ K (a-d) as a function of field applied perpendicular to the scattering plane and along the $(\bar{1}20)$ direction. The scattering has been averaged in the energy transfer window of $\pm 0.1$ meV, and $k \in [-0.1, 0.1]$ along the $(0k0)$ direction. The short ranged nature of the correlations is evident at zero field (a) and in the commensurate ordered state at $\mu_0 H = 0.4$ T (b) through the broadness of the peaks in the $(00l)$ direction. Panels (e-f) further highlight this, comparing cuts at the respective incommensurate wavevectors $\mathbf{q}(H) \equiv \{q_h(H), 0, q_l(H)\}$. For $\mu_0 H = 0$ T, $\mathbf{q} = (0.27, 0, -1.31)$ and for $\mu_0 H = 0.4$ T $\mathbf{q} = (1/3, 0, -1.31)$. Panel (g) compares cuts along the $(h00)$ direction over the $(003)$ structural Bragg peak. The increase in intensity in the field-polarized 3 T phase may be directly accounted for by the induced in-plane moment. The full width of the averaging windows for cuts in (e) and (g) are $\Delta k = 0.1$, $\Delta l = 0.6$, and for (f) from $\Delta h = \Delta k = 0.1$. (h-k) Constant energy slices around the $\Gamma$ point gap energy at four representative fields. The energy windows for panels (h-j) begin at $\hbar\omega = 0.4$ meV and extend to $\hbar\omega = 1.58$ meV, 1.80 meV, 1.90 meV, and 2.29 meV, respectively. Dashed white lines are shown at the incommensurate ordering wavevector for each respective field, with no lines for the magnetized phases without AFM order.

indication of the quasi-2D nature of the magnetic order: The magnetic peaks have tails extending along c$^*$ so they can be detected near $l = 0$. This is distinct from resolution effects and is made clearer in the second measurement in the $(h0l)$ scattering plane (Fig. 5.4).

The spectrum of excitations extends well beyond $k_B T_N \approx 0.5$ meV, which is characteristic of a quasi-two-dimensional magnet with competing interactions where the ordering temperature is deeply suppressed relative to the exchange energy scale[157]. With increasing energy transfer, a faceted ring of intensity centered at Γ points with increasing diameter is observed (Fig. 5.3(b-d)). This indicates anisotropic dispersive excitations with the lowest energy mode at the Γ point as for a ferromagnet.

Even though BCAO is in the paramagnetic phase at $T = 15$ K, dynamic spin correlations give rise to a peak in low energy inelastic neutron scattering at the Γ point (Fig. 5.3(f)). This indicates dynamic ferromagnetic correlations and is consistent with previous THz and inelastic neutron scattering studies [153, 158, 159]. While some broadening indicating loss of spin-wave coherence is apparent, hexagonally faceted rings of inelastic magnetic scattering centered at the Γ point are clearly seen in Fig. 5.3(g,h). This indicates dynamic correlations within honeycomb planes are established well above $T_N$.

Elastic scattering in the $(h0\ell)$ plane is shown in Fig. 5.4 for three different magnetic fields applied within the honeycomb plane. Complex peak structures are observed at the nuclear Bragg peaks (101) and (102). These reflect the mosaic distribution of the multi-crystal sample that defines the transverse momentum resolution within the $(h0\ell)$ scattering plane. Fig. 5.4(b,d) show that elastic magnetic scattering beyond the nuclear allowed Bragg peaks is absent for in-plane fields of 0.75 T and beyond. In zero field (Fig. 5.4(a)), magnetic Bragg peaks are seen at the incommensurate ordering wavevector $\mathbf{k}_c = (0.27(1), 0, -1.31(1))$. The ordering wavevector becomes commensurate within the honeycomb plane $\mathbf{k}_c = (1/3, 0, -1.31)$ in a field of $\mu_0 H = 0.4$ T applied along the $(1\bar{2}0)$ direction (Fig. 5.4(c)). In both the 0 T and 0.4 T measurements, the magnetic scattering extends along the $(00\ell)$ direction, which indicates a reduced correlation length along the $c$-axis.

Fig. 5.4(f) shows cuts through these elastic scattering data along the $(00\ell)$ direction through the magnetic peaks for both $\mu_0 H = 0$ T and $\mu_0 H = 0.4$ T. The Lorentzian fits (dashed red lines) indicate correlation lengths of $\xi = 70(2)$ Å and $\xi = 22(1)$ Å along $c$ in the incommensurate and the commensurate phases, respectively. These may be compared to the interlayer spacing of $d = 7.64$ Å, indicating a quasi-two-dimensional order and weak interactions between honeycomb layers. Correlations along $(h00)$, in contrast, are limited by the instrumental resolution. After correcting for the resolution measured at the nuclear (003) Bragg peak, we infer a correlation length exceeding $\sim$300 Å or $\sim 20 \times a$ as shown in Fig 5.4(e). Fig. 5.4(g) shows that in the fully field polarized state at $\mu_0 H$=3 T, the (003) Bragg peak gains strength, which is consistent with magnetic diffraction from the magnetized cobalt. The 24(1)% increase of the (003) peak intensity in the 3 T applied field corresponds to an induced magnetization of $2.4(7)$ $\mu_B$/Co, which may be compared to the magnetization of $2.9(1)$ $\mu_B$/Co obtained from magnetization data.

It is interesting to contrast the **Q**-dependence of the elastic magnetic scattering as depicted in Fig. 5.4(a-g) with that of the low energy inelastic scattering in Fig. 5.4(h-j). Integrating over energy transfer from $\hbar\omega = 0.4$ meV through the $\Gamma$ point excitation energy for each value of the applied field, we find a rod of scattering extending along **c** and passing through the $\Gamma$ point. This contrast with the **Q**-dependence of the elastic magnetic scattering, which at 0 T and 0.4 T has a finite in-plane component as apparent in Fig. 5.4(a-c) and also indicated by the dashed lines in Fig. 5.4(h-i). The dynamic spin correlations in

BCAO thus resemble those of a 2D FM at all fields and contain no evidence of a soft mode with a wave vector matching that of the low field AFM order.

### 5.2.3 Dispersive magnetic excitations

$\mathbf{Q} - \hbar\omega$ slices through inelastic neutron scattering data for $\mathbf{Q}$ varying along high symmetry directions in the hexagonal Brillouin zone are shown for four values of magnetic field applied along the $(1\bar{2}0)$ direction in Fig. 5.5. The momentum space labels used on the horizontal axis are defined in the inset. In the almost fully magnetized state at 3 T (Fig. 5.5(d) and (e)), the scattering qualitatively follows expectations for a 2D easy plane honeycomb ferromagnet. There is a coherent gapped mode with the lowest energy at the Γ point. In this partially polarized state a sharp flat two-magnon mode is visible near 4.3(1) meV (Fig. 5.5(d,e)). At the lower fields (Fig. 5.5(a-c)), there are strong diffuse contributions to the scattering near twice the field dependent gap energy. At zero field in Fig. 5.5(a) where the magnetic order has an incommensurate modulation within the basal plane there are multiple modes at the $M$ points indicative of a large unit cell. The first panels of these subplots show there is no observable dispersion along $(00\ell)$, again pointing toward very weak magnetic interaction between honeycomb layers.

Once the AFM order is suppressed at $\mu_0 H$=0.75 T, a magnon remains with a gap of $\hbar\omega$=1.0 meV and a continua of two magnon excitations centered at $\hbar\omega = 2.0$ meV. This can be more clearly seen through cuts of the intensity at the Γ point as a function of field, as shown in Fig. 5.6. An unusual feature of the scattering is a difference in the dispersion relation between high symmetry

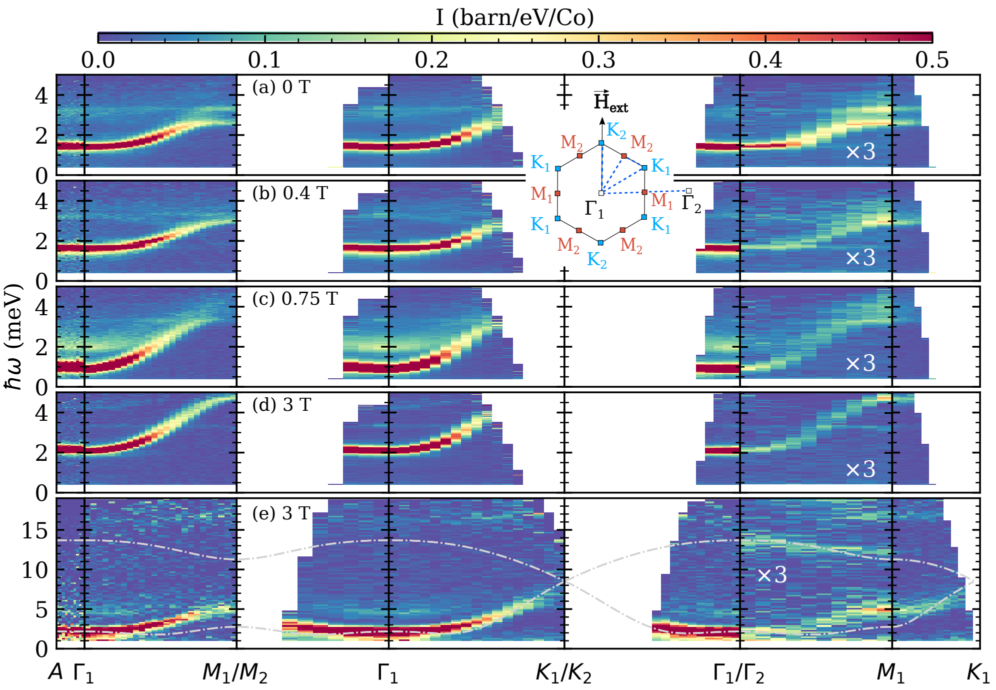

**Figure 5.5:** Magnetic excitation spectrum of BCAO as a function of field along high symmetry directions in the hexagonal Brillouin zone at $T$=1.7 K. The path in r.l.u. notation is $(00\left[\ell+\frac{1}{2}\right])$-$(00\ell)$-$(\frac{1}{2}0\ell)/(0\frac{1}{2}\ell)$-$(00\ell)$-$(\frac{1}{3}\frac{1}{3}\ell)/(\frac{\bar{1}}{3}\frac{2}{3}\ell)$-$(00\ell)/(10\ell)$-$(\frac{1}{2}0\ell)$-$(\frac{1}{3}\frac{1}{3}\ell)$. This is represented by the dashed blue lines pictured in the diagram of the Brillouin zone, where $\mathbf{H}_{\text{ext}}$ denotes the direction of the applied field. In (a-d) $\ell \in [1,3]$ for the in-plane slices in the high resolution $E_i$=6 meV configuration. For the $\Gamma$-$A$ direction, the path of $L$ to $L+\frac{1}{2}$ is averaged over several Brillouin zones ($L = 1,2,3,4$). For the $\Gamma_2 - M_1$ path, intensity has been scaled by a factor of three as indicated and $R\bar{3}m$ symmetry operations have been applied to enhance statistics. The transverse-$\mathbf{Q}$ averaging window is 0.1 Å$^{-1}$ in all cases. Panel (e) shows the $\mu_0 H = 3$ T and $E_i$=27 meV high energy configuration where $\ell \in [1,9]$. Data dominated by the tail of elastic scattering at energies below the FWHM elastic instrumental resolution of $\Delta\hbar\omega$=0.15 meV for the low energy configuration and $\Delta\hbar\omega$ =1.5 meV for the high energy configuration have been masked. In frames (a-d) the enhanced count rate at 3.4(1) meV arises from a spurious accelerator-related process.

paths that differ only in their orientation with respect to the applied magnetic field and thus the magnetization. The high symmetry zone boundary points nearest to the horizontal scattering plane are denoted $M_1$ and $K_1$, whereas the points closest to the vertical field direction are denoted $M_2$ and $K_2$ (see sketch in Fig. 5.5). Though the geometry of the instrument limits experimental access along the latter directions, a flattening of the mode may be observed at all non-zero fields in Fig. 5.5 for the $K_2$-$\Gamma_1$ and $M_2$-$\Gamma_1$ paths that lie along and at $30^o$ to the field direction respectively when compared to the $K_1$-$\Gamma_1$ and $M_1$-$\Gamma_1$ paths that form larger angles with the field direction. This is direct evidence of spin-orbit coupling and anisotropic magnetic interactions.

Fig. 5.5(e) shows a complementary higher energy measurement in the 3 T field-polarized phase. A second magnon mode is observed near $\hbar\omega = 12$ meV for wave vector transfer between $\Gamma_2$ and $M_1$. For a fully polarized magnet with two magnetic ions per unit cell, one indeed expects two magnon bands. This upper mode provides additional constraints on the model Hamiltonian. At the $\Gamma$ point, the intensity of the upper magnon mode is zero due to the spin-structure factor, so that this excitation is not visible in Raman or THz optical spectroscopy. The broad excitation visible near $\hbar\omega$=15 meV in Fig. 5.5(e) is identified as a phonon through Raman scattering [158].

Fig. 5.6(a-d) show the spectrum of inelastic magnetic scattering at the $\Gamma$ point. For the lower fields where BCAO is not fully magnetized, a two-magnon continuum is visible as a broad peak centered at twice the gap mode energy. Fig. 5.5(a) shows an anomaly in the main magnon dispersion relation as it enters the two-magnon continuum[160]. The broad two-magnon peak is

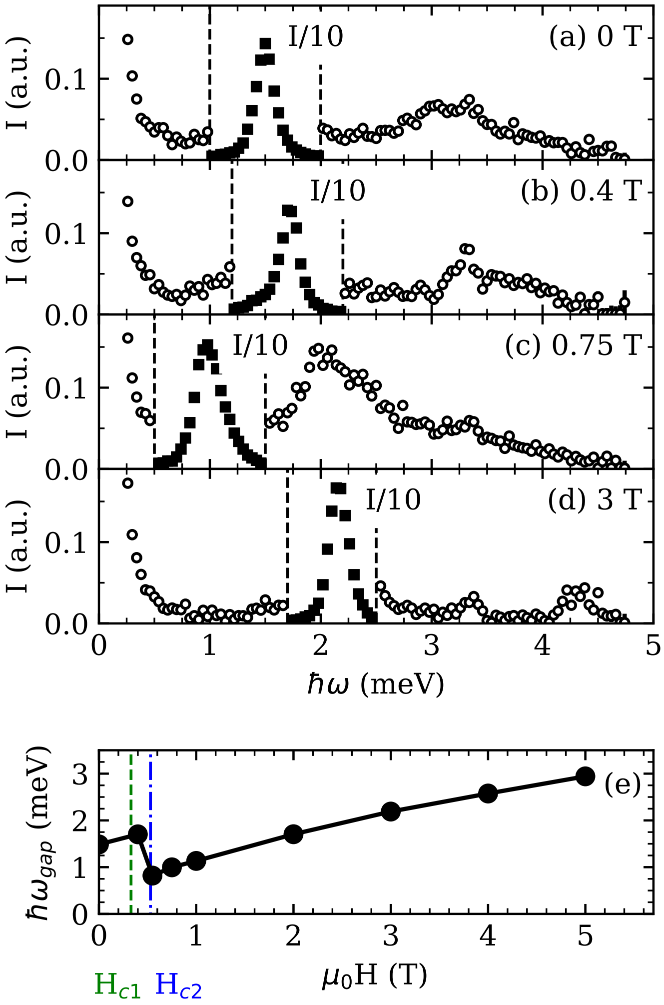

**Figure 5.6:** (a-d) Magnetic excitation spectrum for $BaCo_2(AsO_4)_2$ at the $\Gamma$ point for four different magnetic field strengths applied along the $(\bar{1}20)$ direction. Intensity data near the main peak in each spectrum has been scaled down by a factor of 10 and are shown as filled symbols. (e) The lowest $\Gamma-$point mode energy as a function of magnetic field applied along the $(\bar{1}20)$ direction. In frames (a-d) the enhanced count rate at 3.3 meV arises from a spurious accelerator-related process.

particularly strong when the one-magnon gap is smallest at 0.75 T (Fig. 5.6(c)) and magnons with energies beyond the two-magnon energy scale acquire significant physical width even though BCAO is uniformly magnetized at 0.75 T. Such interaction effects do not occur for the Heisenberg ferromagnet in a field where single magnons are exact eigenstates. At lower fields, the non-collinear and incommensurate nature of the ground state may play an important role in allowing spin waves to interact with the two-magnon continuum. These effects cannot be captured by the conventional $1/S$ expansion and the associated LSWT. When the system is fully magnetized at 3 T, the gap increases, the intensity of the two-magnon excitation decreases, and it approaches the resolution limit (Fig. 5.6(d)). Though the magnon dispersion relation still intersects the two-magnon mode, there is no longer an anomaly. LSWT should provide a good account of the one magnon branch in this almost fully magnetized state. Here, LSWT dispersions were calculated using both analytical methods and the SpinW package [114]. The full field dependence of the gap at the Γ point is consistent with previous THz studies [158].

### 5.2.4 Competing exchange Hamiltonians

In this work we consider two competing theoretical proposals for the microscopic description of BCAO. Following theoretical predictions that a dominant Kitaev interaction can be obtained in high-spin $3d^7$ cobaltates [48, 147], recent experiments were interpreted in terms of a $JK\Gamma\Gamma'$ model

$$\mathcal{H}_{JK\Gamma\Gamma'} = \sum_{\langle i,j\rangle \in \gamma} \mathbf{S}_i^T H_{K,\gamma}^{(1)} \mathbf{S}_j, \tag{5.1}$$

where

$$H_{K,x}^{(1)} = \begin{pmatrix} J+K & \Gamma' & \Gamma' \\ \Gamma' & J & \Gamma \\ \Gamma' & \Gamma & J \end{pmatrix}, H_{K,y}^{(1)} = \begin{pmatrix} J & \Gamma' & \Gamma \\ \Gamma' & J+K & \Gamma' \\ \Gamma & \Gamma' & J \end{pmatrix},$$

$$H_{K,z}^{(1)} = \begin{pmatrix} J & \Gamma & \Gamma' \\ \Gamma & J & \Gamma' \\ \Gamma' & \Gamma' & J+K \end{pmatrix} \tag{5.2}$$

with a large ferromagnetic Kitaev coupling and small isotropic and off-diagonal terms (i.e., $K < 0$ and $|K| \gg |J|, |\Gamma|, |\Gamma'|$). The spins in this model are represented in the Kitaev frame (KF) defined in Fig. 5.2(c). The most general form of the nearest-neighbour coupling matrix consistent with the symmetry of BCAO contains six independent terms and is given in the supplementary information. The simpler form used here neglects the lifting of $C_{2v}$ symmetry associated with the puckering of the honeycomb layer.

Alternatively, *ab initio* calculations [155] suggest that BCAO can be described by an XXZ-$J_1$-$J_3$ model where the spin Hamiltonian is approximately isotropic within the basal plane

$$\mathcal{H}_{\mathrm{XXZ}\text{-}J_1\text{-}J_3} = \sum_{\langle i,j\rangle \in \gamma} \mathbf{S}_i^T H_{\mathrm{XXZ},\gamma}^{(1)} \mathbf{S}_j + \sum_{\langle\langle\langle i,j \rangle\rangle\rangle} \mathbf{S}_i^T H_{\mathrm{XXZ}}^{(3)} \mathbf{S}_j, \tag{5.3}$$

with

$$
\begin{aligned}
H^{(1)}_{\mathrm{XXZ},z} &= \begin{pmatrix} J^{(1)}_{xy} + D & E & 0 \\ E & J^{(1)}_{xy} - D & 0 \\ 0 & 0 & J^{(1)}_{z} \end{pmatrix}, \\
H^{(1)}_{\mathrm{XXZ},y} &= U^{T}_{2\pi/3} H^{(1)}_{\mathrm{XXZ},z} U_{2\pi/3}, \\
H^{(1)}_{\mathrm{XXZ},x} &= U_{2\pi/3} H^{(1)}_{\mathrm{XXZ},z} U^{T}_{2\pi/3}, \\
H^{(3)}_{\mathrm{XXZ}} &= \begin{pmatrix} J^{(3)}_{xy} & 0 & 0 \\ 0 & J^{(3)}_{xy} & 0 \\ 0 & 0 & J^{(3)}_{z} \end{pmatrix},
\end{aligned}
\tag{5.4}
$$

where the second sum is taken over third nearest-neighbors, the spins are represented in the crystallographic frame (CF) (see Fig. 5.2(b)), and $U_{2\pi/3}$ denotes a $2\pi/3$ rotation about the crystallographic $c$-axis perpendicular to the honeycomb plane. The most general form of $H^{(1)}_{\mathrm{XXZ},\alpha}$ consistent with the symmetry of BCAO is given in the supplementary material. The simpler four parameter form used here is based on Ref. [155]. In this model the global $U(1)$ symmetry of the pure $XXZ$ model is broken by the $D$ and $E$ terms. These are assumed to be small albeit finite to open a gap in the magnetic excitation spectrum as observed in this work (see Fig. 5.4(a) and and Fig. 5.4(h-j)).

It is important to note that both models can be described in either the crystallographic frame (CF) or the Kitaev frame (KF). This transformation is shown explicitly in Appendix 7.3, and expressing the XXZ nearest neighbor interaction in terms of the Kitaev frame results in $K = D - \sqrt{2}F \approx 0$. The two models are then distinct approximations relative to the most general form of the interactions, where the XXZ-$J_1$-$J_3$ model is the case of low anisotropy and the $JK\Gamma\Gamma'$model is the case of high bond-dependent anisotropy.

It is also assumed that the essential physics of BCAO can be captured by a purely two-dimensional model. This assumption can be tested using LSWT. Using the dispersion from $A$-$\Gamma_1$ (Fig. 5.5, column 1), we place an upper limit on the interlayer coupling $J_1'$. As can be seen in Fig. 5.5, there is no noticeable dispersion along this path. By tuning $J_1'$ in LSWT, we find an upper limit of $|J_1'| \approx 0.3$ meV, at which point the dispersion predicted in LSWT exceeds the instrumental resolution of $\Delta\hbar\omega = 0.06$ meV (FWHM). We therefore may reasonably model BCAO as a purely two-dimensional spin system.

### 5.2.5 Analysis

To fit a model with a large number of free parameters, it is useful to identify constraints that restrict the problem to a smaller region of phase space. In our case, a straightforward method to initially restrict the set of coupling constants to an experimentally relevant subspace is to fit the field dependence of the $\Gamma$ point magnon gap in the polarized regime illustrated in Fig. 5.6(e), and the position of the second mode at the zone center (Fig. 5.5(e)). Within LSWT, the energies of these modes in the field-polarized state at the $\Gamma$ point are

$$E^{(1)}_{JK\Gamma\Gamma'}(\mathbf{k}=\mathbf{0}) = \sqrt{|\mathbf{h}|^2 + 3S(\Gamma+2\Gamma')|\mathbf{h}|} \tag{5.5a}$$

$$\begin{aligned} E^{(2)}_{JK\Gamma\Gamma'}(\mathbf{k}=\mathbf{0}) = \big[&\big((6J+2K-2\Gamma-4\Gamma')S-|\mathbf{h}|\big) \\ &\big((6J+2K+\Gamma+2\Gamma')S-|\mathbf{h}|\big)\big]^{1/2} \end{aligned} \tag{5.5b}$$

and

$$E^{(1)}_{\mathrm{XXZ}}(\mathbf{k}=\mathbf{0}) = \sqrt{|\mathbf{h}|^2 + 3S(J_z^{(1)} + J_z^{(3)} - J_{xy}^{(1)} - J_{xy}^{(3)})|\mathbf{h}|} \tag{5.6a}$$

$$\begin{aligned} E^{(2)}_{\mathrm{XXZ}}(\mathbf{k}=\mathbf{0}) = \Big[ &\Big( 6(J_{xy}^{(1)} + J_{xy}^{(3)})S - |\mathbf{h}| \Big) \\ &\Big( 3(J_{xy} + J_{xy}^{(3)} + J_z + J_z^{(3)})S - |\mathbf{h}| \Big) \Big]^{1/2} \end{aligned} \tag{5.6b}$$

for the $JK\Gamma\Gamma'$ and XXZ-$J_1$-$J_3$ models respectively. Here $\mathbf{h} = g\mu_B\mathbf{B}$ and we use the *ab initio* determined $g-$factors $g_{ab} = 5$ and $g_c = 2.7$ [155] for in-plane and out-of-plane fields respectively. For both models these mode energies only depend on two specific combinations of the exchange parameters: $3J + K$ and $\Gamma + 2\Gamma'$ for the $JK\Gamma\Gamma'$ model. For the XXZ-$J_1$-$J_3$ model, the $\Gamma$ point magnon energies are controlled by $J_{xy}^{(1)} + J_{xy}^{(3)}$ and $J_z^{(1)} + J_z^{(3)}$. They are independent of $D$ and $E$, which must therefore be constrained by other data.

To find a specific combination of couplings, a $\chi^2$ goodness of fit parameter is introduced comparing the calculated energies at the $\Gamma$ point to those experimentally observed by neutron scattering in the field-polarized regime. The result is a normalized map of $\chi^2$ in parameter space presented in Fig. 5.7(a,b) for the two models. For each, we obtain two localized regions in parameter space that reproduce the field dependence of the zone center magnon energies.

These regions are given by

$$\begin{cases} 3J + K = -12.1(1)\text{meV} \\ \Gamma + 2\Gamma' = 3.0(1)\text{ meV} \end{cases} \tag{5.7a}$$

and

$$\begin{cases} 3J + K = 15.2(1)\text{ meV} \\ \Gamma + 2\Gamma' = 3.0(1)\text{ meV} \end{cases} \tag{5.7b}$$

for the $JK\Gamma\Gamma'$ model, and

$$\begin{cases} J_{xy}^{(1)} + J_{xy}^{(3)} = -5.0(1)\text{meV} \\ J_{z}^{(1)} + J_{z}^{(3)} = -2.0(1)\text{ meV} \end{cases} \tag{5.8a}$$

and

$$\begin{cases} J_{xy}^{(1)} + J_{xy}^{(3)} = 4.0(1)\text{ meV} \\ J_{z}^{(1)} + J_{z}^{(3)} = 7.0(1)\text{ meV}. \end{cases} \tag{5.8b}$$

for the XXZ-$J_1$-$J_3$ model. The remainder of the analysis is restricted to these four sets of constraints.

To further constrain the parameters, we investigate if the two models can reproduce the observed incommensurate magnetic order within this restricted parameter set. Despite recent suggestions of a fluctuating double-zigzag structure [153], this is close in energy to the originally proposed incommensurate spiral structure. Subtle effects like quantum fluctuations or distortions may favor one phase or the other. As such, we do not address these issues ind look to stabilize the single **k** incommensurate spiral order for simplicity.

To obtain a classical magnetic phase diagram, we employ the Luttinger-Tisza approximation [161, 162], in which a direct solution of the classical model

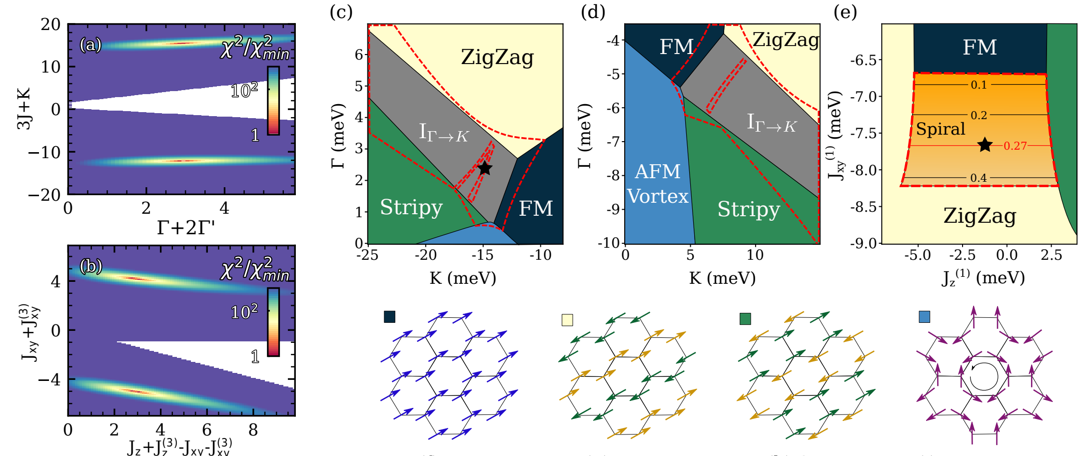

(f) FM (g) ZigZag (h) Stripy (i) AFM Vortex

**Figure 5.7:** (a)-(b) Normalized goodness of fit $\chi^2$ for the field dependence of the $\Gamma-$point mode for the $JK\Gamma\Gamma'$ and XXZ-$J_1$-$J_3$ models. (c)-(e) Classical phase diagram around the only regions where incommensurate order was observed for the restricted parameter space that reproduces the field-dependent $\Gamma-$point mode energies. (c) and (d) correspond to the constraints $\Gamma + 2\Gamma' = 3.0$ meV and $3J + K = -12.1$ meV, whereas (e) corresponds to $J_{xy}^{(1)} + J_{xy}^{(3)} = -5.0$ meV and $J_z^{(1)} + J_z^{(3)} = -2.0$ meV. The red dashed lines enclose the regions where the Luttinger-Tisza approximation fails, and the ground state is instead determined by a combination of simulated annealing and a variational single-Q Ansatz. The contour lines in the spiral phase of (e) represent the magnitude of the ordering wavevector. The black stars in panels (c) and (e) are the representative points used for both models (see (5.11) and (5.10)). (f)-(i) Representative spin configurations for the reported classical commensurate phases with the corresponding color in the phase diagrams.

can be obtained by relaxing the constraint of fixed spin length at every site. In regions where the Luttinger-Tisza approximation fails (i.e., the resulting solution does not respect the hard constraints on the spin length on all sites), we have employed a combination of simulated annealing on finite clusters with $2 \cdot 26^2$ sites, and variational single-Q Ansatz of the form

$$\mathbf{S}_i = \sqrt{1-\alpha_i^2}\left[\cos(\mathbf{Q}\cdot\mathbf{r}_i)\hat{\mathbf{e}}_i^x + \sin(\mathbf{Q}\cdot\mathbf{r}_i)\hat{\mathbf{e}}_i^y\right] + \alpha_i\hat{\mathbf{e}}_i^z, \tag{5.9}$$

where the canting out of the rotation plane $\alpha_i$ and the orthonormal frames $(\hat{\mathbf{e}}_i^x, \hat{\mathbf{e}}_i^y, \hat{\mathbf{e}}_i^z)$ are sublattice-dependent variational parameters. Here, we report the experimentally relevant regions where incommensurate magnetic order was observed for the $JK\Gamma\Gamma'$ model in Fig. 5.7(c) and (d), and for the XXZ-$J_1$-$J_3$ model in Fig. 5.7(e).

In all cases for the $JK\Gamma\Gamma'$ model, despite spiral order being stabilized it is of the wrong type. Rather than the experimentally observed propagation vector that goes from the $\Gamma$ to the $M$ point, the $JK\Gamma\Gamma'$model predicts order from the $\Gamma$ to $K$ point. To see if the introduction of further-neighbor exchange could stabilize the correct type of order, a Heisenberg $J_3$ contribution was also tested from $J_3$=-5 meV to $J_3$=5 meV, which still cannot account for the observed order. Thus, we find no values of the coupling constants for the $JK\Gamma\Gamma'$ model with large Kitaev interactions that can reproduce the field dependence of the $\Gamma$ point magnon energies and the correct classical ground state even with the addition of third nearest-neighbor Heisenberg interactions. This is already a cogent indication that the $JK\Gamma\Gamma'$ model with large bond-dependent interactions may not provide an accurate description of BCAO.

In contrast, it has been reported that the XXZ-$J_1$-$J_3$ model on the honeycomb lattice supports spiral incommensurate order with an ordering wavevector that smoothly interpolates between the $\Gamma$ and $M$ points with a specific magnitude of $|\mathbf{k}_c|$=0.27 for $J_{xy}^{(3)}/|J_{xy}^{(1)}| \approx 0.34$ and $J_{xy}^{(1)} < 0$ [163]. This incommensurate spiral region is represented in Fig. 5.7(e), where there exists a line that reproduces the experimentally determined incommensurate wavevector between zigzag and stripy phases that are stabilized for large values of $|J_z^{(1)}|$. This spiral phase with $|\mathbf{k}_c|$=0.27 is also stable to the addition of anisotropic terms provided they are sufficiently small (i.e., approximately if $|D|, |E| < 0.2$ meV). It is consequently natural to account for both the field dependence of the gap and the incommensurate magnetic structure of BCAO with the XXZ-$J_1$-$J_3$ model.

Within this restricted parameter space, we can compute the dynamical spin structure factors (DSSF) of both models to directly compare against the inelastic neutron scattering results. Based on the previously described constraints, we select the parameters

$$\begin{aligned} J_{xy}^{(1)} &= -7.6 \text{ meV}, \\ J_{z}^{(1)} &= -1.2 \text{ meV}, \\ J_{xy}^{(3)} &= 2.5 \text{ meV}, \\ J_{z}^{(3)} &= -0.85 \text{ meV}, \\ D &= 0.1 \text{ meV}, \\ E &= -0.1 \text{ meV} \end{aligned} \tag{5.10}$$

and

$$\begin{aligned} J &= 0.97 \text{ meV}, \\ K &= -15.0 \text{ meV}, \\ \Gamma &= 2.5 \text{ meV}, \\ \Gamma' &= 0.25 \text{ meV} \end{aligned} \tag{5.11}$$

as the best-fit for both models. The two models support the incommensurate spiral and $\mathrm{I}_{\Gamma\to K}$ phases respectively, as depicted in Fig. 5.7. For XXZ-$J_1$-$J_3$ , The remaining free parameters $J_z^{(1)}$, $D$ and $E$ were chosen to be small enough in magnitude to yield the correct spiral order, approximately reproduce the gap observed at zero field in Fig. 5.5(a), and provide the best reproduction of the neutron scattering in the polarized regime as presented in Fig. 5.5(c-e).

Using these parameters, the dynamical spin structure factor may now be

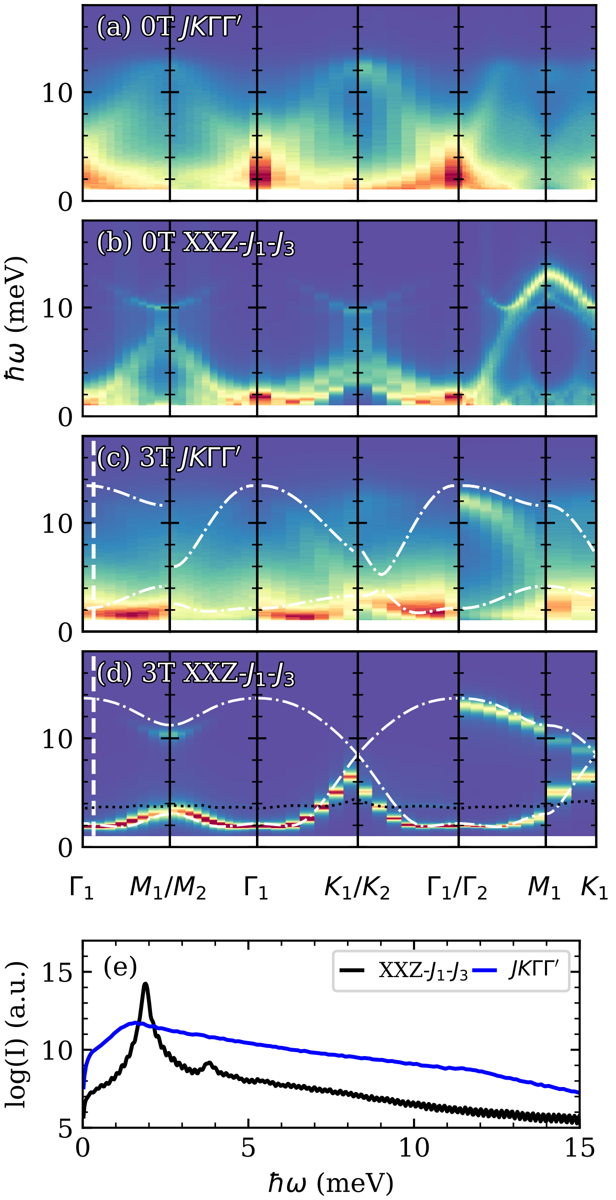

**Figure 5.8:** Dynamical spin-structure factor obtained by MD between high symmetry points for both the $JK\Gamma\Gamma'$ model (a,c) and the XXZ-$J_1$-$J_3$ model (b,d) with an in-plane field of 0 T at $T = 1$ K and 3 T at $T = 2$ K, respectively. Parameters used for both models are given by (5.11) and (5.10). The LSWT dispersion for each model and set of parameters are overlaid in (c) and (d) using the dashed dotted line. For the XXZ-$J_1$-$J_3$ case the dotted black line represents the lower edge of the two-magnon continuum calculated using the LSWT dispersion. (e) Intensity cut near the $\Gamma$ point (along the vertical dashed line in (c) and (d)) for both models at 3 T.

computed for each model. This is done using a technique called Molecular dynamics, which is discussed in more detail in the publication of this work [164], but in a nutshell it performs a classical time evolution of spins using the Laudau-Lifshitz-Gilbert equations of motion. The method is entirely classical, but captures almost all of the features of our data.

The calculated DSSF as a function of energy between high symmetry points in the field-polarized regime at $\mu_0 H = 3$ T with the LSWT dispersion overlaid in Fig. 5.8 (c,d). The MD results for the XXZ-$J_1$-$J_3$ model with our parameters show good agreement with experimental measurements reported in Fig. 5.5(d,e). As can be seen from the intensity cut near the zone center in Fig. 5.8(e), MD simulations even capture the two-magnon mode reported in Fig. 5.6(d) and THz spectroscopy [158, 159]. In contrast, the experimental results are not well described by our parameter set for the $JK\Gamma\Gamma'$ model. LSWT for the $JK\Gamma\Gamma'$ model predicts a magnon dispersion that differs significantly when comparing the $\Gamma - M_1$ with the $\Gamma - M_2$ path. Such a large anisotropy is incompatible with our INS measurements presented in Fig. 5.5. MD further predicts a continuum with no clear resonances as highlighted by the intensity cut near the $\Gamma$ point presented in Fig. 5.8(e). The sharp magnon bands observed experimentally are compatible with the XXZ-$J_1$-$J_3$ model but clearly inconsistent with our MD simulation of the $JK\Gamma\Gamma'$ model.

Overall the calculated dispersion of both LSWT and MD simulation for the XXZ-$J_1$-$J_3$ model are in close correspondence to the observed scattering. The most important discrepancy lies at the $\Gamma$ point, where LSWT predicts a minima at the incommensurate ordering wavevector whereas MD yields a flatter band that is concave up at the Γ-point as observed in the data. The disagreement suggests that the system experiences significant nonlinearities by magnon-magnon interactions not accounted for in LSWT, leading to an overall renormalization of the magnon dispersion. Thus, the lack of a minima in the dispersion relation at the propagation vector is a highly nonlinear effect that is almost certainly present in other cobaltates.

### 5.2.6 Field-angle dependent magnetization

As a final comparison between the two models and experiments, we examine the in-plane magnetization for different magnetic field orientations. Increasing the field from zero, three successive magnetization plateaus can be observed in Fig. 5.9(a), where the transitions from one plateau to the next correspond to the field-induced magnetic phase transitions at $H_{c1}$ and $H_{c2}$ respectively. Measuring the magnetization with magnetic fields along the $x$ and $y$-axis of the CF (Fig. 5.2(b)), only a very small anisotropy is observed around the first and second transitions. Using our parameter set for the XXZ-$J_1$-$J_3$ model, the qualitative resemblance between the measurements and the magnetization curves obtained from finite temperature Monte Carlo at $T = 0.695$ K is striking (Fig. 5.9(b)) . The three successive plateaus are clearly observed, and the small anisotropy between the curves for the two different field orientations near the transitions is reproduced. We have verified that the intermediate field-driven phase also has an ordering wavevector of magnitude $|\mathbf{k}_c| = 1/3$ as observed experimentally. In contrast, the $JK\Gamma\Gamma'$ model does not have the correct number of transitions and polarizes at far higher field scales than

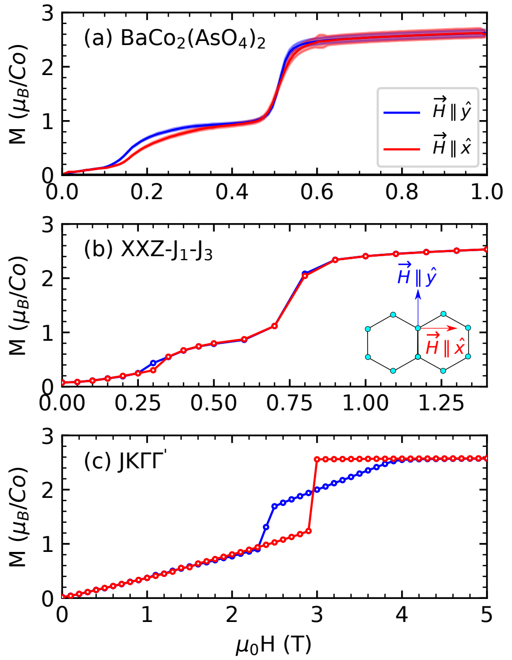

**Figure 5.9:** (a) In-plane angle-dependent magnetization for BaCo$_2$(AsO$_4$)$_2$ measured on a small single crystal sample. The red (blue) curve corresponds to a field orientation along the $\hat{\mathbf{x}}$-axis ($\hat{\mathbf{y}}$-axis) as depicted in the inset. For clarity, the magnetization curves are only shown for an increasing field from 0 T. (b) Magnetization curves calculated using Monte Carlo methods for the XXZ-$J_1$-$J_3$ model with the set of exchange parameters given in (5.10) at a temperature of $T = 0.695$ K, and (c) for the $JK\Gamma\Gamma'$ model with the parameter set in (5.11) ($T = 0$ K).

expected. The temperatures in each case are chosen such that they most closely reproduce the experimentally observed $M(H)$ curves.

## 5.3 Discussion

Though our initial interest in BCAO was as a candidate Kitaev material, our results strongly favor the XXZ-$J_1$-$J_3$ over the Kitaev model. We are able to differentiate between the two models by examining the zero-field ground state of BCAO using constraints from LSWT. We find that the $JK\Gamma\Gamma'$ model cannot simultaneously reproduce the field dependence of the Γ point modes and the magnetic order found in BCAO. Our work stresses the need for a critical reexamination of the proposal for Kitaev physics in cobaltates. These materials may not in fact fall within the regime of interest that was considered in the theoretical proposals for Kitaev physics in 3d systems [48, 147].

In contrast to the XXZ-$J_1$-$J_3$ model, at high fields, the thermodynamic properties of the $JK\Gamma\Gamma'$ model vary strongly with the in-plane field direction (Fig. 5.9(c)) [165, 166]. Such strong in-plane anisotropy has in fact been observed for the leading Kitaev candidates $\alpha$-RuCl$_3$ [167, 168] and $\beta-$Li$_2$IrO$_3$ [98], but it is not present for BCAO (Fig. 5.9). Magnetization measurements versus in-plane field direction can thus be an effective method to screen potential model systems. For cobaltates whose magnetization cannot be accounted for by the XXZ-$J_1$-$J_3$ model, single-crystal INS with an in-plane field can subsequently be employed to establish the spin Hamiltonian as we have done for BCAO in this work. This work culminated in the publication of Ref. [164]

Although BCAO does not appear to realize large Kitaev-type interactions but rather an XXZ-$J_1$-$J_3$ model, its physical properties are still of great interest. BCAO now presents a rare case of an almost perfect two-dimensional honeycomb magnet with well-known values for its dominant exchange interactions ((5.10)). Previous theoretical investigations indicate that a QSL ground state may be possible for in-plane isotropic models with competing interactions on the honeycomb lattice[169–171]. Thus the competition between first and third nearest-neighbor interactions that we have documented for BCAO, may place this materials in proximity to a QSL. Although the theoretical work indicates a second nearest-neighbor interaction (which seems to be negligible for BCAO) is needed to stabilize a QSL, a QSL might be accessible for BCAO in the presence of a suitably oriented external magnetic field. This possibility has, to our knowledge, not been explored yet. The continuum scattering reported by THz spectroscopy with a large c-oriented field [158] may signal the onset of such a phase. Possibly related to this, the strong interaction between the one and two-magnon modes reported here (Fig. 5.4) is also unusual and interesting. Thus there are promising directions for future studies of BCAO and the extended family of honeycomb cobaltates.

## 5.4 Pushing BCAO towards a spin-liquid phase by tilted fields and doping

Before concluding this dissertation, I would like to briefly discuss two attempts that I have participated in to try to push BCAO into a QSL phase. The first, inspired by THz spectroscopy studies [158], used a unique tilted field geometry in an inelastic neutron scattering experiment to try to suppress the order with a small in-plane field and push the system into a fluctuating regime by an out of plane field. The second is another inelastic neutrons scattering study of V-doped BCAO where the vanadium doped on the non-magnetic site slightly changes the lattice parameter and thus the exchange constants, potentially pushing the system towards a quantum critical regime. The goal of this brief section is not a full description of the physics gleaned from each experiment, but instead to briefly share the experimental results and to give examples of the types of studies I would like to pursue in the future.

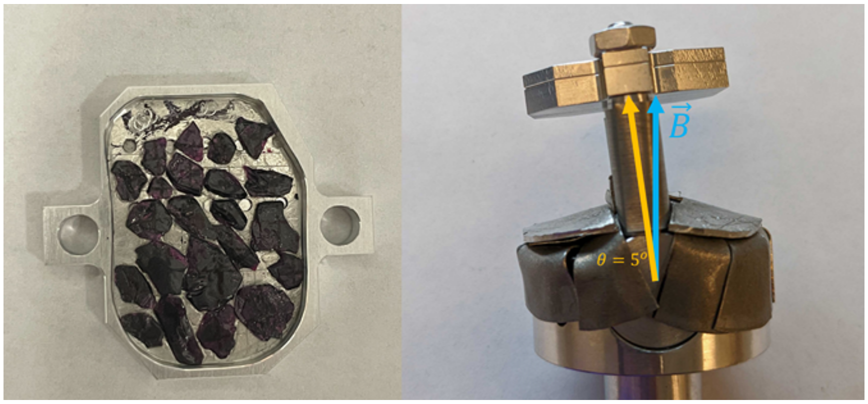

**Figure 5.10:** Tilted field geometry used in second BCAO experiment.

### 5.4.1 Tilted field experiments

The idea of a QSL phase induced by a tilted out of plane field was inspired by the recent THz results suggesting a continua emerging upon the application of a primarily out of plane field [158]. To test this, we performed inelastic neutron scattering studies in the a such that the scattering vector $\boldsymbol{Q}$ was primarily in the $(hk0)$ plane, but tilted such that the field was 5deg from the $\hat{c}$-axis as depicted in Fig. 5.10. The design uses the same plate of samples used in the previous study of BCAO, but encased in a coffin to help brace against the torque applied by the out of plane magnetic field. While the details of the study will be left to a future work, the measurements were all performed at $T$=1.7(1) K on the HYSPEC instrument. The measurement was performed in a 14 T vertical magnet at fields of $H$=0 T, 5 T, 7 T, 9 T, and 11 T. Equal counting times were devoted to each field. The instrumental configuration was for incident energy $\mathrm{E}_i$=7.5 meV neutrons and the high flux chopper at 300 Hz. The results are entirely compatible with the previous THz studies, and a sample of the full INS dataset is shown in Fig. The results are not

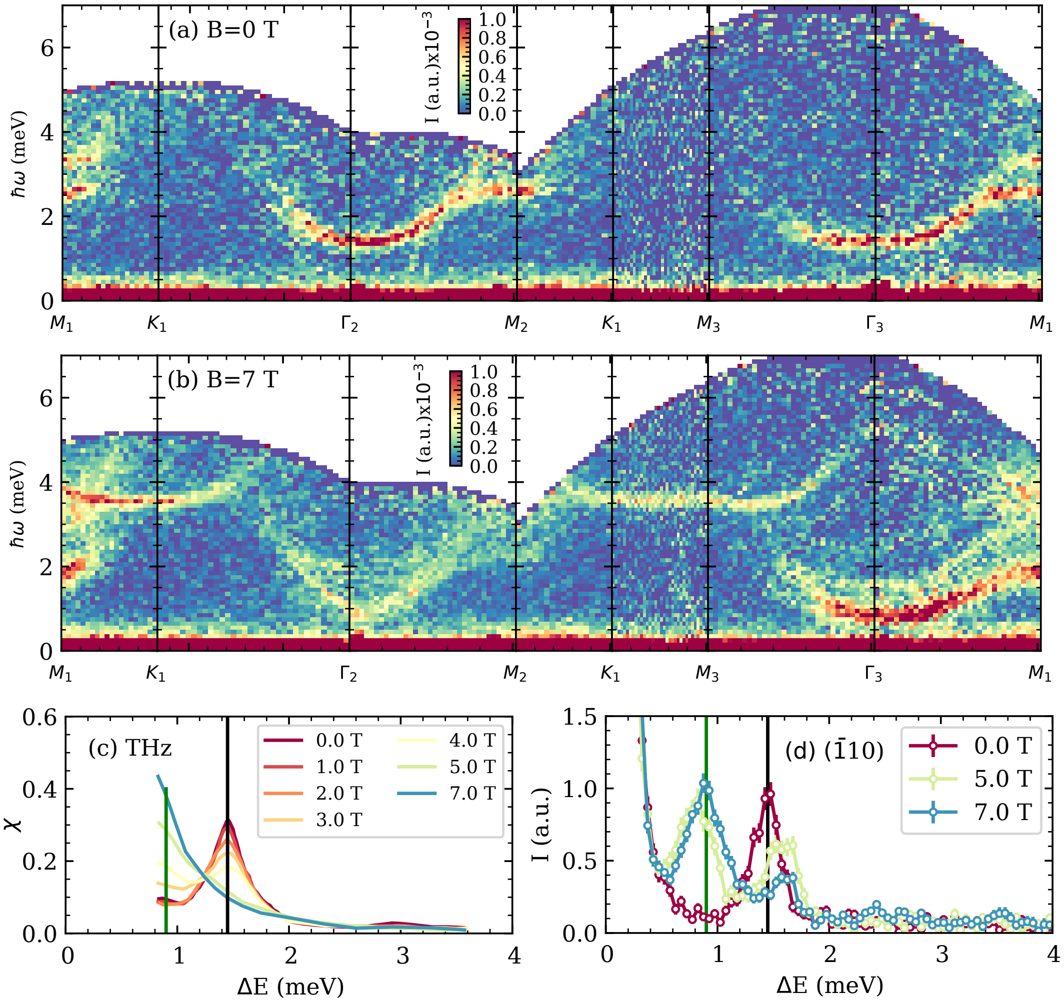

**Figure 5.11:** Observed magnon dispersion through a long path in the Brillioun zone in $BaCo_2(AsO_4)_2$.

compatible with a QSL state, with the magnetic order being of the $\boldsymbol{k} = (\frac{1}{3}, 0, 0)$ commensurate type. This order appears to be stable up to at least 9 T, above which the signal becomes unusable. This is due to the massive torque applied to the crystals in the out of plane field, which caused a significant fraction to be ripped from the plate. In Fig. 5.11(b) the "flat band" contribution around $\hbar\omega$=4 meV originates from the contribution of the loose samples. We are currently in the process of analyzing these data, but this experiment was unsuccessful in producing a QSL phase in tilted fields. Still, this type of experiment will be helpful in the study of future candidate spin-liquid materials as the effect of tilted fields in Kitaev spin-liquids is an actively discussed topic in large part due to the thermal hall effect measurements of $\alpha-\mathrm{RuCl_3}$ [172].

### 5.4.2 Tuning the magnetic exchange Hamiltonian in $\mathrm{BaCo_2(AsO_4)_2}$ by chemical doping

A second attempt to induce a spin-liquid state in BCAO was through the introduction of chemical doping. Colleagues in the McQueen group performed a detailed study of $\mathrm{BaCo_2(AsO_4)_{2-2x}(VO_4)_{2x}}$, $0.025 \leq x \leq 0.70$. Upon increasing vanadium content, a gradual suppression of order is observed with the order being absent for substitutions around $x$ =0.1. The ground state of this material was thought to be a highly fluctuating variant of BCAO with slightly modified exchange interactions, perhaps pushing it into a QSL phase [173]. To test this, we performed studies on the CNCS instrument at ORNL. The single crystalline samples were very small, requiring 149 coaligned crystals for a total mass of 0.90 g.A unique mount was designed consisting of nine hexagonal aluminum plates of width 12 mm, upon which crystals were coaligned.

Still, the results clearly showed the presence of static spin correlations at a commensurate propagation vector of $\mathbf{k} = (\frac{1}{4}, 0, 0)$. This is shown most obviously in the elastic scattering, using a $T$=30 K measurement as background as depicted in Fig. 5.12(a). The order parameter extracted from this is sharp, showing a clear transition between $T$=5 K and $T$=6 K shown directly in Fig. 5.12(b). One may also extract a spin-spin correlation length using a Lorentzian form of

$$I(\boldsymbol{Q}) = \mathcal{A}\frac{\xi}{1 + \{(\boldsymbol{Q} - \boldsymbol{q_0})\xi\}^2} \tag{5.12}$$

where $\xi$ is the correlation length, $\boldsymbol{Q}$ is the wavevector along the $(H00)$ direction, and $\boldsymbol{q}_0$ is the position of the magnetic Bragg peak ($(\frac{3}{4}, 0, 0)$ is used in this case). In this experiment, we find the static spin-spin correlation length to be merely $\chi \approx 15$ Å$^{-1}$. This is only three unit cells, reflecting the highly fluctuating nature of the ground state. Further support of the highly fluctuating nature of the ground state comes from the calculated static moment. Assuming the ↑↑↓↓ is the magnetic structure we observe, one may compare a calculation of the magnetic structure factor of the magnetic Bragg peak to the observed intensity. We find a moment of only $\mu_{static} = 0.7(3)$ $\mu_B$, which is only a small fraction of the expected moment from magnetization of 5 $\mu_B$. In BCAO in particular, it appears that doping serves to stabilize the ↑↑↓↓ ordered phase. The nature of this phase is highly fluctuating, as evidenced through the broad excitations shown in Fig. 5.12 and the lack of long-range order in bulk characterization measurements. While the exact details of this system have not been worked out yet, it is a promising example of the doping of a highly

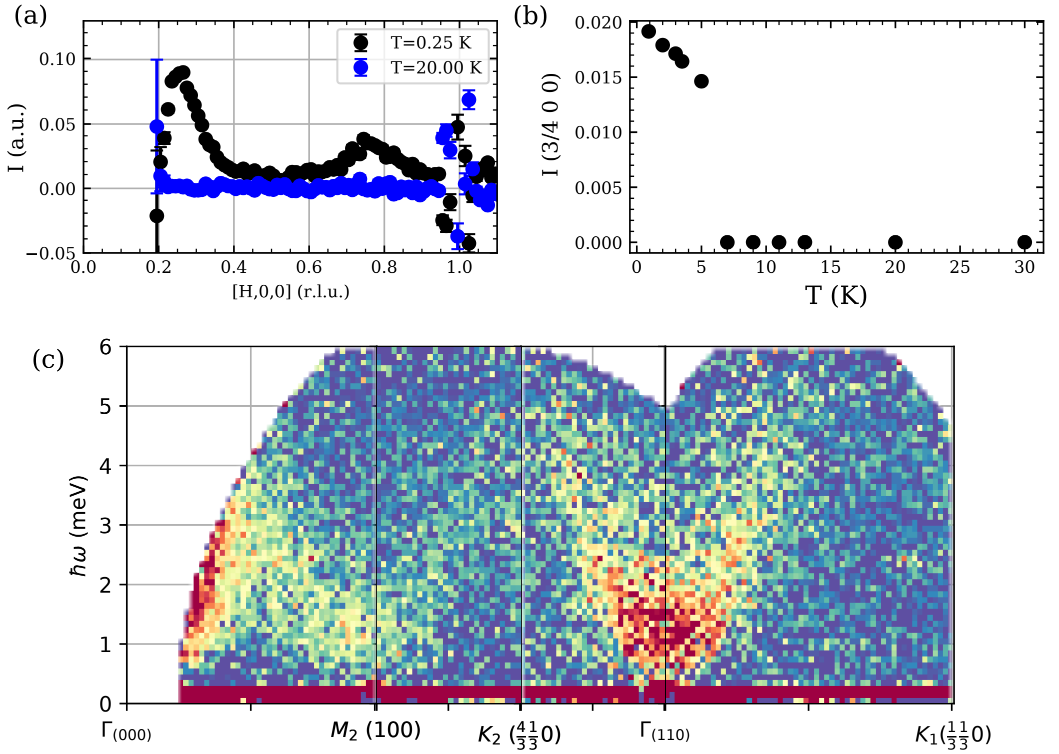

**Figure 5.12:** Summary of neutron scattering results on BaCo$_2$(AsO$_4$)$_{2-2x}$(VO$_4$)$_{2x}$. (a) Commensurate order in the elastic scattering along the $(h00)$ direction with propagation vector $\boldsymbol{k} = (\frac{1}{4}, 0, 0)$. (b) Integrated intensity of the $(\frac{3}{4}, 0, 0)$ peak as a function of temperature. (c) Dispersion of magnetic excitations through a wide path in the first and second Brillouin zones. Backgrounds have been subtracted by a detailed balance method. Intensity scale is arbitrary.

frustrated magnet on the nonmagnetic site to tune exchange parameters. This is reminiscent of the famous cuprate superconductors, which require doping to achieve high superconducting critical temperatures [174]. This approach is relatively unexplored in the realm of frustrated magnetism, and I believe this type of study to be a promising direction for the future study of QSL's in general.

# Chapter 6

# Discussion and Conclusion

The work discussed in this dissertation was squarely focused upon the study of quantum spin-liquid candidate materials, with a particular focus on the search for the realization of Kitaev interactions. Though a number of other numerical and experimental techniques were used for this aim, the primary focus was on inelastic neutron scattering studies of both powder and single crystalline samples.

The trimer-based materials $Ba_4NbRu_3O_{12}$ and $Ba_4NbIr_3O_{12}$ were the first materials discussed. Detailed analysis of specific heat revealed the coexistence of spin-freezing and fermionic heat carriers through a large $\gamma$ term in $C(T)/T$. Elastic powder scattering confirms the presence of short-ranged frozen spin correlations, and powder inelastic neutron studies reveal a highly fluctuating ground state consistent with a nearest-neighbor description and trimer molecular magnetic units. Little work has been performed on $Ba_4NbIr_3O_{12}$, but both present rare and interesting cases of inorganic quantum molecular magnetism.

Next, the honeycomb lithium iridates $\beta$-$Li_2IrO_3$ and $D_3LiIr_2O_6$ are discussed. A study of $\beta$-$Li_2IrO_3$ combining inelastic neutron scattering in the ordered state, THz spectroscopy, heat capacity, and linear spin-wave theory confirms a dominant ferromagnetic Kitaev interaction with tighly constrained Heisenberg $J$ and off-diagonal $\Gamma$ contributions to the spin exchange. The results place the material proximate to a KSL phase. Powder inelastic neutron scattering of $D_3LiIr_2O_6$ reveals a disordered ground state, with an extracted magnetic signal consistent with that of a KSL described by only nearest-neighbor interactions.

Finally, a comprehensive study of the spin exchange in $BaCo_2(AsO_4)_2$ was performed by inelastic neutron scattering in a magnetic field applied in the $(H00)$ plane. A detailed analysis carefully differentiates between two different potential Hamiltonians, finding that the honeycomb cobaltate is better describe by a $XXZ$-$J_1J_3$ model rather than the suggested Kitaev interaction. The work demonstrates the level of care required when searching for Kitaev interactions in next generation materials.

Of the work performed in this thesis, the work on BCAO certainly had the greatest impact on my long term outlook of the topics I would like to study. I believe that field-angle dependent phenomena are largely unexplored, and that the tilted field experiment briefly described at the end of Chapter 5 is an excellent example of the types of studies that I would like to pursue on other spin-liquid candidate materials, Kitaev or otherwise. I look forward to applying these ideas during my upcoming postdoc at the NIST Center for Neutron Research, and hope to continue to collaborate with the many wonderful friends and colleagues that I have made during my graduate studies at Johns Hopkins.

# References

1. Toledano, P. & Toledano, J.-c. *Landau Theory Of Phase Transitions, The: Application To Structural, Incommensurate, Magnetic And Liquid Crystal Systems* (World Scientific Publishing Company, 1987).
2. Chaikin, P. M., Lubensky, T. C. & Witten, T. A. *Principles of condensed matter physics* (Cambridge university press Cambridge, 1995).
3. Anderson, P. W. Resonating valence bonds: A new kind of insulator? *Materials Research Bulletin* **8,** 153–160. ISSN: 00255408 (2 1973).
4. Savary, L. & Balents, L. Quantum spin liquids: A review. *Reports on Progress in Physics* **80,** 016502. ISSN: 00344885. `https://iopscience.iop.org/article/10.1088/0034-4885/80/1/016502https://iopscience.iop.org/article/10.1088/0034-4885/80/1/016502/meta` (1 2017).
5. Norman, M. R. Colloquium: Herbertsmithite and the search for the quantum spin liquid. *Reviews of Modern Physics* **88,** 041002. ISSN: 15390756. `https://journals.aps.org/rmp/abstract/10.1103/RevModPhys.88.041002` (4 2016).
6. Zhou, Y., Kanoda, K. & Ng, T. K. Quantum spin liquid states. *Reviews of Modern Physics* **89,** 025003. ISSN: 15390756. `https://journals.aps.org/rmp/abstract/10.1103/RevModPhys.89.025003` (2 2017).
7. Wang, Y., Reeder, T., Karaki, Y., Kindervater, J., Halloran, T., Maliszewskyj, N., Qiu, Y., Rodriguez, J. A., Gladchenko, S., Koohpayeh, S. M., Nakatsuji, S. & Broholm, C. Monopolar and dipolar relaxation in spin ice Ho2Ti2O7. *Science Advances* **7,** 908–924. ISSN: 23752548. `https://www.science.org` (25 2021).
8. Ashcroft, N. W. & Mermin, N. D. *Solid State Physics* (Holt-Saunders, 1976).

9. Zhang, H., Feng, X., Heitmann, T., Kolesnikov, A. I., Stone, M. B., Lu, Y. M. & Ke, X. Topological magnon bands in a room-Temperature kagome magnet. *Physical Review B* **101,** 100405. ISSN: 24699969. https://journals.aps.org/prb/abstract/10.1103/PhysRevB.101.100405 (10 2020).
10. Hutchings, M. T. Point-Charge Calculations of Energy Levels of Magnetic Ions in Crystalline Electric Fields. *Solid State Physics - Advances in Research and Applications* **16,** 227–273. ISSN: 00811947 (C 1964).
11. Princep, A. J., Walker, H. C., Adroja, D. T., Prabhakaran, D. & Boothroyd, A. T. Crystal field states of Tb3+ in the pyrochlore spin liquid Tb2Ti2 O7 from neutron spectroscopy. *Physical Review B - Condensed Matter and Materials Physics* **91,** 224430. ISSN: 1550235X. https://journals.aps.org/prb/abstract/10.1103/PhysRevB.91.224430 (22 2015).
12. Zhang, X., Luo, Y., Halloran, T., Gaudet, J., Man, H., Koohpayeh, S. M. & Armitage, N. P. Low-energy magneto-optics of Tb2Ti2 O7 in a [111] magnetic field. *Physical Review B* **103,** L140403. ISSN: 24699969. https://journals.aps.org/prb/abstract/10.1103/PhysRevB.103.L140403 (14 2021).
13. Bramwell, S. T. & Harris, M. J. The history of spin ice. *Journal of Physics Condensed Matter* **32,** 374010. ISSN: 1361648X. https://doi.org/10.1088/1361-648X/ab8423 (37 2020).
14. Moriya, T. Anisotropic superexchange interaction and weak ferromagnetism. *Physical Review* **120,** 91–98. ISSN: 0031899X. https://journals.aps.org/pr/abstract/10.1103/PhysRev.120.91 (1 1960).
15. Anderson, P. W. & Suhl, H. Spin alignment in the superconducting state. *Physical Review* **116,** 898–900. ISSN: 0031899X. https://journals.aps.org/pr/abstract/10.1103/PhysRev.116.898 (4 1959).
16. Goodenough, J. B. Theory of the Role of Covalence in the Perovskite-Type Manganites $[\mathrm{La}, M(\mathrm{II})]\mathrm{MnO}_3$. *Phys. Rev.* **100,** 564–573. https://link.aps.org/doi/10.1103/PhysRev.100.564 (2 1955).
17. Kanamori, J. Theory of the Magnetic Properties of Ferrous and Cobaltous Oxides, I. *Progress of Theoretical Physics* **17,** 177–196. ISSN: 0033-068X. eprint: https://academic.oup.com/ptp/article-pdf/17/2/177/5311108/17-2-177.pdf. https://doi.org/10.1143/PTP.17.177 (1957).

18. Anderson, P. W., Baskaran, G., Zou, Z. & Hsu, T. Resonating–valence-bond theory of phase transitions and superconductivity in $La_2CuO_4$-based compounds. *Phys. Rev. Lett.* **58,** 2790–2793. https://link.aps.org/doi/10.1103/PhysRevLett.58.2790 (26 1987).

19. Balents, L. Spin liquids in frustrated magnets. *Nature* **464,** 199–208. ISSN: 00280836. https://www.nature.com/articles/nature08917 (7286 2010).

20. Broholm, C., Cava, R. J., Kivelson, S. A., Nocera, D. G., Norman, M. R. & Senthil, T. Quantum spin liquids. *Science* **367.** ISSN: 10959203. https://science.sciencemag.org/content/367/6475/eaay0668https://science.sciencemag.org/content/367/6475/eaay0668.abstract (6475 2020).

21. Dutton, S. E., Kumar, M., Mourigal, M., Soos, Z. G., Wen, J.-J., Broholm, C. L., Andersen, N. H., Huang, Q., Zbiri, M., Toft-Petersen, R. & Cava, R. J. Quantum Spin Liquid in Frustrated One-Dimensional $LiCuSbO_4$. *Phys. Rev. Lett.* **108,** 187206. https://link.aps.org/doi/10.1103/PhysRevLett.108.187206 (18 2012).

22. Mourigal, M., Enderle, M., Klöpperpieper, A., Caux, J.-S., Stunault, A. & Rønnow, H. M. Fractional spinon excitations in the quantum Heisenberg antiferromagnetic chain. *Nature Physics* **9,** 435–441 (2013).

23. Paddison, J. A., Daum, M., Dun, Z., Ehlers, G., Liu, Y., Stone, M. B., Zhou, H. & Mourigal, M. Continuous excitations of the triangular-lattice quantum spin liquid YbMgGaO 4. *Nature Physics* **13,** 117–122. ISSN: 17452481. www.nature.com/naturephysics (2 2017).

24. Han, T. H., Helton, J. S., Chu, S., Nocera, D. G., Rodriguez-Rivera, J. A., Broholm, C. & Lee, Y. S. Fractionalized excitations in the spin-liquid state of a kagome-lattice antiferromagnet. *Nature* **492,** 406–410. ISSN: 00280836. https://www.nature.com/articles/nature11659 (7429 2012).

25. Law, K. T. & Lee, P. A. 1T-TaS2 as a quantum spin liquid. *Proceedings of the National Academy of Sciences of the United States of America* **114,** 6996–7000. ISSN: 10916490. https://www.pnas.org/doi/abs/10.1073/pnas.1706769114 (27 2017).

26. Kitaev, A. Anyons in an exactly solved model and beyond. *Annals of Physics* **321,** 2–111. ISSN: 0003-4916. https://www.sciencedirect.com/science/article/pii/S0003491605002381 (2006).

27. Cardy, J. *Scaling and Renormalization in Statistical Physics* (Cambridge University Press, 1996).
28. Yan, S., Huse, D. A. & White, S. R. Spin-liquid ground state of the S = 1/2 kagome heisenberg antiferromagnet. *Science* **332,** 1173–1176. ISSN: 00368075. www.physics.utoronto.ca/~aephraim/data/PhotonTrajectories.www.sciencemag.org/cgi/content/full/332/6034/1170/DC1www.sciencemag.orgSCIENCEVOL (6034 2011).
29. Hermanns, M, Kimchi, I & Knolle, J. Physics of the Kitaev Model: Fractionalization, Dynamic Correlations, and Material Connections. *The Annual Review of Condensed Matter Physics is Annu. Rev. Condens. Matter Phys* **9,** 17–33. https://doi.org/10.1146/annurev-conmatphys- (2018).
30. Takagi, H., Takayama, T., Jackeli, G., Khaliullin, G. & Nagler, S. E. Concept and realization of Kitaev quantum spin liquids. *Nature Reviews Physics* **1,** 264–280. ISSN: 25225820. www.nature.com/natrevphys (4 2019).
31. Nayak, C., Simon, S. H., Stern, A., Freedman, M. & Sarma, S. D. Non-Abelian anyons and topological quantum computation. *Reviews of Modern Physics* **80,** 1083–1159. ISSN: 00346861. https://journals.aps.org/rmp/abstract/10.1103/RevModPhys.80.1083 (3 2008).
32. Knolle, J, Kovrizhin, D. L., Chalker, J. T. & Moessner, R. Dynamics of a two-dimensional quantum spin liquid: Signatures of emergent majorana fermions and fluxes. *Physical Review Letters* **112,** 207203. ISSN: 10797114 (20 2014).
33. Nasu, J., Knolle, J., Kovrizhin, D. L., Motome, Y. & Moessner, R. Fermionic response from fractionalization in an insulating two-dimensional magnet. *Nature Physics 2016 12:10* **12,** 912–915. ISSN: 1745-2481. https://www.nature.com/articles/nphys3809 (10 2016).
34. Feng, K., Perkins, N. B. & Burnell, F. J. Further insights into the thermodynamics of the Kitaev honeycomb model. *Physical Review B* **102,** 224402. ISSN: 24699969. https://journals.aps.org/prb/abstract/10.1103/PhysRevB.102.224402 (22 2020).
35. Nasu, J., Yoshitake, J. & Motome, Y. Thermal Transport in the Kitaev Model. *Physical Review Letters* **119,** 127204. ISSN: 10797114. https://journals.aps.org/prl/abstract/10.1103/PhysRevLett.119.127204 (12 2017).

36. Lefrançois, E., Grissonnanche, G., Baglo, J., Lampen-Kelley, P., Yan, J. Q., Balz, C., Mandrus, D., Nagler, S. E., Kim, S., Kim, Y. J., Doiron-Leyraud, N. & Taillefer, L. Evidence of a Phonon Hall Effect in the Kitaev Spin Liquid Candidate a-RuCl3. *Physical Review X* **12,** 021025. ISSN: 21603308. https://journals.aps.org/prx/abstract/10.1103/PhysRevX.12.021025 (2 2022).

37. Jackeli, G & Khaliullin, G. Mott insulators in the strong spin-orbit coupling Limit: From Heisenberg to a Quantum Compass and Kitaev Models. *Physical Review Letters* **102.** ISSN: 00319007 (1 2009).

38. Singh, Y., Manni, S, Reuther, J, Berlijn, T, Thomale, R, Ku, W, Trebst, S & Gegenwart, P. Relevance of the Heisenberg-Kitaev model for the honeycomb lattice iridates A 2IrO 3. *Physical Review Letters* **108.** ISSN: 00319007 (12 2012).

39. Kim, H. S., Shankar, V., Catuneanu, A. & Kee, H. Y. Kitaev magnetism in honeycomb RuCl3 with intermediate spin-orbit coupling. *Physical Review B - Condensed Matter and Materials Physics* **91,** 241110. ISSN: 1550235X. https://journals.aps.org/prb/abstract/10.1103/PhysRevB.91.241110 (24 2015).

40. Freund, F, Williams, S. C., Johnson, R. D., Coldea, R, Gegenwart, P & Jesche, A. Single crystal growth from separated educts and its application to lithium transition-metal oxides. *Scientific Reports* **6.** ISSN: 20452322. www.nature.com/scientificreports (2016).

41. Takayama, T, Kato, A, Dinnebier, R, Nuss, J, Kono, H, Veiga, L. S., Fabbris, G, Haskel, D & Takagi, H. Hyperhoneycomb iridate $\beta$-Li2IrO3 as a platform for kitaev magnetism. *Physical Review Letters* **114.** ISSN: 10797114 (7 2015).

42. Modic, K. A., Smidt, T. E., Kimchi, I., Breznay, N. P., Biffin, A., Choi, S., Johnson, R. D., Coldea, R., Watkins-Curry, P., McCandless, G. T., Chan, J. Y., Gandara, F., Islam, Z., Vishwanath, A., Shekhter, A., McDonald, R. D. & Analytis, J. G. Realization of a three-dimensional spin-anisotropic harmonic honeycomb iridate. *Nature Communications* **5,** 1–6. ISSN: 20411723. www.nature.com/naturecommunications (1 2014).

43. Biffin, A, Johnson, R. D., Choi, S., Freund, F, Manni, S, Bombardi, A, Manuel, P, Gegenwart, P & Coldea, R. Unconventional magnetic order on the hyperhoneycomb Kitaev lattice in $\beta$-Li 2 IrO 3 : Full solution via magnetic resonant x-ray diffraction. *PHYSICAL REVIEW B* **90,** 205116 (2014).

44. Williams, S. C., Johnson, R. D., Freund, F, Choi, S., Jesche, A, Kimchi, I, Manni, S, Bombardi, A, Manuel, P, Gegenwart, P & Coldea, R. Incommensurate counterrotating magnetic order stabilized by Kitaev interactions in the layered honeycomb $\alpha$-Li2IrO3. *Physical Review B* **93,** 195158. ISSN: 24699969 (19 2016).

45. Sears, J. A., Songvilay, M., Plumb, K. W., Clancy, J. P., Qiu, Y., Zhao, Y., Parshall, D. & Kim, Y. J. Magnetic order in $\alpha$ - RuCl3: A honeycomb-lattice quantum magnet with strong spin-orbit coupling. *Physical Review B - Condensed Matter and Materials Physics* **91,** 144420. ISSN: 1550235X. https://journals.aps.org/prb/abstract/10.1103/PhysRevB.91.144420 (14 2015).

46. Rau, J. G., Lee, E. K. H. & Kee, H. Y. Generic spin model for the honeycomb iridates beyond the Kitaev limit. *Physical Review Letters* **112.** ISSN: 00319007 (7 2014).

47. Kimchi, I., Coldea, R. & Vishwanath, A. Unified theory of spiral magnetism in the harmonic-honeycomb iridates $\alpha$,$\beta$, and $\gamma$ Li2IrO3. *Physical Review B - Condensed Matter and Materials Physics* **91,** 245134. ISSN: 1550235X (24 2015).

48. Liu, H. & Khaliullin, G. Pseudospin exchange interactions in d7 cobalt compounds: Possible realization of the Kitaev model. *Physical Review B* **97.** ISSN: 24699969 (1 2018).

49. Fisher, M. E., Ma, S.-k. & Nickel, B. G. Critical Exponents for Long-Range Interactions. *Phys. Rev. Lett.* **29,** 917–920. https://link.aps.org/doi/10.1103/PhysRevLett.29.917 (14 1972).

50. Scheie, A, Dasgupta, S, Sanders, M, Sakai, A, Matsumoto, Y, Prisk, T. R., Nakatsuji, S, Cava, R. J. & Broholm, C. Homogeneous reduced moment in a gapful scalar chiral kagome antiferromagnet. *Physical Review B* **100,** 24414. ISSN: 24699969 (2 2019).

51. Halloran, T., Wang, Y., Li, M., Rousochatzakis, I., Chauhan, P., Stone, M. B., Takayama, T., Takagi, H., Armitage, N. P., Perkins, N. B. & Broholm, C. Magnetic excitations and interactions in the Kitaev hyperhoneycomb iridate $\beta$ - Li 2 IrO 3. *Physical Review B* **106,** 064423. ISSN: 2469-9950. https://journals.aps.org/prb/abstract/10.1103/PhysRevB.106.064423 (6 2022).

52. Yamashita, S., Nakazawa, Y., Oguni, M., Oshima, Y., Nojiri, H., Shimizu, Y., Miyagawa, K. & Kanoda, K. Thermodynamic properties of a spin-1/2 spin-liquid state in a $\kappa$-type organic salt. *Nature Physics* **4,** 459–462. ISSN: 17452481. `www.nature.com/naturephysicshttps://www.nature.com/articles/nphys942` (6 2008).

53. Hammar, P. R., Stone, M. B., Reich, D. H., Broholm, C., Gibson, P. J., Turnbull, M. M., Landee, C. P. & Oshikawa, M. Characterization of a quasi-one-dimensional spin-1/2 magnet which is gapless and paramagnetic for $g\mu_B H \lesssim J$ and $k_B T \ll J$. *Phys. Rev. B* **59,** 1008–1015. `https://link.aps.org/doi/10.1103/PhysRevB.59.1008` (2 1999).

54. Zaliznyak, I. A. & Lee, S.-H. *Magnetic neutron scattering* in *Spin* **5** (2005).

55. Squires, G. L. *Introduction to the theory of thermal neutron scattering* (Courier Corporation, 1996).

56. Lovesey, S. W. *Theory of neutron scattering from condensed matter* ISBN: 0198520174 (Clarendon Press, 1984).

57. Squires, G. L. *Introduction to the theory of thermal neutron scattering* 1–260. ISBN: 9781139107808. `https://www.cambridge.org/core/books/introduction-to-the-theory-of-thermal-neutron-scattering/A156AD08D11B8A9968A0735C4974ED3C` (Cambridge University Press, 2012).

58. Hohenberg, P. C. & Brinkman, W. F. Sum rules for the frequency spectrum of linear magnetic chains. *Physical Review B* **10,** 128–131. ISSN: 01631829. `https://journals.aps.org/prb/abstract/10.1103/PhysRevB.10.128` (1 1974).

59. Xu, G., Xu, Z. & Tranquada, J. M. Absolute cross-section normalization of magnetic neutron scattering data. *Review of Scientific Instruments* **84.** ISSN: 00346748. `https://doi.org/10.1063/1.4818323` (8 2013).

60. Sears, V. F. Neutron scattering lengths and cross sections. *Neutron news* **3,** 26–37 (3 1992).

61. Yang, J., Samarakoon, A., Dissanayake, S., Ueda, H., Klich, I., Iida, K., Pajerowski, D., Butch, N. P., Huang, Q., Copley, J. R. & Lee, S. H. Spin jam induced by quantum fluctuations in a frustrated magnet. *Proceedings of the National Academy of Sciences of the United States of America* **112,** 11519–11523. ISSN: 10916490. `https://www.pnas.org/content/112/37/11519https://www.pnas.org/content/112/37/11519.abstract` (37 2015).

62. Lee, S. H., Broholm, C., Aeppli, G., Ramirez, A. P., Perring, T. G., Carlile, C. J., Adams, M., Jones, T. J. & Hessen, B. Spin-glass and non-spin-glass features of a geometrically frustrated magnet. *Europhysics Letters* **35,** 127–132. ISSN: 02955075. https://iopscience.iop.org/article/10.1209/epl/i1996-00543-xhttps://iopscience.iop.org/article/10.1209/epl/i1996-00543-x/meta (2 1996).

63. Bolotin, K. I., Ghahari, F., Shulman, M. D., Stormer, H. L. & Kim, P. Observation of the fractional quantum Hall effect in graphene. *Nature* **462,** 196–199 (2009).

64. Caffarel, M. & Krauth, W. Exact diagonalization approach to correlated fermions in infinite dimensions: Mott transition and superconductivity. *Phys. Rev. Lett.* **72,** 1545–1548. https://link.aps.org/doi/10.1103/PhysRevLett.72.1545 (10 1994).

65. Zhang, S., Changlani, H. J., Plumb, K. W., Tchernyshyov, O. & Moessner, R. Dynamical Structure Factor of the Three-Dimensional Quantum Spin Liquid Candidate $NaCaNi_2F_7$. *Phys. Rev. Lett.* **122,** 167203. https://link.aps.org/doi/10.1103/PhysRevLett.122.167203 (16 2019).

66. Shimokawa, T., Watanabe, K. & Kawamura, H. Static and dynamical spin correlations of the S= 1/2 random-bond antiferromagnetic Heisenberg model on the triangular and kagome lattices. *Physical Review B - Condensed Matter and Materials Physics* **92,** 134407. ISSN: 1550235X (13 2015).

67. Nguyen, L. T. & Cava, R. Hexagonal Perovskites as Quantum Materials. *Chemical Reviews* **121,** 2935–2965. https://pubs.acs.org/doi/full/10.1021/acs.chemrev.0c00622 (5 2021).

68. Dey, T., Majumder, M., Orain, J. C., Senyshyn, A., Prinz-Zwick, M., Bachus, S., Tokiwa, Y., Bert, F., Khuntia, P., Büttgen, N., Tsirlin, A. A. & Gegenwart, P. Persistent low-temperature spin dynamics in the mixed-valence iridate Ba3InIr2O9. *Physical Review B* **96,** 174411. ISSN: 24699969. https://journals.aps.org/prb/abstract/10.1103/PhysRevB.96.174411 (17 2017).

69. Dey, T., Mahajan, A. V., Kumar, R., Koteswararao, B., Chou, F. C., Omrani, A. A. & Ronnow, H. M. Possible spin-orbit driven spin-liquid ground state in the double perovskite phase of Ba3YIr2O9. *Physical Review B - Condensed Matter and Materials Physics* **88,** 134425. ISSN: 10980121. https://journals.aps.org/prb/abstract/10.1103/PhysRevB.88.134425 (13 2013).

70. Nguyen, L. T. & Cava, R. J. Trimer-based spin liquid candidate Ba4NbIr3O12. *Physical Review Materials* **3,** 014412. ISSN: 24759953 (1 2019).

71. Hassan, N., Cunningham, S., Mourigal, M., Zhilyaeva, E. I., Torunova, S. A., Lyubovskaya, R. N., Schlueter, J. A. & Drichko, N. Evidence for a quantum dipole liquid state in an organic quasi-two-dimensional material. *Science* **360,** 1101–1104. ISSN: 10959203. `https://science.sciencemag.org/content/360/6393/1101https://science.sciencemag.org/content/360/6393/1101.abstract` (6393 2018).

72. Shimizu, Y, Miyagawa, K, Kanoda, K, Maesato, M & Saito, G. Spin Liquid State in an Organic Mott Insulator with a Triangular Lattice. *Physical Review Letters* **91.** ISSN: 10797114 (10 2003).

73. Sheckelton, J. P., Neilson, J. R., Soltan, D. G. & McQueen, T. M. Possible valence-bond condensation in the frustrated cluster magnet LiZn2 Mo3 O8. *Nature Materials* **11,** 493–496. ISSN: 14764660. `www.nature.com/naturematerials` (6 2012).

74. Mourigal, M, Fuhrman, W. T., Sheckelton, J. P., Wartelle, A, Rodriguez-Rivera, J. A., Abernathy, D. L., McQueen, T. M. & Broholm, C. L. Molecular quantum magnetism in LiZn 2 Mo 3 O 8. *Physical Review Letters* **112.** ISSN: 00319007 (2 2014).

75. Sheckelton, J. P., Foronda, F. R., Pan, L., Moir, C, McDonald, R. D., Lancaster, T, Baker, P. J., Armitage, N. P., Imai, T, Blundell, S. J. & McQueen, T. M. Local magnetism and spin correlations in the geometrically frustrated cluster magnet LiZn 2 Mo3 O8. *Physical Review B - Condensed Matter and Materials Physics* **89,** 64407. ISSN: 10980121 (6 2014).

76. Kimchi, I., Nahum, A. & Senthil, T. Valence Bonds in Random Quantum Magnets: Theory and Application to YbMgGaO 4. *Physical Review X* **8** (2018).

77. Nguyen, L. T., Halloran, T., Xie, W., Kong, T., Broholm, C. L. & Cava, R. J. Geometrically frustrated trimer-based Mott insulator. *Physical Review Materials* **2,** 054414. ISSN: 24759953 (5 2018).

78. Komleva, E. V., Khomskii, D. I. & Streltsov, S. V. Three-site transition-metal clusters: Going from localized electrons to molecular orbitals. *Physical Review B* **102.** ISSN: 24699969 (17 2020).

79. Nguyen, L. T., Kong, T. & Cava, R. J. Trimers of MnO 6 octahedra and ferrimagnetism of Ba4NbMn3O12. *Materials Research Express* **6.** ISSN: 20531591. `https://doi.org/10.1088/2053-1591/ab0695` (5 2019).

80. Streltsov, S. V. & Khomskii, D. I. Cluster Magnetism of Ba 4 NbMn 3 O 12 : Localized Electrons or Molecular Orbitals? *JETP Letters* **108,** 686–690. ISSN: 10906487. https://link.springer.com/article/10.1134/S0021364018220071 (10 2018).

81. Scheie, A, Dasgupta, S, Sanders, M, Sakai, A, Matsumoto, Y, Prisk, T. R., Nakatsuji, S, Cava, R. J. & Broholm, C. Homogeneous reduced moment in a gapful scalar chiral kagome antiferromagnet. *Physical Review B* **100,** 24414. ISSN: 24699969 (2019).

82. Blanc, N., Trinh, J., Dong, L., Bai, X., Aczel, A. A., Mourigal, M., Balents, L., Siegrist, T. & Ramirez, A. P. Quantum criticality among entangled spin chains. *Nature Physics* **14,** 273–276. ISSN: 17452481. https://doi.org/10.1038/s41567-017-0010-y (3 2018).

83. Zhao, L., Lan, T. W., Wang, K. J., Chien, C. H., Hung, T. L., Luo, J. Y., Chao, W. H., Chang, C. C., Chen, Y. Y., Wu, M. K. & Martin, C. Multiferroicity in geometrically frustrated $\alpha$-MCr 2O 4 systems (M=Ca, Sr, Ba). *Physical Review B - Condensed Matter and Materials Physics* **86,** 064408. ISSN: 10980121. https://journals.aps.org/prb/abstract/10.1103/PhysRevB.86.064408 (6 2012).

84. Ramirez, A. P. Strongly Geometrically Frustrated Magnets. *Annual Review of Materials Science* **24,** 453–480. ISSN: 0084-6600. https://www.annualreviews.org/doi/10.1146/annurev.ms.24.080194.002321 (1 1994).

85. Rodriguez, J. A., Adler, D. M., Brand, P. C., Broholm, C, Cook, J. C., Brocker, C, Hammond, R, Huang, Z, Hundertmark, P, Lynn, J. W., Maliszewskyj, N. C., Moyer, J, Orndorff, J, Pierce, D, Pike, T. D., Scharfstein, G, Smee, S. A. & Vilaseca, R. MACS—a new high intensity cold neutron spectrometer at NIST. *Meas. Sci. Technol* **19,** 34023–34030 (2008).

86. Granroth, G. E., Kolesnikov, A. I., Sherline, T. E., Clancy, J. P., Ross, K. A., Ruff, J. P., Gaulin, B. D. & Nagler, S. E. *SEQUOIA: A newly operating chopper spectrometer at the SNS* in. **251** (Institute of Physics Publishing, 2010), 012058. https://iopscience.iop.org/article/10.1088/1742-6596/251/1/012058https://iopscience.iop.org/article/10.1088/1742-6596/251/1/012058/meta.

87. Cheng, Y. Q., Daemen, L. L., Kolesnikov, A. I. & Ramirez-Cuesta, A. J. Simulation of Inelastic Neutron Scattering Spectra Using OCLIMAX. *Journal of Chemical Theory and Computation* **15,** 1974–1982. ISSN: 15499626 (3 2019).

88. Kresse, G. & Furthmüller, J. Efficient iterative schemes for ab initio total-energy calculations using a plane-wave basis set. *Physical Review B - Condensed Matter and Materials Physics* **54,** 11169–11186. ISSN: 1550235X. https://journals.aps.org/prb/abstract/10.1103/PhysRevB.54.11169 (16 1996).

89. Togo, A. & Tanaka, I. First principles phonon calculations in materials science. *Scripta Materialia* **108,** 1–5. ISSN: 13596462 (2015).

90. Hong, T., Kenzelmann, M., Turnbull, M. M., Landee, C. P., Lewis, B. D., Schmidt, K. P., Uhrig, G. S., Qiu, Y., Broholm, C. & Reich, D. Neutron scattering from a coordination polymer quantum paramagnet. *Physical Review B - Condensed Matter and Materials Physics* **74,** 094434. ISSN: 10980121. https://journals.aps.org/prb/abstract/10.1103/PhysRevB.74.094434 (9 2006).

91. Do, S. H., Park, S. Y., Yoshitake, J., Nasu, J., Motome, Y., Kwon, Y. S., Adroja, D. T., Voneshen, D. J., Kim, K., Jang, T. H., Park, J. H., Choi, K. Y. & Ji, S. Majorana fermions in the Kitaev quantum spin system $\alpha$-RuCl 3. *Nature Physics* **13,** 1079–1084. ISSN: 17452481. www.nature.com/naturephysics (11 2017).

92. Capriotti, L., Trumper, A. E. & Sorella, S. Long-range néel order in the triangular heisenberg model. *Physical Review Letters* **82,** 3899–3902. ISSN: 10797114 (1999).

93. White, S. R. & Chernyshev, A. L. Neél order in square and triangular lattice heisenberg models. *Physical Review Letters* **99.** ISSN: 00319007 (2007).

94. Chaloupka, J., Jackeli, G. & Khaliullin, G. Kitaev-heisenberg model on a honeycomb lattice: Possible exotic phases in iridium oxides A2IrO3. *Physical Review Letters* **105.** ISSN: 10797114 (2 2010).

95. Chaloupka, J., Jackeli, G. & Khaliullin, G. Zigzag magnetic order in the iridium oxide Na2IrO3. *Physical Review Letters* **110,** 097204. ISSN: 00319007. https://journals.aps.org/prl/abstract/10.1103/PhysRevLett.110.097204 (9 2013).

96. Li, Y., Winter, S. M. & Valentí, R. Role of Hydrogen in the Spin-Orbital-Entangled Quantum Liquid Candidate H3LiIr2 O6. *Physical Review Letters* **121.** ISSN: 10797114 (24 2018).

97. Katukuri, V. M., Nishimoto, S., Yushankhai, V., Stoyanova, A., Kandpal, H., Choi, S., Coldea, R., Rousochatzakis, I., Hozoi, L. & Brink, J. V. D. Kitaev interactions between j = 1/2 moments in honeycomb Na 2IrO3 are large and ferromagnetic: Insights from ab initio quantum chemistry calculations. *New Journal of Physics* **16,** 13056. ISSN: 13672630. https://iopscience.iop.org/article/10.1088/1367-2630/16/1/013056https://iopscience.iop.org/article/10.1088/1367-2630/16/1/013056/meta (1 2014).

98. Majumder, M, Freund, F, Dey, T, Prinz-Zwick, M, Büttgen, N, Skourski, Y, Jesche, A, Tsirlin, A. A. & Gegenwart, P. Anisotropic temperature-field phase diagram of single crystalline $\beta$-Li2IrO3: Magnetization, specific heat, and Li 7 NMR study. *Physical Review Materials* **3.** ISSN: 24759953 (7 2019).

99. Kitagawa, K, Takayama, T, Matsumoto, Y., Kato, A., Takano, R., Kishimoto, Y., Bette, S, Dinnebier, R., Jackeli, G & Takagi, H. A spin-orbital-entangled quantum liquid on a honeycomb lattice. *Nature* **554,** 341–345. ISSN: 14764687 (7692 2018).

100. Mandal, S. & Surendran, N. Exactly solvable Kitaev model in three dimensions. *Physical Review B - Condensed Matter and Materials Physics* **79.** ISSN: 10980121 (2 2009).

101. Momma, K. & Izumi, F. VESTA3 for three-dimensional visualization of crystal, volumetric and morphology data. *Journal of Applied Crystallography* **44,** 1272–1276. https://doi.org/10.1107/S0021889811038970 (6 2011).

102. Ruiz, A., Frano, A., Breznay, N. P., Kimchi, I., Helm, T., Oswald, I., Chan, J. Y., Birgeneau, R. J., Islam, Z. & Analytis, J. G. Correlated states in $\beta$-Li2IrO3 driven by applied magnetic fields. *Nature Communications* **8,** 1–6. ISSN: 20411723. www.nature.com/naturecommunications (1 2017).

103. Li, Y., Winter, S. M., Kaib, D. A., Riedl, K. & Valentí, R. Modified Curie-Weiss law for jeff magnets. *Physical Review B* **103,** L220408. ISSN: 24699969. https://journals.aps.org/prb/abstract/10.1103/PhysRevB.103.L220408 (22 2021).

104. Kim, H. S., Lee, E. K. H. & Kim, Y. B. Predominance of the Kitaev interaction in a three-dimensional honeycomb iridate: From ab initio to spin model. *EPL* **112.** ISSN: 12864854. www.epljournal.org (6 2015).

105. Ducatman, S., Rousochatzakis, I. & Perkins, N. B. Magnetic structure and excitation spectrum of the hyperhoneycomb Kitaev magnet $\beta$-Li2IrO3. *Physical Review B* **97,** 125125. ISSN: 24699969 (12 2018).

106. Granroth, G. E., Kolesnikov, A. I., Sherline, T. E., Clancy, J. P., Ross, K. A., Ruff, J. P., Gaulin, B. D. & Nagler, S. E. SEQUOIA: A newly operating chopper spectrometer at the SNS. *Journal of Physics: Conference Series* **251.** ISSN: 17426596 (2010).

107. Arnold, O., Bilheux, J. C., Borreguero, J. M., Buts, A., Campbell, S. I., Chapon, L., Doucet, M., Draper, N., Ferraz Leal, R., Gigg, M. A., Lynch, V. E., Markvardsen, A., Mikkelson, D. J., Mikkelson, R. L., Miller, R., Palmen, K., Parker, P., Passos, G., Perring, T. G., Peterson, P. F., Ren, S., Reuter, M. A., Savici, A. T., Taylor, J. W., Taylor, R. J., Tolchenov, R., Zhou, W. & Zikovsky, J. Mantid - Data analysis and visualization package for neutron scattering and $\mu$ SR experiments. *Nuclear Instruments and Methods in Physics Research, Section A: Accelerators, Spectrometers, Detectors and Associated Equipment* **764,** 156–166. ISSN: 01689002 (2014).

108. Seabold, S. & Perktold, J. *statsmodels:Econometric and statistical modeling with python* 2010.

109. Smith, A, Knolle, J, Kovrizhin, D. L., Chalker, J. T. & Moessner, R. Neutron scattering signatures of the 3D hyperhoneycomb Kitaev quantum spin liquid. *RAPID COMMUNICATIONS PHYSICAL REVIEW B* **92,** 180408 (2015).

110. Laurita, N. J. *Low Energy Electrodynamics of Quantum Magnets* PhD thesis (Johns Hopkins University, 2017), 78–81.

111. Er, N. B., Cqrak, W. S., Garfunkel, M. P., Bsattkrthwaite, C & WExLER, A. *PHYSICAL REVIEW Atomic Heats of Copper, Silver, and Gold from 1'K to 5'K** tech. rep. ().

112. Meads, P. F., Forsythe, W. R., Giauque, W. F. & 63, V. *The Heat Capacities and Entropies of Silver and Lead from 15° to 300°K* tech. rep. (). `https://pubs.acs.org/sharingguidelines`.

113. Bldg mi, I. *Library, OCT 2 6 t of Standards Specific Heats and Entiialpies of J Technical Solids at Low Temperatures A Compilation From the Literature* tech. rep. ().

114. Toth, S. & Lake, B. Linear spin wave theory for single-Q incommensurate magnetic structures. *Journal of Physics Condensed Matter* **27,** 166002. ISSN: 1361648X. https://iopscience.iop.org/article/10.1088/0953-8984/27/16/166002https://iopscience.iop.org/article/10.1088/0953-8984/27/16/166002/meta (16 2015).

115. Lee, E. K. H., Rau, J. G. & Kim, Y. B. Two iridates, two models, and two approaches: A comparative study on magnetism in three-dimensional honeycomb materials. *Physical Review B* **93,** 184420. ISSN: 24699969 (18 2016).

116. Li, M., Rousochatzakis, I. & Perkins, N. B. Unconventional magnetic field response of the hyperhoneycomb Kitaev magnet $\beta$-Li2IrO3. *Physical Review Research* **2,** 013065. ISSN: 26431564. https://journals.aps.org/prresearch/abstract/10.1103/PhysRevResearch.2.013065 (1 2020).

117. Lee, E. K. H. & Kim, Y. B. Theory of magnetic phase diagrams in hyperhoneycomb and harmonic-honeycomb iridates. *Physical Review B* **91,** 64407. ISSN: 1550235X (6 2015).

118. Rousochatzakis, I. & Perkins, N. B. Magnetic field induced evolution of intertwined orders in the Kitaev magnet $\beta$-Li2IrO3. *Physical Review B* **97,** 174423. ISSN: 24699969 (17 2018).

119. Ruiz, A., Breznay, N. P., Li, M., Rousochatzakis, I., Allen, A., Zinda, I., Nagarajan, V., Lopez, G., Islam, Z., Upton, M. H., Kim, J., Said, A. H., Huang, X. R., Gog, T., Casa, D., Birgeneau, R. J., Koralek, J. D., Analytis, J. G., Perkins, N. B. & Frano, A. Magnon-spinon dichotomy in the Kitaev hyperhoneycomb $\beta$-Li2IrO3. *Physical Review B* **103,** 184404. ISSN: 24699969. https://journals.aps.org/prb/abstract/10.1103/PhysRevB.103.184404 (18 2021).

120. Yang, Y., Wang, Y., Rousochatzakis, I., Ruiz, A., Analytis, J. G., Burch, K. S. & Perkins, N. B. Signatures of non-Loudon-Fleury Raman scattering in the Kitaev magnet $\beta$-$Li_2IrO_3$. http://arxiv.org/abs/2202.00581 (2022).

121. Oshikawa, M., Turnbull, M. M. & Landee, C. P. Characterization of a quasi-one-dimensional spin-1/2 magnet which is gapless and paramagnetic for (formula presented) and (formula presented). *Physical Review B - Condensed Matter and Materials Physics* **59,** 1008–1015. ISSN: 1550235X. https://journals.aps.org/prb/abstract/10.1103/PhysRevB.59.1008 (1999).

122. Yamashita, S., Nakazawa, Y., Oguni, M., Oshima, Y., Nojiri, H., Shimizu, Y., Miyagawa, K. & Kanoda, K. Thermodynamic properties of a spin-1/2 spin-liquid state in a $\kappa$-type organic salt. *Nature Physics* **4,** 459–462. ISSN: 17452481. www.nature.com/naturephysicshttps://www.nature.com/articles/nphys942 (2008).

123. Bourgeois-Hope, P., Laliberté, F., Lefrançois, E., Grissonnanche, G., De Cotret, S. R., Gordon, R., Kitou, S., Sawa, H., Cui, H., Kato, R., Taillefer, L. & Doiron-Leyraud, N. Thermal Conductivity of the Quantum Spin Liquid Candidate EtMe3Sb [Pd (dmit)2] 2: No Evidence of Mobile Gapless Excitations. *Physical Review X* **91.** ISSN: 21603308 (2019).

124. Stavropoulos, P. P., Catuneanu, A. & Kee, H. Y. Counter-rotating spiral order in three-dimensional iridates: Signature of hidden symmetry in the Kitaev- Γ model. *Physical Review B* **98.** ISSN: 24699969 (2018).

125. Katukuri, V. M., Yadav, R., Hozoi, L., Nishimoto, S. & van den Brink, J. The vicinity of hyper-honeycomb $\beta$-Li2IrO3 to a three-dimensional Kitaev spin liquid state. *Sci. Rep.* **6,** 29585. http://dx.doi.org/10.1038/srep29585 (2016).

126. Li, M., Rousochatzakis, I. & Perkins, N. B. Reentrant incommensurate order and anomalous magnetic torque in the Kitaev magnet $\beta-\mathrm{Li_2IrO_3}$. *Phys. Rev. Research* **2,** 033328. https://link.aps.org/doi/10.1103/PhysRevResearch.2.033328 (3 2020).

127. Aoki, D., Nakamura, A., Honda, F., Li, D. X., Homma, Y., Shimizu, Y., Sato, Y. J., Knebel, G., Brison, J. P., Pourret, A., Braithwaite, D., Lapertot, G., Niu, Q., Vališka, M., Harima, H. & Flouquet, J. Unconventional superconductivity in heavy fermion Ute2. *Journal of the Physical Society of Japan* **88,** 43702. ISSN: 13474073. https://doi.org/10.7566/JPSJ.88.043702 (2019).

128. Chen, G., Ohara, S., Hedo, M., Uwatoko, Y., Saito, K., Sorai, M. & Sakamoto, I. Observation of Superconductivity in Heavy-Fermion Compounds of Ce 2CoIn8. *Journal of the Physical Society of Japan* **71,** 2836–2838. ISSN: 00319015 (2002).

129. Brüning, E. M., Krellner, C, Baenitz, M, Jesche, A, Steglich, F & Geibel, C. CeFePO: A Heavy Fermion Metal with Ferromagnetic Correlations (2008).

130. Majumder, M., Prinz-Zwick, M., Reschke, S., Zubtsovskii, A., Dey, T., Freund, F., Büttgen, N., Jesche, A., Kézsmárki, I., Tsirlin, A. A. & Gegenwart, P. Field evolution of low-energy excitations in the hyperhoneycomb magnet $\beta - \mathrm{Li_2IrO_3}$. *Phys. Rev. B* **101,** 214417. https://link.aps.org/doi/10.1103/PhysRevB.101.214417 (21 2020).

131. Bette, S., Takayama, T., Kitagawa, K., Takano, R., Takagi, H. & Dinnebier, R. E. Solution of the heavily stacking faulted crystal structure of the honeycomb iridate H3LiIr2O6. *Dalton Transactions* **46,** 15216–15227. ISSN: 14779234 (44 2017).

132. Bhatt, R. N. & Lee, P. A. Scaling studies of highly disordered spin-1/2 Antiferromagnetic Systems. *Physical Review Letters* **48,** 344–347. ISSN: 00319007. https://journals.aps.org/prl/abstract/10.1103/PhysRevLett.48.344 (5 1982).

133. Geirhos, K, Lunkenheimer, P, Blankenhorn, M, Claus, R, Matsumoto, Y, Kitagawa, K, Takayama, T, Takagi, H, Kézsmárki, I & Loidl, A. Quantum paraelectricity in the Kitaev quantum spin liquid candidates H3LiI r2 O6 and D3LiI r2 O6. *Physical Review B* **101,** 184410. ISSN: 24699969 (18 2020).

134. Lee, C., Lee, S., Choi, Y., Wang, C., Luetkens, H., Shiroka, T., Jang, Z., Yoon, Y. G. & Choi, K. Y. Coexistence of random singlets and disordered Kitaev spin liquid in H3LiIr2 O6. *Physical Review B* **107,** 014424. ISSN: 24699969. https://journals.aps.org/prb/abstract/10.1103/PhysRevB.107.014424 (1 2023).

135. De la Torre, A., Zager, B., Bahrami, F., Upton, M. H., Kim, J., Fabbris, G., Lee, G. H., Yang, W., Haskel, D., Tafti, F. & Plumb, K. W. Momentum-independent magnetic excitation continuum in the honeycomb iridate $\mathrm{H_3LiIr_2O_6}$. http://arxiv.org/abs/2302.07907 (2023).

136. Stone, M. B., Niedziela, J. L., Abernathy, D. L., Debeer-Schmitt, L., Ehlers, G., Garlea, O., Granroth, G. E., Graves-Brook, M., Kolesnikov, A. I., Podlesnyak, A. & Winn, B. A comparison of four direct geometry time-of-flight spectrometers at the Spallation Neutron Source. *Review of Scientific Instruments* **85,** 045113. ISSN: 10897623. http://aip.scitation.org/doi/10.1063/1.4870050 (2014).

137. *The XYZ-difference method with polarized neutrons and the separation of coherent, spin incoherent, and magnetic scattering cross sections in a multidetector*

138. Schneider, M., Schanzer, C., Böni, P., Filges, U., Fujita, M., Nambu, Y., Ohkawara, M., Yokoo, T. & Itoh, S. POLANO: Wide angle spin analysis using polarizing supermirrors m = 5.5. *Nuclear Instruments and Methods in Physics Research Section A: Accelerators, Spectrometers, Detectors and Associated Equipment* **976,** 164272. ISSN: 0168-9002 (2020).

139. Revelli, A., Sala, M. M., Monaco, G., Hickey, C., Becker, P., Freund, F., Jesche, A., Gegenwart, P., Eschmann, T., Buessen, F. L., Trebst, S., Loosdrecht, P. H. V., Brink, J. V. D. & Grüninger, M. Fingerprints of Kitaev physics in the magnetic excitations of honeycomb iridates. *Physical Review Research* **2,** 43094. ISSN: 26431564. `https://journals.aps.org/prresearch/abstract/10.1103/PhysRevResearch.2.043094` (4 2020).

140. Kasahara, Y., Suetsugu, S., Asaba, T., Kasahara, S., Shibauchi, T., Kurita, N., Tanaka, H. & Matsuda, Y. Quantized and unquantized thermal Hall conductance of the Kitaev spin liquid candidate $\alpha$-RuCl3. *Physical Review B* **106,** L060410. ISSN: 24699969. `https://journals.aps.org/prb/abstract/10.1103/PhysRevB.106.L060410` (6 2022).

141. Johnson, R. D., Williams, S. C., Haghighirad, A. A., Singleton, J., Zapf, V., Manuel, P., Mazin, I. I., Li, Y., Jeschke, H. O., Valentí, R. & Coldea, R. Monoclinic crystal structure of $\alpha$-RuCl3 and the zigzag antiferromagnetic ground state. *Physical Review B - Condensed Matter and Materials Physics* **92,** 235119. ISSN: 1550235X. `https://journals.aps.org/prb/abstract/10.1103/PhysRevB.92.235119` (23 2015).

142. Baek, S. H., Do, S. H., Choi, K. Y., Kwon, Y. S., Wolter, A. U., Nishimoto, S., Brink, J. V. D. & Böchner, B. Evidence for a field-induced quantum spin liquid in $\alpha$-RuCl3. *Physical Review Letters* **119.** ISSN: 10797114 (3 2017).

143. Banerjee, A., Yan, J., Knolle, J., Bridges, C. A., Stone, M. B., Lumsden, M. D., Mandrus, D. G., Tennant, D. A., Moessner, R. & Nagler, S. E. Neutron scattering in the proximate quantum spin liquid $\alpha$-RuCl3. *Science* **356,** 1055–1059. ISSN: 10959203. `http://science.sciencemag.org/` (6342 2017).

144. Bruin, J. A., Claus, R. R., Matsumoto, Y., Kurita, N., Tanaka, H. & Takagi, H. Robustness of the thermal Hall effect close to half-quantization in $\alpha$-RuCl3. *Nature Physics* **18,** 401–405. ISSN: 17452481. `https://doi.org/10.1038/s41567-021-01501-y` (4 2022).

145. Yokoi, T., Ma, S., Kasahara, Y., Kasahara, S., Shibauchi, T., Kurita, N., Tanaka, H., Nasu, J., Motome, Y., Hickey, C., Trebst, S. & Matsuda, Y. Half-integer quantized anomalous thermal Hall effect in the Kitaev material candidate a-RuCl3. *Science* **373,** 568–572. ISSN: 10959203. https://www.science.org/doi/10.1126/science.aay5551 (6554 2021).

146. Maksimov, P. A. & Chernyshev, A. L. Rethinking $\alpha\{-\}\{\mathrm{RuCl}\}_3$. *Physical Review Research* **2,** 33011 (2020).

147. Sano, R., Kato, Y. & Motome, Y. Kitaev-Heisenberg Hamiltonian for high-spin d7 Mott insulators. *Physical Review B* **97,** 014408. ISSN: 24699969. https://journals.aps.org/prb/abstract/10.1103/PhysRevB.97.014408 (1 2018).

148. Songvilay, M., Robert, J., Petit, S., Rodriguez-Rivera, J. A., Ratcliff, W. D., Damay, F., Balédent, V., Jiménez-Ruiz, M., Lejay, P., Pachoud, E., Hadj-Azzem, A., Simonet, V. & Stock, C. Kitaev interactions in the Co honeycomb antiferromagnets Na3Co2SbO6 and Na2Co2TeO6. *Physical Review B* **102,** 224429. ISSN: 24699969. https://journals.aps.org/prb/abstract/10.1103/PhysRevB.102.224429 (22 2020).

149. Vivanco, H. K., Trump, B. A., Brown, C. M. & McQueen, T. M. Competing antiferromagnetic-ferromagnetic states in a d7 Kitaev honeycomb magnet. *Physical Review B* **102,** 224411. ISSN: 24699969. https://journals.aps.org/prb/abstract/10.1103/PhysRevB.102.224411 (22 2020).

150. Dordević, T. BaCo2(AsO4)2. *Acta Crystallographica Section E: Structure Reports Online* **64,** i58. ISSN: 16005368. /pmc/articles/PMC2960660//pmc/articles/PMC2960660/?report=abstracthttps://www.ncbi.nlm.nih.gov/pmc/articles/PMC2960660/ (9 2008).

151. Regnault, L. P., Burlet, P. & Rossat-Mignod, J. Magnetic ordering in a planar X - Y model: BaCo2(AsO4)2. *Physica B+C* **86-88,** 660–662. ISSN: 03784363 (PART 2 1977).

152. Regnault, L. P., Rossat-Mignod, J. & Henry, J. Magnetic Properties of the Quadi-2D Easy Plane Magnets BaM2(XO4)2 (M=Co, Ni; X=P, As). *Journal of the Physical Society of Japan* **52,** 1–9 (1983).

153. Regnault, L. P., Boullier, C. & Lorenzo, J. E. Polarized-neutron investigation of magnetic ordering and spin dynamics in BaCo2(AsO4)2 frustrated honeycomb-lattice magnet. *Heliyon* **4.** ISSN: 24058440. https://pubmed.ncbi.nlm.nih.gov/29560426/ (1 2018).

154. Zhong, R., Gao, T., Ong, N. P. & Cava, R. J. Weak-field induced nonmagnetic state in a Co-based honeycomb. *Science Advances* **6.** ISSN: 23752548. https://www.science.org (4 2020).

155. Das, S., Voleti, S., Saha-Dasgupta, T. & Paramekanti, A. XY magnetism, Kitaev exchange, and long-range frustration in the Jeff= 12 honeycomb cobaltates. *Physical Review B* **104,** 134425. ISSN: 24699969. https://journals.aps.org/prb/abstract/10.1103/PhysRevB.104.134425 (13 2021).

156. Nair, H. S., Brown, J. M., Coldren, E, Hester, G, Gelfand, M. P., Podlesnyak, A, Huang, Q & Ross, K. A. Short-range order in the quantum XXZ honeycomb lattice material BaCo2(PO4)2. *Physical Review B* **97,** 134409. ISSN: 24699969 (13 2018).

157. Stock, C., Jonas, S., Broholm, C., Nakatsuji, S., Nambu, Y., Onuma, K., Maeno, Y. & Chung, J. H. Neutron-scattering measurement of incommensurate short-range order in single crystals of the S=1 triangular antiferromagnet NiGa2S 4. *Physical Review Letters* **105,** 037402. ISSN: 00319007. https://journals.aps.org/prl/abstract/10.1103/PhysRevLett.105.037402 (3 2010).

158. Zhang, X., Xu, Y., Halloran, T., Zhong, R., Broholm, C., Cava, R. J., Drichko, N. & Armitage, N. P. A magnetic continuum in the cobalt-based honeycomb magnet BaCo2(AsO4)2. *Nature Materials* **22,** 58–63. ISSN: 14764660. https://doi.org/10.1038/s41563-022-01403-1 (1 2023).

159. Shi, L. Y., Wang, X. M., Zhong, R. D., Wang, Z. X., Hu, T. C., Zhang, S. J., Liu, Q. M., Dong, T., Wang, F. & Wang, N. L. Magnetic excitations of the field-induced states in probed by time-domain terahertz spectroscopy. *Physical Review B* **104,** 144408. ISSN: 24699969. https://journals.aps.org/prb/abstract/10.1103/PhysRevB.104.144408 (14 2021).

160. Stone, M., Zaliznyak, I., Hong, T, Broholm, C. & Reich, D. Quasiparticle breakdown in a quantum spin liquid. *Nature* **440,** 187–190. ISSN: 0028-0836 (2006).

161. Luttinger, J. & Tisza, L. Theory of dipole interaction in crystals. *Physical Review* **70,** 954 (1946).

162. Litvin, D. B. The luttinger-tisza method. *Physica* **77,** 205–219 (1974).

163. Fouet, J. B., Sindzingre, P. & Lhuillier, C. An investigation of the quantum $J_1$-$J_2$-$J_3$ model on the honeycomb lattice. *European Physical Journal B* **20,** 241–254. ISSN: 14346028. `https://link.springer.com/article/10.1007/s100510170273` (2001).

164. Halloran, T., Desrochers, F., Zhang, E. Z., Chen, T., Chern, L. E., Xu, Z., Winn, B., Graves-Brook, M., Stone, M. B., Kolesnikov, A. I., Qiu, Y., Zhong, R., Cava, R., Kim, Y. B. & Broholm, C. Geometrical frustration versus Kitaev interactions in BaCo2(AsO4)2. *Proceedings of the National Academy of Sciences of the United States of America* **120,** e2215509119. ISSN: 10916490. `http://www.pnas.org/lookup/suppl/doi:10.1073/pnas.2215509119/-/DCSupplemental.` (2 2023).

165. Gordon, J. S. & Kee, H.-Y. Testing topological phase transitions in Kitaev materials under in-plane magnetic fields: Application to $\alpha$- RuCl 3. *Physical Review Research* **3,** 013179 (2021).

166. Janssen, L. & Vojta, M. Heisenberg-Kitaev physics in magnetic fields. *Journal of Physics: Condensed Matter* **31,** 423002 (2019).

167. Bachus, S., Kaib, D. A., Jesche, A., Tsurkan, V., Loidl, A., Winter, S. M., Tsirlin, A. A., Valentí, R. & Gegenwart, P. Angle-dependent thermodynamics of $\alpha$-RuCl$_3$. *Physical Review B* **103,** 054440. ISSN: 24699969. `https://journals.aps.org/prb/abstract/10.1103/PhysRevB.103.054440` (2021).

168. Tanaka, O., Mizukami, Y., Harasawa, R., Hashimoto, K., Hwang, K., Kurita, N., Tanaka, H., Fujimoto, S., Matsuda, Y., Moon, E. G. & Shibauchi, T. Thermodynamic evidence for a field-angle-dependent Majorana gap in a Kitaev spin liquid. *Nature Physics* **18,** 429–435. ISSN: 17452481. `https://doi.org/10.1038/s41567-021-01488-6` (2022).

169. Merino, J. & Ralko, A. Role of quantum fluctuations on spin liquids and ordered phases in the Heisenberg model on the honeycomb lattice. *Physical Review B* **97,** 205112 (2018).

170. Zhu, Z. & White, S. R. Quantum phases of the frustrated XY models on the honeycomb lattice. *Modern Physics Letters B* **28,** 1430016 (2014).

171. Bishop, R., Li, P., Farnell, D. J. & Campbell, C. The frustrated Heisenberg antiferromagnet on the honeycomb lattice: J1–J2 model. *Journal of Physics: Condensed Matter* **24,** 236002 (2012).

172. Gordon, J. S., Catuneanu, A., Sørensen, E. S. & Kee, H. Y. Theory of the field-revealed Kitaev spin liquid. *Nature Communications* **10,** 1–8. ISSN: 20411723. `https://doi.org/10.1038/s41467-019-10405-8` (1 2019).

173. Ferrenti, A. M., Siegler, M. A., Ghosh, S., Vivanco, H. K., Kintop, N., Lygouras, C., Halloran, T., Klemenz, S., Broholm, C., Drichko, N. & Mcqueen, T. M. Chemical tuning of a honeycomb magnet through a critical point. *arXiv:2210.14439.* `http://arxiv.org/abs/2302.07907` (2022).

174. Chu, C. W., Deng, L. Z. & Lv, B. Hole-doped cuprate high temperature superconductors. *Physica C: Superconductivity and its Applications* **514,** 290–313. ISSN: 09214534 (2015).

# Chapter 7

# Appendix

## 7.1 Calculated scattering $J, K, \Gamma$ dependence for $\beta$-$Li_2IrO_3$

The fits to the measured INS data were performed by the systematic calculation of neutron scattering spectra for many sets of exchange parameters. Spectra were first calculated globally in the region of $J - K - \Gamma$ parameter space that stabilizes the incommensurate magnetic order [1]. Then the calculations were refined for the smaller range of parameters that best reproduce the observed spectra.

The pattern of scattering varies differently with each of the exchange parameters, as illustrated in Fig. 7.1. $J$ has very little effect on the spectra. The value of $\Gamma$ has the greatest impact on the excitation spectra, controlling the overall energy scale of the spin-waves. The influence of $K$ is more subtle. It impacts the energies and intensities of select bands at energies higher than $\Gamma$. This is seen in the second row of spectra in Fig. 7.1. Thus, inelastic magnetic neutron scattering scattering from a powder sample of $^7$Li and $^{193}$Ir can be

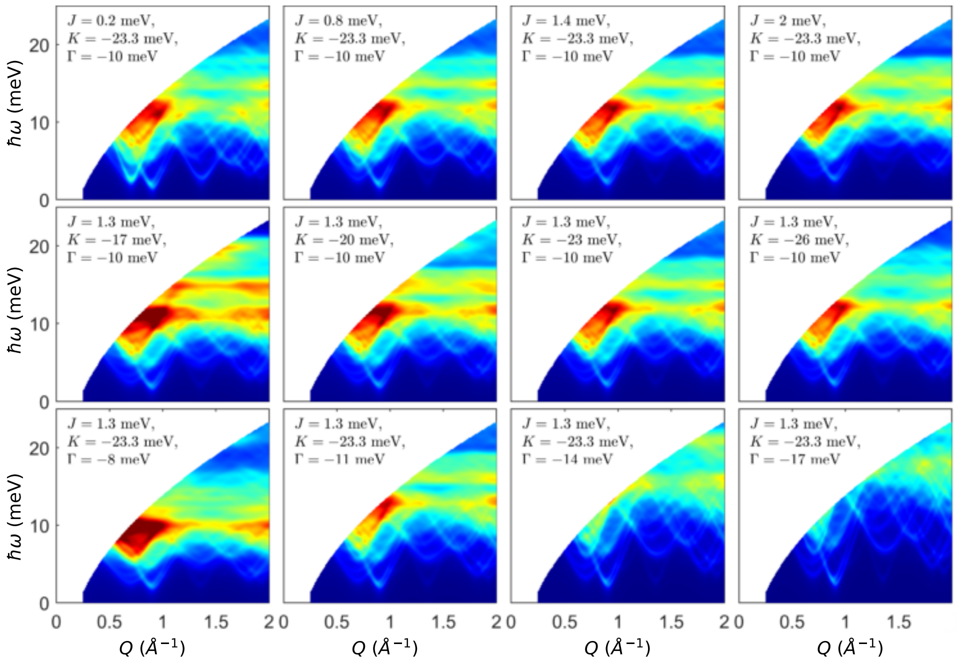

**Figure 7.1:** Calculated powder averaged INS intensities for $E_i = 30$ meV with variations in $J$, $K$, and $\Gamma$. The magnetic form factor of Ir$^{4+}$ is not considered in the calculation, and a constant broadening in energy of width 1 meV is used to approximate instrumental resolution effects. While $\Gamma$ and $K$ are well constrained by this method, $J$ has little influence on the scattering data that is accessible for $E_i = 30$ meV. The intensity scale is arbitrary but consistent across the calculations.

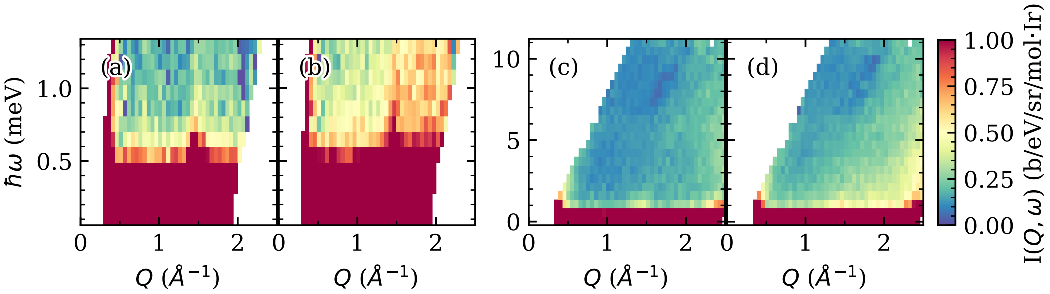

**Figure 7.2:** Normalized scattering intensity from the MACS instrument for the four main experimental configurations. $E_f$=3.7 meV $T$=1.72(1) K is shown in (a), $E_f$=3.7 meV $T$=55.0(1) K is shown in (b), $E_f$=5.0 meV $T$=1.72(1) K is shown in (c), and $E_f$=5.0 meV $T$=55.0(1) K is shown in (d). Scattering has been corrected for absorption and a background measurement has been subtracted.

used to extract values for $K$ and $\Gamma$ but not $J$.

## 7.2 Isolation of $D_3LiIr_2O_6$ magnetic scattering from MACS measurement

Scattering from the 2 g sample in an aluminum sachet was normalized to nuclear Bragg scattering as described in Sec. 2.2.4. As this sample geometry was not as well optimized as the annular can used later, multiple scattering is a significant problem despite the halved sample mass. After normalization to Bragg peaks and subtraction by a sample out measurement with an appropriate self-shielding factor, absorption was corrected by a Monte-Carlo method implemented in the DAVE software suite [2]. The resulting scattering for all instrumental configurations is shown in Fig. 7.2. One immediate observation in the $E_f$=3.7 meV measurements is what looks like the (001) Bragg peak extending far into the inelastic channel. While at first glance this seems to be associated with the instrumental resolution, the energy resolution FWHM of the MACS instrument in this configuration on the order of $\Delta\hbar\omega$ =0.1 meV. Instead, the origin of the spurious scattering may be summarized as the elastic line leaking into the inelastic channel. This has been seen before both on MACS and other triple-axis spectrometers and originates from allowed inelastic phonon scattering processes from the monochromator. For the inelastic channel, we consider both of the following processes to be equally likely:

- Bragg (002) reflection from graphite monochromator (strong process), followed by inelastic magnetic scattering at the sample (weak process).
- Acoustic phonon scattering originating from the (002) Bragg position at the graphite monochromator (weak process), followed by elastic scattering at the sample position (strong process).

Because elastic cross sections are in general an order of magnitude higher than inelastic, we assign these to be strong and inelastic scattering such as phonon or magnetic scattering to be weak. Before discussing the precise mechanism of this effect, we may describe the scattering using the following functional form:

$$I(Q,\omega) = A(\omega)I_{el}(Q) + B(\omega)I_{mag}(Q) + I_{ph}(Q,\omega). \tag{7.1}$$

The lineshape $I_{el}(Q)$ is the elastic lineshape that persists to finite energy transfers, $I_{mag}(Q)$ is $Q$-dependent form of the magnetic scattering, $B(\omega)$ describes the spectral weight of the magnetic scattering at each energy transfer, and $I_{ph}(Q,\omega)$ is the dominant contribution to the background which is phonon scattering. Performing the same Bose-Einstein subtraction of phonons as

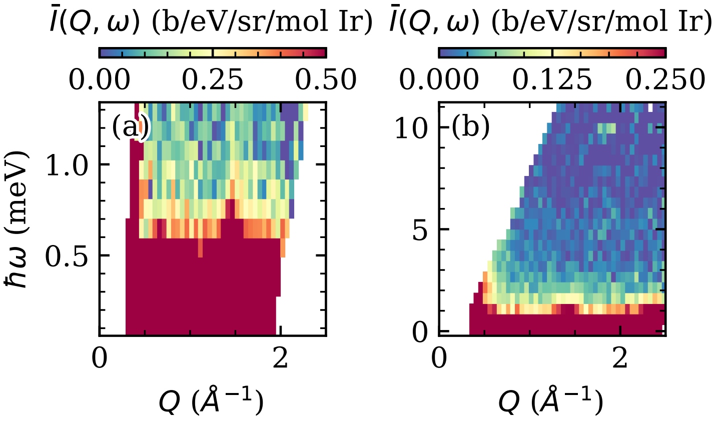

**Figure 7.3:** Scattering from the MACS experiment after subtraction of high temperature data as defined by Eq. 7.2 from the E$_f$=5.0 meV (a) and E$_f$=3.7 (b) configurations.

before produces the following:

$$\bar{I}(Q,\omega) = I_L(Q,\omega) - \frac{1-e^{-\beta_H\omega}}{1-e^{-\beta_L\omega}} I_H(Q,\omega)$$

$$\bar{I}(Q,\omega) = A(\omega)(1 - \frac{1-e^{-\beta_H\omega}}{1-e^{-\beta_L\omega}})I_{el}(Q) + B(\omega)I_{mag}(Q). \tag{7.2}$$

The nearest neighbor distance $d$ is 3.54 Å, and the parameters $C(\omega)$ and $B(\omega)$ are constants allowed to fit at each energy transfer. In Fig, 7.3 the quantity $\bar{I}$ is presented for both $E_f$ configurations. The remaining scattering of elastic origin is completely dominant in the E$_f$=3.7 meV $\bar{I}$ (Fig. 7.3(b)) and the elastic Bragg peak is seen in the E$_f$=5.0 meV measurement clearly up to energy transfer of $\hbar\omega$=2 meV.

To understand the origin of this background, we consider allowed phonon scattering processes from the MACS monochromator. MACS is a unique spectrometer in that it features an extremely large double focusing monochromator

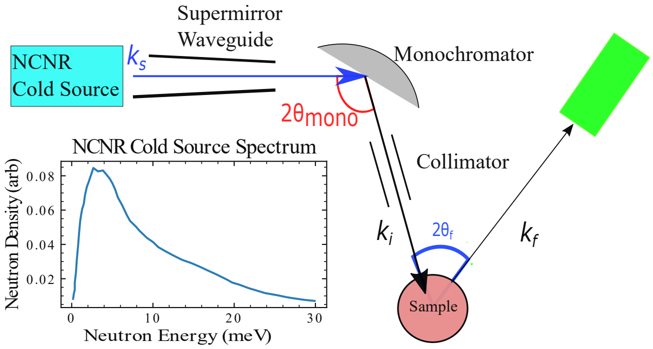

**Figure 7.4:** Sketch showing generic scattering process for a triple-axis spectrometer, where the incident energy setting defines the value of $2\theta_{mono}$. The inset shows the density of incident neutron energies from the cold source.

which provides an intense beam, but also admits any spurious features inherent to pyrolytic graphite. The intended Bragg reflection from the monochromator is the (002) Bragg peak, which under the assumption of elastic scattering defines the scattering angle of the monochromator $2\theta_{mono}$. This solely depends on the incident neutron energy setting. The instrumental configuration also defines the final neutron energy at the detector position $k_f$ using a double analyzer crystal array. Any scattering process that simultaneously satisfies the $2\theta_{mono}$ and $k_f$ requirements is allowed including phonons originating from the (002) peak in pyrolytic graphite. The scattering process is sketched in Fig. 7.4, and is summarized by the scattering condition

$$Q_{mono}^2 = k_s^2 + k_f^2 - 2k_s k_f cos(2\theta_{mono}). \tag{7.3}$$

The wavevector $k_s$ is an arbitrary wavevector for incident neutrons, and the momentum transfer at the monochromator is no longer fixed to be $|\tau_{002}|^2$ but instead an arbitrary value $Q_{mono}$. Of course, the elastic scattering condition with $Q = |\tau_{002}|^2$ will satisfy this condition, but using the distribution of

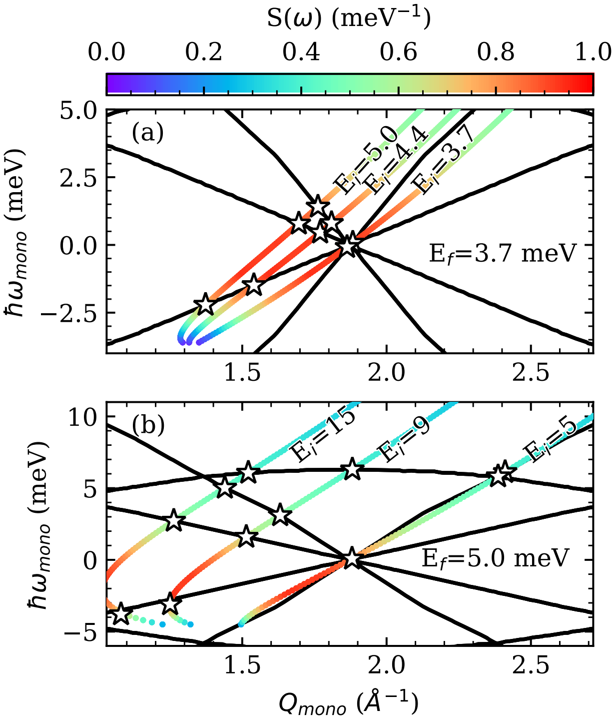

**Figure 7.5:** Depiction of allowed scattering vectors on the MACS instrument considering inelastic scattering at the monochromator for representative incident energy settings for the $E_f$=3.7 meV and $E_f$=5.0 meV used in the experiment. The $Q$ direction is along the (00$L$) axis of pyrolytic graphite, and the color map shows potential scattering vectors that satisfy the $2\theta$ condition to scatter from the monochromator to the sample. Solid black lines show phonon dispersion of pyrolytic graphite along the (00$L$) direction reproduced from Ref. [3].

neutrons incident on the monochromator from the cold source we find a large map of allowed scattering in $Q-\omega$ space. We may now weight this map by the spectral density of neutrons from the cold source which will be referred to as $S(\omega)$, which is reproduced in the inset of Fig. 7.4.

The color map in Fig. 7.5 depicts all allowed scattering paths that satisfy the scattering condition in Eq. 7.3. $2\theta_{mono}$ is fixed by the $E_i$ setting, $k_f$ is fixed by the $E_f$ setting, so using Eq. 7.5 one may calculate the $k_S$ wavevector for incoming neutrons for any momentum transfer at the monochromator $Q$. The result is the color map, upon which the low energy dispersion of pyrolytic graphite along the $(00L)$ direction has been plotted in black lines. The intercept of the color plot and the black lines represents a direct allowed paths for inelastic scattering from the monochromator to reach the sample for these particular $\mathrm{E}_f$ configurations. This results in lower incident energy neutron incident on the sample than intended, providing a measured energy transfer for elastic scattering processes which was previously described as the "leaking" of the elastic line into the inelastic channel. The spectral weight from the cold source and the $1/\omega$ contribution to the neutron phonon cross section both contribute to the absence of this effect at higher energy transfers.

This simple result has a tremendous effect on the background in the MACS measurements. To model this, the lowest accessible energy transfer in each $\mathrm{E}_f$ configuration is treated as purely elastic scattering. An elastic lineshape is then extracted to this by fitting a combination of a flat elastic incoherent term with Gaussian functions for Bragg peaks, which defines the elastic lineshape $I_{el}(Q)$. The quantity $\bar{I}(Q,\omega)$ is then fit using the following form to find the elastic contribution

$$\bar{I}(Q,\omega) = C(\omega)I_{el}(Q) + B(\omega)(1 + \frac{\sin(Qd)}{Qd}). \tag{7.4}$$

The nearest neighbor distance $d$ is 3.54 Å, and the parameters $C(\omega)$ and $B(\omega)$ are constants allowed to fit at each energy transfer. The extracted elastic line $I_{el}(Q)$ and its fitted contribution to the inelastic scattering are depicted in Fig. 7.6.

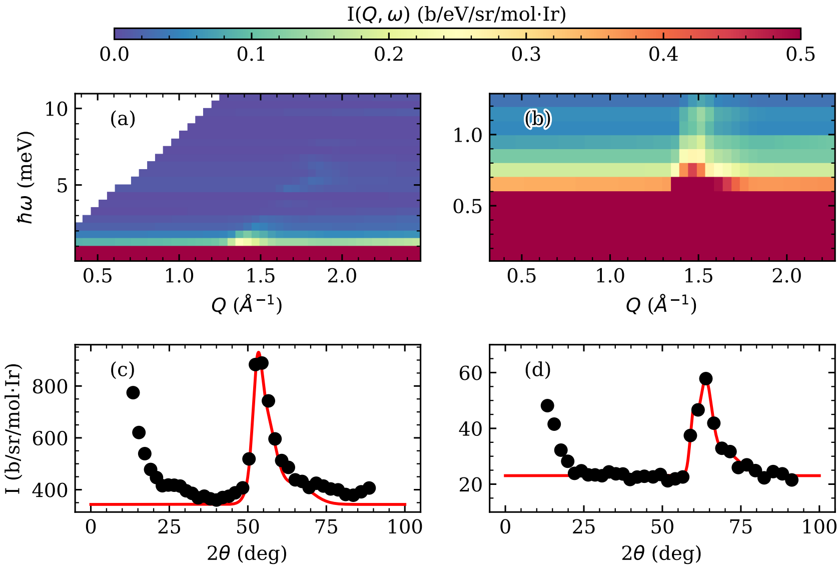

**Figure 7.6:** Extracted elastic contribution to inelastic signal from $D_3LiIr_2O_6$ for $E_f$=5.0 (a) and $E_f$=3.7 (b) configurations. Plots (c) and (d) show the elastic line shapes used to generate these inelastic backgrounds for the $E_f$=5 meV and $E_f$=3.7 meV configurations respectively.

The clearest way to track the elastic contribution to the background is by the Bragg peak, which will have a constant scattering angle $2\theta$ at every measured energy transfer as it is actually an elastic process. Fig. 7.6 clearly shows that the background completely dominates the $E_f$=3.7 meV measurement up to about 0.5 meV energy transfer, well beyond the expected resolution limited elastic FWHM of 0.1 meV. The issue is less significant in the $E_f$=5 meV measurement, where the Bragg peak becomes insignificant by about 2 meV energy transfer. These color plots are the backgrounds which are directly subtracted from $\bar{I}(Q,\omega)$, giving the magnetic scattering scattering in Fig. 4.15.

In retrospect, a better method of subtracting this scattering would have been to use a detailed-balance approach as was done for $\beta-Li_2IrO_3$. As the origin of the scattering is from the monochromator and elastic sample scattering, it is in theory temperature independent and would be removed quite easily using that method. Unfortunately for TAS spectrometers the negative energy transfer is not normally measured, as the beam time is better spent collecting statistics on faint signals. If possible in the future I would like to repeat this measurement using the new superior sample can on the MACS instrument and measure negative energy transfers to use the detailed balance method, which is much better constrained.

## 7.3 Transformation between Kitaev and XXZ coordinate systems

The XXZ-$J_1$-$J_3$ model can be related to the $JK\Gamma\Gamma'$ model by rotating the CF to the KF. Written in the KF, the local basis vectors of the CF are given by

$$\hat{x} = \frac{1}{\sqrt{6}}\left(1,1,-2\right)^T \tag{7.5a}$$

$$\hat{y} = \frac{1}{\sqrt{2}}\left(-1,1,0\right)^T \tag{7.5b}$$

$$\hat{z} = \frac{1}{\sqrt{3}}\left(1,1,1\right)^T \tag{7.5c}$$

It follows that the spins written in the CF and the KF are related by the following transformation

$$\mathcal{U} = \begin{pmatrix} \frac{1}{\sqrt{6}} & -\frac{1}{\sqrt{2}} & \frac{1}{\sqrt{3}} \\ \frac{1}{\sqrt{6}} & \frac{1}{\sqrt{2}} & \frac{1}{\sqrt{3}} \\ -\sqrt{\frac{2}{3}} & 0 & \frac{1}{\sqrt{3}} \end{pmatrix}. \tag{7.6}$$

The local exchange matrices are accordingly mapped from the CF to the KF by

$$H^{(i)}_{\mathrm{KF},\gamma} = \mathcal{U} H^{(i)}_{\mathrm{CF},\gamma} \mathcal{U}^T. \tag{7.7}$$

Mapping general bilinear couplings on the nearest-neighbor $z$ bond in the CF of the form

$$H^{(1)}_{\mathrm{CF},z} = \begin{pmatrix} J^{(1)}_{xy} + D & E & F \\ E & J^{(1)}_{xy} - D & G \\ F & G & J^{(1)}_z \end{pmatrix} \tag{7.8}$$

to the KF, we obtain the exchange matrix

$$H^{(1)}_{\mathrm{KF},z} = \begin{pmatrix} J + \eta & \Gamma & \Gamma'_1 \\ \Gamma & J - \eta & \Gamma'_2 \\ \Gamma'_1 & \Gamma'_2 & J + K \end{pmatrix} \tag{7.9}$$

with the following identification

$$J = -\frac{D}{3} + \frac{\sqrt{2}F}{3} + \frac{2J^{(1)}_{xy}}{3} + \frac{J^{(1)}_z}{3} \tag{7.10a}$$

$$\eta = -\frac{E}{\sqrt{3}} - \sqrt{\frac{2}{3}}G \tag{7.10b}$$

$$\Gamma = \frac{2D}{3} + \frac{\sqrt{2}F}{3} - \frac{J^{(1)}_{xy}}{3} + \frac{J^{(1)}_z}{3} \tag{7.10c}$$

$$\Gamma'_1 = -\frac{D}{3} + \frac{E}{\sqrt{3}} - \frac{F}{3\sqrt{2}} - \frac{G}{\sqrt{6}} - \frac{J^{(1)}_{xy}}{3} + \frac{J^{(1)}_z}{3} \tag{7.10d}$$

$$\Gamma'_2 = -\frac{D}{3} - \frac{E}{\sqrt{3}} - \frac{F}{3\sqrt{2}} + \frac{G}{\sqrt{6}} - \frac{J^{(1)}_{xy}}{3} + \frac{J^{(1)}_z}{3} \tag{7.10e}$$

$$K = D - \sqrt{2}F. \tag{7.10f}$$

We may write an equivalent conversion from the KF to the CF

$$J_{xy}^{(1)} = \frac{1}{3}(-\Gamma - \Gamma_1' - \Gamma_2' + 3J + K) \tag{7.11a}$$

$$J_z^{(1)} = \frac{1}{3}(2\Gamma + 2\Gamma_1' + 2\Gamma_2' + 3J + K) \tag{7.11b}$$

$$D = \frac{1}{3}(2\Gamma - \Gamma_1' - \Gamma_2' + K) \tag{7.11c}$$

$$E = \frac{\sqrt{3}}{8}(3\Gamma_1' - 3\Gamma_2' - 2\eta) \tag{7.11d}$$

$$F = \frac{\sqrt{2}}{6}(2\Gamma - \Gamma_1' - \Gamma_2' - 2K) \tag{7.11e}$$

$$G = \frac{\sqrt{6}}{8}(-\Gamma_1' + \Gamma_2' - 2\eta). \tag{7.11f}$$

It should be noted that assuming ideal edge-sharing bonds with $C_{2v}$ symmetry, the NN couplings in the KF of (7.9) are constrained to $\eta = 0$ and $\Gamma_1' = \Gamma_2'$. These constraints translate to $E = G = 0$ for the couplings in the CF of (7.8). The $R\bar{3}$ spacegroup associated with BCAO does break the $C_{2v}$ symmetry for the nearest-neighbor bond. Co occupies the 6c Wyckoff site at $(00z)$ where $z = 0.17014$[4]. This corresponds to a puckering of Co in and out of the honecomb plane by a distance $\pm(z - \frac{1}{6})c$=0.082Å.

The values in Eq. (14) of the main text are then represented in the KF by the following

$$\begin{aligned}
J^{(1)} &= -5.5 \text{ meV}, && \text{(7.12a)}\\
K^{(1)} &= 0.1 \text{ meV}, && \text{(7.12b)}\\
\eta^{(1)} &= 0.06 \text{ meV}, && \text{(7.12c)}\\
\Gamma^{(1)} &= 2.2 \text{ meV}, && \text{(7.12d)}\\
\Gamma_1'^{(1)} &= 2.0 \text{ meV} && \text{(7.12e)}\\
\Gamma_2'^{(1)} &= 2.2 \text{ meV} && \text{(7.12f)}\\
J^{(3)} &= 1.38 \text{ meV}, && \text{(7.12g)}\\
K^{(3)} &= 0.0 \text{ meV}, && \text{(7.12h)}\\
\eta^{(3)} &= 0.0 \text{ meV}, && \text{(7.12i)}\\
\Gamma^{(3)} &= -1.2 \text{ meV}, && \text{(7.12j)}\\
\Gamma_1'^{(3)} &= -1.2 \text{ meV}, && \text{(7.12k)}\\
\Gamma_2'^{(3)} &= -1.2 \text{ meV}. && \text{(7.12l)}
\end{aligned}$$

Here, the superscripts denote the NN and third NN bonds. Equivalently, the set of test parameters in Eq. 5.11 the main text may be written in the CF as

$$\begin{aligned}
J_{xy}^{(1)} &= -5.0 \text{ meV}, && \text{(7.13a)}\\
J_z^{(1)} &= -2.0 \text{ meV}, && \text{(7.13b)}\\
D &= -3.5 \text{ meV}, && \text{(7.13c)}\\
E &= 0 \text{ meV}, && \text{(7.13d)}\\
F &= 8.1 \text{ meV}, && \text{(7.13e)}\\
G &= 0 \text{ meV}. && \text{(7.13f)}
\end{aligned}$$

# Appendix References

1. Ducatman, S., Rousochatzakis, I. & Perkins, N. B. Magnetic structure and excitation spectrum of the hyperhoneycomb Kitaev magnet $\beta$-Li2IrO3. *Physical Review B* **97,** 125125. ISSN: 24699969 (12 2018).
2. Azuah, R. T., Kneller, L. R., Qiu, Y., Tregenna-Piggott, P. L., Brown, C. M., Copley, J. R. & Dimeo, R. M. DAVE: A comprehensive software suite for the reduction, visualization, and analysis of low energy neutron spectroscopic data. *Journal of Research of the National Institute of Standards and Technology* **114,** 341–358. ISSN: 1044677X. `https://pubmed.ncbi.nlm.nih.gov/27504233/` (6 2009).
3. Nicklow, R., Wakabayashi, N. & Smith, H. G. Lattice dynamics of pyrolytic graphite. *Physical Review B* **5,** 4951–4962. ISSN: 01631829. `https://journals.aps.org/prb/abstract/10.1103/PhysRevB.5.4951` (12 1972).
4. Zhong, R., Gao, T., Ong, N. P. & Cava, R. J. Weak-field induced nonmagnetic state in a Co-based honeycomb. *Science Advances* **6.** ISSN: 23752548. `https://www.science.org` (4 2020).

width=!,height=!,pages=-, pagecommand=